Departament de Física Aplicada i Òptica
Grup de Física i Enginyeria de Materials Amorfs i Nanoestructures

Mueller matrix polarimetry of anisotropic chiral media

Oriol Arteaga Barriel

Memòria presentada per optar al títol de Doctor en Física
Tesi dirigida pel Dr. Adolf Canillas i Biosca

Octubre de 2010

UNIVERSITAT DE BARCELONA

Programa de doctorat de Tècniques Instrumentals de la Física i la Ciència de Materials
Bienni 2005–2006
Universitat de Barcelona

A la meva família

Contents

Agraïments

Aquesta tesi ha estat possible gràcies a la col · laboració de tot un seguit de persones. Serveixi aquest apartat per expressar el meu agraïment a totes elles.

Per començar haig de destacar el paper de l'Adolf Canillas, el director de la tesi. Ell em va introduir en aquest tema de recerca i em va ensenyar bona part dels conceptes bàsics d'el · lipsometria. Li haig d'agrair especialment la llibertat que m'ha donat per poder seguir el meu criteri durant aquest anys de recerca i la seva inestimable ajuda i paciència a l'hora de resoldre totes les dificultats que han anat sortint, tant en el treball al laboratori com en la part teòrica. A més, també li haig donar les gràcies per la seva acurada revisió d'aquest manuscrit.

Em sento profundament afortunat d'haver pogut treballar amb en Josep Maria Ribó. És l'investigador més entusiasta que conec, i ha estat un gran exemple per a mi i una font constant de motivació per dur a terme aquest treball. També ell m'ha introduït en aspectes més lligats a la química que m'eren completament desconeguts fins fa poc i que ni imaginava que acabarien formant part d'aquesta tesi.

I am specially indebted to Jay Jellison. This thesis wouldn't have been possible without his participation. The two months I spent at his laboratory were, without any doubt, the most profitable period of work for this thesis. I have to acknowledge him for his warm welcome, for the freedom he gave me to work with his instruments and, above all, for the many things I was able to learn during my stay at his laboratory.

During conferences and workshops I have met many interesting people that also deserve to be mentioned here because, although I have only met them briefly, they have been a source for inspiration and new ideas. Among them I can remark Razvigor Ossikovsky, Enric Garcia-Caurel, Sergey Savenkov and, also, Bart Kahr for his interest in this work and for his kind invitation to visit NYU. I hope we can work together in the future and maintain fruitful collaborations.

Zoubir és una de les persones amb qui més he treballat durant aquests anys. Són moltes les hores que ha passat preparant bona part de les mostres que s'estudien en aquesta tesi. El seu optimisme i seu afany incasable per a la feina són tot un exemple. Juntament a ell, altres membres o ex-membres del grup d'en Josep Maria Ribó com ara en Carlos, en Joaquim i l'Alessandro han contribuït a la realització de molts dels experiments inclosos en aquest treball.

Haig d'agrair a tots els membres del grup FEMAN per la seva bona acollida

i el bon ambient de treball. Ferran, Carles, Roger, Coté, Esther, Albert, Miquel i Jordi són només alguns dels companys que formen o han format part d'aquest grup. L'Enric Bertran sempre ha estat disposat a ajudar-me en tot el possible i a més ha facilitat part del finançament que aquest treball ha requerit. Amb la Sabine hem compartit moltes estones al laboratori i a més de permetre'm practicar el meu francès desastrós li haig d'agrair l'interès que sempre ha mostrat per aquest treball. Menció especial mereix la Noemí, que durant la major part d'aquests anys ha estat una companya de despatx excepcional i que serà la pròxima a acabar la tesi.

També haig de fer extensiu l'agraïment a molts altres membres i ex-membres del departament de Física Aplicada i Òptica: becaris, professors, personal administratiu i tècnics.

La meva família ha estat el suport més preuat durant aquest període i per això aquesta tesi els hi està dedicada. Els meus pares, Montse i Jordi, que sempre m'han recolzat i que gràcies a ells sóc qui sóc. Del meu germà Daniel sempre he après moltes coses i va ser de qui vaig "copiar" estudiar Física i fer el doctorat. A més d'haver-me guiat en molts aspectes lligats la recerca científica, ha estat, juntament amb l'Estela, en tot moment pendent de com m'anava la tesi. Un tros d'aquest manuscrit també pertany a la meva àvia Maria i a la tia Maribel que sempre m'han ajudat en tot i estaran contentes de veure-la, per fi, acabada. De ben segur que a la iaia Pepita i avi Vicenç també els hi hagués fet il · lusió poder-la veure.

En definitiva, gràcies a totes les persones que han compartit aquest camí amb mi, sense vosaltres no hauria estat possible.

Preface

Optical activity is one of the most fascinating phenomena revealed by polarized light. It is observed when chiral materials interact with polarized electromagnetic beams and selectively couple with the left- or right-handed circularly polarized components. From a historic perspective, the study of optical activity has received more attention in chemistry than in any other field of science. Probably this is due to the dramatic consequences that the chirality of molecules or supramolecular structures has in life, as it is understood nowadays from a biochemistry perspective. Traditionally, among physicists, the interest in optical activity and its measurement has been relied to the study of the optical properties of anisotropic crystals. In any case, in applied physics and material science optical activity has not been usually in the focus of investigations.

Ellipsometry or, more generally, polarimetry are optical characterization techniques centered in the study and interpretation of polarized electromagnetic beams after interacting with media. Optically active materials have always been in the spotlight of these techniques, but only in comparatively few occasions the emphasis has been put on the specific problems that the measurements of optical activity and their interpretation presents. In spite of the steadily growing interest in media with complex response to polarized light, often specialists on polarimetry are not aware of the new challenges that the study of optical activity in supramolecular structures offers, or in the long-term problems that crystallographers have had to measure optical rotation for directions out of the optical axis in crystals.

When this thesis started, around five years ago, we had no idea that at the end it would be so much focused on the study of optical activity. At that time I hardly knew what optical activity was, but I could not imagine how much I would enjoy working on it. In fact, I am not sure I even knew the classic example of a solution of sugar molecules in water that rotates an incoming polarized light by a certain angle that depends on the concentration of sugar. Our starting point was the long-term experience that our research group had with ellipsometry and with self-built spectroscopic ellipsometers, and our initial plan was to renew them to start working with anisotropic samples. At the moment of writing this preface we realize that the term “Mueller polarimetry” describes better the type of measurements we have employed than the term “Mueller ellipsometry”, as this later tends to be associated, although not exclusively, to the reflection of light

at thin films and interfaces. In spite of this precision, in this memory we will indistinctly use either "ellipsometry" or "polarimetry" to refer to the technique we have employed.

This work uses polarimetry to study the phenomenon of interaction of polarized light with chiral samples. The development of polarimetry as a measurement technique and the interpretation of the corresponding data that it offers falls mostly within the domain of optics or electromagnetism. However most of the work we have done has been motivated by the study of problems that nowadays mostly belong to the domain of chemistry. The interaction between aspects from chemistry, based on the optical activity of molecular or supramolecular systems, and aspects from physics, based on light polarization, will be a constant during this work. Therefore this is a multidisciplinary work, in which the references to questions about molecular optical activity will be very frequent despite having been written under the perspective of physics. Due to the diversity of aspects that we have worked with, and to their associated multidisciplinarity, we are aware that this thesis is neither a good introductory text for newcomers to polarimetry nor a introductory explanation about molecular optical activity. In contrast, we hope that those readers with some background on polarization optics will find here some innovative and nonconventional application of polarimetry, and that readers with some experience in the study of optical activity will discover here how the Mueller matrix polarimetry can be useful to study complex optical active media.

I also take advantage of this preface to give a personal vision about the historical perspective of the study of the interaction of samples with optical activity with polarized light. During the 19th century this was a subject of feverous scientific investigation, because much of the progress made in the study and comprehension of light polarization and its interaction with materials came from the study of optical activity. This intense investigation on the subject was kept during the first part of 20th century. However, and although the work with optical active media in polarization optics has never stopped, during the second part of the 20th century and also during the first years of the 21st century the active research on new or in refined methods of measurement has apparently decreased. In contrast, during these decades the measurement of optical activity emerged as a routine characterization technique and was worldwide popularized in chemistry laboratories. As a result, measurements of optical activity became more numerous than ever before, but perhaps not many efforts were put on how to improve them. This can leave the sensation, in my opinion misleading, that everything in this field is already known and there is no place for new discoveries. The specialization in modern science has probably implied that the researchers that are more interested in optical activity are not specialists in polarized light and com-

munications between different scientific communities are not always fluid. This is probably the reason why, surprisingly for an applied research in the 21st century, to develop the part of the work we have performed with crystals, I had to resort many references that were many decades old to find there still unsurpassed reports about measurements of the optical activity of certain crystals. Fortunately, at the time of finishing the redaction of this thesis, I keep the gratifying feeling that there is still much to be done in this field, and I will be satisfied if at least a part of this sensation is transmitted to the reader.

Organization

This thesis is structured so as to give a complete account of the study of anisotropic optical active samples with Mueller polarimetry, covering aspects that range from theory of light propagation in anisotropic media to details of instrumental design. We have made an effort to make this thesis as self-contained as possible and we have included several review material for this purpose.

The work developed in this thesis can be divided in three big areas: study and interpretation of light propagation through an anisotropic optical active media in terms of the transmission Mueller matrix, design and construction of an appropriate instrument for the measurements of the Mueller matrix and the experimental results on particular anisotropic samples showing optical activity. We consider that this work introduces some degree of novelty in each of these three aspects and if there is a particular one that suscitate more interest will probably depend on the reader's background. Globally this thesis is divided in five parts.

Part I is formed by the two first preliminary chapters. In chapter 1 we introduce some basic concepts about light polarization and light propagation in optical media. In chapter 2 we give a general review on questions related to the measurements of molecular and supramolecular optical activity that serve as a motivation for later chapters.

Part II is devoted to the development of the theory that will be later used for the interpretation of experimental data. Chapter 3 focuses on the study of light propagation through anisotropic optical active media. The difficulty associated with this study is outlined in this chapter and special emphasis is put in presenting a differential matrix method formalism. Chapter 4 deals with the explicit problem of interpretation of a measured Mueller matrix. Two main alternatives are offered: an analytic inversion method and a decomposition method based on the algebra of Mueller matrices.

Part III is dedicated to the presentation of the experimental technique used in this thesis for the determination of the Mueller matrices. In chapter 5 we

introduce the instrument we have built for the spectroscopic measurement of the experimental Mueller matrices, the two-modulator generalized ellipsometer (2-MGE). Aspects about the design of the instrument as well as calibration procedures are presented. Chapter 6 describes a novel method that supposes a further improvement of the 2-MGE capabilities, because it permits us to obtain measurements with a high lateral resolution. In particular, it enables the characterization of samples which are in-plane heterogeneous.

Part IV includes some of the most significant experimental investigations about optical activity developed in the framework of this thesis. It begins with chapter 7, which presents the spectroscopic measurement of the gyration tensor of quartz crystal. Chapter 8 is dedicated to a series of experiments developed on solutions containing supramolecular structures that show a reversible chiral induction by effect of hydrodynamic flows. In chapter 9, heterogeneous solid state samples are studied using spatially resolved Mueller matrix mappings.

Part V comprises the main conclusions of the present work and two appendices. Appendix A is a Catalan summary of the thesis, while appendix B is an informal revision of the software written for the development of several of the tasks cited in the previous chapters.

Note on the second reprint

As of January 2011 new copies of this thesis have been printed (the first print was from September 2010). No appreciable changes in the contents of this thesis have been made in this new version, but several small errors detected in the first print have been corrected. The author is indebted to Maria Isabel Alonso and Gerald E. Jellison for kindly pointing out most of these errors.

Part I.

Backgrounds

Chapter 1.

Light propagation fundamentals. Jones and Mueller descriptions

With the formulation of the electromagnetic theory by James C. Maxwell it was shown that light is an electromagnetic wave with a frequency within a particular range. At that time it was already known from previous works on optics (e.g. Young and Fresnel) that when light propagates through an optical medium shows rather complicated behavior due to refraction and absorption phenomena. The electromagnetic theory has permitted the development of a rigorous theoretical framework for the successful analysis of the optical properties of a wide range of media. Nowadays the interest in this topic has not decreased because this is not a finished research, specially for anisotropic and/or inhomogeneous media.

In this chapter we give a short theoretical background on the propagation of light in a medium and we review some basic topics about polarization optics. This revision focuses on the presentation of Maxwell's equations and the constitutive relations for different type of media and on the different vector representations for polarized light. We finish with a phenomenological description of the various anisotropic polarization-dependent effects that can be present in a medium.

1.1. Light propagation

Maxwell's equations in differential form are given by:

$$\nabla \times \mathbf{E}(\mathbf{r},t) = -\frac{\partial \mathbf{B}(\mathbf{r},t)}{\partial t} \tag{1.1a}$$

$$\nabla \times \mathbf{H}(\mathbf{r},t) = \mathbf{J}(\mathbf{r},t) + \frac{\partial \mathbf{D}(\mathbf{r},t)}{\partial t} \tag{1.1b}$$

$$\nabla \cdot \mathbf{D}(\mathbf{r},t) = \rho(\mathbf{r},t) \tag{1.1c}$$

$$\nabla \cdot \mathbf{B}(\mathbf{r},t) = 0 \tag{1.1d}$$

where $\mathbf{E}$ is the electric field, $\mathbf{H}$ the magnetic field, $\mathbf{D}$ the electric displacement, $\mathbf{B}$ the magnetic flux density, $\mathbf{J}$ the current density and ρ the free charge density.

Relations between the physical quantities appearing in Eqs. (1.1) (i.e. between $\mathbf{E}$ and $\mathbf{D}$ and between $\mathbf{H}$ and $\mathbf{B}$) are required to solve the Maxwell equations. They are known as constitutive relations, and they are established by the physical properties of the medium in which light propagates. Maxwell's equations are generally held to be inviolable and, therefore, the properties of matter enter solely through the constitutive equations. In free space the constitutive relations are:

$$\mathbf{D} = \varepsilon_0 \mathbf{E}, \tag{1.2}$$

$$\mathbf{B} = \mu_0 \mathbf{H}, \tag{1.3}$$

where ε_0 and μ_0 are the permittivity and the permeability of vacuum, respectively. In general, the constitutive relations in regions filled by matter have the form

$$\mathbf{D} = \varepsilon_0 \mathbf{E} + \mathbf{P}, \tag{1.4}$$

$$\mathbf{B} = \mu_0 (\mathbf{H} + \mathbf{M}), \tag{1.5}$$

where $\mathbf{P}$ and $\mathbf{M}$ are, respectively, the electric and the magnetic polarizations and they can be interpreted as the average electric and magnetic dipole moment per unit volume. In a homogeneous linear isotropic dielectric medium, the electric polarization is parallel and proportional to the electric field:

$$\mathbf{P} = \varepsilon_0 \chi_e \mathbf{E}, \tag{1.6a}$$

so that

$$\mathbf{D} = \varepsilon_0 (1 + \chi_e) \mathbf{E} = \varepsilon \mathbf{E}, \tag{1.6b}$$

where χ_e is the electric susceptibility that is always positive and ε, the permittivity. Similarly, in isotropic homogeneous linear magnetic media, the magnetic polarization is parallel and proportional to the magnetic field.

$$\mathbf{M} = \chi_m \mathbf{H}, \tag{1.7a}$$

so that

$$\mathbf{B} = \mu_0 (1 + \chi_m) \mathbf{H} = \mu \mathbf{H}, \tag{1.7b}$$

where χ_m is the magnetic susceptibility that can be positive and negative; and μ is the permeability.

In an anisotropic material, the polarization and the electric field are not necessarily in the same direction. For these materials the electric and magnetic susceptibilities are in general tensors, which means that the permittivity $\boldsymbol{\varepsilon}$ and the permeability $\boldsymbol{\mu}$ are tensors:

$$\mathbf{D} = \boldsymbol{\varepsilon} \mathbf{E}, \tag{1.8a}$$

$$\mathbf{B} = \boldsymbol{\mu}\mathbf{H}. \tag{1.8b}$$

In this introductory section we will restrict our attention to the study of Maxwell's equations with linear isotropic constitutive relations. [Eqs. (1.6b) and (1.7b)]. Maxwell's equations (1.1) with these constitutive relations and in a source-free space (i.e. without current or charge densities) can be written as

$$\nabla \times \mathbf{E}(\mathbf{r},t) = -\mu \frac{\partial \mathbf{H}(\mathbf{r},t)}{\partial t}, \tag{1.9a}$$

$$\nabla \times \mathbf{H}(\mathbf{r},t) = \varepsilon \frac{\partial \mathbf{E}(\mathbf{r},t)}{\partial t}, \tag{1.9b}$$

$$\nabla \cdot \mathbf{E}(\mathbf{r},t) = 0, \tag{1.9c}$$

$$\nabla \cdot \mathbf{H}(\mathbf{r},t) = 0. \tag{1.9d}$$

Taking the curl at both sides of Eq. (1.9a) and substituting Eq. (1.9b) we get

$$\nabla \times (\nabla \times \mathbf{E}) = -\mu\varepsilon \frac{\partial^2 \mathbf{E}}{\partial t^2}. \tag{1.10}$$

Applying the identity $[\nabla \times \nabla \times = \nabla(\nabla\cdot) - \nabla^2]$ and using Eq. (1.9c) we obtain the wave equation:

$$\nabla^2 \mathbf{E} - \frac{1}{u^2}\frac{\partial^2 \mathbf{E}}{\partial t^2} = 0 \tag{1.11}$$

where $u = (\mu\varepsilon)^{-1/2}$ is the phase velocity of light propagating in the medium [in vacuum $u = (\mu_0\varepsilon_0)^{-1/2} \equiv c$]. $n = c/u$ is referred to as the index of refraction.

For a monochromatic wave the time variation of the electric field vector is sinusoidal: $\mathbf{E}(\mathbf{r},t) = E(r)e^{i\omega t}$ where ω is the angular frequency. Substituting it into Eq. (1.11) and introducing the wavenumber, $k = \omega/u$, we get

$$\nabla^2 \mathbf{E}(\mathbf{r}) + k^2 \mathbf{E}(\mathbf{r}) = 0, \tag{1.12}$$

which is known as the Helmholtz equation.

In this thesis we will focus our attention on chiral anisotropic media. Such media, also called gyrotropic media, exhibit optical activity and the physics underlying their interaction with the electromagnetic fields is more complex than for nongyrotropic systems. If a medium is chiral and anisotropic its constitutive relations are different from those presented in Eqs. (1.8). We discuss in detail light propagation through this type of media in chapter 3.

1.2. Plane waves and polarization of light

A plane wave is a constant-frequency wave whose wavefronts are infinitely parallel planes of constant amplitude normal to the phase velocity vector. A uniform

plane wave is a particular solution of Maxwell's equations in a homogeneous region of the space.

Given a plane wave with a direction of propagation $\hat{\mathbf{k}}$, Maxwell's equations impose that the electric and magnetic field should be perpendicular to the direction of propagation and one to each other. Conventionally, when considering polarization, only the electric field vector is described, since the magnetic field is perpendicular to the electric field and proportional to it. For instance, the electric field vector of a plane wave propagating along the z-axis ($\hat{\mathbf{k}} \equiv \hat{\mathbf{z}}$) is

$$\mathbf{E}(z,t) = (E_{x0}e^{i\delta_x}\hat{\mathbf{x}} + E_{y0}e^{i\delta_y}\hat{\mathbf{y}})e^{[i(\omega t - kz)]} \tag{1.13}$$

where the amplitudes E_{x0} and E_{y0} are real numbers. The polarization state is given by the relative difference in magnitude and phase between these components. Note that we have chosen the $e^{i\omega t}$ time-dependence instead of $e^{-i\omega t}$. This results in negative imaginary parts of the dielectric functions of materials.

If we consider the electric field at a certain point z as a function of time [Eq. (1.13) with a fixed z value] we obtain the representation of an ellipse in the plane xy (Fig. 1.1). The parameters that describe the ellipse are the azimuth $\theta \in [-\frac{\pi}{2}, \frac{\pi}{2}]$ and the ellipticity[1] $\epsilon \in [-\frac{\pi}{4}, \frac{\pi}{4}]$. For a vanishing ellipticity the two components of the electric field are in phase and the light wave is linearly polarized. When $\epsilon = \pm\frac{\pi}{4}$ the polarization is circular. When ϵ does not satisfy any of the above conditions the light wave is elliptically polarized.

The handedness of the ellipse of polarization determines the sense in which the ellipse is described. The polarization is *right-handed* if the field vector rotates clockwise when looking against the direction of $\hat{\mathbf{k}}$ (i.e. looking "into the beam" for a travelling wave). Similarly, the polarization is *left-handed* for a counter-clockwise rotation sense.

1.3. Jones vectors and Jones matrices

The *Jones vector* is a direct way to describe polarized light. It was introduced by the American Physicist R. Clark Jones in 1941 [1]. The *Jones vector* can be built by noting that Eq. (1.13) can be casted in the form of a column vector:

$$\mathbf{E}(z,t) = \begin{bmatrix} E_{x0}\exp\left[i(\omega t - kz + \delta_x)\right] \\ E_{y0}\exp\left[i(\omega t - kz + \delta_y)\right] \end{bmatrix} = \exp\left[i(\omega t - kz)\right] \begin{bmatrix} E_{x0}e^{i\delta_x} \\ E_{y0}e^{i\delta_y} \end{bmatrix}. \tag{1.14}$$

[1] Sometimes the denomination of *ellipticity* is given to $e = \pm\tan\epsilon$ where the + and − signs correspond to right- and left-handed polarizations, respectively. In these cases ϵ is referred to as *ellipticity angle*.

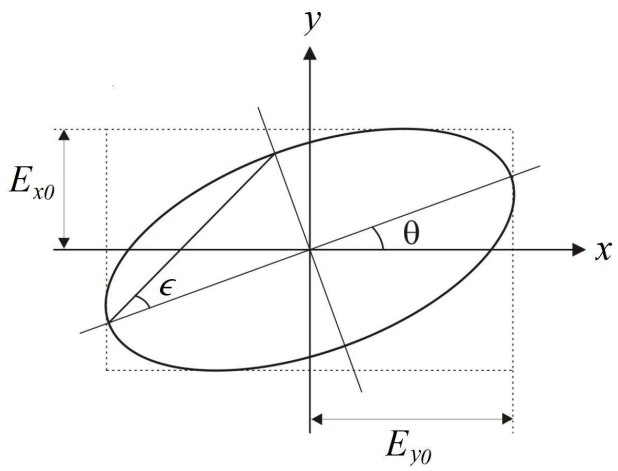

Figure 1.1.: The polarization state can be described by two characteristic angles of the polarization ellipse: the azimuth θ, and the ellipticity ϵ.

To express a Jones vector the term $\exp[i(\omega t - kz)]$ is usually omitted and Eq. (1.14) is thus simplified to

$$\mathbf{E}(z,t) = \begin{bmatrix} E_x \\ E_y \end{bmatrix}, \tag{1.15}$$

where E_x and E_y are complex amplitudes:

$$E_x = E_{x0} e^{i\delta_x}, \tag{1.16a}$$

$$E_y = E_{y0} e^{i\delta_y}. \tag{1.16b}$$

The Jones vector is a direct representation of a single, monochromatic, uniform and transverse-electric plane wave. It contains complete information about the amplitudes and phases of the field components, hence about the polarization of the wave. Jones vectors describe completely polarized light. As a strictly monochromatic wave is always completely polarized, i.e. E_{x0}, E_{y0}, δ_x and δ_y are constants, there is always a Jones vector associated to a monochromatic wave. However, real life light beams are, at best, quasi-monochromatic, which means that some slow fluctuations of amplitudes and phases of the fields may be present. A quasi-monochromatic wave can be regarded as a superposition of mutually incoherent monochromatic light beams whose frequencies vary in a narrow bandwidth $\delta\omega$ around a central frequency ω_0. A quasi-monochromatic wave behaves like a monochromatic wave for times much shorter than the coherence

time of the wave and, within this limit, the description of the polarization states of quasi-monochromatic light in terms of the Jones vectors is valid.

Light intensity can be obtained by pre-multiplying the Jones vector $\mathbf{E}$ by its Hermitian adjoint $\mathbf{E}^{\dagger}$ [2]:

$$I = \mathbf{E}^{\dagger}\mathbf{E} = E_x^* E_x + E_y^* E_y. \tag{1.17}$$

The overall effect of the interaction of light with a medium or an optical system can be described by a 2×2 complex matrix $\mathbf{J}$, referred to as *Jones matrix*:

$$\begin{bmatrix} E'_x \\ E'_y \end{bmatrix} = \mathbf{J} \begin{bmatrix} E_x \\ E_y \end{bmatrix}. \tag{1.18}$$

$E_{x,y}$ and $E'_{x,y}$ are, respectively, the electric vector components of incident and outgoing light.

The Jones matrix $\mathbf{J}$ is composed of four elements which in general are complex. Therefore, to completely define a Jones matrix 8 independent real parameters are needed. The Jones matrix describing a series of optical elements is equal to the matrix product of the Jones matrix of each element. If we focus our attention on the incident and the emergent plane wave, the overall effect of an entire cascade of N optical elements is described by

$$\mathbf{E_o} = \mathbf{J_N J_{N-1} ... J_{II} J_I E_i} = \mathbf{J_{comb} E_i}, \tag{1.19}$$

where $\mathbf{J_{comb}} = \mathbf{J_N J_{N-1} ... J_{II} J_I}$. The incident plane wave encounters the optical element I first, then element II, etc.

Jones matrices are related to the particular coordinate system used to specify the orientations of the incident and emergent light beams. The effect of rotating both the input and output coordinate system by the same angle α (positive for a counter-clockwise rotation looking against the direction of propagation[3]) is to transform the Cartesian Jones matrix of the optical system according to:

$$\mathbf{J'} = \mathbf{R}(\alpha)\mathbf{J}\mathbf{R}(-\alpha), \quad \text{where} \quad \mathbf{R}(\alpha) = \begin{bmatrix} \cos\alpha & \sin\alpha \\ -\sin\alpha & \cos\alpha \end{bmatrix}. \tag{1.20}$$

In this equation the polarization element remains fixed but the coordinate system rotates by α. In the case in which the coordinate system remains fixed but there

[2] The Hermitian adjoint of a matrix is the complex conjugate of the transpose of the matrix, thus $\mathbf{E}^{\dagger}$ is a row vector.

[3] This definition of positive azimuthal rotation angles is not universal in optics. There are authors that use the opposite convention and, sometimes, this is not clearly noticed. If the opposite convention was used the Jones matrix of rotation would be $\mathbf{R}(\alpha) = \begin{bmatrix} \cos\alpha & -\sin\alpha \\ \sin\alpha & \cos\alpha \end{bmatrix}$.

is a rotation of the polarization element by an angle α such that the angle of incidence is unchanged (for a normal-incidence beam, rotating the element about the normal), the resulting Jones matrix is

$$\mathbf{J}_\alpha = \mathbf{R}(-\alpha)\mathbf{J}\mathbf{R}(\alpha). \tag{1.21}$$

Quasi-monochromatic radiation is not necessarily completely polarized. It can also be unpolarized or partially polarized and, in practice, partially polarized light is frequently found experimentally. The Jones formalism can only handle completely polarized light. A different formalism that can be also applied to partially polarized or unpolarized radiation is described in the next section.

1.4. Stokes parameters and Mueller matrices

The polarization state of light can also be specified by a set of parameters that form the so-called *Stokes vector* **S**:

$$\mathbf{S} = \begin{bmatrix} S_0 \\ S_1 \\ S_2 \\ S_3 \end{bmatrix} = \begin{bmatrix} I \\ Q \\ U \\ V \end{bmatrix} = \begin{bmatrix} < E_x^* E_x + E_y^* E_y > \\ < E_x^* E_x - E_y^* E_y > \\ < E_y^* E_x + E_x^* E_y > \\ < i(E_y^* E_x - E_x^* E_y) > \end{bmatrix}. \tag{1.22}$$

The angle brackets $< ... >$ denote a time average and it is introduced to account for the fluctuations in the amplitude and phase of quasi-monochromatic light. The first Stokes parameter, I, is the total intensity of electromagnetic radiation, while the other three parameters describe the polarization state of radiation. For every Stokes vector the Stokes parameters satisfy the inequality

$$I^2 \geq Q^2 + U^2 + V^2, \tag{1.23}$$

in which the equality is only satisfied for completely polarized light. The degree of polarization p is defined from the Stokes parameters as

$$p = \frac{\sqrt{Q^2 + U^2 + V^2}}{I}. \tag{1.24}$$

Thus, for completely polarized light $p = 1$, for unpolarized light $p = 0$, and for partially polarized $0 < p < 1$.

The Stokes parameters were introduced by Stokes in the XIX century. However the matrix method for manipulating Stokes vectors was developed by Hans Mueller much later, in the 1940's [2]. The Stokes vector representation is directly connected with experiment, because it uses real and measurable intensities instead of complex numbers. This has caused that Mueller matrices have

become popular when performing experimental work in polarization optics; in fact, many modern optical instruments are able to partially or completely determine the Mueller matrix of an optical sample.

A Mueller matrix $\mathbf{M}$ is a 4×4 matrix with 16 real elements that connects the input and output Stokes vectors after the interaction of electromagnetic radiation with an optical medium.

$$\mathbf{S}^{out} = \mathbf{M}\mathbf{S}^{in}. \tag{1.25}$$

The upper-left element of Mueller matrix $\mathbf{M}$, m_{00}, is a gain for unpolarized incident light and it must hold the inequality $m_{00} > 0$. A normalized Mueller matrix is obtained by scaling the matrix such that the upper left element is equal to one.

$$\mathbf{M}^* = \begin{bmatrix} 1 & m_{01}/m_{00} & m_{02}/m_{00} & m_{03}/m_{00} \\ m_{10}/m_{00} & m_{11}/m_{00} & m_{12}/m_{00} & m_{13}/m_{00} \\ m_{20}/m_{00} & m_{21}/m_{00} & m_{22}/m_{00} & m_{23}/m_{00} \\ m_{30}/m_{00} & m_{31}/m_{00} & m_{32}/m_{00} & m_{33}/m_{00} \end{bmatrix}. \tag{1.26}$$

The elements of a normalized Mueller matrix have values between -1 and 1. All the experimental Mueller matrices that will be shown in this work are normalized.

A rotation of the coordinate system by an angle α (positive for a counterclockwise rotation looking against the direction of propagation) can be expressed as a matrix multiplication, in analogy to the coordinate rotation of Jones matrices presented in Eq. (1.20):

$$\mathbf{M}' = \mathbf{R}(\alpha)\mathbf{M}\mathbf{R}(-\alpha), \quad \text{where} \quad \mathbf{R}(\alpha) = \begin{bmatrix} 1 & 0 & 0 & 0 \\ 0 & \cos 2\alpha & \sin 2\alpha & 0 \\ 0 & -\sin 2\alpha & \cos 2\alpha & 0 \\ 0 & 0 & 0 & 1 \end{bmatrix}. \tag{1.27}$$

On the other hand, if the polarization element described by the Mueller matrix is rotated by an angle α, then the resulting Mueller matrix is

$$\mathbf{M}_\alpha = \mathbf{R}(-\alpha)\mathbf{M}\mathbf{R}(\alpha). \tag{1.28}$$

The inequality in Eq. (1.23) is important because it allows the classification of the character of light-medium interaction. For completely polarized input light, if the output light satisfies Eq. (1.23) as an equality, then we say that the medium is non-depolarizing (i.e. the exiting beam is still completely polarized).

For every Jones matrix there exists a corresponding Mueller matrix. To emphasize this connection, we will call those Mueller matrices which can be derived from a Jones matrix as "Mueller-Jones" matrices. The Mueller-Jones matrix corresponding to any Jones matrix can be calculated using the following relation [3]:

$$\mathbf{M} = A(\mathbf{J} \otimes \mathbf{J}^*)A^{-1}, \tag{1.29}$$

where $\otimes$ denotes de Kronecker product and A is

$$A = \frac{1}{\sqrt{2}} \begin{bmatrix} 1 & 0 & 0 & 1 \\ 1 & 0 & 0 & -1 \\ 0 & 1 & 1 & 0 \\ 0 & i & -i & 0 \end{bmatrix}. \tag{1.30}$$

A general Jones matrix has 8 independent parameters. The absolute phase information is lost in the Mueller-Jones matrix, leading to only 7 independent matrix elements for a Mueller-Jones matrix derived from a Jones matrix. Therefore, it is evident that in a Mueller-Jones matrix there exist 9 interrelations o constraints among its 16 elements[4]. In the case of normalized Jones or Mueller-Jones matrices the number of independent parameters is 6, because both the absolute phase and absolute intensity information are lost. It has been demonstrated [6] that a necessary and sufficient condition for a Mueller matrix $\mathbf{M}$ to be a Mueller-Jones matrix is:

$$\sum_{i=0}^{3}\sum_{j=0}^{3} m_{ij}^2 = 4m_{00}^2. \tag{1.31}$$

A 4×4 real matrix is not a physically realizable Mueller matrix if it can operate on an incident Stokes vector to produce a vector with a degree of polarization greater than one, which is a physically unrealizable polarization state. Experimentally it is possible to obtain a physically unrealizable Mueller matrix because of the noise inherent to experimental data and since the matrices of several ideal optical elements (polarizers, retarders) lie in the boundary between physically realizable Mueller matrices and nonphysical unrealizable matrices. The conditions for physical realizability have been thoroughly studied in the literature and several necessary conditions for the physical realizability have been published [7, 8]. One of the most cited criteria for Mueller matrix physically realizability is that the eigenvalues of the associated coherency matrix need to be non-negative [7].

1.4.1. Depolarization

Depolarization is the reduction of the degree of polarization of light. Depolarization can be the result of decorrelation of the phases and the amplitudes of the electric vector as well as the selective absorption of the polarization state [9]. In fact, a measured Mueller matrix is a mixture of pure (non-depolarizing) states, depolarization and a certain amount of noise [10]. Despite depolarization phenomenon is involved in many experimental measurements, it is perhaps the least

[4]See Refs. [4] and [5] for the explicit equations.

understood characteristic concerning polarized light, being the problem of light-medium interaction in presence of depolarization studied with considerably less degree of accuracy than the non-depolarizing case. In polarimetry the causes of depolarization can be multiple, many of them are due to some type of incoherent scattering introduced by the sample or the incoherent superposition of the light interacting from different materials. Another source of depolarization is caused by the finite spectral resolution of the instruments (determined in most cases by the monochromator). Instead of being perfectly monochromatic they integrate over a range of wavelengths, resulting in quasi-depolarization.

Some media depolarize all the input polarization states equally (isotropic depolarization). Other media depolarize some polarization states but may not depolarize some particular polarization states (anisotropic depolarization). The Mueller matrix of an isotropic depolarizer is:

$$\begin{bmatrix} 1 & 0 & 0 & 0 \\ 0 & p & 0 & 0 \\ 0 & 0 & p & 0 \\ 0 & 0 & 0 & p \end{bmatrix}. \tag{1.32}$$

When $p = 0$ one has the Mueller matrix of the ideal depolarizer.

To investigate the depolarization features of a medium it is useful to use the polarization fraction β of a Mueller matrix that was introduced by Gil and Bernabeu [11,12] . It is the euclidian distance of the normalized Mueller matrix from the ideal depolarizer:

$$\beta = \frac{\sqrt{(\sum_{ij} m_{ij}^2) - m_{00}^2}}{\sqrt{3} m_{00}}, \tag{1.33}$$

here β varies from zero for an ideal depolarizer to 1 for all non-depolarizing Mueller matrices. All intermediate values are associated with partial depolarization.

Eq. (1.33) is the figure of merit that we will use through this work to quantify depolarization of experimental Mueller matrices. Nevertheless it is not the only available criterion for depolarization in the literature. Another used criterion was introduced by Cloude [13] and is based on the normalized eigenvalues of the coherency matrix associated with the Mueller matrix to define a "entropy" parameter that is understood as a degree of depolarization. Recently, Ossikovski has published two alternative criteria [14] that are claimed to offer a better identification of depolarization for certain classes of Mueller matrices.

1.5. Basic polarization changes induced by transmissive optical elements

In this section we will consider a simplified phenomenological approach to describe the various forms in which an optical element can modify the polarization of a light beam that traverses it. Let us consider a monochromatic plane wave propagating along the positive direction of the z axis of an x, y, z orthogonal, right-handed, Cartesian coordinate laboratory system. Further, we will assume that the light beam traverses the optical element and does not change the direction of propagation; thus the electric field components are always in the xy plane.

When an electromagnetic wave passes through a non-depolarizing medium it can change in intensity, phase and polarization, all of them defined relative to the case where there is no medium. Although in this work we are mostly interested in the changes of polarization, we cannot forget that every medium can also introduce a change in intensity and absolute phase of the electromagnetic waves that traverse it.

With these premises we will consider light propagation through a dichroic (diattenuating) and birefringent (retarding) anisotropic and non-depolarizing medium. In this medium eight different types of optical behaviour are measurable in the xyz laboratory coordinate system: six of them are related to changes in polarization, one to changes in the absolute phase, and another one to changes in the intensity. These can be described using Jones vectors since they contain complete information about the amplitudes and phases of the field components.

1.5.1. Absolute phase and intensity changes

We start presenting the simple case of free propagation of a plane wave of light through a medium that does not induce any change in the polarization. Light propagates through this medium at a different speed with respect to the case where there is no medium. Also absorption processes can change the amplitude of the components of the field. The complex index of refraction $\tilde{n}$ can be used to calculate the complex phase shift induced by the medium:

$$\mathbf{E}' = \mathbf{E}e^{-i\frac{2\pi}{\lambda}\tilde{n}l} = \mathbf{E}e^{-i\frac{2\pi}{\lambda}nl}e^{-\frac{2\pi}{\lambda}kl} \equiv \mathbf{E}e^{-i\chi}, \tag{1.34}$$

where the complex index of refraction is $\tilde{n} \equiv n - ik$ and $\chi \equiv \eta - i\kappa$. Therefore:

$$\eta = \frac{2\pi}{\lambda}nl, \tag{1.35a}$$

$$\kappa = \frac{2\pi}{\lambda}kl. \tag{1.35b}$$

The Jones vector transformation of Eq. (1.34) in matrix form is:

$$\begin{bmatrix} E'_x \\ E'_y \end{bmatrix} = \begin{bmatrix} e^{-i\chi} & 0 \\ 0 & e^{-i\chi} \end{bmatrix} \begin{bmatrix} E_x \\ E_y \end{bmatrix}. \tag{1.36}$$

The term $e^{-i\frac{2\pi}{\lambda}nl}$ of Eq. (1.34) expresses the simple fact that the wave has been retarded by $\frac{2\pi}{\lambda}nl$, while the term $e^{-\frac{2\pi}{\lambda}kl}$ expresses the amplitude attenuation of the Jones vector components.

The factor $e^{-\frac{2\pi}{\lambda}kl}$ is related to the well-known Beer-Lambert law, which is used to study the absorption of light when it travels through a material. This law states that there is a logarithmic dependence between the transmission, T, and the product of the absorption coefficient of a substance, α, and the distance the light travels through the material, l:

$$T = \frac{I}{I_0} = 10^{-\alpha l} = 10^{-A}, \tag{1.37}$$

This equation can be also written in the base of natural logarithms

$$T = \frac{I}{I_0} = e^{-\alpha_e l} = e^{-A_e}. \tag{1.38}$$

Consequently the relation between A and A_e is $A = \ln 10 A_e$. Eq. (1.38) can be rewritten as $I = I_0 e^{-A_e}$, and as the intensity of a wave is the square of its amplitude A we have $A = A_0 e^{-A_e/2}$ and we get the relation:

$$A_e = \frac{4\pi}{\lambda}kl, \tag{1.39}$$

that written in terms of α_e is $\alpha_e = 4\pi k/\lambda$. By default all the absorptions given in this work will be displayed in the base of natural logarithms.

1.5.2. Polarization changes

Linear birefringence

Suppose that the medium through which the wave is propagating is linearly birefringent, which means that there is one axis of symmetry, called the optic axis, which imposes constraints upon the propagation of light beams within the material. Two particular modes of propagation can be described, either as an ordinary beam polarized in a plane perpendicular to the optic axis, or as an extraordinary beam polarized in a plane containing the optic axis[5]. Each one of

[5] These two modes are sometimes referred to as *eigenmodes*, because radiation linearly polarized according to any of these two modes will not be changed when going through the medium. For any other direction of polarization, or for circular polarization, the polarization form will change as the radiation passes through a linearly birefringent medium

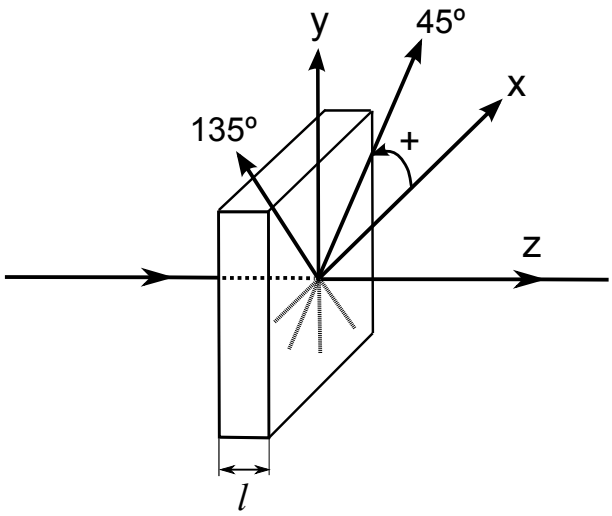

Figure 1.2.: Scheme of Cartesian coordinate system used for the description of the optical effects. The optical element is supposed to be a plane-parallel section of width l.

the beams has an associated refractive index and the difference between these refractive indices is eventually known as linear birefringence.

When the value of the linear birefringence of a certain material is given in the literature, it is implicitly assumed that this value corresponds to the natural basis of the material (a coordinate system that corresponds with its optic axis), so that the given value of the linear birefringence is the difference between the refractive indices for extraordinary, n_e, and ordinary polarizations, n_o. Nevertheless, during experiments, the orientation of the optic axis for a certain sample is in general unknown and the measurements take place in a laboratory coordinate frame not coincident with the optical axis. For optical calculus it is useful to define the laboratory axes shown in Fig. 1.2: x, y, 45° to x and 135° to x because these axes permit to define two parameters, for the projection of linear birefringence along x and another for the projection along 45° that come in linearly in the Mueller matrix calculus.

In an arbitrarily oriented linearly birefringent medium if the wave that propagates in the z direction is linearly polarized parallel to the x axis, the wave will experiment a specific refractive index n_x and will travel at a speed c/n_x, where c is the speed of light in vacuum. On the other hand, if the wave is linearly polarized orthogonal to the x axis, the wave will experience a different refractive index n_y and will travel at a speed c/n_y. Again, if the wave is polarized at 45°

to the x direction it will experience a refractive index n_{45}, and if it is orthogonal to this last direction the refractive index will be n_{135}. It is worth to stress that n_x, n_y, n_{45} and n_{135} are not independent between them; they all can be related to n_e and n_o if the orientation of the optical axis in our laboratory coordinate frame is known, as it will be further discussed in Section 3.2.3. Using these newly defined refractive indices, the effect of wave propagation in birefringent media can be described using the following two parameters :

- the horizontal linear birefringence projection,

$$\mathrm{LB} = \frac{2\pi}{\lambda}(n_x - n_y)l, \tag{1.40}$$

- and the 45° linear birefringence projection,

$$\mathrm{LB}' = \frac{2\pi}{\lambda}(n_{45} - n_{135})l, \tag{1.41}$$

where l is the travelled distance.

The effect of the horizontal linear birefringence on a Jones vector is given by the Jones matrix.

$$\mathbf{J}_{\mathrm{LB}} = \begin{bmatrix} e^{-i\frac{2\pi}{\lambda}n_x l} & 0 \\ 0 & e^{-i\frac{2\pi}{\lambda}n_y l} \end{bmatrix}, \tag{1.42}$$

and, alternatively, this matrix can be written in a more convenient form:

$$\begin{aligned} \mathbf{J}_{\mathrm{LB}} &= e^{-i\frac{2\pi}{\lambda}n_x l}\begin{bmatrix} 1 & 0 \\ 0 & e^{i\frac{2\pi}{\lambda}(n_x-n_y)l} \end{bmatrix} = e^{-i\frac{\pi}{\lambda}(n_x+n_y)l}\begin{bmatrix} e^{-i\frac{\pi}{\lambda}(n_x-n_y)l} & 0 \\ 0 & e^{i\frac{\pi}{\lambda}(n_x-n_y)l} \end{bmatrix} \\ &= e^{-i\eta/2}\begin{bmatrix} e^{-i\mathrm{LB}/2} & 0 \\ 0 & e^{i\mathrm{LB}/2} \end{bmatrix}, \end{aligned} \tag{1.43}$$

where the outside scalar factor represents an isotropic phase delay.

Leaving aside the isotropic factor, the effect of the 45° linear birefringence on a Jones vector in the coordinate axes $x-y$ can be easily calculated by a coordinate rotation of $-45°$ from the $45° - 135°$ axes to the $x - y$ axes:

$$\mathbf{J}_{\mathrm{LB}'} = \mathbf{R}(-45°)\begin{bmatrix} e^{-i\mathrm{LB}'/2} & 0 \\ 0 & e^{i\mathrm{LB}'/2} \end{bmatrix}\mathbf{R}(45°) = \begin{bmatrix} \cos\mathrm{LB}'/2 & -i\sin\mathrm{LB}'/2 \\ -i\sin\mathrm{LB}'/2 & \cos\mathrm{LB}'/2 \end{bmatrix}. \tag{1.44}$$

If the maximum value of the birefringence, LB_θ, is obtained at angle θ then LB and LB′ are related to LB_θ and θ by:

$$\mathrm{LB} = \mathrm{LB}_\theta \cos 2\theta, \tag{1.45a}$$

$$\mathrm{LB}' = \mathrm{LB}_\theta \sin 2\theta. \tag{1.45b}$$

It is important to stress that neither of the quantities defined LB or LB′ and that we, respectively, name as horizontal or 45° linear birefringence are equivalent to the common definition of linear birefringence that is made in crystal optics bibliography[6]. Our definitions of LB or LB′ are always given with reference to the laboratory coordinate system instead of from the own optic-axis based coordinate system of the anisotropic medium. In other words, values of LB and LB′ change if the orientation of the anisotropic medium changes.

Linear dichroism

If the wave propagates through a linearly dichroic medium, a linearly-polarized wave travelling in a direction perpendicular to the optic axis will be attenuated by different amounts depending upon the direction of the vibration of the transverse electric field with respect to the optic axis. Following an analogous argumentation to that presented in the previous section let k_x and k_y respectively denote the extinction coefficients of the medium for light linearly polarized parallel and orthogonal to the x axis, while k_{45} and k_{145} are the extinction coefficients for light linearly polarized parallel and orthogonal to the 45° axis. With these coefficients we can define the following parameters:

- the horizontal linear dichroism projection,

$$\mathrm{LD} = \frac{2\pi}{\lambda}(k_x - k_y)l, \tag{1.46}$$

- the 45° linear dichroism projection,

$$\mathrm{LD}' = \frac{2\pi}{\lambda}(k_{45} - k_{135})l. \tag{1.47}$$

The Jones matrix related to the horizontal linear dichroism is

$$\mathbf{J}_{\mathrm{LD}} = e^{-i\eta/2}\begin{bmatrix} e^{-\frac{2\pi}{\lambda}k_x l} & 0 \\ 0 & e^{-\frac{2\pi}{\lambda}k_y l} \end{bmatrix} = e^{-i\eta/2}e^{-i\kappa/2}\begin{bmatrix} e^{-\mathrm{LD}/2} & 0 \\ 0 & e^{\mathrm{LD}/2} \end{bmatrix}. \tag{1.48}$$

where the κ term accounts for the isotropic absorption.

The same coordinate rotation procedure that we used to calculate the Jones matrix corresponding to the 45° linear birefringence can be introduced here to determine the Jones matrix associated to a 45° linear dichroism:

$$\mathbf{J}_{\mathrm{LD}'} = \mathbf{R}(-45°)\begin{bmatrix} e^{-\mathrm{LD}/2} & 0 \\ 0 & e^{\mathrm{LD}/2} \end{bmatrix}\mathbf{R}(45°) = \begin{bmatrix} \cosh \mathrm{LD}'/2 & -\sinh \mathrm{LD}'/2 \\ -\sinh \mathrm{LD}'/2 & \cosh \mathrm{LD}'/2 \end{bmatrix}. \tag{1.49}$$

[6] See section 3.2.3 for more details.

If LD_ϕ is the maximum value of the linear dichroism, obtained at an angle ϕ from the the x axis, then LD and LD′ are related to LD_ϕ and ϕ by:

$$\mathrm{LD} = \mathrm{LD}_\phi \cos 2\phi, \tag{1.50a}$$

$$\mathrm{LD}' = \mathrm{LD}_\phi \sin 2\phi. \tag{1.50b}$$

The angles θ and ϕ appearing in Eqs. (1.45) and (1.50) are not necessarily equal. In practice, however, for a considerable number of situations (i.e. uniaxial crystals, oriented molecules, etc) the principal axes for linear retardation and linear dichroism coincide.

Circular birefringence

Linearly polarized light that propagates through a medium exhibiting circular birefringence remains linearly polarized as the light progresses, but the direction of the vibration of the electric vector rotates uniformly and continuously with distance. This is why a material with circular birefringence is said to possess *optical rotatory power* or produce *optical rotation*.

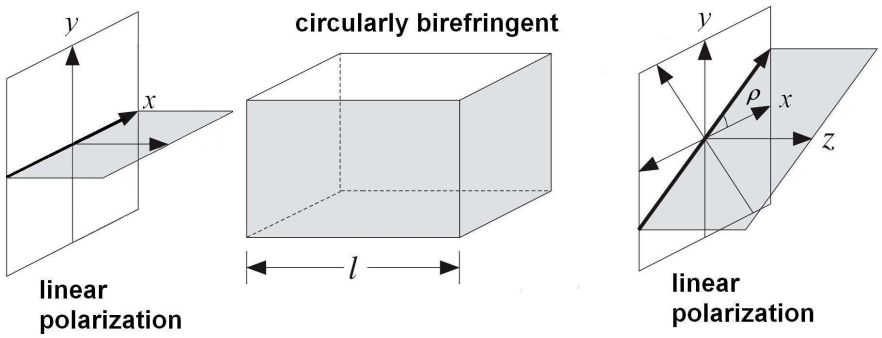

Figure 1.3.: Rotation of an incident polarization state induced by a circularly birefringent medium.

Circular birefringence occurs due to a difference between the indices of refraction n_- and n_+ for left and right circularly polarized light waves, respectively, with a typical magnitude of $|n_- - n_+| \sim 10^{-5}$. Circular birefringence arises from intrinsic quiral structures present in atom or in molecules. The parameter CB that quantifies the circular birefringence is defined as:

$$\mathrm{CB} = \frac{2\pi}{\lambda}(n_- - n_+)l, \tag{1.51}$$

A circularly birefringent medium can be described by the following Jones matrix [3]:

$$\mathbf{J}_{\mathrm{CB}} = \begin{bmatrix} \cos \mathrm{CB}/2 & \sin \mathrm{CB}/2 \\ -\sin \mathrm{CB}/2 & \cos \mathrm{CB}/2 \end{bmatrix}. \tag{1.52}$$

Comparing this matrix to matrix in Eq. (1.20) is easy to realize that CB is twice the angle of rotation. Therefore the angle of rotation ρ induced by a medium with circular birefringence is $\rho = \mathrm{CB}/2$. According to our sign convention, Fig. 1.3 shows a positive optical rotation on linearly polarized radiation induced by a circularly birefringent medium.

Circular dichroism

In a circularly dichroic medium there is a different absorption for the left an right circularly polarized light. The differences in the extinction coefficient for left, k_-, and right, k_+ circularly polarized light waves is quantified as

$$\mathrm{CD} = \frac{2\pi}{\lambda}(k_- - k_+)l. \tag{1.53}$$

The Jones matrix corresponding to CD is

$$\mathbf{J}_{\mathrm{CD}} = \begin{bmatrix} \cosh \mathrm{CD}/2 & i \sinh \mathrm{CD}/2 \\ -i \sinh \mathrm{CD}/2 & \cosh \mathrm{CD}/2 \end{bmatrix}. \tag{1.54}$$

Any medium that causes the differential absorption of circularly polarized light –circular dichroism– will transform a linearly polarized light into elliptically polarized. Usually, a medium containing CB or CD but not LB, LD, LB$'$, LD$'$ is said to be optically active and isotropic. An illustrative example is a sugar solution, although it can change the polarization of incident light (because of its CB) its optical properties are the same in all directions.

Table 1.1 summarizes the eight optical effects that we have revisited in this section. The two first ones (η, κ) are not included in a normalized Mueller-Jones matrix, but, as it will be shown later, the remaining 6 effects can generate the 6 independent parameters that form a Mueller-Jones matrix. The dispersive effects η, LB, LB$'$ and CB are related to the real part of the complex index of refraction, while the absorptive parameters κ, LD, LD$'$ and CD involve the imaginary part. For later convenience it is useful to go one step further and define a general complex retardation for each birefringence-dichroism pairs:

$$\chi = \eta - i\kappa, \tag{1.55a}$$

$$\mathrm{L} = \mathrm{LB} - i\mathrm{LD}, \tag{1.55b}$$

$$\mathrm{L}' = \mathrm{LB}' - i\mathrm{LD}', \tag{1.55c}$$

$$\mathrm{C} = \mathrm{CB} - i\mathrm{CD}. \tag{1.55d}$$

Table 1.1.: Symbols used and definitions

effect	symbol	definition[a]	Jones matrix
isotropic phase retardation	η	$\frac{2\pi}{\lambda}(n_x + n_y)l$	$\begin{bmatrix} e^{-i\eta} & 0 \\ 0 & e^{-i\eta} \end{bmatrix}$
isotropic amplitude absorption	κ	$\frac{2\pi}{\lambda}(k_x + k_y)l$	$\begin{bmatrix} e^{-\kappa} & 0 \\ 0 & e^{-\kappa} \end{bmatrix}$
horizontal linear dichroism projection	LD	$\frac{2\pi}{\lambda}(k_x - k_y)l$	$\begin{bmatrix} e^{-\mathrm{LD}/2} & 0 \\ 0 & e^{\mathrm{LD}/2} \end{bmatrix}$
horizontal linear birefringence projection	LB	$\frac{2\pi}{\lambda}(n_x - n_y)l$	$\begin{bmatrix} e^{-i\mathrm{LB}/2} & 0 \\ 0 & e^{i\mathrm{LB}/2} \end{bmatrix}$
45° linear dichroism projection	LD′	$\frac{2\pi}{\lambda}(k_{45} - k_{135})l$	$\begin{bmatrix} \cosh \mathrm{LD}'/2 & -\sinh \mathrm{LD}'/2 \\ -\sinh \mathrm{LD}'/2 & \cosh \mathrm{LD}'/2 \end{bmatrix}$
45° linear birefringence projection	LB′	$\frac{2\pi}{\lambda}(n_{45} - n_{135})l$	$\begin{bmatrix} \cos \mathrm{LB}'/2 & -i \sin \mathrm{LB}'/2 \\ -i \sin \mathrm{LB}'/2 & \cos \mathrm{LB}'/2 \end{bmatrix}$
circular dichroism	CD	$\frac{2\pi}{\lambda}(k_- - k_+)l$	$\begin{bmatrix} \cosh \mathrm{CD}/2 & i \sinh \mathrm{CD}/2 \\ -i \sinh \mathrm{CD}/2 & \cosh \mathrm{CD}/2 \end{bmatrix}$
circular birefringence	CB	$\frac{2\pi}{\lambda}(n_- - n_+)l$	$\begin{bmatrix} \cos \mathrm{CB}/2 & \sin \mathrm{CB}/2 \\ -\sin \mathrm{CB}/2 & \cos \mathrm{CB}/2 \end{bmatrix}$

[a] n stands for refractive index, k for the extinction coefficient, l for path length through the medium, and λ for the vacuum wavelength of light. Subscripts specify the polarization of light as, x, y, 45° to the x axis, 135° to the x axis, circular right $+$, or left $-$.

Chapter 2.

Molecular and supramolecular optical activity

2.1. Historical introduction

Historically the study of chirality in molecules is intimately relied to the chirality in crystals. In fact quartz crystal played an important role in the first studies about optical activity that date from the beginning of the nineteenth century. The first observation is reported to having been done by the French catalan astronomer Arago in 1811 [15] when he observed colours in the sunlight that had passed along the optic axis of a quartz crystal placed between crossed polarizers. Soon after, Jean Baptiste Biot (1812) [16] reported more experiments with quartz and discovered a second form of the crystal which rotated the plane of polarization in the opposite direction.

Biot also discovered that the rotation could also be observed in organic liquids such as turpentine. At that time, it was already appreciated that the optical activity of fluids must reside in the individual molecules, and may be observed even when the molecules are randomly oriented; whereas that of quartz was a property of the crystal structure and not of the individual molecules, since molten quartz was not optically active.

The first phenomenological theory about optical activity was completed by Fresnel in 1825 [17]. At that time he had discovered circular polarization and he realized that incident linearly polarized light can be regarded as a superposition of the two possible forms of circularly polarized light [right (R) and left (L)]. He correctly attributed optical rotation to the propagation at different speeds in an optically active medium of the left- and right-circularly polarized components of the linearly polarized beam in the medium. Fresnel was able to show the existence of the two circular components and separate them by an ingenious construction of a composite prism consisting of R- and L- quartz: as the two components travel with different velocities in an optical active medium they also refract by different amounts at an oblique interface.

By 1846, Haidinger [18] reported differences in the measured absorptions of left and right circularly polarized light, which is the origin of CD, but until the work of Aimé Cotton in 1895 [19] the phenomenon was not put in relief. The

first theoretical molecular model of optical activity was proposed by Drude in 1900. In his model absorbing media contain charged particles or ions, which posses natural periods of vibration. The vibrations of these particles around an equilibrium position are more or less violent if their periods of vibration agree more or less closely with the periods of the incident light. In the Drude model the rotation of the plane of polarization ρ is given by the equation[1]

$$\rho = \sum_r \frac{Q_r}{\lambda^2 - \lambda_r^2}, \tag{2.1}$$

where Q_r is a constant depending on the number of vibrators in unit volume and other constants of the medium and λ_r is the wavelength corresponding with the natural period of vibration of the molecule. The Drude equation has a great application in the molecular optical activity, however its application in the crystalline optical activity is relatively small

It is worth also mentioning that a thorough account of the experimental and theoretical side of the subject was given in a book by Lowry in 1935 [20] that for years was the main reference on the subject and still is a valuable source of information due to the great amount of experimental measurements of optical activity he reviews. During the XXth century the coupled oscillator model for optical activity introduced by Chandrasekhar in 1956 [21] had special relevance because it was the basis for several of the theoretical approaches to study molecular optical activity. It is based on the conception that the valence electrons of atoms or molecules forming the optically active crystals can be represented by the helically arranged and mutually coupled linear harmonic oscillators. The Chandrasekhar formula involves only two constants k and λ_0:

$$\rho = \frac{k\lambda^2}{(\lambda^2 - \lambda_0^2)^2}. \tag{2.2}$$

One of the earliest applications of optical activity was in sugar industry, where the rotatory power of sugar solutions was used as a measure of the quality of the sugar (saccharimetry). Besides this industrial application, in recent years molecular optical activity has arisen as a very important subject of fundamental research in several branches of chemistry and that also has many applications in pharmacology and biochemistry for the study of the molecules of living organisms.

[1] The form of the Drude equation can be directly derived from Eq. (1.51) if one asumes a Sellmeier dispersion for the refractive index: $n^2(\lambda) = 1 + \sum_i \frac{B_i \lambda^2}{\lambda^2 - C_i}$. B_i would be slightly different for left- and right-circularly polarized light.

In this chapter we will descriptively review several aspects about the presence of electronic optical activity in molecules and molecular aggregates. Further we will also introduce the concept of homochirality and then we will briefly discuss the implications that it has in the study of the emergence of life in Earth. An additional section will present the basic characteristics of the commercial instruments that are used in laboratories all over the world to measure the optical activity and, there, we will discuss the limitations they have. In the last section we will review some of the most notable published contributions on the measurement of optical activity in anisotropic media and the current state-of-art of the subject. All the concepts discussed in this chapter will be studied from a purely descriptive approach and without introducing many details, as the only objective of this chapter is to set a proper background for a better understanding of the following chapters.

2.2. Circular dichroism and circular birefringence in molecules

The optical definitions for circular dichroism (CD) and circular birefringence (CB) has been given in the previous chapter. A molecule is chiral when the mirror image of the molecular structure cannot be brought to coincide with itself. Here "brought" refers to translations and rotations. A chiral molecule is said to be *optical active* (or possess *optical activity*) if it exhibits CD and CB.

The structure of chiral molecules belong to symmetry point groups[2] that lack the symmetry elements of a mirror plane, a center of inversion, or a rotation-reflection axis $n > 2$.[3] Other symmetry elements like axis of rotation are allowed. Image and mirror image of a chiral molecule are called enantiomers. As a consequence of the lack of mirror symmetry the enantiomers of a chiral molecule are "non-superposable". In chemistry, the word *racemic* is used for compounds or mixtures of chiral molecules that have equal amounts of left- and right-handed enantiomers of a chiral molecule. Therefore, a racemic compound despite containing chiral molecules is optically inactive, i. e. shows no CD or CB, because the contributions of both enantiomers, that are present in equal amounts, cancel each other.

The electronic transitions between two different electronic configurations of a molecule induced by electromagnetic radiation of any wavelength is called a chro-

[2] Point groups are mathematical groups of geometric symmetries. In chemistry they are used to describe the symmetries of a molecule.

[3] A rotation-reflection axis $n > 2$ means a rotation around an axis by $\frac{360°}{n}$, followed by a reflection in a plane perpendicular to it. n must be an even number > 2.

mophoric transition. Usually we understand the chromophore as that region of a molecule where the energy difference between two different localized molecular orbitals falls within the range of the uv-visible spectrum. Visible light that hits the chromophore can thus be absorbed by exciting an electron from its ground state into an excited state, and, as a consequence, these chromophoric transitions at the visible range are responsible for the colour of the molecule. To a first approximation chromophores themselves are usually not chiral, although there are notable exceptions, like helicenes. In case of achiral chromophores the observed optical activity then arises from interaction between different chromophores within the chiral geometrical framework of the molecule.

A substance can, however, also be optically active due to an asymmetrical arrangement of molecules. In these cases, the molecules themselves need not necessarily to be chiral. Arranging non-chiral molecules on a helix, results, for instance, in an optically active molecule because a helix and its mirror image cannot be superposed since reflection reverses the screw sense. Chirality excludes improper symmetry elements (operations involving reflection and inversion), namely centers of inversion, reflection planes and rotation-reflection axes. A chiral molecule is not necessarily asymmetric as it can have, for example, rotational symmetry. The spatial symmetry restrictions that impose chirality are not only applicable to molecules, but also to crystals and they are mathematically studied with the point group classification and constitute a very important subject in stereochemistry (which studies molecular geometry) and crystallography.

The origin of the optical activity in crystals can be of two types. An optically active crystal can be formed of optically active molecules –molecular origin– or it can result from the crystal structure –crystalline origin–. It is known that in the case of the crystalline origin the crystal is characterized by an helix structure, i.e. the molecules or atoms lie on the helices the axes of which are parallel to the optical axis of the crystal. The best known optically active crystals are those of the space groups of symmetry D_3^4 and D_3^6 the elementary cell of which consist of three atoms or molecules. Typical examples of these crystals are α-quartz, tellurium, selenium, benzil or cinnabar. The majority of them are optical active due to the crystalline structure, which means that, for example, if they are fused they lose the optical activity. However, in a certain number of crystals, camphor and benzil are well-known examples, the optical activity has both contributions: molecular and crystalline.

Although CD and CB are two effects that are interrelated they are usually treated separately. CD is nonzero only in the spectral regions in which the molecule under study has optical transitions. However, CB is a dispersive measurement, and for an accurate study requires a scan over a wide spectrum, while CD is better suited for studies of complex chromophores having closely spaced

electronic transitions because of its inherently better resolution. With CD is easier to measure isolated transitions whereas CB measurements usually combine information about many electronic transitions.

CD spectroscopy is used routinely to study biological molecules and the applications of this spectroscopy in chemistry are multiple. We will not go into many details about these applications as they fall out of the scope of this thesis as we are more interested on fundamental research about homochirality (see subsection 2.3). We can mention, for example, that the far-UV CD spectrum of proteins reveal important characteristics of their secondary structure. For example CD spectra is used to estimate the fraction of a molecule that is in the alpha-helix conformation, in the beta-sheet conformation, in the beta-turn conformation, etc. The tertiary structure of proteins can be studied in the near-UV region (250 nm to 350 nm), for example, the chromophores are sensitive to a folded structure in this region.

2.2.1. Cotton effect

Optically active substances can present CB and CD simultaneously in the range of frequencies where they have an absorption band. Such phenomenon is usually referred as *Cotton-effect*. When an absorption band of an isolated electronic transition is scanned in wavelength the typical Cotton-effect profiles displayed in Fig. 2.1 are obtained. A Cotton-effect is called to be positive, when the CB maximum is found at longer wavelengths than the absorption maximum (case b of Fig. 2.1). Otherwise it is called negative.

The Cotton effect results from nothing else than the application of the Kramers-Kronig relations to an absorption band. They are relations between the real and imaginary parts of a response function, and they are widely used in solid-state physics to evaluate the corresponding quantity if only one component is measured. In the subject of optical activity the real part, CB, and the imaginary part, CD, [see Eq. (1.55d)] are related by a Kramers-Kronig transform and, therefore, from a purely theoretical standpoint, provide the same information. However, from a practical standpoint it is highly desirable to have access to both parameters, since the application of a Kramers-Kronig transform theoretically requires the knowledge of the CB or CD response in the complete electromagnetic spectrum and, as a consequence,the transformation between experimental CD and CB has been rarely undertaken. Complete studies about the application of Kramers-Kronig transformation in experimental measurements of CD and CB can be found in Refs. [22, 23].

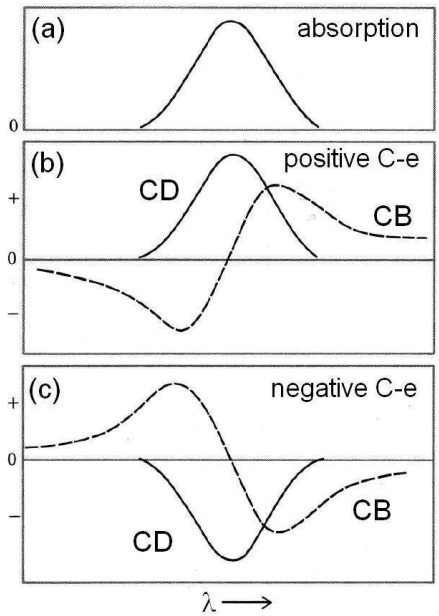

Figure 2.1.: Scheme of the characteristic profiles that appear in the Cotton effect. The Cotton effect is called positive if the CB first decreases as the wavelength increases, and negative if CB first increases.

2.2.2. Excitons

Changes in the distribution of the electron density in the chromophores are associated with changes in the UV-visible absorption spectrum. The movement of the electron density in going from the ground electronic state to an excited state creates a momentary dipole, that is called a transition dipole. Each transition has both a direction and an intensity that vary according to the nature of the chromophore and the particular excitation. When two or more chromophores are brought into proximity, their electric transition dipoles may interact through dipole-dipole (or exciton) coupling. Therefore if one molecule in a group of close packed molecules is excited, the excitation can be transferred from molecule to molecule in the manner of a moving particle. Such moving excitation is called exciton. Excitons play an important role in determining the optical response of condensed-phase systems.

A Frenkel exciton [24] is basically an intramolecular excited state, in which the excited electron and the vacancy or "hole" migrate together from one unit cell to another unit cell. The Frenkel exciton differs from an electron in the

fact that is neutral and carries no current, but it carries energy. The Frenkel exciton describes a delocalized electronic excitation, while the electron remains localized in the same unit cell. Therefore a Frenkel exciton can be considered as a neutral particle that can diffuse from site to site, perhaps moving hundreds of molecules away from its origin (energy is transported without migration of the electric charge). The Wannier excitons, typical of inorganic semiconductors, are different from Frenkel excitons in the fact that the electron and hole are separated by many lattice spacings, and, as a result the electron and hole are not tightly bounded as in the case of Frenkel excitons. The coupling of the optical transitions of the molecules results in the formation of a band of Frenkel exciton states. The concept of exciton can be also applied to the atoms or molecules of a crystalline solid [25], but in this thesis we are only interested in this concept when applied to a molecular aggregate.

The absorption spectrum of an organic compound can differ in the solid and solution states. The formation of ordered structures usually referred as aggregates is fairly common in concentrated dye solutions and is often difficult to avoid when the molecules are in the solid state. Aggregates are of fundamental interest as model materials to study the nature of excitons in molecular systems of reduced dimensionality often with a chain-like configuration. The optical properties of these molecular aggregates are, to a large extent, governed by exciton delocalizations and other transport and relaxation phenomena. The aggregate formation can be usually well identified by the observation of the UV-visible absorption spectra because aggregation leads to a shifted, broadened, and sometimes split bands. Likewise, the interaction of two or more achiral chromophores that are held in close proximity can also give rise to optical activity. Assuming achiral chromophores there are three recognized methods (see Ref. [26]) of generation of optical activity: (i) dipole coupling mechanism; (ii) μ-m mechanism and (iii) one-electron mechanism.

The dipole coupling requires two chromophoric groups coupled via dipole-dipole interaction [27]. Fig. 2.2 displays the different coupling possibilities between the induced dipoles, that depend on the orientation of the aggregates. If the mutual orientation of the dipoles is chiral it results in a couple of CD bands that correspond (see the oblique case of Fig. 2.2) to in-phase and out-of-phase combinations of uncoupled components. The pair of CD bands are equal in intensity but have opposite signs, and usually result in bisignate spectrum. The μ-m mechanism is similar in concept but in this case the interaction is not between two dipoles but between one dipole and one quadrupole (magnetic moment) and it also requires at least two chirally oriented chromophores. The one-electron mechanism is conceptually different and, in principle, it does not requires a chiral orientation of the chromophores. It describes a mixing of electronic configura-

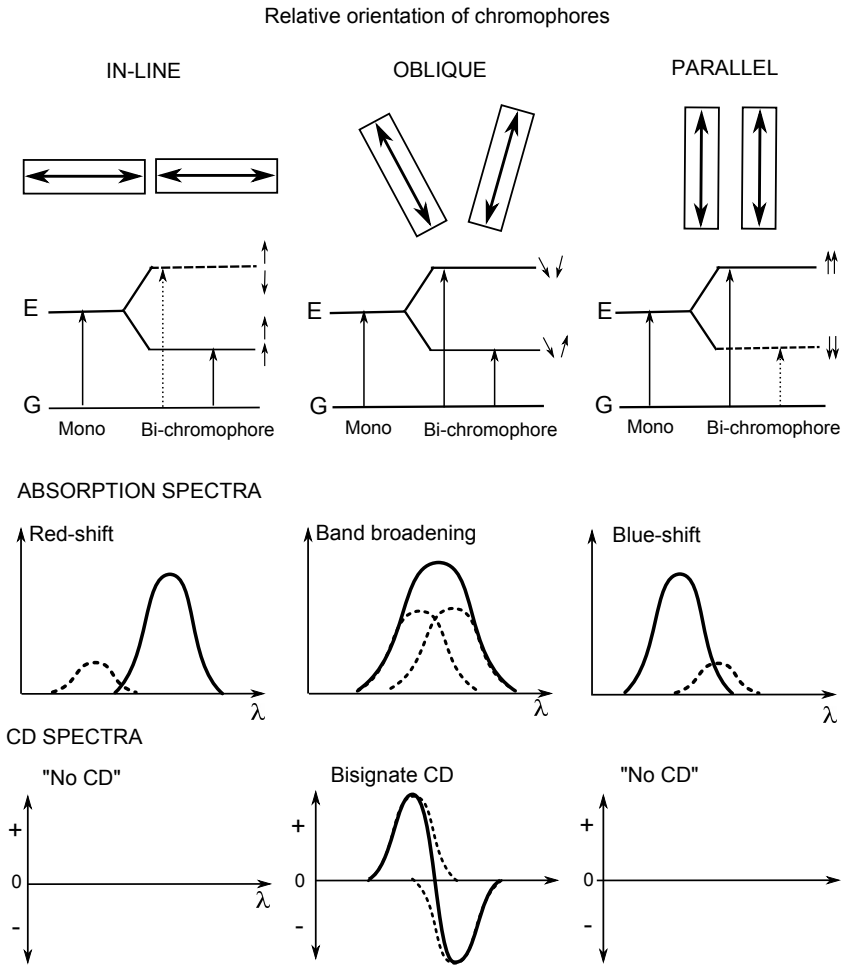

Figure 2.2.: Orientation dependence in exciton coupling between two chromophores (rectangles) and their long-axis induced dipoles (represented by double-headed arrows). When the two chromophores lie sufficiently close the excitations are delocalized between the two chromophores and the excited state (E) is split. The solid arrows connecting the ground (G) and excited (E) states represent allowed transitions, while dashed arrows represent forbidden transitions. The relative orientation of the chromophores are found in the wavelength-shifted absorption spectra –red-shifted for in-line and blue-shifted for parallel orientations–. The oblique orientation, when both transitions are allowed, leads to a broadened absorption band. CD transitions are only allowed when the dipoles have a chiral oblique orientation and results in a bisignate CD curve.

tions within a single originally non-chiral chromophore under the influence of a chiral perturbation potential.

For an observed chiral transition it is highly likely that it would contain contributions of all three mechanisms. These are only highly simplified models that are used to understand the complicated nature of the excitonic states in molecules.

2.2.3. J-aggregates

We devote a special section of this introductory chapter to the description of a particular type of aggregates: the J-aggregates. We do so because several of the experimental studies that will be presented in further chapters are developed on systems with J-aggregation. Furthermore J-aggregates are of fundamental importance for the general understanding of molecular and solid-state physics because they bridge the gap between the physics of single molecules and perfectly ordered crystals

J-aggregates were independently discovered in 1930's by Günter Scheibe and Edwin E. Jelley [28, 29] (from him comes the J letter in their name). They discovered that by increasing the concentration of a solution of the dye pseudoisocyanine the absorption spectrum underwent dramatic changes. In low concentration there was a relatively broad absorption band that upon increasing the concentration was replaced by a red-shifted much narrower absorption band[4]. Both authors attributed the changes to the formation of a molecular aggregate of dye molecules. Since then the aggregation behavior of cyanine dyes has been studied extensively and nowadays they are probably the best-known self-aggregating dyes.

J-aggregates have been investigated as model material for one-dimensional Frenkel excitons. According to exciton theory the dye molecule is regarded as a point dipole and the excitonic state of the dye aggregate splits into two levels through the interaction of transition dipoles. Exciton theories such as the one shown in Fig. 2.2 are able to predict position of the absorption band of the J-aggregates and the unique feature of the narrowness of this so-called J band is explained by the absence of vibrational broadening, because the J band is shifted to energies where monomer electronic vibrational coupling is absent. Coherent exciton scattering theories play also an important role to fully understand the formation of J-aggregates.

Due to their narrow absorption spectra J-aggregates only absorb photons with a very narrow energy distribution and, for example, this gave them applications in the (analogical) photographic industry as film sensitizer. Applications of these

[4]There also exist aggregates which show a blue-shifted absorption spectrum (compared to the monomer), which is broader and less visible. These aggregates are called H-aggregates

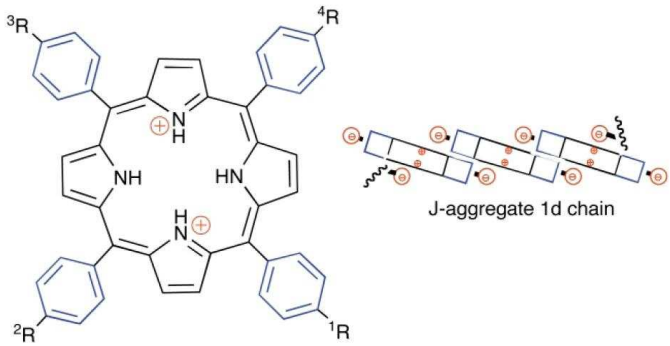

Figure 2.3.: J-aggregate chain made of porphyrin molecules. J-aggregation takes place due to the electrostatic intermolecular interaction between the anionic sulphonate (R radicals in the figure) and the positive-charged ring.

molecules in various devices or for constructing molecular machines are also investigated because J-aggregates show interesting linear and nonlinear optical properties. We dedicate special attention to J-aggregates in this work because when they are in solution they can undergo asymmetric transformations that convert non-chiral molecules into chiral fiber-like associations.

2.3. Homochirality

Homochirality is a term used to refer to a group of molecules that possess the same sense of chirality. Homochirality is observed in living organisms because the nucleotides are only composed of right handed (D-) carbohydrates (sugars) and the proteins are formed by left handed (L-) amino acids. There are no traces on Earth of life based on D-aminoacids and L-carbohydrates.

Life is considered to be basically a molecular phenomenon and, at the moment, there is no clue why the existing life broke the mirror symmetry and chose these forms of aminoacids and carbohydrates instead of their mirror images. When aminoacids are being synthesized in the laboratory, e. g. via the famous Urey-Miller experiment, a racemic mixture of right and left handed molecules is produced (equal amount of L and D molecules). However, it is known that life cannot originate in a racemic mixture because processes that are crucial for life such as replication or regulation of the genetic expression imply chiral supramolecular structures. Therefore the intriguing point of biological homochirality is not only the exclusive presence of L-aminoacids and D-carbohydrates in the biological

forms, but also why life is tied to molecular structures and molecular recognition processes that are determined by chirality [30].

Theories for the origin of chirality in biological world can be grouped in two major categories: biotic and abiotic [31]. The biotic theory states that selection of one of the enantiomers took place at a late stage in the biological evolution of living matter. The second scenario proposes that chiral material were formed prior to the appearance of earlier biological polymers. In any of these two possible scenarios the first question to be asked is whether there was a cause that provoked the mirror-symmetry breaking. There have been several "explanations" about how this asymmetry was generated and we can group them in deterministic and stochastic or "chance" theories [31, 32]. Deterministic theories defend that the observed mirror symmetry breaking was caused by an earlier external chiral influence (i.e. an asymmetric physical agent) even if this was on a minuscule state. Stochastic or chance –in the sense of randomness– theories [33] state that the mirror symmetry breaking takes place due to a very small random enantiomeric excess.

Among the most cited deterministic mechanisms there is circularly polarized light or the combination of plane polarized light and oriented magnetic field that could induce asymmetric synthesis or asymmetric decomposition of enantiomers. Astrophysicists have observed that light emitted from interstellar stars is circularly polarized and thus it might have some influence in the generation of non-racemic extra-terrestrial materials that landed on Earth. Nevertheless there is a long-standing controversy as to whether these effects are large enough to have determined the selection of the handedness of life [34]. The stochastic scenarios can happen in far-from-equilibrium systems that undergo phase transitions, and there are several experimental examples of symmetry breaking phenomena related to crystallization or phase-transition phenomena.

Both stochastic and deterministic theories of biomolecular homochirality evolved through the same sequential stages: mirror-symmetry breaking followed by chiral amplification and chiral transmission [31]. The mirror-symmetry breaking imply the creation of a primordial minute enantiomeric imbalance. It is the key process in deterministic mechanism, whereas it is not for stochastic mechanisms, since for them the symmetry breaking occurs spontaneously the crucial process is an efficient mechanism of chiral amplification [31]. The chiral amplification stage has attracted great interest and the attention has been put in autocatalytic reactions that amplify the chirality (i. e. the chirality of the reaction products is greater that of the starting materials). In this context Frank proposed a well-known model [35] for the autocatalytic self-replicating process in which a chemical substance catalyzes its own production and acts as an anticatalyst for the production of the opposite enantiomer [32]. This permits the amplification of even an ex-

traordinary small initial enantiomeric excess to high levels. Only a small number of autocatalytic processes are known so far, the most famous one is the reaction discovered by Soai *et al.* [36].

In this thesis we defend that homochirality emerged in the abiotic stages of evolution. There exists the likelihood that most of the early organic material on Earth was brought in by comets and asteroids, and supporting our hypothesis, there are reports that indicate that aminoacids extracted from some meteorites such as the Murchison meteorite already contain some chiral bias towards L-enantiomers [37, 38]. Most of the investigations presented in this thesis could be described, as a last resort, as a research on homochirality. Several of the results of this work were motivated by investigation on mechanisms that act in processes that undergo mirror symmetry breaking. In this respect we can anticipate that in the following chapters we will study macroscopic processes such as simple stirring (mechanical force) that can lead to chiral selection in certain aggregates, which are mechanisms that until very recently where not recognized to affect the molecular chirality. However we should warn the reader that the results that will be presented in this work concern only a small and quite specialized part with respect to the complete and multidisciplinary investigation carried on homochirality. Furthermore this thesis is, more generally, intended to contribute to the understanding of the interaction of polarized with chiral anisotropic media, so only occasionally we will refer to the implications that our research has in the study of the processes of emergence of homochirality.

2.4. Standard methods to measure optical activity

CD is now a routine tool in many laboratories and CD instruments are usually referred to as circular dichrometers, dichrographs or CD spectropolarimeters. The essential feature of a CD spectropolarimeter is the implementation of a polarization phase modulation technique that enhances the sensibility of the instrument in the detection of the absorbance signal of a CD spectrum, that typically is orders of magnitude weaker than a normal absorbance spectrum.

In most commercial CD spectrometers, a photoelastic modulator[5]-polarizer pair (in older instruments a Pockels cell) modulates the polarization of the incident light at a typical frequency of 50kHz. Typically CD spectropolarimeters use a double prism monochromator rather than one based on gratings, because they tend to perform better in the UV. The radiation source in UV-visible CD spectrometers is a high energy (150-450 W) xenon arc lamp. In some instruments the lamp in water cooled. Sometimes, as a result of the high energy lamps used,

[5]See section 5.2 for more details about the characteristics of photoelastic modulators

the optics of the instruments are purged with nitrogen gas to avoid ozone being created and reacting with the surfaces of the optical elements. Nitrogen purging is also necessary in the sample compartment for measurements running below 200 nm to avoid absorption by ozone of UV radiation.

Among the available commercial designs of dicrographs those from the Japanese manufacturer Jasco[6] are probably the ones present in a larger number of laboratories. In this work when we mention commercial instruments or standard measurements of optical activity we will be implicitly referring measurements obtained with Jasco instruments. CD Measurements made with Jasco instruments appear to have extremely low noise levels. This is partially due to the fact that they usually use a continuous scanning of the spectra, instead of a more appropriate stepped scan. The continuous scan results in an "artificial" electronic smooth of the the spectra, which makes difficult to associate a meaningful physical error to a CD measurement. Interestingly, dicrographs made by Applied Photophysics [7] use the more convenient stepped scan and emphasize the importance of using unsmoothed spectra.

The most used optical arrangement that commercial instruments use for CD measurement is the sequence: polarizer, phase modulator, sample and detector. In some instruments the measurement of CB is also possible through the addition of an "accessory"(a polarizer) between the sample and the detector resulting in the sequence: polarizer, phase modulator, sample, polarizer and detector. We should point out that these optical setups are very similar or even identical to the ones one might find in spectroscopic phase-modulated ellipsometers. In spite of these evident similarities it seems that CD and CB techniques and ellipsometric techniques have progressed in parallel but with little communication between the two communities. Our feeling is that, in general, there is no consciousness about the important similarities between dichrographs and ellipsometers, and this avoids technical exchanges between both communities that otherwise could be very valuable. This intercommunication will become even more justified in the future because, from a technical standpoint, our opinion is both communities will share the interest of measuring complete Mueller matrices.

CD spectrometers are usually designed to work with solutions contained in cuvettes. For UV-visible CD, high quality fused quartz that transmits a broad UV-visible wavelength range is required. The default cuvette pathlength is 1 cm, but for samples with large absorbance signal the use of shorter pathlength cells (1 mm, 0.1 mm) is also common. In the 1950s there were commercial CB spectropolarimers but they are no longer available, and now the CB capability

[6] http://www.jascoinc.com
[7] http://www.photophysics.com

is typically offered as an add-on to a CD spectropolarimeter.

2.5. The concern of anisotropic media in chemistry

The problem of measuring optical activity in systems coexisting circular and linear anisotropies is a long-term concern in chemistry. As far back as 1969 Disch an Sverdlik [39] realized that their method to record CD spectra was influenced by linear dichroism an linear birefringence[8].Due to this influence several authors use the terminology *true CD* to refer to the circular dichroism of the system under study, which may not correspond to the *measured CD*. The contributions that cause this miscorrespondence are commonly referred as *artifacts*, or, more specifically, as *chiroptical artifacts* and may occur due to the presence of linear dichroism and linear birefringence in the medium or due to the non-ideal behaviour of the instrument used to perform the measurement (uncorrected strain of the optical elements for example). In the next chapter we will introduce the theory that justifies the apparition of these artifacts; in this section we will only introduce some approaches that have been proposed to sort this difficulty.

Since the introduction of CD measurement techniques the artifact problem has received a permanent interest from the chemistry community [40–42]. Several different instruments or measurement techniques have been proposed to sort this problem but, probably, none of them has yet been widely recognized or has transformed into a commercial measurement system. In this section we will critically review some of the most significant contributions published in this field.

One of the most important works on the subject, which is the reference for several other following works, is the excellent review of Schellman and Jensen published in 1987 [42]. In this work they extensively review every aspect related to the measurement of CD and CB in presence of linear dichroism and linear birefringence. They introduce the Jones approach to describe anisotropic homogeneous media and they suggest instrumental configurations that could be used in the measurements. This work compiled the results of several other previous publications by the authors [43, 44] and introduced the notation based on the parameters CD, CB, LD, LB, LD′ and LB′ to designate the optical effects described in section 1.5 that we also use in this thesis.

Japanese authors are among the ones that have dedicated more attention to the problem from an instrumental point of view. The group of Y. Shindo was

[8]The influence that linear birefringence has in the measurement of CB is much more evident than in case of CD and it was a known topic since the first experiments about optical rotation of quartz in the XIX century. The measurement of CB was considered to be not possible in presence of linear birefringence.

pioneer in determining the problems that presented commercial CD spectrometers [40, 45, 46] and proposed specific modifications for them [47, 48]. More recently the group of R. Kuroda (also in collaboration with group of Shindo) has made significant contributions to the measurement of CD in solid samples [49–51] –which tend to show linear birefringence and linear dichroism– and, in collaboration with Jasco, the japanese manufacturer of CD spectrometers, they have developed prototypes based on modifications of commercial instruments [52, 53]. However the proposed measurement methods seem to be only valid for specific types of homogeneous solid samples because they require the rotation of the samples. As their measurements continue to be restricted to the determination of few elements of the Mueller matrix, they do not provide a complete characterization of the optical behavior of the sample. In Ref. [54] one can find a recent review, from a chemistry perspective, of the different approaches developed to measure CD in solid state samples.

Several of the most interesting recent approaches to the problem have come from the field of crystallography. In 1983 Kobayashi and Uesu [55] invented an apparatus to study the optical activity of crystals in directions out of the optic axis. This instrument was called HAUP – after "High Accuracy Universal Polarimeter"– and since then similar instruments have been used in a number of laboratories mainly to study crystals [56–59]. W. Kaminsky have recently proposed and developed several innovating measurements for various tensorial properties of crystals including the gyrotropy that gives rise to optical activity [60–64]. One might find in Ref. [65] a comprehensive review about the measurement of optical activity in crystals.

Current work on the subject is also directed towards circular dichroism and circular birefringence imaging techniques which permit the study of heterogeneous samples along their surface. In 1982, Maestre and Katz adapted a commercial Cary spectropolarimeter to a microscope [66] and performed several measurements. However, they faced important artifacts arising from the optical components of the instrument. The group of Bart Kahr has extensively worked on polarimetric imaging techniques [67] applied to crystal optics and, more recently, they have started using Mueller matrix imaging polarimetry coupled with microscope optics to study chiroptical phenomena in crystals [68, 69].

Part II.

Theory

Chapter 3.

Light propagation in anisotropic optical active media

The description of light propagation in anisotropic optical active media[1] can be highly complex. Maxwell did not treat chiral media and, probably, this has motivated that in comparison with the vast amount of references to Maxwell's equations the number or books and papers dealing with the resolution of Maxwell equations in anisotropic optical active media is scarce.

Optical activity is a clear manifestation of the molecular or atomic structure of matter. The circular birefringence or the rotation of the polarization's direction per unit thickness of light propagating in an optically-active material scales as the ratio d/λ^2, where d is some typical molecular length and λ is the light wavelength. In fact optical activity is due to the *inhomogeneous* nature of the medium, but as d is usually much smaller than λ we can effectively use *homogeneous* models to describe optical activity.

By using homogeneous models we can distinguish two different approaches to study light propagation through anisotropic optically active media. The first one consists in solving Maxwell equations with adequate tensorial constitutive relations. The calculations corresponding to this method are rather complicated and several elegant matrix formalisms have been developed to systematize and simplify the calculations, the most well-known being the Berreman method [70]. Even with these tools, to our knowledge, analytic solutions are only available either for anisotropic but non-gyrotropic media [71] or for gyrotropic but isotropic media [72]. No analytic expressions have been found for the rest of cases but they can be treated numerically. The second approach is semi-phenomenological and was introduced by Jones in the framework of his formalism to represent polarized light. It is based on an infinitesimal representation of the medium using a differential matrix calculus. In this chapter we will briefly introduce the Berreman method, and we will revisit in detail the method of Jones, as most of the results of our work have been studied using this method.

[1] A medium with optical activity is often referred in theoretical works as a *gyrotropic medium* or a medium with *gyrotropy*

3.1. Constitutive Equations. Introduction to Berreman matrix formalism

Different authors have been using different forms for the constitutive equations[2] of chiral media. Here we will present a set of constitutive equations based on those proposed by Condon [73], who noted that the essential feature of chiral media is that the polarization $\mathbf{P}$, appearing in Eq. (1.4), is dependent on $\partial\mathbf{H}/\partial t$ and that the magnetization $\mathbf{M}$, appearing in Eq. (1.5), is dependent on $\partial\mathbf{E}/\partial t$:

$$\mathbf{D} = \boldsymbol{\varepsilon}\mathbf{E} - \mathbf{g}\frac{\partial \mathbf{H}}{\partial t}, \tag{3.1a}$$

$$\mathbf{B} = \boldsymbol{\mu}\mathbf{H} + \mathbf{g}\frac{\partial \mathbf{E}}{\partial t}, \tag{3.1b}$$

where $\mathbf{g}$ is the tensor of gyrotropy. Although the derivation of these relations was heuristic and not particularly rigorous, microscopic models have been presented that support these equations. For monochromatic waves with a e^{iwt} time dependence of the fields they can be rewritten as

$$\mathbf{D} = \boldsymbol{\varepsilon}\mathbf{E} + \boldsymbol{\rho}\mathbf{H}, \tag{3.2a}$$

$$\mathbf{B} = \boldsymbol{\mu}\mathbf{H} + \boldsymbol{\rho}'\mathbf{E}, \tag{3.2b}$$

in which $\boldsymbol{\rho} = -i\omega\mathbf{g}$ and $\boldsymbol{\rho}' = i\omega\mathbf{g}$. Upon the literature one might find different names for these equations, being probably the most adequate Drude-Condon-Fedorov constitutive relations, as these three authors made contributions to this formulation. For anisotropic media $\boldsymbol{\varepsilon}$, $\boldsymbol{\mu}$ and $\boldsymbol{\rho}$ are tensors, while for an isotropic optically active medium they simplify to a scalar.

All these complex-valued tensors, e.g. the permittivity, can be expressed in laboratory Cartesian coordinates (x, y, z) as:

$$\boldsymbol{\varepsilon} = \begin{bmatrix} \varepsilon_{xx} & \varepsilon_{xy} & \varepsilon_{xz} \\ \varepsilon_{yx} & \varepsilon_{yy} & \varepsilon_{yz} \\ \varepsilon_{zx} & \varepsilon_{zy} & \varepsilon_{zz} \end{bmatrix} \tag{3.3}$$

It is interesting to note that for orthorhombic, tetragonal, hexagonal and trigonal symmetry systems it is possible to perform a coordinate transformation from the laboratory (x, y, z) coordinates to another Cartesian coordinate system (x', y', z') characteristic of the anisotropic medium (its natural basis), for which the tensor becomes diagonal [74].

$$\boldsymbol{\varepsilon} = \mathbf{A}\begin{bmatrix} \varepsilon_{x'} & 0 & 0 \\ 0 & \varepsilon_{y'} & 0 \\ 0 & 0 & \varepsilon_{z'} \end{bmatrix}\mathbf{A}^{-1}. \tag{3.4}$$

[2] See section 1.1 for an introductory discussion about the constitutive relations

where $\mathbf{A}$ is a real-valued unitary rotation matrix that depends on the three Euler angles (φ, ψ, θ) that can be found somewhere else [7, 74]. This equation has fundamental importance in crystal optics, because, for example, it makes the distinction between uniaxial and biaxial crystals depending on if the components of the diagonalized permittivity tensor are all different (biaxial) or two of them are equal (uniaxial). If all of them are equal we have the isotropic case we described in chapter 1. It is also important to stress that the ρ tensor may not have the same form as the dielectric tensor. Also, since we focus our attention in nonmagnetic materials, μ is the identity matrix.

The Eqs. (3.2) can be casted in matrix form:

$$\begin{bmatrix} \mathbf{D} \\ \mathbf{B} \end{bmatrix} = \mathbf{M}_o \begin{bmatrix} \mathbf{E} \\ \mathbf{H} \end{bmatrix}, \qquad \mathbf{M}_o = \begin{bmatrix} \boldsymbol{\varepsilon} & \boldsymbol{\rho} \\ \boldsymbol{\rho'} & \boldsymbol{\mu} \end{bmatrix} \tag{3.5}$$

where $\mathbf{M}_o$ is a 6×6 matrix called the optical matrix.

Now we are ready to briefly introduce the Berreman method [70] which can be described as a re-formulation of Maxwell's equations. It is a plane wave method; that is, no scattering is taken into account. It uses transverse components of the electric and magnetic field vectors and thus, in a first term, it is not intuitively related to the experiment and requires some steps of calculation. We will not deal with this subject in detail, we will only outline the most significant calculations it involves.

The Berreman equation is given by

$$\frac{d\boldsymbol{\Psi}}{dz} = -i\omega\boldsymbol{\Delta}\boldsymbol{\Psi}, \tag{3.6}$$

where $\boldsymbol{\Psi}^T = (E_x, H_y, E_y, -H_x)$ and the z direction is perpendicular to the sample surface. $\boldsymbol{\Delta}$ is a 4×4 complex matrix that contains all the information about the dielectric functions of the medium. The elements of the matrix $\boldsymbol{\Delta}$ are functions of the elements of the optical matrix $\mathbf{M}_o$ and the direction of the wave normal of the incident wave. The explicit relations can be found in Refs. [70, 75]. If $\mathbf{M}_o$ (and thus $\boldsymbol{\Delta}$) is independent of z over a continuous interval Eq. (3.6) is integrable and yields:

$$\boldsymbol{\Psi}(z+h) = \mathbf{L}(h)\boldsymbol{\Psi}(z), \quad \text{where} \quad \mathbf{L}(h) = e^{-i\omega h\boldsymbol{\Delta}}. \tag{3.7}$$

$\mathbf{L}(h)$ is the layer matrix that relates the vector Ψ at two different parallel planes, separated by a distance h, in a homogeneous anisotropic medium whose fields are excited by an incident plane wave. The case where $\mathbf{M}_o$ depends on z can be treated similarly if the medium is divided into layers that are thin enough to make $\mathbf{M}_o$ independent of z within each layer

The main difficulty of the Berreman calculus remains in the obtention of the layer matrix, i.e. in the calculation of the exponential of the matrix $\boldsymbol{\Delta}$. An

analytical form of the layer matrix has only been found for a limited number of forms of $\mathbf{\Delta}$, for the rest of cases the layer matrix can be numerically computed. Analytic expressions of the layer matrix (sometimes also referred as characteristic matrix or transfer matrix) can be found in the works of Berreman [70], Lin-Chung [76], Wöhler [77] and Schubert [71].

The Berreman method permits the calculation of the optical properties at oblique incidence and also takes into account multiple reflections at the interfaces. It is also an appropriate and flexible technique to deal with layered systems since it can be seen as a generalization of the Abelès 2×2 matrix method for layered isotropic media. In spite of all these virtues this matrix method is perhaps not as used as one might think. In a first moment it was mainly used to study the optics of liquid crystals and only lately has gained much attention in the field of generalized ellipsometry. The reason probably is that it is a method of rather difficult application (at least algebra-wise) if one wants to retrieve analytical solutions and, for many problems, specially those involving gyrotropic media, the solutions can only be treated numerically. Another reason is that in certain fields, a clear example is in crystal optics, there exist "traditional" analytic expressions, sometimes derived phenomenologically, that are useful to study particular problems of crystal optics related with optical anisotropy and that already cover many of the situations that a experimentalist can find.

3.2. The lamellar representation

Jones solved a number of years ago the general problem of the polarization description of a medium possessing eight different optical parameters [78]. These parameters correspond to the eight physical measurements one can make on such a system with a given light path; namely: mean absorption, mean refraction, optical rotation, circular dichroism, and two parameters for linear birefringence and two more for linear dichroism. He studied these properties in terms of a "layered"-medium interpretation that, by means of a differential equation analysis, leads to a exponential representation of the Jones matrix. Years later R.M.A. Azzam [79] developed and analogous infinitesimal calculus based on Mueller matrices that can be used for the same purposes.

The use of the differential matrix calculus introduced by Jones to describe the continuous propagation of partially polarized light through linear anisotropic media is somewhat less general that the Berreman method. As it will be presented, this method is only described for normal incidence and it does not take into account multiple reflections at the layer interfaces. However, this method is specially useful to study light transmission through a homogeneous anisotropic

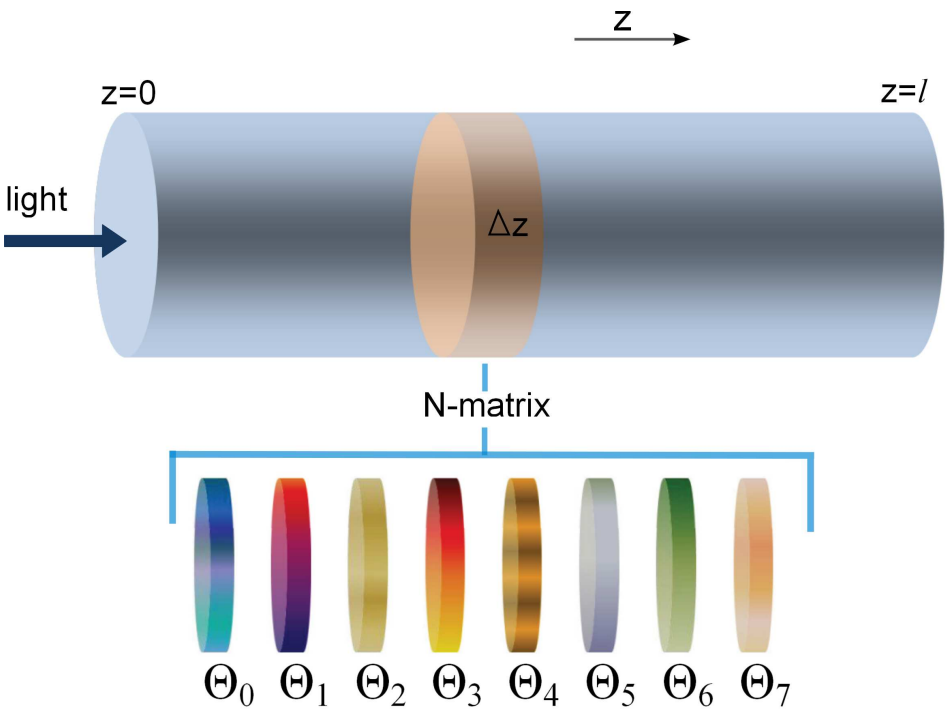

Figure 3.1.: According to the Jones lamellar representation, a thin slab of the medium, of thickness Δz, can be considered as the sum eight elemental subslabs, $\mathbf{\Theta}_k$, each of them corresponding to only one optical property. Together they form the so-called $\mathbf{N}$-matrix. Figure adapted from Ref. [80].

medium with optical activity, because it is easy to apply and yields analytic results that can be directly related to the experiment. The approach for this method is quite different from the Berreman method: instead of using the constitutive relations between the different electromagnetic elements as basic elements of the calculus, it uses the optical effects that such medium exhibits as the basis set for the construction of the model.

The Jones matrix $\mathbf{J}$ governing an optical system can be written in exponential form [81]:

$$\mathbf{J}(\omega, z) = \exp[z\mathbf{N}(\omega)], \tag{3.8}$$

where ω is the frequency and z is the distance into the medium ($z = 0$ denotes the origin of the scattering medium). The matrix $\mathbf{N}$ is the infinitesimal generator of $\mathbf{J}$, and satisfies:

$$\mathbf{N}(\omega) = \lim_{z \to 0} \frac{\mathbf{J}(\omega, z) - \mathbf{I}}{z}. \tag{3.9}$$

Note that the matrix $\mathbf{N}$ no longer depends on z; also in future equations we will omit everywhere the explicit dependence in ω and z. The $\mathbf{N}$-matrix can be also understood as the operator that gets $d\mathbf{J}/dz$ from $\mathbf{J}$:

$$\frac{d\mathbf{J}}{dz} = \mathbf{N}\mathbf{J}. \tag{3.10}$$

According to Jones lamellar representation, a thin slab of a given medium is equivalent to a stack of eight subslabs each possessing one and only one of the eight fundamental optical effects listed in table 1.1. Each one of these effects on this infinitesimal layer was described by Jones with a matrix $\mathbf{\Theta}_k$; namely $\mathbf{\Theta}_0$ for the isotropic refraction, $\mathbf{\Theta}_1$ for the isotropic absorption, $\mathbf{\Theta}_2$ for the horizontal linear dichroism, $\mathbf{\Theta}_3$ for the horizontal linear birefringence, $\mathbf{\Theta}_4$ for the 45° linear dichroism, $\mathbf{\Theta}_5$ for the 45° linear birefringence, $\mathbf{\Theta}_6$ for the 45° circular birefringence and $\mathbf{\Theta}_7$ for the circular birefringence. Each one of this eight matrices can be calculated by applying Eq. (3.9) on the corresponding Jones matrices given in table 1.1. In the limit of infinitesimal thickness, the trigonometric, hyperbolic and exponential functions of the Jones matrices of table 1.1 can be taken to first order and every $\mathbf{\Theta}_k$ gets a very simple form. Then the $\mathbf{N}$-matrix can be then calculated by adding all $\mathbf{\Theta}_k$ matrices [78]:

$$\mathbf{N} = \sum_{k=0}^{7} \mathbf{\Theta}_k. \tag{3.11}$$

The most general expression of the $\mathbf{N}$ matrix for a infinitesimal layer containing all the eight basic optical properties introduced in section 1.5 is:

$$\mathbf{N} = \frac{1}{2z}\begin{pmatrix} -\mathrm{LD} - i\mathrm{LB} - 2(i\eta + \kappa) & -\mathrm{LD}' - i\mathrm{LB}' + \mathrm{CB} - i\mathrm{CD} \\ -\mathrm{LD}' - i\mathrm{LB}' - \mathrm{CB} + i\mathrm{CD} & \mathrm{LD} + i\mathrm{LB} - 2(i\eta + \kappa) \end{pmatrix}. \tag{3.12}$$

where we divide by z to drop the dependence on the slab thickness that is implicit in the optical effects as they were defined in table 1.1. Note also that the notation we use is mostly the one introduced by Schellman, Jensen and Troxell [42, 43], which slightly differs from the notation used by Jones. The notation given in table 1.1 is appropriate to keep the theoretical discussion close to the experiment, because these basic retardances and absorbances correspond to standard experimental quantities which are related to eight measurable physical effects.

Note that, for example, the matrix $\mathbf{N}$ associated with LB commutes with the matrix $\mathbf{N}$ associated with LD but not with the matrix associated to CB, CD, LB′ or LD′. The same can also be verified for the others: they commute with their partner of Eqs. (1.55) but not with the ones that appear in the other lines. This means that, for example, a system that has both LD and LB can be simulated

by a dichroic sample and a birefringent sample no matter which order they are placed. Conversely, for a system with LD and LB′ this is not true. This question will be further discussed in section 4.3.2. It is useful to introduce in the **N** matrix the general complex retardations defined in Eqs. (1.55). With these definitions **N** can be rewritten as:

$$\mathbf{N} = \frac{-i}{2z}\begin{pmatrix} \chi + \mathrm{L} & \mathrm{L}' + i\mathrm{C} \\ \mathrm{L}' - i\mathrm{C} & \chi - \mathrm{L} \end{pmatrix}. \tag{3.13}$$

Using equation (3.13) in (3.8) we obtain:

$$\mathbf{J} = \exp[-i\mathbf{R}] \quad \text{where} \quad \mathbf{R} = \frac{1}{2}\begin{pmatrix} \chi + \mathrm{L} & \mathrm{L}' + i\mathrm{C} \\ \mathrm{L}' - i\mathrm{C} & \chi - \mathrm{L} \end{pmatrix}. \tag{3.14}$$

And if we define a generalized retardance vector $\vec{\mathrm{T}} \equiv (\mathrm{L}, \mathrm{L}', -\mathrm{C})$ we can write **R** in a compact form:

$$\mathbf{R} = \frac{1}{2}(\chi \boldsymbol{\sigma}_0 + \vec{\boldsymbol{\sigma}} \cdot \vec{\mathrm{T}}), \tag{3.15}$$

where $\boldsymbol{\sigma}_0$ is a 2×2 identity matrix, $\vec{\boldsymbol{\sigma}} = (\boldsymbol{\sigma}_1, \boldsymbol{\sigma}_2, \boldsymbol{\sigma}_3)$, and $\boldsymbol{\sigma}_1$, $\boldsymbol{\sigma}_2$ and $\boldsymbol{\sigma}_3$ are the three Pauli spin matrices:

$$\begin{aligned} \boldsymbol{\sigma}_0 &= \begin{bmatrix} 1 & 0 \\ 0 & 1 \end{bmatrix}, \quad \boldsymbol{\sigma}_1 = \begin{bmatrix} 1 & 0 \\ 0 & -1 \end{bmatrix}, \\ \boldsymbol{\sigma}_2 &= \begin{bmatrix} 0 & 1 \\ 1 & 0 \end{bmatrix}, \quad \boldsymbol{\sigma}_3 = \begin{bmatrix} 0 & -i \\ i & 0 \end{bmatrix}. \end{aligned} \tag{3.16}$$

Using this definition, Eq. (3.14) transforms in

$$\mathbf{J} = \exp[-i\mathbf{R}] = e^{-i\chi/2} e^{-i(\vec{\boldsymbol{\sigma}}\cdot\vec{\mathrm{T}})/2} = e^{-i\chi/2} e^{-i(\vec{\boldsymbol{\sigma}}\cdot\vec{\mathrm{T}}_R + \vec{\boldsymbol{\sigma}}\cdot(-i\vec{\mathrm{T}}_D))/2}. \tag{3.17}$$

On the right hand side we have written $\vec{\mathrm{T}}$ as the sum of two vectors: $\vec{\mathrm{T}} = \vec{\mathrm{T}}_R - i\vec{\mathrm{T}}_D$ where $\vec{\mathrm{T}}_R \equiv (\mathrm{LB}, \mathrm{LB}', -\mathrm{CB})$ contains only dispersive terms and $\vec{\mathrm{T}}_D \equiv (\mathrm{LD}, \mathrm{LD}', -\mathrm{CD})$ is formed by absorptive terms.

The Jones matrix **J** can also be written in terms of trigonometric functions:

$$\mathbf{J} = e^{-i\chi/2} \exp(-i\frac{\mathrm{T}}{2}\frac{\vec{\mathrm{T}}}{\mathrm{T}} \cdot \vec{\boldsymbol{\sigma}}) = e^{-i\chi/2}[\boldsymbol{\sigma}_0 \cos\frac{\mathrm{T}}{2} - \frac{i}{\mathrm{T}}\vec{\mathrm{T}} \cdot \vec{\boldsymbol{\sigma}} \sin\frac{\mathrm{T}}{2}] \tag{3.18}$$

where $\vec{\mathrm{T}} = (\mathrm{L}, \mathrm{L}', -\mathrm{C})$ and T is the module of this vector ($\mathrm{T} = \sqrt{\mathrm{L}^2 + \mathrm{L}'^2 + \mathrm{C}^2}$). Using complete matrix notation (3.18) can be rewritten as:

$$\mathbf{J} = e^{-i\chi/2}\begin{pmatrix} \cos\frac{\mathrm{T}}{2} - \frac{i\mathrm{L}}{\mathrm{T}}\sin\frac{\mathrm{T}}{2} & \frac{(\mathrm{C}-i\mathrm{L}')}{\mathrm{T}}\sin\frac{\mathrm{T}}{2} \\ -\frac{(\mathrm{C}+i\mathrm{L}')}{\mathrm{T}}\sin\frac{\mathrm{T}}{2} & \cos\frac{\mathrm{T}}{2} + \frac{i\mathrm{L}}{\mathrm{T}}\sin\frac{\mathrm{T}}{2} \end{pmatrix}. \tag{3.19}$$

The infinitesimal method reviewed in this section uses the eight optical effects given in table 1.1 as a basis set for constructing the properties of any complex optical element. In contrast, the Berreman method presented before uses the dielectric and gyration tensors of the medium as a basis set. Although both methods are constructed from a different perspective it should be possible to correlate both basis sets and, in fact, this was already attempted by Jones in the last paper of his series [82]. Future work should be directed towards revising this paper, that otherwise has remained quite overlooked, to strengthen the connections between both methods.

3.2.1. Calculation of the Mueller-Jones matrix

Our purpose here is to find the Mueller-Jones matrix corresponding to the Jones matrix of Eq. (3.19). This Mueller matrix can be directly found applying the transformation relationship of Eq. (1.29) to our Jones matrix. Alternatively, we can also calculate the elements of the Mueller matrix, m_{ij}, one by one, using the following expression:

$$m_{ij} = \frac{1}{2}\mathrm{Tr}(\sigma_i \mathbf{J} \sigma_j \mathbf{J}^\dagger) \tag{3.20}$$

where $\mathbf{J}^\dagger$ is the conjugate transpose of $\mathbf{J}$. With any of the two possible approaches after some lengthly algebra [83] we find:

$$\mathbf{M} = e^{-2\kappa} \begin{bmatrix} X & -U\mathrm{LD} - V\mathrm{LB} \\ +(W/2)(\vec{\mathrm{T}}^* \cdot \vec{\mathrm{T}}) & +W(\mathrm{CBLD}' - \mathrm{LB}'\mathrm{CD}) \\ -U\mathrm{LD} - V\mathrm{LB} & X + W(\mathrm{LD}^2 + \mathrm{LB}^2) \\ -W(\mathrm{CBLD}' - \mathrm{LB}'\mathrm{CD}) & -(W/2)(\vec{\mathrm{T}}^* \cdot \vec{\mathrm{T}}) \\ -U\mathrm{LD}' - V\mathrm{LB}' & -U\mathrm{CB} + V\mathrm{CD} \\ -W(\mathrm{LBCD} - \mathrm{CBLD}) & +W(\mathrm{LBLB}' + \mathrm{LDLD}') \\ U\mathrm{CD} + V\mathrm{CB} & -U\mathrm{LB}' + V\mathrm{LD}' \\ -W(\mathrm{LBLD}' - \mathrm{LB}'\mathrm{LD}) & -W(\mathrm{CBLB} + \mathrm{CDLD}) \end{bmatrix}$$

$$\begin{bmatrix} -U\mathrm{LD}' - V\mathrm{LB}' & U\mathrm{CD} + V\mathrm{CB} \\ +W(\mathrm{LBCD} - \mathrm{CBLD}) & +W(\mathrm{LBLD}' - \mathrm{LB}'\mathrm{LD}) \\ U\mathrm{CB} - V\mathrm{CD} & U\mathrm{LB}' - V\mathrm{LD}' \\ +W(\mathrm{LBLB}' + \mathrm{LDLD}') & -W(\mathrm{CBLB} + \mathrm{CDLD}) \\ X + W(\mathrm{LB}'^2 + \mathrm{LD}'^2) & -U\mathrm{LB} + V\mathrm{LD} \\ -(W/2)(\vec{\mathrm{T}}^* \cdot \vec{\mathrm{T}}) & -W(\mathrm{CBLB}' + \mathrm{CDLD}') \\ U\mathrm{LB} - V\mathrm{LD} & X + W(\mathrm{CD}^2 + \mathrm{CB}^2) \\ -W(\mathrm{CBLB}' + \mathrm{CDLD}') & -(W/2)(\vec{\mathrm{T}}^* \cdot \vec{\mathrm{T}}) \end{bmatrix} \tag{3.21}$$

where

$$\begin{aligned} U &= (\mathrm{T}^i \sinh \mathrm{T}^i + \mathrm{T}^r \sin \mathrm{T}^r)/\mathrm{TT}^*, \\ V &= (\mathrm{T}^i \sin \mathrm{T}^r - \mathrm{T}^r \sinh \mathrm{T}^i)/\mathrm{TT}^*, \\ W &= (\cosh \mathrm{T}^i - \cos \mathrm{T}^r)/\mathrm{TT}^*, \\ X &= (\cosh \mathrm{T}^i + \cos \mathrm{T}^r)/2, \end{aligned} \tag{3.22}$$

and where T^r is the real part of T and T^i is the imaginary part of T ($\mathrm{T} = \sqrt{\mathrm{L}'^2 + \mathrm{C}^2 + \mathrm{L}^2}$). This Mueller matrix was first given by Jensen, Schellman and Troxell in 1978 [43], and it was rewritten in a more convenient way by Shellman and Jensen in 1987 [42] using the same U, V, W and X functions that we have introduced. However, note that the order of the elements of the Mueller matrix given in [42] differs from this one, because a different order of the Stokes parameters has been used.

The matrix appearing in Eq. (3.21) is rather complex, but it can be easily simplified assuming small values for the anisotropic effects of table 1.1, as often happens for thin specimens. In this case the parameters U, V W and X of Eq. (3.22) tend, respectively, to 1, 0, 1/2 and 1, as it is shown in Fig. 3.2, and the following simplification can be rather useful:

$$\mathbf{M} \simeq e^{-2\kappa} \begin{bmatrix} 1 + \frac{1}{2}(\mathrm{LD}'^2 + \mathrm{LD}^2) & -\mathrm{LD} \\ -\mathrm{LD} & 1 + \frac{1}{2}(\mathrm{LD}^2 - \mathrm{LB}'^2) \\ -\mathrm{LD}' & -\mathrm{CB} + \frac{1}{2}(\mathrm{LBLB}' + \mathrm{LDLD}') \\ \mathrm{CD} - \frac{1}{2}(\mathrm{LBLD}' - \mathrm{LB}'\mathrm{LD}) & -\mathrm{LB}' \end{bmatrix}$$

$$\begin{bmatrix} -\mathrm{LD}' & \mathrm{CD} \\ & +\frac{1}{2}(\mathrm{LBLD}' - \mathrm{LB}'\mathrm{LD}) \\ \mathrm{CB} & \mathrm{LB}' \\ +\frac{1}{2}(\mathrm{LBLB}' + \mathrm{LDLD}') & \\ 1 & -\mathrm{LB} \\ +\frac{1}{2}(\mathrm{LD}'^2 - \mathrm{LB}^2) & \\ \mathrm{LB} & 1 \\ & -\frac{1}{2}(\mathrm{LB}^2 + \mathrm{LB}'^2) \end{bmatrix} \tag{3.23}$$

This matrix indicates that for small values of the anisotropic effects the elements of the antidiagonal (m_{03}, m_{12}, m_{21} and m_{30}) are the most important for the study of optical activity: $(m_{03} + m_{30})/2$ can be a measure of CD and CB can be obtained from $(m_{12} - m_{21})/2$. In this particular situation the linear effects can be directly "read" from the elements of the Mueller matrix (i.e. $-m_{01}$ is LD, $-m_{02}$ is LD′, etc).

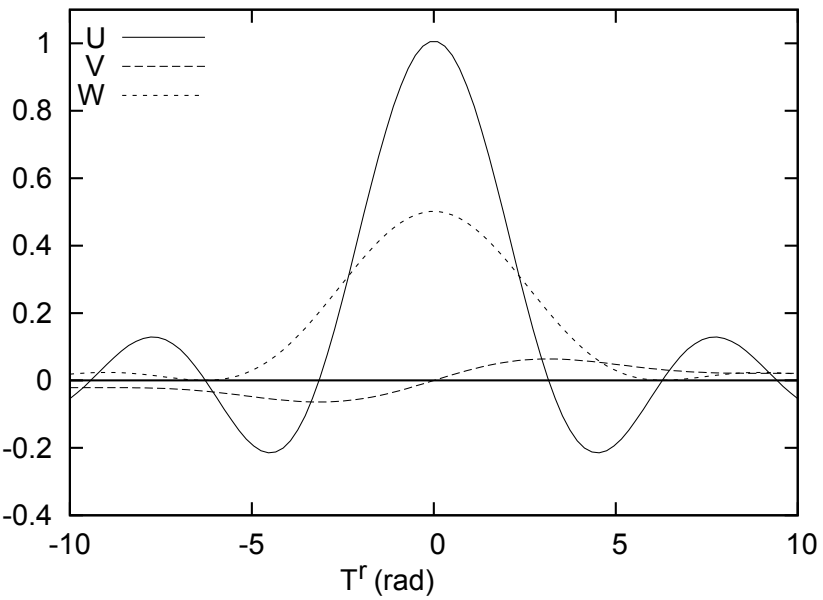

Figure 3.2.: Values of U, V and W as a function of T^r (the real part of total complex retardance $\mathrm{T} = \sqrt{\mathrm{L}'^2 + \mathrm{C}^2 + \mathrm{L}^2}$). The imaginary part, T^i, has been fixed to 0.2 rad. In the limit of small anisotropies, we obtain small values of $|\mathrm{T}^r|$ (typically < 0.5 rad) and U, W and V can be respectively approximated as 1, 1/2 and 0.

Commercial CD spectropolarimeters take the CD values directly from a Mueller matrix element (usually m_{03}, although m_{30} would be also possible). However, from the analysis presented above it is easy to realize that 3 conditions must be fulfilled to permit m_{03} and m_{30} to be "real" measurements of CD:

- the light beam must go through a homogeneous medium,
- all the optical effects (birefringence and dichroism) must be small enough to permit the simplification that results in matrix of Eq. (3.23),
- the factor $\frac{1}{2}(\mathrm{LBLD'} - \mathrm{LB'LD})$ must vanish.

These conditions seem very restrictive but, fortunately, for most of the standard samples that are measured in chemistry, biology, pharmacy, etc these conditions are fulfilled. This is the reason why commercial instruments usually work well.

The mathematical characterization of the general Mueller matrix of a homogeneous nondepolarizing media has an important interest for experimentalists because it allows the physical interpretation of the information that provides the sixteen elements of the Mueller matrix. Two interesting Mueller matrices can be straightforwardly derived from Eq. (3.21). Imposing $\mathrm{CB} = \mathrm{LB} = \mathrm{LB'} = 0$ we obtain the Mueller matrix of a general diattenuator, $\mathbf{M}_D$, i.e. the Mueller matrix of an optical element that shows no birefringence or retardation. With the condition $\mathrm{CD} = \mathrm{LD} = \mathrm{LD'} = 0$ we obtain the Mueller matrix of a general retarder, $\mathbf{M}_R$, an optical element that has no dichroism and diattenuation [3]:

$$\mathbf{M}_R = \begin{bmatrix} 1 & 0 & 0 & 0 \\ 0 & \cos \mathrm{T}_R + \mathrm{LB}^2\alpha & \mathrm{LBLB'}\alpha + \mathrm{CB}\beta & -\mathrm{LBCB}\alpha + \mathrm{LB'}\beta \\ 0 & \mathrm{LBLB'}\alpha - \mathrm{CB}\beta & \cos \mathrm{T}_R + \mathrm{LB'}^2\alpha & -\mathrm{LB'CB}\alpha - \mathrm{LB}\beta \\ 0 & -\mathrm{LBCB}\alpha - \mathrm{LB'}\beta & -\mathrm{LB'CB}\alpha + \mathrm{LB}\beta & \cos \mathrm{T}_R + \mathrm{CB}^2\alpha \end{bmatrix}, \tag{3.24}$$

with $\alpha = (1 - \cos \mathrm{T}_R)/\mathrm{T}_R^2$, $\beta = \sin \mathrm{T}_R/\mathrm{T}_R$ and $\mathrm{T}_R = \sqrt{\mathrm{LB}^2 + \mathrm{LB'}^2 + \mathrm{CB}^2}$.

$$\mathbf{M}_D = e^{-2k} \begin{bmatrix} \cosh \mathrm{T}_D & -\mathrm{LD}\nu & -\mathrm{LD'}\nu & \mathrm{CD}\nu \\ -\mathrm{LD}\nu & 1 + \mathrm{LD}^2\mu & \mathrm{LDLD'}\mu & -\mathrm{LDCD}\mu \\ -\mathrm{LD'}\nu & \mathrm{LDLD'}\mu & 1 + \mathrm{LD'}^2\mu & -\mathrm{LD'CD}\mu \\ \mathrm{CD}\nu & -\mathrm{LDCD}\mu & -\mathrm{LD'CD}\mu & 1 + \mathrm{CD}^2\mu \end{bmatrix}, \tag{3.25}$$

[3] Note that in the context of this work the words "diattenuation" and "dichroism" are synonyms. The same is applicable to the pair "birefringence" and "retardation".

with $\mu = (\cosh \mathrm{T}_D - 1)/\mathrm{T}_D^2$, $\nu = \sinh \mathrm{T}_D/\mathrm{T}_D$ and $\mathrm{T}_D = \sqrt{\mathrm{LD}^2 + \mathrm{LD}'^2 + \mathrm{CD}^2}$.

3.2.2. The effect of the interfaces

The infinitesimal matrix method described in section 3.2 does not take into account the effect of the interfaces. When studying light transmission through a certain homogeneous material the most common situation is having two well defined interfaces: one delimiting the incident medium (usually air) to the material and the other one between the material and the exiting medium (also usually air). If multiple reflections are excluded, the transmission Mueller matrix of the complete system is then given by:

$$\mathbf{M} = \mathbf{M}_{I1}\mathbf{M}_S\mathbf{M}_{I0}, \tag{3.26}$$

where $\mathbf{M}_{I0}$ and $\mathbf{M}_{I1}$ are, respectively, the Mueller matrices corresponding to the incident and exiting interfaces. $\mathbf{M}_S$ is the Mueller-Jones matrix of the "bulk" material given in Eq. (3.21), and constructed from the thickness-dependent parameters given in table 1.1.

At normal-incidence, $\mathbf{M}_{I0}$ and $\mathbf{M}_{I1}$ can only have a certain contribution if the measured sample is anisotropic, otherwise the matrices $\mathbf{M}_{I0}$ and $\mathbf{M}_{I1}$ are the identity matrix. If the sample under study is nonabsorbent (i.e. if LD, LD' and CD in $\mathbf{M}_S$ vanish) then $\mathbf{M}_{I0}$ and $\mathbf{M}_{I1}$ describe the difference polarization transmission at the interface, i.e. a diattenuation, and, in this case, the interface matrices do not include any retardation, as it will be demonstrated later in this section. In the case where $\mathbf{M}_S$ contains any anisotropic absorption then there appears a phase shift at the interface that translates in Mueller matrices $\mathbf{M}_{I0}$ and $\mathbf{M}_{I1}$ including also retardation terms.

The interface diattenuation for two orthogonal polarization states, e.g. x and y, as it appears in the Mueller matrix, can be calculated as:

$$D^I_{yx} = \frac{t_y t_y^* - t_x t_x^*}{t_y t_y^* + t_x t_x^*}, \tag{3.27}$$

where the superscript I refers to the interface and t_y and t_x are the complex transmission coefficients, that, at normal incidence, are:

$$t_k = \frac{2n_0}{n_0 + n_k - ik_k}, \quad k = x, y \tag{3.28}$$

where n_0 is the refractive index in the incident medium and $n_k - ik_k$ is the complex refractive index of the sample for light polarized along the k direction.

A subtlety that needs to be noted is that, for an interface diattenuation, the real-valued terms $t_k t_k^*$ used in Eq.(3.27) are not directly the intensity transmission

coefficients T_x and T_y for light polarized along the x or y, used in other definitions of the global diattenuation [84]. These transmission coefficients are

$$T_k = t_k t_k^* \frac{n_k}{n_0} = 1 - R_k. \quad \text{(normal incidence)} \tag{3.29}$$

where the factor n_k/n_0 is due to the change of medium. The reason why this transmittance coefficient, T_k, should not be used here is that the diattenuation occurring at one interface depends only on the amplitude of the transmitted fields as a function of the incident polarization, and the index of refraction is not included in the definitions of the Jones vectors or in the Stokes parameters. In case we were looking at the diattenuation of the reflected light, the reflection coefficients R_k could be used for the calculation of the diattenuation [85].

The retardation[4] Δ for the transmitted beam upon the interface for two orthogonal polarization states, e.g. x and y, is

$$\Delta_{yx} = \arg(t_y) - \arg(t_x), \tag{3.30}$$

which, at normal incidence, is

$$\Delta_{yx} = \operatorname{atan}\left[\frac{k_y(n_0 + n_x) - k_x(n_0 + n_y)}{(n_0 + n_x)(n_0 + n_y) + k_x k_y}\right], \tag{3.31}$$

demonstrating that for $k_x = k_y = 0$ no retardation appears in the interface.

At normal incidence the effect of the interfaces will be, in general, very small and only will be noticeable for samples with large anisotropy. For example, in a crystal with huge birefringence such as calcite, the transmission Mueller matrices at the interfaces[5] are:

$$\begin{aligned}
\mathbf{M}_{I0} &= \begin{bmatrix} 1 & 0.0668 & 0 & 0 \\ 0.0668 & 1 & 0 & 0 \\ 0 & 0 & 0.9978 & 0 \\ 0 & 0 & 0 & 0.9978 \end{bmatrix}, \\
\mathbf{M}_{I1} &= \begin{bmatrix} 1 & -0.0426 & 0 & 0 \\ -0.0426 & 1 & 0 & 0 \\ 0 & 0 & 0.9991 & 0 \\ 0 & 0 & 0 & 0.9991 \end{bmatrix},
\end{aligned} \tag{3.32}$$

[4] We use here the symbol Δ for the retardation to clearly distinguish it from the reflection coefficients R. However, in other parts of these thesis, most notably in chapter 4, the retardations will be referred with a R to be consistent with the published literature.

[5] The transmission Mueller matrix of an interface can be readily calculated from the Jones matrix of the interface (that is built from the Fresnel transmission coefficients) using Eq. (1.29). Alternatively, it can be also obtained using the dichroism and birefringence parameters of the interface [calculated with formulas analog to Eqs. (3.27) and (3.31)] in Eq.(3.21). More information can be found in Refs. [3, 85, 86].

where we have assumed that the optic axis is parallel to the y axis of the laboratory frame ($n_y = n_e = 1.486$, $n_x = n_o = 1.658$).

Only when studying samples with large anisotropy does the effect of the interfaces need to be considered in detail. Otherwise the Mueller interface matrices may be taken as the identity matrix without introducing significant errors. In the normal-incidence transmission experiments performed in this thesis the effect of the interfaces has not been considered.

3.2.3. The controversy about Jones birefringence (LB′) and Jones dichroism (LD′)

Certain of the contents of this section are probably redundant considering the introduction to the optical effects we made in section 1.5.2. However we consider that they are important enough to be studied here in more detail as they have led to confusion in a considerable number of publications.

In 1983 Graham and Raab published a paper [87] stating that in Jones 1948 work [78] a new kind of linear birefringence, together with its corresponding dichroism, had been postulated, and proposed the names *Jones birefringence* and *Jones dichroism* for such effects. They argued that the linear birefringence and the linear dichroism parallel with the bisectors of the coordinate axes x, y, that in this work we have respectively named as LB′ and LD′ [see Eq. (1.41) and Eq. (1.47)], were new types of optical effects that were unknown up to the date. In their work they predicted that Jones birefringence can occur naturally in certain uniaxial and biaxial non-magnetic crystals, where it should accompany the "familiar" linear birefringence. They also predicted the presence of Jones birefringence in liquids subjected to parallel electric and magnetic fields. Later, in Ref. [88] they found, by using a multipole approach to the electromagnetic effects, that Jones birefringence would be typically four orders of magnitude smaller than the usual linear birefringence.

To our knowledge no experimental observations of the Jones birefringence in crystals have been reported. According to [89], Jones birefringence occurring naturally in crystals is probably too weak to be measurable. However, the first experimental observation of Jones birefringence in systems with parallel electric and magnetic fields was published in 2000 [90], and, in 2003, the first experimental observation of Jones dichroism was reported [91]. Since then, the interest on the subject of Jones birefringence and Jones dichroism seems to increase [92–97] and recent books, most notably the well-known book about optical activity by Barron [98], review the subject. Much like Ref. [87], most of these publications state that these supposed new effects were deduced by Jones, and even, in Ref. [90], it is said that their experimental observation constitutes the final validation of the

Jones formalism in polarization optics.

We argue that in his 1948 paper Jones did not introduce neither deduce any intriguing new optical phenomenon. We think that linear birefringence and linear dichroism parallels with the bisectors of the coordinate axes that Jones used are not new optical effects of difficult experimental observation, and that the controversy about these effects stems from a misinterpretation of the coordinated system used in the original Jones publication, misinterpretation that probably started with Ref. [87].

Jones calculus can be developed for an arbitrary basis, although the most usual choice is a laboratory Cartesian coordinate system in which light propagates along the positive z axis as the one we have been using in this chapter. Rather than a new type of birefringence, LB$'$ is only a measure of the part of the linear birefringence which is parallel to the bisector of the coordinate axes and it does not suppose any new finding. We suspect that the confusion must have arisen with the incorrect assumption that Jones used a coordinate system based on the optic axis of the optical element under study. As we said when we introduced the optical effects, it is important to stress that, in general, neither LB nor LB$'$, as defined by Jones, are equivalent to the usual definition of linear birefringence given in crystal optics:

$$\delta = \frac{2\pi}{\lambda}(n_e - n_o)l, \tag{3.33}$$

because this definition is given for the natural basis of the birefringent element, i.e. a coordinate system based on the crystallographic (ordinary and extraordinary) axes of the optical element. If the optic axis lies in the xy plane (it may be not always the case) the relation between δ and LB and LB$'$ clearly shows that LB and LB$'$ can be understood as measurements of the "projected" of birefringence:

$$\mathrm{LB} = \delta\cos(2\theta), \quad \mathrm{LB}' = \delta\sin(2\theta), \tag{3.34}$$

where θ is the angle shown in Fig. 3.3. For an arbitrary orientation of the optic axis, the correspondence between δ and LB and LB$'$ is more complex and involves the complete set of Euler angles.

To our knowledge there are no further and solid arguments proving the existence of a supposed new type of birefringence or dichroism independent from the "usual" one. Theoretical works on this subject are not aimed to demonstrate the Jones birefringence and Jones dichroism as new phenomena independent from the standard linear birefringence; instead, they assume that they exist by citing Jones work, and focus their attention on identifying systems in which these effects may be possible.

According to our thesis [99], experimental observations of that part of the linear birefringence or the linear dichroism parallel to the bisector of the laboratory co-

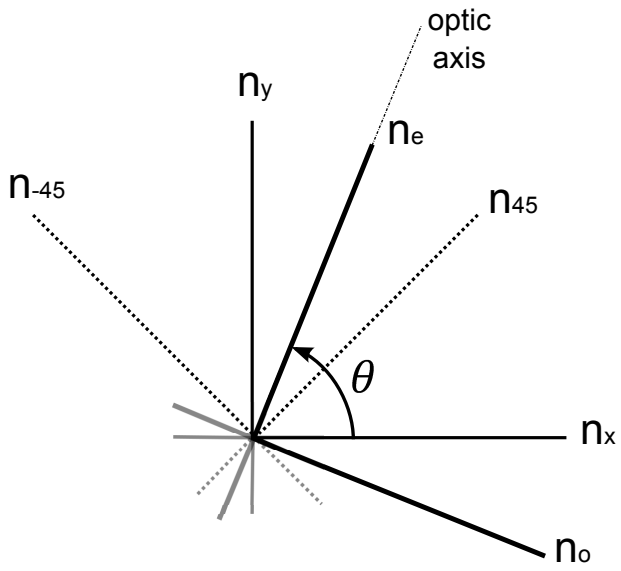

Figure 3.3.: For an optical element with the optic axis lying in the xy plane, the laboratory coordinates x and y (reference basis) are related to the crystallographic coordinates (natural basis) by a simple rotation.

ordinate axes can be easily done with polarimetric techniques, as it is shown, for example, in [100], and it does not involve any special difficulty. Probably, most of the reported experimental results on Jones birefringence or Jones dichroism could be interpreted as measurements of "projected" birefringence or dichroism, and, therefore, their physical meaning would be given by their correspondence, in terms of Euler angles, to the birefringence or dichroism of the natural basis. We also use these lines to advise against the use of the terms of "Jones birefringence" and "Jones dichroism" as we consider that they were proposed following a misinterpretation of Jones' work.

3.2.4. Twisted crystal

We have used the lamellar representation to study in detail the important but particular case in which the **N**-matrices are independent of z. There is a another special dependence of **N** upon z that permits a simple solution: the case of a uniformly twisted crystal in which light is incident along the helical axis. This problem was already solved by Jones [78] and it is specially suitable for the study of the cholesteric phase of liquid crystals. We will dedicate our attention to study this problem, since it constitutes a simple example of how a material constituted

by achiral elements can give rise to optical activity.

Let $\mathbf{N}_0$ be the $\mathbf{N}$-matrix of the untwisted crystal. For simplicity we consider that each thin slab does not have an own CB or CD and its natural basis coincides with the laboratory basis (in this case $\mathrm{LB}' = \mathrm{LD}' = 0$). Then the untwisted $\mathbf{N}_0$ is:

$$\mathbf{N}_0 = \frac{1}{2z}\begin{pmatrix} -\mathrm{LD} - i\mathrm{LB} - 2(i\eta + \kappa) & 0 \\ 0 & \mathrm{LD} + i\mathrm{LB} - 2(i\eta + \kappa) \end{pmatrix}. \tag{3.35}$$

Then, according to Eq. (1.21), the $\mathbf{N}$-matrix corresponding to a twisted crystal at a distance z is given by

$$\mathbf{N} = \mathbf{R}(-az)\mathbf{N}_0\mathbf{R}(az), \tag{3.36}$$

where a is the angular twist per unit of thickness (e.g. radians per meter). Fig. 3.4 shows that the progressive and uniform rotation of the infinitesimal slices yields an helical structure. The z axis of this structure coincides with the direction of light propagation. The pitch P of the helix (the width of one complete helix turn) is related to a by

$$a = \frac{2\pi}{P}. \tag{3.37}$$

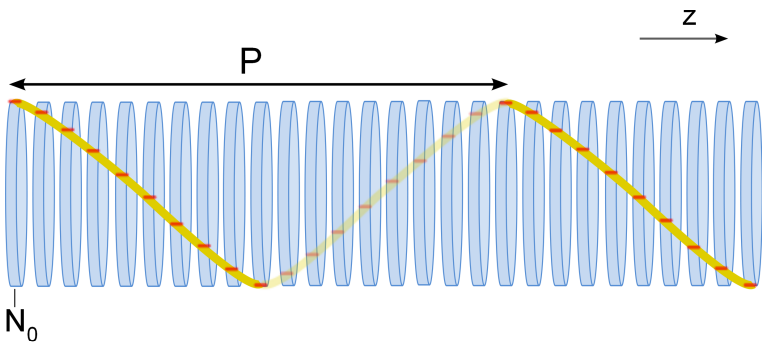

Figure 3.4.: Scheme of the lamellar representation for a homogeneously twisted crystal. Red marks indicate the direction of the axis of birefringence for each one of the infinitesimal slices. The pitch P indicates the distance at which the axis has made a complete turn.

Eq. (3.10) can now be written as

$$\frac{d\mathbf{J}}{dz} = \mathbf{R}(-az)N_0\mathbf{R}(az)\mathbf{J}, \tag{3.38}$$

that after introducing the substitution

$$\mathbf{J}' \equiv \mathbf{R}(az)\mathbf{J}, \tag{3.39}$$

becomes

$$\frac{d\mathbf{J}'}{dz} = [\mathbf{N}_0 - \mathbf{R}(az)\frac{d\mathbf{R}(-az)}{dz}]\mathbf{J}' = \mathbf{N}'\mathbf{J}, \tag{3.40}$$

where $\mathbf{N}' = \mathbf{N}_0 - \mathbf{R}(az)\frac{d\mathbf{R}(-az)}{dz}$.

After calculating $d\mathbf{R}(-az)/dz$ we realize that $\mathbf{N}'$ can be written in the following form:

$$\mathbf{N}' = \mathbf{N}_0 + a\mathbf{R}(\pi/2), \tag{3.41}$$

so that the solution of Eq. (3.40) may be written as

$$\mathbf{J}' = \exp[\mathbf{N}'z], \tag{3.42}$$

and with the help of Eq. (3.39) we find that $\mathbf{J}$ is

$$\mathbf{J} = \mathbf{R}(-az)\exp[\mathbf{N}'z] = \mathbf{R}(-az)\exp\left(\mathbf{N}_0 + a\mathbf{R}(\pi/2)\right)z. \tag{3.43}$$

This result indicates that the Jones matrix of the twisted crystal is equal to $\mathbf{R}(-az)$ multiplied by the Jones matrix corresponding to a homogeneous medium with a $\mathbf{N}$-matrix equal to $\mathbf{N}_0 + a\mathbf{R}(\pi/2)$.

Eq. (3.43) can be easily written in terms of a product of Mueller-Jones matrices. The rotation matrix $\mathbf{R}$ for the Mueller formalism has been given in Eq. (1.27) and the Mueller-Jones matrix corresponding to a homogeneous medium with a N-matrix equal to $\mathbf{N}_0 + a\mathbf{R}(\pi/2)$ is easily derivable from the general Mueller-Jones matrix of a homogeneous medium given in Eq. (3.21). To make things even easier we can consider that the $\mathbf{N}_0$ matrix does not contain absorption effects (i.e. LD and κ terms of (3.35) vanish). In this case we can write the Mueller-Jones matrix for a twisted crystal as the following product of matrices:

$$\mathbf{M} = \begin{bmatrix} 1 & 0 & 0 & 0 \\ 0 & \cos 2az & -\sin 2az & 0 \\ 0 & \sin 2az & \cos 2az & 0 \\ 0 & 0 & 0 & 1 \end{bmatrix} \begin{bmatrix} 1 & 0 & 0 & 0 \\ 0 & \cos \mathrm{T}_L + \mathrm{LB}^2\alpha & 2az\beta & -\mathrm{LB}2az\alpha \\ 0 & -2az\beta & \cos \mathrm{T}_L & -\mathrm{LB}\beta \\ 0 & -2az\mathrm{LB}\alpha & \mathrm{LB}\beta & \cos \mathrm{T}_L + (2az)^2\alpha \end{bmatrix} \tag{3.44}$$

with $\alpha = (1 - \cos \mathrm{T}_L)/\mathrm{T}_L^2$, $\beta = \sin \mathrm{T}_L/\mathrm{T}_L$ and $\mathrm{T}_L = \sqrt{\mathrm{LB}^2 + (2az)^2}$.

Note that if we impose that isotropy of the medium (i.e. we take $\mathrm{LB} = 0$) the Mueller matrix on Eq. (3.44) simplifies to an identity matrix (the second matrix

factor becomes the inverse of the first factor). This is a expected result, since the polarization of light that passes through an isotropic medium, no matter how it is oriented, is not altered.

If the pitch is not too large the quantity $2az$ will be much greater than LB ($2az \gg \mathrm{LB}$). When this happens we can approximate $\mathrm{T}_L \simeq 2az$ and the Mueller matrix becomes:

$$\mathbf{M} = \begin{bmatrix} 1 & 0 & 0 & 0 \\ 0 & 1+\cos 2az\frac{\mathrm{LB}^2}{(2az)^2}(1-\cos 2az) & 0 & \frac{\mathrm{LB}}{2az}(1-\cos 2az) \\ 0 & \mathrm{LB}^2 \sin 2az \frac{1-\cos 2az}{(2az)^2} & 1 & -\frac{\mathrm{LB}}{2az}\sin 2az \\ 0 & -\frac{\mathrm{LB}}{2az}(1-\cos 2az) & \frac{\mathrm{LB}}{2az}\sin 2az & 1 \end{bmatrix}. \tag{3.45}$$

The **N**-matrix for each one of the infinitesimal layers considered in this model did not include optical effects related to optical activity (CB and CD). However the Jones or the Mueller-Jones matrix of the complete twisted crystal will appear to be that of a homogeneous medium exhibiting optical activity. We can check it by noting that for a general retarder [Eq. (3.24)], the CB is proportional to the difference of Mueller matrix elements m_{12} and m_{21} and LB is proportional to $m_{23} - m_{32}$:

$$\mathrm{CB} = \frac{\mathrm{T}_R}{\sin \mathrm{T}_R}(m_{12} - m_{21})/2, \tag{3.46a}$$

$$\mathrm{LB} = \frac{\mathrm{T}_R}{\sin \mathrm{T}_R}(m_{32} - m_{23})/2, \tag{3.46b}$$

where T_R is the total retardance of the optical element. These two equations allow to find the relation:

$$\mathrm{CB} = \mathrm{LB}\frac{m_{32} - m_{23}}{m_{12} - m_{21}}. \tag{3.47}$$

By using this equation with the Mueller matrix shown in Eq. (3.45) we can find the approximate circular birefringence induced by the twist of the crystal:

$$\mathrm{CB} = -\frac{\mathrm{LB}^2}{4az}(1 - \cos 2az), \tag{3.48}$$

and using the definitions $\mathrm{LB} = 2\pi\delta n z/\lambda$ [Eq. (1.40)] and $a = 2\pi/P$ [Eq. (3.37)] we obtain that the circular birefringence of the twisted crystal is

$$\mathrm{CB} = -\frac{\pi(\delta n)^2 P z}{2\lambda^2}(1 - \cos 2az). \tag{3.49}$$

The negative sign indicates that the sense of the rotation is opposite to that of the helical twist of the structure. This solution is quite interesting because it shows that even a simple phenomenological model is able to reproduce the typical $\sim 1/\lambda^2$ dependence for optical rotation which is usually observed experimentally. Note also that in this case the pitch, P, plays the role of the parameter d (a typical molecular length) we mentioned at the beginning of this chapter. This solution describes, for example, the propagation of light along the helical axis of a cholesteric liquid crystal but only for cases in which the pitch is not much greater than the wavelength. Otherwise we should use a more complex model to consider the reflection and interference effects that we have been neglecting. The same calculus can be performed without introducing the **N** matrix (as it is shown in Ref. [101]). This method yields the same results but involves more cumbersome algebra.

As a final remark is worth to recall here that from the point of view of the Jones or the Mueller-Jones matrices an optical rotation of, let's say, 20° is indistinguishable from an optical rotation of 380° (also from 740°, 1100°, etc). This is the reason why Eq. (3.49) contains the term $(1 - \cos 2az)$. There is always a 2π indetermination associated to the Jones/Mueller matrix of a retarder and this facts needs to be considered if we deal with samples that are expected to exhibit a retardance greater than 2π radians. This indetermination also appears when measuring linear birefringence although it is somewhat less evident.

Chapter 4.

Inversion and decomposition of Mueller matrices

In this chapter we will focus our attention in obtaining of the relevant polarization-dependent optical effects from a given experimental Mueller matrix. The first method we will present is the analytic inversion of the more general Jones or Mueller-Jones matrices discussed in the previous chapter. This inversion is restricted to the case of light propagation through an homogeneous medium with arbitrary absorptive and refractive anisotropies, which is one of the most common situations one can find when studying complex materials with polarimetric techniques.

However, the problem of the physical interpretation of a measured Mueller matrix can also be studied with an algebraic approach based on the decomposition of the Mueller matrix. Constructing a physical model for a Jones or a Mueller matrix is only feasible in a limited number of optical systems (some of them have been shown in the previous chapter). Moreover, even if a certain model for a system with optical anisotropy is available, it will probably give a description based on the Jones matrix, and, because of the phenomenon of depolarization, it may not directly correspond to an experimental Mueller matrix, i.e. it can be not possible to extract easily a Jones matrix from an experimental Mueller matrix. If used with care, decomposition methods can be useful to extract valuable information from a Mueller matrix without the need of a physical model.

4.1. Analytic inversion of the Mueller-Jones polarization matrices for homogeneous media

The purpose of this section is to present an analytic solution to the inversion problem of a Jones or a Mueller-Jones matrix corresponding to a homogeneous medium with combined arbitrary absorptive and refractive anisotropies. For many simple situations, e.g. for media presenting only linear birefringent anisotropy or media that exhibits only circular dichroism, the inversion problem is almost trivial [see Eq. (3.24) and Eq. (3.25)]. However, when combined amplitude and phase anisotropy are present [Eq. (3.21)] the situation is more complex because the optical effects are coupled together and, to our knowledge, prior to our publi-

cation [102], no compact equations had been given to make possible an analytic inversion in this more general case.

For convenience we will express the elements of the Jones matrix in polar form:

$$\mathbf{J} = \begin{pmatrix} j_{00} & j_{01} \\ j_{10} & j_{11} \end{pmatrix} = e^{i\theta_{00}} \begin{pmatrix} r_{00} & r_{01}e^{i(\theta_{01}-\theta_{00})} \\ r_{10}e^{i(\theta_{10}-\theta_{00})} & r_{11}e^{i(\theta_{11}-\theta_{00})} \end{pmatrix}. \tag{4.1}$$

The Jones matrix elements, as given in Eq. (4.1), corresponding to a given Mueller-Jones matrix can be calculated using the following equations [7]:

$$r_{00} = [(m_{00} + m_{01} + m_{10} + m_{11})/2]^{1/2}, \tag{4.2}$$

$$r_{01} = [(m_{00} - m_{01} + m_{10} - m_{11})/2]^{1/2}, \tag{4.3}$$

$$r_{10} = [(m_{00} + m_{01} - m_{10} - m_{11})/2]^{1/2}, \tag{4.4}$$

$$r_{11} = [(m_{00} - m_{01} - m_{10} + m_{11})/2]^{1/2}, \tag{4.5}$$

$$e^{i(\theta_{01}-\theta_{00})} = \frac{m_{02} + m_{12} - i(m_{03} + m_{13})}{[(m_{00} + m_{10})^2 - (m_{01} + m_{11})^2]^{1/2}}, \tag{4.6}$$

$$e^{i(\theta_{10}-\theta_{00})} = \frac{m_{20} + m_{21} + i(m_{30} + m_{31})}{[(m_{00} + m_{01})^2 - (m_{10} + m_{11})^2]^{1/2}}, \tag{4.7}$$

$$e^{i(\theta_{11}-\theta_{00})} = \frac{m_{22} + m_{33} + i(m_{32} - m_{23})}{[(m_{00} + m_{11})^2 - (m_{10} + m_{01})^2]^{1/2}}. \tag{4.8}$$

For any Mueller-Jones matrix the Eqs. (4.2)–(4.8) can be used to calculate r_{00}, r_{01}, r_{10}, r_{11}, $e^{i(\theta_{01}-\theta_{00})}$, $e^{i(\theta_{11}-\theta_{00})}$ and $e^{i(\theta_{11}-\theta_{00})}$. These factors can be identified with the parameterized general Jones matrix in Eq. (3.19):

$$\begin{pmatrix} \cos\frac{\mathrm{T}}{2} - \frac{i\mathrm{L}}{\mathrm{T}}\sin\frac{\mathrm{T}}{2} & \frac{(\mathrm{C}-i\mathrm{L}')}{\mathrm{T}}\sin\frac{\mathrm{T}}{2} \\ -\frac{(\mathrm{C}+i\mathrm{L}')}{\mathrm{T}}\sin\frac{\mathrm{T}}{2} & \cos\frac{\mathrm{T}}{2} + \frac{i\mathrm{L}}{\mathrm{T}}\sin\frac{\mathrm{T}}{2} \end{pmatrix} = K \begin{pmatrix} r_{00} & r_{01}e^{i(\theta_{01}-\theta_{00})} \\ r_{10}e^{i(\theta_{10}-\theta_{00})} & r_{11}e^{i(\theta_{11}-\theta_{00})} \end{pmatrix}, \tag{4.9}$$

where K is a complex constant that can be determined combining the matrix elements of Eq. (4.9) and using the identity $\cos^2\frac{\mathrm{T}}{2} + \sin^2\frac{\mathrm{T}}{2} = 1$:

$$K = \left[r_{00}r_{11}e^{i(\theta_{11}-\theta_{00})} - r_{01}r_{10}e^{i(\theta_{01}-\theta_{00})}e^{i(\theta_{10}-\theta_{00})}\right]^{-1/2}. \tag{4.10}$$

Once K is known, the determination of LB, LB′, CB, LD, LD′ and CD from Eq. (4.9) becomes straightforward [102]:

$$\mathrm{LB} = \mathrm{Re}\left[i\Omega\left(r_{00} - r_{11}e^{i(\theta_{11}-\theta_{00})}\right)\right], \tag{4.11}$$

$$\mathrm{LB}' = \mathrm{Re}\left[i\Omega\left(r_{01}e^{i(\theta_{01}-\theta_{00})} + r_{10}e^{i(\theta_{10}-\theta_{00})}\right)\right], \tag{4.12}$$

$$\mathrm{CB} = \mathrm{Re}\left[\Omega\left(r_{01}e^{i(\theta_{01}-\theta_{00})} - r_{10}e^{i(\theta_{10}-\theta_{00})}\right)\right], \tag{4.13}$$

$$\mathrm{LD} = -\,\mathrm{Im}\left[i\Omega\left(r_{00} - r_{11}e^{i(\theta_{11}-\theta_{00})}\right)\right], \tag{4.14}$$

$$\mathrm{LD}' = -\,\mathrm{Im}\left[i\Omega\left(r_{01}e^{i(\theta_{01}-\theta_{00})} + r_{10}e^{i(\theta_{10}-\theta_{00})}\right)\right], \tag{4.15}$$

$$\mathrm{CD} = -\,\mathrm{Im}\left[\Omega\left(r_{01}e^{i(\theta_{01}-\theta_{00})} - r_{10}e^{i(\theta_{10}-\theta_{00})}\right)\right], \tag{4.16}$$

where $\Omega = \mathrm{T}K/[2\sin(\mathrm{T}/2)]$, $\mathrm{T} = 2\cos^{-1}\left[K(r_{00} + r_{11}e^{i(\theta_{11}-\theta_{00})})/2\right]$ and the symbols Re and Im respectively denote the real and imaginary parts.

4.2. Inversion of a experimental Mueller matrix

A polarimetric experiment does not provide an exact Mueller-Jones matrix because of sample depolarization effects and measurement uncertainties. In order to overcome this problem and to safely apply the analytic inversion method described in Eqs. (4.11)–(4.16) we use the approach based on the sum decomposition introduced by Cloude [103] to obtain a nondepolarizing Mueller (i.e. a Mueller-Jones) matrix estimation for a depolarizing experimental matrix. This sum decomposition is based in the coherency matrix associated to a Mueller matrix. The coherency matrix is a 4×4 positive semidefinite Hermitian matrix that is used for eigen-analysis (i.e. the calculation of the corresponding eigenvalues and eigenvectors) because it yields information into the different polarimetric contributions that a depolarizing Mueller matrix can contain. The elements h_{ij} of the coherency matrix $\mathbf{H}$ can be derived from the corresponding Mueller matrix as follows [8]:

$$\begin{aligned}
h_{00} &= (m_{00}+m_{11}+m_{22}+m_{33})/4, & h_{01} &= (m_{01}+m_{10}-im_{23}+im_{32})/4,\\
h_{02} &= (m_{02}+m_{20}+im_{13}-im_{31})/4, & h_{03} &= (m_{03}-im_{12}+im_{21}+m_{30})/4,\\
h_{10} &= (m_{01}+m_{10}+im_{23}-im_{32})/4, & h_{11} &= (m_{00}+m_{11}-m_{22}-m_{33})/4,\\
h_{12} &= (im_{03}+m_{12}+m_{21}-im_{30})/4, & h_{13} &= (-im_{02}+im_{20}+m_{13}+m_{31})/4,\\
h_{20} &= (m_{02}+m_{20}-im_{13}+im_{31})/4, & h_{21} &= (-im_{03}+m_{12}+m_{21}+im_{30})/4,\\
h_{22} &= (m_{00}-m_{11}+m_{22}-m_{33})/4, & h_{23} &= (im_{01}-im_{10}+m_{23}+m_{32})/4,\\
h_{30} &= (m_{03}+im_{12}-im_{21}+m_{30})/4, & h_{31} &= (im_{02}-im_{20}+m_{13}+m_{31})/4,\\
h_{32} &= (-im_{01}+im_{10}+m_{23}+m_{32})/4, & h_{33} &= (m_{00}-m_{11}-m_{22}+m_{33})/4.
\end{aligned}$$

This matrix is positive semidefinite Hermitian and, hence, has always four real non-negative eigenvalues λ_i. Given the eigenvalues λ_i any physically realizable Mueller matrix $\mathbf{M}$ can be written as[1]:

$$\mathbf{M} = \lambda_0\mathbf{M}_J^0 + \lambda_1\mathbf{M}_J^1 + \lambda_2\mathbf{M}_J^2 + \lambda_3\mathbf{M}_J^3, \tag{4.17}$$

[1] This sum factorization is sometimes referred to as *spectral decomposition*. See Refs. [6, 103] for more details

where $\mathbf{M}_J^k$ are Mueller-Jones matrices that are derived from the following Jones matrices by using Eq. (1.29):

$$j_{00}^{(k)} = \Psi_0^{(k)} + \Psi_1^{(k)}, \qquad j_{01}^{(k)} = \Psi_2^{(k)} - i\Psi_3^{(k)} \tag{4.18}$$

$$j_{10}^{(k)} = \Psi_2^{(k)} + i\Psi_3^{(k)}, \qquad j_{11}^{(k)} = \Psi_0^{(k)} - i\Psi_2^{(k)} \tag{4.19}$$

where $\Psi^k = (\Psi_0 \quad \Psi_1 \quad \Psi_2 \quad \Psi_3)_k^T$ is the kth eigenvector of the coherency matrix $\mathbf{H}$.

If $\mathbf{M}$ is a Mueller-Jones matrix one has $\lambda_0 \neq \lambda_1 = \lambda_2 = \lambda_3 = 0$. For a experimentally determined $\mathbf{M}$, if depolarization is not very intense, usually $\lambda_0 \gg \lambda_1, \lambda_2, \lambda_3$ and then the summand $\lambda_0 \mathbf{M}_{J0}$ can be considered as the nondepolarizing estimate for the measured $\mathbf{M}$.

In this section we have shown that the polarization effects of a homogeneous medium contained in a Mueller-Jones matrix can be easily revealed by means of simple analytic equations. In contrast to the matrix product decomposition methods that we will describe in the following section, this inversion offers exact results for Mueller-Jones matrices. In the case of experimentally determined Mueller matrices the Eqs. (4.11) to (4.16) can also be used if a nondepolarizing estimate of the experimental Mueller matrix ($\lambda_0 \mathbf{M}_{J0}$) is found with anticipation. In general we can say that the reliability of the results offered by this method when applied to experimental matrices will largely depend on their degree of depolarization. For the case of homogeneous media exhibiting little depolarization this is the best option for the interpretation of Mueller matrices.

4.3. Decomposition of Mueller matrices

In this section we switch to a different philosophy: in the absence of a physical model describing and explaining the interaction of an electromagnetic wave with a sample, it may be still possible to phenomenologically interpret an experimental Mueller matrix by decomposing it into simple components having a simpler physical interpretation. In this section we review various decompositions of nondepolarizing and depolarizing Mueller matrices.

The algorithms of all the product decompositions described in this chapter have been incorporated in a computer program that acts as a complement to the software developed for the instrument described in the following part of the work. This program takes series of experimental Mueller matrices (either from spectroscopic measurements or space resolved measurement) to calculate the type of decomposition selected by the user. Usually these decompositions are useful to obtain a first (and sometimes definitive) interpretation of experimental measurements.

4.3.1. Polar and Lu-Chipman decompositions

One approach to model homogeneous anisotropic media is based on the polar decomposition theorem, which states that any complex matrix $\mathbf{A}$ can be represented by a product

$$\mathbf{A} = \mathbf{UP} \quad \text{or} \quad \mathbf{A} = \mathbf{P'U}, \tag{4.20}$$

where $\mathbf{P}$ and $\mathbf{P'}$ are Hermitian matrices and $\mathbf{U}$ is a unitary matrix. Polar decomposition has been applied in the polarization theory to represent arbitrary optical systems either in Jones [104, 105] or Mueller space [84, 106]. The Hermitian matrix appearing in the polar decomposition is associated to the amplitude anisotropy while the unitary matrix is associated to the phase anisotropy. The polar decomposition applied to a nondepolarizing Mueller matrix is:

$$\mathbf{M} = \mathbf{M}_{D1}\mathbf{M}_R = \mathbf{M}_R\mathbf{M}_{D2}. \tag{4.21}$$

where $\mathbf{M}_{Di}$ and $\mathbf{M}_R$ are respectively the matrices shown in Eq. (3.25) and (3.24). Because of the noncommutativity of the matrix product the two diattenuators $\mathbf{M}_{D1}$ and $\mathbf{M}_{D2}$ are not identical and are related through

$$\mathbf{M}_{D2} = \mathbf{M}_R^T\mathbf{M}_{D1}\mathbf{M}_R \quad \text{and} \quad \mathbf{M}_{D1} = \mathbf{M}_R\mathbf{M}_{D2}\mathbf{M}_R^T. \tag{4.22}$$

The algorithm to calculate the polar decomposition is presented in the following section in the more general depolarizing case.

Depolarizing case, Lu-Chipman decomposition

The *Lu-Chipman* decomposition [84] is a natural generalization of the polar decomposition to the case of depolarizing Mueller matrices. In this case an arbitrary depolarizing Mueller matrix $\mathbf{M}$ is decomposed into the product of a diattenuator, a retarder and a depolarizer:

$$\mathbf{M} = \mathbf{M}_\Delta\mathbf{M}_R\mathbf{M}_D \tag{4.23}$$

$\mathbf{M}_\Delta$ is the Mueller matrix of a depolarizer with polarizance[2], which can be expressed as:

$$\mathbf{M}_\Delta = \begin{bmatrix} 1 & \vec{0}^T \\ \vec{P}_\Delta & \mathbf{m_\Delta} \end{bmatrix}, \tag{4.24}$$

in which $\mathbf{m_\Delta}$ is a 3×3 symmetric matrix, $\vec{0}$ denotes the three-element zero vector, and $\vec{P}_\Delta$ is the so-called polarizance vector of the depolarizer which is formed by Mueller matrix elements m_{10}, m_{20} and m_{30} of the depolarizer.

[2]Frequently depolarizers are described with diagonal Mueller matrices. However note that Lu-Chipman decomposition uses a depolarizer with depolarizance, which, in general, has a non-diagonal Mueller matrix.

Here we describe briefly the algorithm to perform the polar decomposition on a experimental Mueller matrix. To be consistent with the published algorithms on this decomposition and because it permits a more compact development we will use here the same notation used by Lu and Chipman (that otherwise is common in polarization optics) which is based in the diattenuating, $\vec{D} = (D_H, D_{45}, D_c)$, and retardance, $\vec{R} = (R_H, R_{45}, R_c)$ vectors. There is a simple equivalence between our usual notation and that of Lu and Chipman and it is given in table 4.1.

Table 4.1.: Relation to the notation of Lu-Chipman

Retardances	Absorbances
$\mathrm{LB} = -R_H$	$\mathrm{LD} = -(\mathrm{T}_D/D)D_H$
$\mathrm{LB}' = -R_{45}$	$\mathrm{LD}' = -(\mathrm{T}_D/D)D_{45}$
$\mathrm{CB} = R_c$	$\mathrm{CD} = (\mathrm{T}_D/D)D_c$
$\vec{\mathrm{T}}_R = (\mathrm{LB}, \mathrm{LB}', -\mathrm{CB}) = -\vec{R}$	$\vec{\mathrm{T}}_D = (\mathrm{LD}, \mathrm{LD}', -\mathrm{CD}) = -(\mathrm{T}_D/D)\vec{D}$
$\mathrm{T}_R = R$	$\mathrm{T}_D = \mathrm{arctanh} D$

The first step of the algorithm consist on identifying the experimental normalized Mueller matrix with the following matrix:

$$\mathbf{M} = \begin{bmatrix} 1 & \vec{D}^T \\ \vec{P} & \mathbf{m} \end{bmatrix}. \tag{4.25}$$

where the m_{01}, m_{02} and m_{03} form the diattenuation vector, $\vec{D}$, $\vec{P}$ is the so-called polarizance vector which is formed by m_{10}, m_{20} and m_{30} and $\mathbf{m}$ is 3×3 matrix obtained by striking out the first row and the first column of $\mathbf{M}$. Using the relations given in table 4.1 we use the diattenuation vector to find the values of LD, LD$'$ and CD and then to construct $\mathbf{M}_D$ according to Eq. (3.25). If the matrix $\mathbf{M}_D$ is not singular (i.e. it is invertible) we can define a new matrix $\mathbf{M}'$:

$$\mathbf{M}' \equiv \mathbf{M}\mathbf{M}_D^{-1} = \mathbf{M}_\Delta \mathbf{M}_R. \tag{4.26}$$

$\mathbf{M}'$ has no diattenuation and contains both retardance and depolarization. $\mathbf{M}'$ is of the form:

$$\mathbf{M}' = \begin{bmatrix} 1 & \vec{0}^T \\ \vec{P}_\Delta & \mathbf{m}' \end{bmatrix}, \tag{4.27}$$

in which $\vec{P}_\Delta$ is the polarizance vector of the depolarizer and $\mathbf{m}'$ is a 3×3 submatrix

of $\mathbf{M}'$. $\vec{P}_\Delta$ is:

$$\vec{P}_\Delta = \frac{\vec{P} - \mathbf{m}\vec{D}}{1 - D^2}. \tag{4.28}$$

The submatrix $\mathbf{m}_\Delta$ appearing in Eq. (4.24) can be now obtained by

$$\begin{aligned}\mathbf{m}_\Delta = &\pm [\mathbf{m}'(\mathbf{m}')^T + (\sqrt{\lambda_0\lambda_1} + \sqrt{\lambda_1\lambda_2} + \sqrt{\lambda_2\lambda_0})\mathbf{I}]^{-1} \\ &\times [(\sqrt{\lambda_0} + \sqrt{\lambda_1} + \sqrt{\lambda_2})\mathbf{m}'(\mathbf{m}')^T + \sqrt{\lambda_0\lambda_1\lambda_2}\mathbf{I}].\end{aligned} \tag{4.29}$$

where λ_0, λ_1, λ_2 are the eigenvalues of $\mathbf{m}'(\mathbf{m}')^T$. The minus sign is applied if the determinant of $\mathbf{m}'$ is negative, otherwise, the plus sign is applied. Thus, $\mathbf{M}_\Delta$ can be determined through Eqs. (4.28) and (4.29). Then $\mathbf{M}_R$ is obtained by

$$\mathbf{M}_R = \mathbf{M}_\Delta^{-1}\mathbf{M}'. \tag{4.30}$$

The Lu-Chipman estimation for LB, LD, LB′, LD′, CD and CB can be obtained using the following relations:

$$\mathrm{LD} = -\mathrm{m}_{D_{01}}\mathrm{arctanh(D)/D}, \tag{4.31a}$$
$$\mathrm{LD}' = -\mathrm{m}_{D_{02}}\mathrm{arctanh}(D)/D, \tag{4.31b}$$
$$\mathrm{CD} = \mathrm{m}_{D_{03}}\mathrm{arctanh}(D)/D, \tag{4.31c}$$
$$\mathrm{LB} = (\mathrm{m}_{R_{32}} - \mathrm{m}_{R_{23}})R/2\sin R, \tag{4.31d}$$
$$\mathrm{LB}' = (\mathrm{m}_{R_{13}} - \mathrm{m}_{R_{31}})R/2\sin R, \tag{4.31e}$$
$$\mathrm{CB} = (\mathrm{m}_{R_{12}} - \mathrm{m}_{R_{21}})R/2\sin R, \tag{4.31f}$$

where

$$R = \arccos(\mathrm{tr}(\mathbf{M}_R)/2 - 1), \tag{4.32}$$

$$D = (\mathrm{m}_{D_{01}}^2 + \mathrm{m}_{D_{02}}^2 + \mathrm{m}_{D_{03}}^2)^{1/2}, \tag{4.33}$$

and the terms $\mathrm{m}_{R_{ij}}$ and $\mathrm{m}_{D_{ij}}$ $(i, j = 0, .., 3)$ respectively indicate matrix elements of i^{th} row and j^{th} column of $\mathbf{M}_R$ and $\mathbf{M}_D$.

Noncommutativity

The polar decompositions is affected by the noncommutativity of the matrix product as shown in Eqs. (4.21) and (4.22). In the case of the Lu-Chipman decomposition something similar happens: the three factors give six possible variations of the decomposition that depend on the order in which the factors

are multiplied [107]:

$$\mathbf{M} = \mathbf{M}_{\Delta}\mathbf{M}_{R}\mathbf{M}_{D}, \tag{4.34a}$$
$$\mathbf{M} = \mathbf{M}_{\Delta 1}\mathbf{M}_{D1}\mathbf{M}_{R1}, \tag{4.34b}$$
$$\mathbf{M} = \mathbf{M}_{R2}\mathbf{M}_{\Delta 2}\mathbf{M}_{D2}, \tag{4.34c}$$
$$\mathbf{M} = \mathbf{M}_{R3}\mathbf{M}_{R3}\mathbf{M}_{\Delta 3}, \tag{4.34d}$$
$$\mathbf{M} = \mathbf{M}_{D4}\mathbf{M}_{R4}\mathbf{M}_{\Delta 4}, \tag{4.34e}$$
$$\mathbf{M} = \mathbf{M}_{D5}\mathbf{M}_{\Delta 5}\mathbf{M}_{R5}. \tag{4.34f}$$

These six equations can be separated in two families, depending on whether the depolarizer factor is behind the diattenuating factor [Eqs. (4.34a), (4.34b) and (4.34c)] –sometimes referred as "forward" family– or in front of the diattenuating factor [Eqs. (4.34d) (4.34e) and (4.34f)] of the diattenuating factor –"reverse" family–. A detailed discussion on the decomposition families and how to obtain them is available in [107]. It is important to stress that although there are some particular coincidences (for example $\mathbf{M}_R = \mathbf{M}_{R1}$, see [107] for more examples) the factors $\mathbf{M}_{Ri}$, $\mathbf{M}_{Di}$ and $\mathbf{M}_{\Delta i}$ are different depending on the order in which they are multiplied. Also the depolarizer factor on the reverse family is that of a depolarizer with diattenuation, while in the forward family is a depolarizer with polarizance [Eq. (4.24)].

Due to the noncommutativity of the polar and the Lu-Chipman decompositions, in the most general case, the matrices resulting from these decompositions have lost their physical interpretability, in the sense that the diattenuation properties of the Hermitian matrix and the retardation characteristics of the unitary matrix do not correspond to the diattenuation and retardation of the original Jones or Mueller matrix. This has been already demonstrated by Savenkov in Ref. [108].

4.3.2. Pseudopolar decomposition

The genesis of this decomposition started when we noted that the optical effects (CD, CB, LD, etc) obtained from the factors of polar decomposition of a Mueller-Jones matrix were not equivalent to those obtained from the analytic inversion introduced in this chapter. This is an obvious fact if one attends to the noncommutativity of the matrix factors involved in polar or in the Lu-Chipman decomposition. However we found that this question was forgotten or not sufficiently stressed in some experimental investigations [109–113] and the Lu-Chipman is erroneously taken as a "universal" method to obtain the optical effects of any optical system.

The pseudopolar decomposition remains in close relationship with the polar or the Lu-Chipman decompositions, however, this product decomposition is intended to maintain the physical interpretability of its factors by offering a treatment for the noncommutativity of retarder and diattenuating factors. The noncommutative characteristics of the matrices that describe the optical polarization properties of a system were already noted by Jones [78]. He wrote: "as first attempt, one might try to find a simple way of factoring the matrix M of the crystal into the product of a finite number of simple M-matrices, each of which would represent a simple crystal property, such as circular dichroism, linear birefringence, or isotropic absorption. This effort fails, because the constants which specify the component matrices depend on the order in which the matrices are multiplied".

The theoretical development of the pseudopolar decomposition is partly based on the decomposition of an optical element into infinitesimal sublayers that we already introduced in the previous chapter. At this point we can recuperate Eq. (3.17), that gives the exponential version of Jones matrix of homogeneous optical element having both diattenuating and retarding properties:

$$\mathbf{J} = \exp[-i\mathbf{R}] = e^{-i\chi/2} e^{-i[\vec{\sigma}\cdot\vec{\mathrm{T}}_R + \vec{\sigma}\cdot(-i\vec{\mathrm{T}}_D)]/2} \tag{4.35}$$

Note that $\vec{\sigma}\cdot\vec{\mathrm{T}}_R$ and $\vec{\sigma}\cdot\vec{\mathrm{T}}_D$ define two non-commutative matrices ($[\vec{\sigma}\cdot\vec{\mathrm{T}}_R, \vec{\sigma}\cdot\vec{\mathrm{T}}_D] \neq 0$) and that the exponential of their sum cannot be found from the product of their individual exponentials. At this point it is interesting to introduce the so called Zassenhaus formula, which states that the exponential of the sum of two non-commutative operators X and Y can be obtained as an infinite product of exponentials of the operators and their commutators:

$$e^{t(X+Y)} = e^{tX}\ e^{tY}\ e^{-\frac{t^2}{2}[X,Y]}\ e^{\frac{t^3}{6}(2[Y,[X,Y]]+[X,[X,Y]])}\ e^{t^4\cdots}\cdots \tag{4.36}$$

and further terms are given by a recursion relation [114, 115]. This is an infinite and convergent series [116] and the Zassenhaus exponents can be obtained in terms of nested commutators with growing complexity. Here we will consider only the first and second Zassenhaus exponents because, although more correction terms could be considered, they are enough for most of the applications in polarimetry.

Comparing equation (4.36) with (3.17) we can use the Zassenhaus formula making the identifications $X = \vec{\sigma}\cdot\vec{\mathrm{T}}_R$, $Y = -i\vec{\sigma}\cdot\vec{\mathrm{T}}_D$ and $t = -i/2$. We can write $\mathbf{J}$ as follows:

$$\mathbf{J} \cong \mathbf{J}_R\mathbf{J}_D\mathbf{J}_{1C}\mathbf{J}_{2C}, \tag{4.37}$$

where

$$\mathbf{J}_R = e^{-i\eta}\exp(-i\frac{\mathrm{T}_R}{2}\frac{\vec{\mathrm{T}}_R}{\mathrm{T}_R}\cdot\vec{\sigma}) = e^{-i\eta}[\sigma_0\cos\frac{\mathrm{T}_R}{2} - \frac{i}{\mathrm{T}_R}\vec{\mathrm{T}}_R\cdot\vec{\sigma}\sin\frac{\mathrm{T}_R}{2}], \tag{4.38a}$$

$$\mathbf{J}_D = e^{-k}\exp(-\frac{\mathrm{T}_D}{2}\frac{\vec{\mathrm{T}}_D}{\mathrm{T}_D}\cdot\vec{\sigma}) = e^{-k}[\sigma_0\cosh\frac{\mathrm{T}_D}{2} - \frac{1}{\mathrm{T}_D}\vec{\mathrm{T}}_D\cdot\vec{\sigma}\sinh\frac{\mathrm{T}_D}{2}], \quad (4.38b)$$

$$\mathbf{J}_{1C} = \exp(\frac{\mathrm{A}}{8}\left[\frac{\vec{\mathrm{A}}}{\mathrm{A}}\cdot\vec{\sigma}\right]) = \sigma_0\cosh\frac{\mathrm{A}}{8} + \frac{1}{\mathrm{A}}\vec{\mathrm{A}}\cdot\vec{\sigma}\sinh\frac{\mathrm{A}}{8}, \quad (4.38c)$$

$$\mathbf{J}_{2C} = \exp(i\frac{\mathrm{B}}{48}\left[\frac{\vec{\mathrm{B}}}{\mathrm{B}}\cdot\vec{\sigma}\right]) = \sigma_0\cos\frac{\mathrm{B}}{48} + \frac{i}{\mathrm{B}}\vec{\mathrm{B}}\cdot\vec{\sigma}\sin\frac{\mathrm{B}}{48}, \quad (4.38d)$$

and $\vec{\mathrm{A}} = (\mathrm{A}_1, \mathrm{A}_2, \mathrm{A}_3)$ and $\vec{\mathrm{B}} = (\mathrm{B}_1, \mathrm{B}_2, \mathrm{B}_3)$. The expressions for A_i, B_i, A, B, T_R and T_D are given in table 4.2. In Eqs. (4.38) we have used common algebra properties related to Pauli matrices to write the exponential in terms of trigonometric and hyperbolic functions. In table 4.2 the matrices $\mathbf{J}_R$, $\mathbf{J}_D$, $\mathbf{J}_{1C}$, $\mathbf{J}_{2C}$ are written explicitly without making use of the Pauli notation.

Table 4.2.: Factorized Jones Matrix, $\mathbf{J} \cong \mathbf{J}_R\mathbf{J}_D\mathbf{J}_{1C}\mathbf{J}_{2C}$

matrices	definitions
$\mathbf{J} = e^{-i\chi/2}\begin{bmatrix} \cos\frac{\mathrm{T}}{2} - \frac{i\mathrm{L}}{\mathrm{T}}\sin\frac{\mathrm{T}}{2} & \frac{[\mathrm{C}-i\mathrm{L}']}{\mathrm{T}}\sin\frac{\mathrm{T}}{2} \\ -\frac{[\mathrm{C}+i\mathrm{L}']}{\mathrm{T}}\sin\frac{\mathrm{T}}{2} & \cos\frac{\mathrm{T}}{2} + \frac{i\mathrm{L}}{\mathrm{T}}\sin\frac{\mathrm{T}}{2} \end{bmatrix}$	$\mathrm{L}' = \mathrm{LB}' - i\mathrm{LD}'$ $\mathrm{C} = \mathrm{CB} - i\mathrm{CD}$ $\mathrm{L} = \mathrm{LB} - i\mathrm{LD}$ $\mathrm{T} = \sqrt{\mathrm{L}'^2 + \mathrm{C}^2 + \mathrm{L}^2}$
$\mathbf{J}_R = e^{-i\eta}\begin{bmatrix} \cos\frac{\mathrm{T}_R}{2} - \frac{i\mathrm{LB}}{\mathrm{T}_R}\sin\frac{\mathrm{T}_R}{2} & \frac{[\mathrm{CB}-i\mathrm{LB}']}{\mathrm{T}_R}\sin\frac{\mathrm{T}_R}{2} \\ -\frac{[\mathrm{CB}+i\mathrm{LB}']}{\mathrm{T}_R}\sin\frac{\mathrm{T}_R}{2} & \cos\frac{\mathrm{T}_R}{2} + \frac{i\mathrm{LB}}{\mathrm{T}_R}\sin\frac{\mathrm{T}_R}{2} \end{bmatrix}$	$\mathrm{T}_R = \sqrt{\mathrm{LB}^2 + \mathrm{LB}'^2 + \mathrm{CB}^2}$
$\mathbf{J}_D = e^{-k}\begin{bmatrix} \cosh\frac{\mathrm{T}_D}{2} - \frac{\mathrm{LD}}{\mathrm{T}_D}\sinh\frac{\mathrm{T}_D}{2} & -\frac{[\mathrm{LD}'+i\mathrm{CD}]}{\mathrm{T}_D}\sinh\frac{\mathrm{T}_D}{2} \\ \frac{[i\mathrm{CD}-\mathrm{LD}']}{\mathrm{T}_D}\sinh\frac{\mathrm{T}_D}{2} & \cosh\frac{\mathrm{T}_D}{2} + \frac{\mathrm{LD}}{\mathrm{T}_D}\sinh\frac{\mathrm{T}_D}{2} \end{bmatrix}$	$\mathrm{T}_D = \sqrt{\mathrm{LD}^2 + \mathrm{LD}'^2 + \mathrm{CD}^2}$
$\mathbf{J}_{1C} = \begin{bmatrix} \cosh\frac{\mathrm{A}}{8} + \frac{\mathrm{A}_1}{\mathrm{A}}\sinh\frac{\mathrm{A}}{8} & \frac{[\mathrm{A}_2-i\mathrm{A}_3]}{\mathrm{A}}\sinh\frac{\mathrm{A}}{8} \\ \frac{[\mathrm{A}_2+i\mathrm{A}_3]}{\mathrm{A}}\sinh\frac{\mathrm{A}}{8} & \cosh\frac{\mathrm{A}}{8} - \frac{\mathrm{A}_1}{\mathrm{A}}\sinh\frac{\mathrm{A}}{8} \end{bmatrix}$	$\mathrm{A}_1 = 2(\mathrm{LD}'\mathrm{CB} - \mathrm{LB}'\mathrm{CD})$ $\mathrm{A}_2 = 2(\mathrm{LBCD} - \mathrm{LDCB})$ $\mathrm{A}_3 = 2(\mathrm{LBLD}' - \mathrm{LDLB}')$ $\mathrm{A} = \sqrt{\mathrm{A}_1^2 + \mathrm{A}_2^2 + \mathrm{A}_3^2}$
$\mathbf{J}_{2C} = \begin{bmatrix} \cos\frac{\mathrm{B}}{48} + \frac{i\mathrm{B}_1}{\mathrm{B}}\sin\frac{\mathrm{B}}{48} & \frac{[\mathrm{B}_3+i\mathrm{B}_2]}{\mathrm{B}}\sin\frac{\mathrm{B}}{48} \\ -\frac{[\mathrm{B}_3-i\mathrm{B}_2]}{\mathrm{B}}\sin\frac{\mathrm{B}}{48} & \cos\frac{\mathrm{B}}{48} - \frac{i\mathrm{B}_1}{\mathrm{B}}\sin\frac{\mathrm{B}}{48} \end{bmatrix}$	$\mathrm{B}_1 = 4(\mathrm{A}_3\mathrm{LD}' + \mathrm{A}_2\mathrm{CD})$ $+2i(\mathrm{A}_2\mathrm{CB} + \mathrm{A}_3\mathrm{LB}')$ $\mathrm{B}_2 = -4(\mathrm{A}_3\mathrm{LD} + \mathrm{A}_1\mathrm{CD})$ $-2i(\mathrm{A}_1\mathrm{CB} + \mathrm{A}_3\mathrm{LB})$ $\mathrm{B}_3 = 4(\mathrm{A}_2\mathrm{LD} - \mathrm{A}_1\mathrm{LD}')$ $+2i(\mathrm{A}_2\mathrm{LB} - \mathrm{A}_1\mathrm{LB}')$ $\mathrm{B} = \sqrt{\mathrm{B}_1^2 + \mathrm{B}_2^2 + \mathrm{B}_3^2}$

We have christened the decomposition of Eq. (4.37) as the *pseudopolar decomposition*. Like in the polar-decomposition, $\mathbf{J}_R$ is an unitary matrix that changes only the phases of the components of the electric field and $\mathbf{J}_D$ is a Hermitian matrix that changes only the amplitudes of the components of the electric field vector. $\mathbf{J}_{1C}$, which is also Hermitian, and $\mathbf{J}_{2C}$ are respectively the first and second correction matrices.

More terms of the expansion series of Eq. (4.36) could be considered, and this would give us more correction matrices (we could name them $\mathbf{J}_{3C}$, $\mathbf{J}_{4C}$, etc). However, note that the elements of the first correction matrix are quadratic with the anisotropies, while the elements of the second correction matrix are cubic. Third and higher order correction matrix would respectively have elements with fourth and higher order dependence in anisotropies. Provided that for most of the experimentally-described systems the basic building blocks for the correction terms (the elements A_1, A_2 and A_3 defined in table 4.2) are much smaller than one, the correction matrices rapidly approach to the identity matrix.

It is important to stress again that all the linear and circular anisotropies involved in this factorization are the real anisotropies of the system. Conversely, the linear and circular birefringence and dichroism involved in the polar decomposition are mathematical entities that, in general, do not correspond with the anisotropies of the sample. Moreover, the pseudopolar decomposition verifies:

$$\mathbf{J} \cong \mathbf{J}_R\mathbf{J}_D\mathbf{J}_{1C}\mathbf{J}_{2C} \cong \mathbf{J}_D\mathbf{J}_R\mathbf{J}_{1C}^{-1}\mathbf{J}_{2C}^{-1}. \tag{4.39}$$

This property can be verified from Eq. (4.36): permuting X with Y does not alter the first two terms of the Zassenhaus formula, but the fact that $[X,Y] = -[Y,X]$ modifies the exponent sign of all the following factors.

In the way the matrices $\mathbf{J}_R$ and $\mathbf{J}_D$ are built [see Eqs. (4.38)], it can be clearly seen that the pseudopolar decomposition also satisfies the following property:

$$\vec{\mathrm{T}}_D(\mathbf{J}) = \vec{\mathrm{T}}_D(\mathbf{J}_D) \quad \text{and} \quad \vec{\mathrm{T}}_R(\mathbf{J}) = \vec{\mathrm{T}}_R(\mathbf{J}_R), \tag{4.40}$$

which means that the diattenuation vectors of $\mathbf{J}_D$ and the retardation vector of $\mathbf{J}_R$ correspond with those of $\mathbf{J}$. This indicates that the dichroic and birefringent physical parameters of original matrix $\mathbf{J}$ (Eq. (3.18)) are respectively preserved and separated in factors $\mathbf{J}_D$ and $\mathbf{J}_R$ [Eqs. (4.38)].

There are some cases in which both first and second corrections do not have any contribution, which means that $\mathbf{J}_{1C} = \mathbf{J}_{2C} = \sigma_0$. From the matrices and the definitions given in table 4.2, we find that the conditions for this to happen are:

$$\begin{aligned} &\mathrm{LD'CB} - \mathrm{LB'CD} = 0, \\ &\mathrm{LBCD} - \mathrm{LDCB} = 0, \\ &\mathrm{LBLD'} - \mathrm{LB'LD} = 0. \end{aligned} \tag{4.41}$$

Leaving aside the mathematical restrictions we can derive from this set of equations and recalling the physical meaning of the parameters involved in these equations, we can easily realize that there are two common types of anisotropic optical media that satisfy the three conditions of Eqs. (4.41). The first one corresponds to a circular birefringent and dichroic media $\mathrm{CD}, \mathrm{CB} \neq 0$ without linear anisotropies $\mathrm{LB} = \mathrm{LD} = \mathrm{LD}' = \mathrm{LB}' = 0$. Typically, solutions of chiral molecules constitute a good example for this kind of media although, in some cases, they have associated linear anisotropies too. The second one corresponds to a non-chiral high symmetry sample in which the principal axes for linear retardation and for linear dichroism coincide $\mathrm{LD}/\mathrm{LB} = \mathrm{LD}'/\mathrm{LB}'$. Uniaxial crystals and flow- or field-oriented molecules are common optical media in which these conditions might be found. For these two media we can certainly write $\mathbf{J} = \mathbf{J}_R\mathbf{J}_D = \mathbf{J}_D\mathbf{J}_R$ and, therefore, the pseudopolar decompositions transforms into the polar decomposition. This demonstrates that, in these media, the polar decomposition can be applied without losing the physical significance of the involved anisotropies. The media in which Eqs. (4.41) hold are media without non-commuting optical properties and, in those kind of media, polar decomposition can be safely applied.

We can derive the Mueller-Jones matrices corresponding to the Jones matrices given in table 4.2 by using Eq. (1.29) or Eq. (3.20). The Mueller-Jones matrices $\mathbf{M}_R$ and $\mathbf{M}_D$ associated to $\mathbf{J}_R$ and $\mathbf{J}_M$ have been already given in Eq. (3.24) and Eq. (3.25) respectively. The Mueller-Jones matrix, $\mathbf{M}_{1C}$, corresponding to the correction term result into a symmetric matrix:

$$\mathbf{M}_{1C} = \begin{bmatrix} \cosh^2\frac{\mathrm{A}}{8} + \sinh^2\frac{\mathrm{A}}{8} & \mathrm{A}_1\gamma & \mathrm{A}_2\gamma & \mathrm{A}_3\gamma \\ \mathrm{A}_1\gamma & 1 + 2\mathrm{A}_1^2\delta & 2\mathrm{A}_1\mathrm{A}_2\delta & 2\mathrm{A}_1\mathrm{A}_3\delta \\ \mathrm{A}_2\gamma & 2\mathrm{A}_1\mathrm{A}_2\delta & 1 + 2\mathrm{A}_2^2\delta & 2\mathrm{A}_2\mathrm{A}_3\delta \\ \mathrm{A}_3\gamma & 2\mathrm{A}_1\mathrm{A}_3\delta & 2\mathrm{A}_2\mathrm{A}_3\delta & 1 + 2\mathrm{A}_3^2\delta \end{bmatrix}, \tag{4.42}$$

with $\gamma = \frac{1}{A}\sinh\frac{\mathrm{A}}{4}$ and $\delta = \frac{1}{\mathrm{A}^2}\sinh^2\frac{A}{8}$. The calculation of the Mueller matrix associated to the second correction term, $\mathbf{M}_{2C}$, requires some more algebra than the matrices above, since $\vec{\mathrm{B}}$ is a complex vector. After some algebra we find

$$\mathbf{M}_{2C} = \begin{bmatrix} \rho \\ +(\xi/2)(\vec{\mathrm{B}}^* \cdot \vec{\mathrm{B}}) & -\varepsilon \mathrm{B}_1^i + \zeta \mathrm{B}_1^r \\ & +\xi(\mathrm{B}_3^r \mathrm{B}_2^i - \mathrm{B}_2^r \mathrm{B}_3^i) \\ -\varepsilon \mathrm{B}_1^i + \zeta \mathrm{B}_1^r & \rho + \xi((-\mathrm{B}_1^i)^2 + (\mathrm{B}_1^r)^2) \\ -\xi(\mathrm{B}_3^r \mathrm{B}_2^i - \mathrm{B}_2^r \mathrm{B}_3^i) & -(\xi/2)(\vec{\mathrm{B}}^* \cdot \vec{\mathrm{B}}) \\ -\varepsilon \mathrm{B}_2^i + \zeta \mathrm{B}_2^r & -\varepsilon \mathrm{B}_3^r - \zeta \mathrm{B}_3^i \\ -\xi(\mathrm{B}_1^r \mathrm{B}_3^i - \mathrm{B}_3^r \mathrm{B}_1^i) & +\xi(\mathrm{B}_1^r \mathrm{B}_2^r + \mathrm{B}_1^i \mathrm{B}_2^i) \\ -\varepsilon \mathrm{B}_3^i + \zeta \mathrm{B}_3^r & \varepsilon \mathrm{B}_2^r + \zeta \mathrm{B}_2^i \\ -\xi(-\mathrm{B}_1^r \mathrm{B}_2^i + \mathrm{B}_2^r \mathrm{B}_1^i) & -\xi(-\mathrm{B}_3^r \mathrm{B}_1^r - \mathrm{B}_3^i \mathrm{B}_1^i) \end{bmatrix}$$

$$\begin{bmatrix} -\varepsilon \mathrm{B}_2^i + \zeta \mathrm{B}_2^r & -\varepsilon \mathrm{B}_3^i + \zeta \mathrm{B}_3^r \\ +\xi(\mathrm{B}_1^r \mathrm{B}_3^i - \mathrm{B}_3^r \mathrm{B}_1^i) & +\xi(-\mathrm{B}_1^r \mathrm{B}_2^i + \mathrm{B}_2^r \mathrm{B}_1^i) \\ \varepsilon \mathrm{B}_3^r + \zeta \mathrm{B}_3^i & -\varepsilon \mathrm{B}_2^r - \zeta \mathrm{B}_2^i \\ +\xi(\mathrm{B}_1^r \mathrm{B}_2^r + \mathrm{B}_1^i \mathrm{B}_2^i) & -\xi(-\mathrm{B}_3^r \mathrm{B}_1^r - \mathrm{B}_3^i \mathrm{B}_1^i) \\ \rho + \xi((\mathrm{B}_2^r)^2 + (-\mathrm{B}_2^i)^2) & \varepsilon \mathrm{B}_1^r + \zeta \mathrm{B}_1^i \\ -(\xi/2)(\vec{\mathrm{B}}^* \cdot \vec{\mathrm{B}}) & -\xi(-\mathrm{B}_3^r \mathrm{B}_2^r - \mathrm{B}_3^i \mathrm{B}_2^i) \\ -\varepsilon \mathrm{B}_1^r - \zeta \mathrm{B}_1^i & \rho + \xi((\mathrm{B}_3^i)^2 + (-\mathrm{B}_3^r)^2) \\ -\xi(-\mathrm{B}_3^r \mathrm{B}_2^r - \mathrm{B}_3^i \mathrm{B}_2^i) & -(\xi/2)(\vec{\mathrm{B}}^* \cdot \vec{\mathrm{B}}) \end{bmatrix}, \quad (4.43)$$

where

$$\begin{aligned} \varepsilon &= (\mathrm{B}^i \sinh \tfrac{\mathrm{B}^i}{24} + \mathrm{B}^r \sin \tfrac{\mathrm{B}^r}{24})/\mathrm{B}\mathrm{B}^*, \\ \zeta &= (\mathrm{B}^i \sin \tfrac{\mathrm{B}^r}{24} - \mathrm{B}^r \sinh \tfrac{\mathrm{B}^i}{24})/\mathrm{B}\mathrm{B}^*, \\ \xi &= (\cosh \tfrac{\mathrm{B}^i}{24} - \cos \tfrac{\mathrm{B}^r}{24})/\mathrm{B}\mathrm{B}^*, \\ \rho &= (\cosh \tfrac{\mathrm{B}^i}{24} + \cos \tfrac{\mathrm{B}^r}{24})/2 \end{aligned} \quad (4.44)$$

and the superscript r refers to the real part and the superscript i refers to the imaginary part.

The pseudopolar decomposition for a nondepolarizing Mueller can then be written as follows:

$$\mathbf{M} \cong \mathbf{M}_R \mathbf{M}_D \mathbf{M}_{1C} \mathbf{M}_{2C}, \quad (4.45)$$

where $\mathbf{M}$ is the general Mueller matrix given in Eq. (3.21).

Application to experimental matrices

Until now we have introduced the pseudopolar decomposition and we have shown how to build up the factors from the physical effects defined in table 1.1. The purpose of this section is to briefly examine how to find the factors of the decomposition (this is $\mathbf{J}_R$, $\mathbf{J}_D$, $\mathbf{J}_{1C}$ or $\mathbf{J}_{2C}$ or $\mathbf{M}_R$, $\mathbf{M}_D$, $\mathbf{M}_{1C}$ and $\mathbf{M}_{2C}$) from one

input matrix **J** or **M**. In this case we will focus our attention only in the Mueller matrices, which are the ones that normally are determined experimentally.

The procedure to obtain the pseudopolar decomposition of a given experimental Mueller matrix is based on a process of filtering of the experimental Mueller matrix and on a recursive application of the algorithm corresponding to the Lu-Chipman decomposition that we have presented in section 4.3.1. In most cases the polar decomposition will offer a reasonable estimation of the physical parameters involved in the decomposition although, as discussed before, it may be not accurate if there are noncommuting optical properties. Therefore we can use the Lu-Chipman decomposition to find a first estimate of LB, LD, LB′, LD′, CD and CB.

Eqs. (4.42) and (4.43) describe the way to calculate $\mathbf{M}_{1C}$ and to $\mathbf{M}_{2C}$ from the calculated optical properties, so that an estimation of these two correction matrices can be found. We will denote this first approximation as $\mathbf{M}_{1C}^{(0)}$ $\mathbf{M}_{2C}^{(0)}$. We recall that these two matrices account for the noncommutative optical properties of the medium and, as shown in section 2, in the cases where the non-commutative optical properties vanish [Eqs. (4.41)] the polar and pseudopolar decompositions coincide. As long as we are able to find these two correction matrices, we will use them to filter the experimental Mueller matrix in a way that the polar decomposition of the filtered matrix matches the pseudopolar decomposition of the experimental matrix.

Once $\mathbf{M}_{1C}^{(0)}$ and $\mathbf{M}_{2C}^{(0)}$ are calculated we can define a new matrix, $\mathbf{M}_{e}^{\prime(1)}$, that, in some sense, will be the experimental matrix but corrected, for the non-commutative optical properties:

$$\mathbf{M}_{e}^{\prime(1)} = \mathbf{M}_{e}(\mathbf{M}_{2C}^{(0)})^{-1}(\mathbf{M}_{1C}^{(0)})^{-1}. \tag{4.46}$$

Note that the idea to make this definition comes from the pseudopolar decomposition as it is given in Eq. (4.45), where the $\mathbf{M}_{1C}^{(0)}$ and $\mathbf{M}_{2C}^{(0)}$ factors have been moved to the left part of the equation. Certainly, we can apply again the Lu-Chipman decomposition to $\mathbf{M}_{e}^{\prime(1)}$ and we will be able to calculate some new values for the physical effects. Now these values will be somehow more accurate than in the previous step since our corrected experimental Mueller matrix, $\mathbf{M}_{e}^{\prime(1)}$, would already have less non-commutative optical properties than the original. Again, after finding the physical parameters and using equations (4.42) and (4.43) we can calculate a new version of the correction matrices $\mathbf{M}_{1C}^{(1)}$ and $\mathbf{M}_{2C}^{(1)}$ which, again, can be used to filter the experimental matrix. Clearly this process can be generalized and, at each step, we can find a better correction for the original experimental Mueller matrix:

$$\mathbf{M}_{e}^{\prime(i)} = \mathbf{M}_{e}(\mathbf{M}_{2C}^{(i-1)})^{-1}(\mathbf{M}_{1C}^{(i-1)})^{-1}, \tag{4.47}$$

in which each time we apply one Lu-Chipman decomposition to filter the experimental Mueller matrix the superscript (i) increases in one unit.

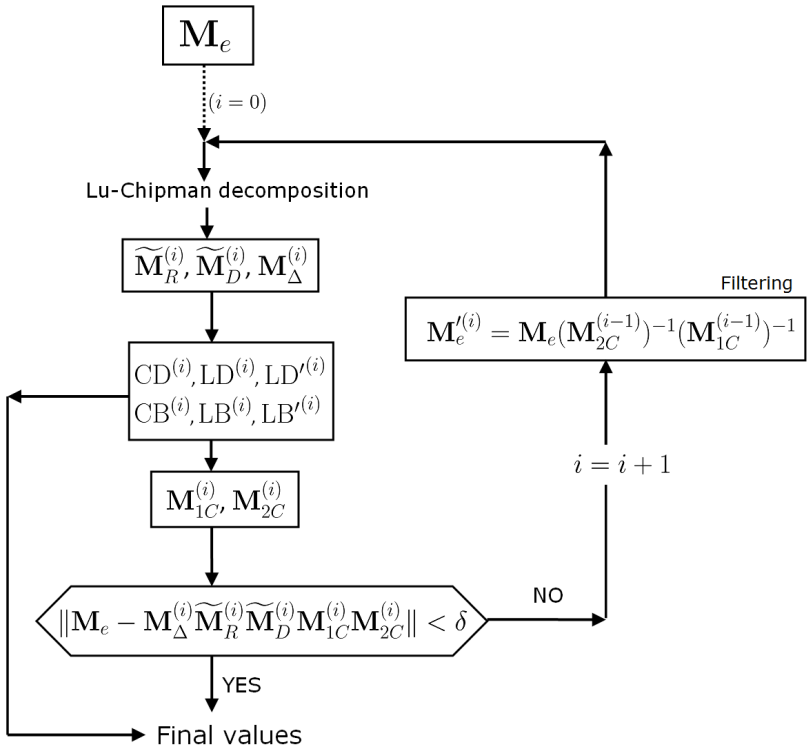

Figure 4.1.: Flow chart for the application of the pseudopolar decomposition on a experimental Mueller matrix $\mathbf{M}_e$. δ is the parameter, chosen manually, that decides the convergence of the algorithm. The choice $\delta = (\|\mathbf{M}_e - \mathbf{M}_\Delta^{(0)}\widetilde{\mathbf{M}}_R^{(0)}\widetilde{\mathbf{M}}_D^{(0)}\mathbf{M}_{1C}^{(0)}\mathbf{M}_{2C}^{(0)}\|)/5$ can be, for some experimental Mueller matrices, adequate. Alternatively, it is possible to run the algorithm with a fixed number of iterations (e.g. 100).

At each step we will have a better correction for the experimental Mueller matrix, which implies that the polar decomposition will produce more accurate results. We will arrive clearly to the situation in which the polar decomposition factors $\widetilde{\mathbf{M}}_R$ and $\widetilde{\mathbf{M}}_D$ of the corrected experimental matrix will be mostly the same that the factors $\mathbf{M}_R$ and $\mathbf{M}_D$ of the pseudopolar decomposition of the experimental matrix. After a certain number of steps (n) the condition $\|\mathbf{M}_e -$

$\mathbf{M}_{\Delta}^{(n)}\widetilde{\mathbf{M}}_{R}^{(n)}\widetilde{\mathbf{M}}_{D}^{(n)}\mathbf{M}_{1C}^{(n)}\mathbf{M}_{2C}^{(n)}\| \simeq 0$, where the bars denote the Frobenius norm[3], will fulfill and the product $\mathbf{M}_{\Delta}^{(n)}\widetilde{\mathbf{M}}_{R}^{(n)}\widetilde{\mathbf{M}}_{D}^{(n)}\mathbf{M}_{1C}^{(n)}\mathbf{M}_{2C}^{(n)}$ could be interpreted as the pseudopolar decomposition of $\mathbf{M}_e$. The algorithm for the application of the pseudopolar decomposition on a experimental Mueller matrix is summarized in the flow-chart of Fig. 4.1.

4.3.3. Symmetric decomposition

The symmetric decomposition was recently proposed by Ossikovsky [117] and it constitutes one of the most interesting approaches to study physical systems that introduce significant depolarization. The decomposition takes the form:

$$\mathbf{M} = \mathbf{M}_{D2}\mathbf{M}_{R2}\mathbf{M}_{\Delta d}\mathbf{M}_{R1}^{T}\mathbf{M}_{D1}. \tag{4.48}$$

The main particularity of this decomposition is that the depolarizer factor is placed "in the middle" of a symmetric optical sequence and that it is diagonal:

$$\mathbf{M}_{\Delta d} = \begin{bmatrix} d_0 & 0 & 0 & 0 \\ 0 & d_1 & 0 & 0 \\ 0 & 0 & d_2 & 0 \\ 0 & 0 & 0 & d_3 \end{bmatrix}. \tag{4.49}$$

This term contrasts with the depolarizer factor that was found in the Lu-Chipman decomposition [see Eq. (4.24)], which was nondiagonal because it corresponded to a depolarizer with polarizance. It is known both from theory and experiment that a great number of depolarizing media are better characterized by a diagonal depolarizers.

We will not describe in this section the algorithm to apply the symmetric decomposition. Although the algorithm is relatively simple its application to experimental matrices contain some subtleties that require further discussion. The details can be found in Refs. [117, 118].

If the depolarizer of the symmetric decomposition is "close" to the identity matrix (i.e. the depolarization is small) then there may be no clear separation between the factors placed before and after the depolarization factor of Eq. (4.48). If this happens probably the factors of the decomposition lose the physical significance. Therefore this decomposition is, in practice, more intended to the study of Mueller matrices corresponding to strongly depolarizing media, and, for example, can be very useful when trying to localize the various effects of a sample that for example is composed of two well-differentiated parts.

[3]The Frobenius norm of a $n \times n$ matrix $\mathbf{X}$ is defined as $\|\mathbf{X}\| = \left(\sum_{i=0}^{n-1}\sum_{j=0}^{n-1}|x_{ij}|^2\right)^{1/2} = [\mathrm{Tr}(\mathbf{X}^*\mathbf{X})]^{1/2}$.

4.4. Comparison between inversion and decomposition methods

As an example of the application of the analytic inversion, the polar decomposition and the pseudopolar decomposition, we have inverted two Mueller-Jones matrices that were generated using some representative values of CD, CB, LD, LB, LD′ and LB′. Table 4.3 shows these two matrices along with values of the optical effects retrieved by these different methods of analysis. The analytic inversion offers an exact solution to the problem, i.e. we obtain again the same parameters used for the generation, while the results on the others methods, specially for the polar decomposition, largely depend on the magnitude of the effects and/or on their noncommutativity. In case 1 all the optical effects are small and the noncommutative effects (that always are second and superior order effects) can be omitted, thus obtaining a satisfactory result by any of the three methods. It is interesting to note that here the pseudopolar decomposition, although it is an approximate method, is able to reproduce exact results with an accuracy up to the fourth decimal digit. Case 2 represents a situation in which much bigger effects are present and, in such a way, that they generate significant noncommutativity between the diattenuating and retarding effects. Here the pseudopolar decomposition offers a much better approximation to the exact result provided by the analytic inversion than the polar decomposition, that fails to find accurate results specially for CD.

Fig. 4.2 shows the values of the polarization fraction [β, see Eq. (1.33)], CD and CB obtained from experimental Mueller matrices for a water solution of J-aggregates of the pseudocyanine dye in a 0.1 mm path length cuvette. The only difference between *case a* and *case b* is the amount of aggregate that was present in the cuvette. The samples can be well described as an homogeneous anisotropic medium that contains linear birefringence and dichroism, due to the oriented elongated aggregates, and as well as circular dichroism and birefringence, due to the chirality of the involved molecules. These J-aggregates have a bisignate CD band around 570 nm, with a corresponding CB dispersion band of the type shown in Fig. 4.3. The Mueller matrices were spectroscopically measured with the instrument that we will describe in chapters 5 and 6 and, analyzed with the different methods presented in this chapter.

The top panels of Fig. 4.2 indicate that for the studied samples there exists a band of with depolarization around 570 nm that is caused by light scattering by aggregates of electronically interacting chromophores. At these wavelengths the depolarization is important for *case a* ($\beta \sim 0.5$), while it is much less significant for *case b* ($\beta \sim 0.8$). The CD and CB panels of the figure show a comparison of the

Table 4.3.: Comparison of methods to analyze homogeneous Mueller-Jones matrices

Case	Mueller Matrix			
1.	$\begin{pmatrix} 1 & -0.0291 & -0.0111 & 0.0295 \\ -0.0287 & 0.9993 & -0.0190 & 0.0049 \\ -0.0093 & 0.0188 & 0.9957 & 0.0802 \\ 0.0305 & -0.0073 & -0.0804 & 0.9963 \end{pmatrix}$			
Generation/Analytic inver.[a]	Polar decomp.		Pseudopolar decomp.[b]	
$CD = 0.0300$	$CD = 0.0295$		$CD = 0.0300$	
$CB = -0.0189$	$CB = -0.0189$		$CB = -0.0189$	
$LD = 0.0289$	$LD = 0.0291$		$LD = 0.0289$	
$LB = -0.0805$	$LB = -0.0805$		$LB = -0.0805$	
$LD' = 0.0102$	$LD' = 0.0111$		$LD' = 0.0102$	
$LB' = 0.0061$	$LB' = 0.0061$		$LB' = 0.0061$	
2.	$\begin{pmatrix} 1 & -0.6125 & 0.3377 & -0.2433 \\ -0.5766 & 0.7807 & 0.0096 & 0.4176 \\ 0.3756 & -0.1007 & 0.6804 & -0.3459 \\ 0.2736 & -0.4551 & 0.3205 & 0.4656 \end{pmatrix}$			
Generation/Analytic inver.[a]	Polar decomp.		Pseudopolar decomp.[b]	
$CD = 0.0202$	$CD = -0.3127$		$CD = 0.0337$	
$CB = 0.0778$	$CB = 0.0725$		$CB = 0.0746$	
$LD = 0.8289$	$LD = 0.7871$		$LD = 0.8428$	
$LB = 0.4805$	$LB = 0.4525$		$LB = 0.4481$	
$LD' = -0.5102$	$LD' = -0.4335$		$LD' = -0.5172$	
$LB' = 0.6061$	$LB' = 0.5599$		$LB' = 0.5639$	

[a] The analytic inversion gives the original parameters used for the generation of the Mueller-Jones matrices because it is an exact solution.
[b] Pseudopolar decomposition have been calculated with two correction terms and 100 iterations.

results offered by the inversion and decomposition methods of the experimental Mueller matrices. An adequate method of interpretation of the experimental Mueller matrices is expected to give the qualitative correlation between CD and CB shown in Fig. 4.3. For *case a* the results of the analytic inversion seem to be not really adequate at around 570 nm, which can be attributed to the fact that the process of finding a nondepolarizing estimate for Mueller matrices containing a strong depolarization using the Cloude sum decomposition fails because the measured Mueller matrices are not close to any nondepolarizing matrix. In contrast, for *case b*, we see that the product decompositions do not handle the CB as well as the inversion: the analytic inversion method gives CB

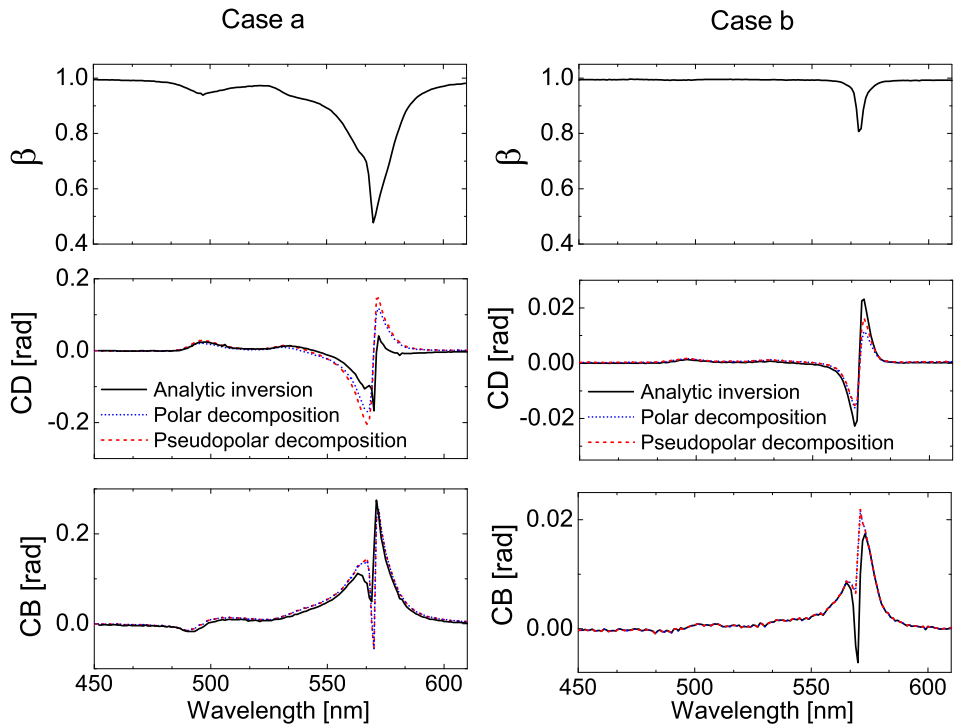

Figure 4.2.: Comparison between CD and CB calculated by three different methods: analytic inversion (solid line), polar decomposition (dotted line) and pseudopolar decomposition (dashed line). Case a and case b correspond to two different samples of the same compound (J-aggregates of a pseudocyanine dye) that had different degrees of aggregation. The sample on case a showed the greatest level of aggregation with an intense absorption and scattering band around 470 nm that causes important depolarization (low values of the polarization fraction β).

values that are more Kramers-Kronig consistent with a CD bisignate band (see Fig. 4.3). We can conclude that in this example we would use the pseudopolar decomposition method to study *case a* (pseudopolar and polar decomposition often yields similar results, but we prefer those of the pseudopolar for being more accurate), and the analytic inversion method to analyze *case b*.

There is not an universal criteria for choosing one method over another one to analyze experimental measurements. A good option is to test them all. Usually they will yield very similar results but, in the case of different results, it will be possible to use similar arguments to the ones we have used in this example to

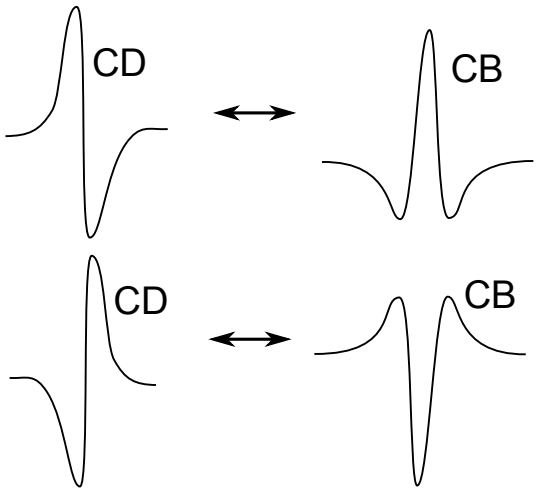

Figure 4.3.: Qualitative Kramers-Kronig transformation of a CD bisignate band that yields its corresponding CB. Bisignate CD bands are found in most of the J-aggregate samples studied in this thesis.

choose the most appropriate method of analysis.

Part III.

Experimental sets

Chapter 5.

Two-modulator generalized ellipsometer

The experimental device used to develop the present work has been a two-modulator generalized ellipsometer (2-MGE). This apparatus was customly build in a long process that started in 2006 and reached the status of development that will be detailed in this part of the thesis.

The 2-MGE was introduced by G. E. Jellison and F. A. Modine in 1997 with two papers: one dealing with the theory behind the analysis of the time-dependent detected signal [119] and the other focused on the experimental description and the calibration of the instrument [120]. Many of the contents of this chapter are based on these papers so, together with the patent [121], they can be an appropriate complement for the interested reader because we have kept in this chapter their same notation. Besides some subtle differences in the experimental configuration between our instrument and those of Jellison an Modine, in this chapter we have tried to provide a more step-by-step approach to the calculations required to interpret the detected waveform.

5.1. Introduction

The 2-MGE is an instrument that measures the change of light polarization upon interacting with a sample. The 2-MGE can operate either in reflection or transmission. In reflection, it acts as a generalized ellipsometer, measuring the standard ellipsometry parameters, as well as the cross-polarization parameters. In transmission, it measures all parameters associated with a general diattenuator or a general retarder. All the elements of the transmission or reflection Mueller matrix of a sample are accessible to this apparatus combining different measurement configurations.

The 2-MGE is based on the use of photoelastic modulators (PEMs). For years these phase modulators have been used in ellipsometry, allowing high sensitivity and high acquisition rate that are required for spectral measurements, in situ applications and fast processes monitoring. The first report of a spectroscopic ellipsometer that used a PEM was published by Jasperson and Schnatterly in 1970 [122], but phase modulated ellipsometry did not grew more popular until

'80s and '90s with the availability of fast computers. Drévillon and coworkers were pioneers in performing a digital Fourier analysis on the intensity waveform [123, 124] and Canillas *et al.* developed a phase-modulated ellipsometer using a Fourier transform spectrometer to work in the infrared [125, 126]. In 1997 G. E. Jellison and F. Modine published in a series of two papers the first implementation of an ellipsometer that used two free running PEMs of different frequencies and introduced the acronym *2-MGE* for such instrument [119, 120].

Instruments based on four PEMs of different frequencies have also been suggested [127]. Such polarimeter would be capable of measuring all the 16 elements of a Mueller matrix in a single measurement and without any moving parts. However, to our knowledge, no experimental realizations of this setup have been developed to the moment.

5.2. The photoelastic modulator

The working principle of a modern photoelastic modulator (PEM) is based on the optical birefringence induced by periodical stress. A PEM is composed of an optically transparent material with a high elasto-optic efficiency and low mechanical dissipation (e.g. fused quartz) and of an oscillating piezoelectric transducer. The light beam passes through the optical element which is mechanically stressed by a periodic strain variation (typically at 20-80 kHz) by the transducer. This oscillating stress causes changes in the the refractive index of the optical element, which exhibits a birefringence proportional to the strain. Therefore, the optical element acts as a dynamic wave plate so, if a polarizer is fixed before the PEM, where the azimuthal angle of the polarizer is not aligned with the modulation axis of the PEM, dynamically elliptically polarized light is generated with the ellipticity changing at the frequency of the PEM.

The modern PEM was introduced in 1969 by James Kemp [128], then manufactured by a private company in the USA (Hinds Instruments, Inc., Hillsboro, Oregon, USA). That design has been dominant in almost all PEM applications, although the construction and performance have changed a little. A second type PEM was proposed by Canit and Badoz in France in 1983 [129]. The Kemp design, utilizes a -18.5 degree X-cut quartz crystal as the excitation source, which delivers a nearly pure longitudinal wave. The Canit-Badoz design, uses a thin slab of piezoelectric ceramic transducer that is adhered to the optical element. This design is less vulnerable to temperature changes but causes considerable unwanted vibrations and acoustic reflections.

The photoelastic modulators used in our 2-MGE were manufactured by Hinds Instruments and consist of a piece of precisely-cut crystalline quartz (the piezo-

electric transducer) mechanically coupled to a piece of optically-isotropic fused quartz (the optical element). An ac voltage is applied between the front and back faces of the crystalline quartz transducer in order to drive it at its resonant frequency. The time-dependent retardation is expressed as

$$\delta(t) = A\sin(\omega t + \phi), \tag{5.1}$$

where A is the amplitude of modulation, $2\pi\omega$ is the frequency of the modulator and ϕ is the phase of the modulator. The light beam passing through the central region of the fused quartz bar undergoes a retardation that is periodic at the resonant frequency of the crystal quartz bar. This frequency is dependent on the size and shape of crystalline and fused quartz elements and somewhat on the temperature. The two PEMs of our instrument have frequencies around 50 kHz and 60 kHz. The amplitude of modulation is usually set with an external dc voltage, being the corresponding phase retardation dependent on the wavelength of light; dependence that can be easily calibrated.

As a result of its design, a PEM has unique optical features, such as high modulation purity and efficiency, broad spectral range, high power handling capability, large acceptance angle, large useful aperture and high retardation stability [130]. These features make the PEM the best choice for polarization modulation in applications that require high sensitivity, because it offers a modulation quality unsurpassed by other types of electro-optic modulators or liquid crystal modulators.

A PEM may exhibit a small static strain in the optical element that is independent of dynamic retardation. If it is collinear with the modulation axis of the optical element it is possible to calibrate it and to correct the data for its effect. In this case the time-dependent retardation of Eq. (5.1) transforms to

$$\delta(t) = A\sin(\omega t + \phi) + \delta_0, \tag{5.2}$$

where δ_0 is the static retardation. For a more complete description about PEMs and their use in ellipsometry see for example [131] and the chapter about polarization modulation ellipsometry by Jellison and Modine in [132].

5.3. Experimental configuration

The 2-MGE, understood as a whole apparatus, is composed of several different elements. In order to review their characteristics, position and functionality in the instrument we will distribute them in two big groups: optical components and electronic hardware.

5.3.1. Optical components

This group of components comprises all the elements that affect or modify the light beam from its generation until its detection. Table 5.1 lists all the optical with their respective brand name, model, and other relevant characteristics. Fig. 5.1 shows and scheme of all optical elements as well as a qualitative ray trace of the light beam as it goes through them.

Table 5.1.: List of light related components

Element	Brand, model	Details
Light Source	Oriel	Xe 75 W short arc Lamp
Optical fiber 0	Oriel LLS308	800μm quartz core, solarization resistant
Focusing optics	Horiba Jobin-Yvon MicroSpot	Working distance $\sim$ 50 cm. Available spots: $\sim 1500, 200, 100$ μm
Polarizers	Fichou	MgF_2 Rochon polarizer. Suitable for UV
PEM 0	Hinds Instruments I/FS50	Fused Si, $\nu_0 \sim 50$ kHz
PEM 1	Hinds Instruments I/FS60	Fused Si, $\nu_1 \sim 60$ kHz
Lens	Thorlabs LB4879	Fused Si, $f = 35$ mm
Optical fiber 1	Oriel LLS306	600μm quartz core, solarization resistant
Order Filters	Fichou	340 nm and 570 nm
Monochromator	Horiba Jobin-Yvon iHR-320	2400 l/mm and 1800 l/mm gratings available
PMT	Hamamatsu R3896	Spectral response from 185 to 900 nm

In Fig. 5.1 the light source is a 75 watt xenon arc lamp that is focused on the end of a quartz fiber optic using a condenser lens. The other end of the fiber optic is attached to the light entrance of the focusing optics module which is composed of two mirrors and focuses light at a 50 cm from the module. The spot diameter can be tuned by changing the diameter of a pinhole mask centered

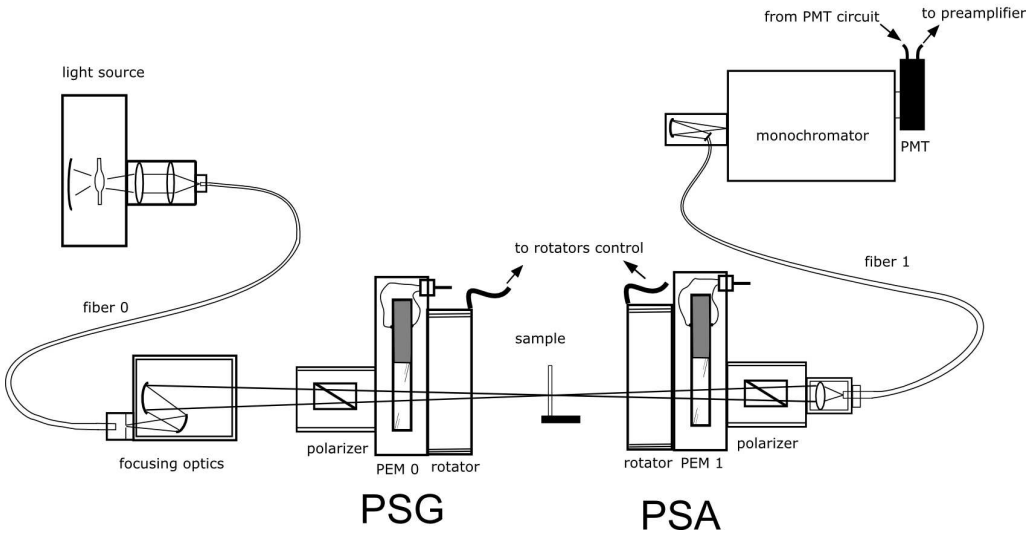

Figure 5.1.: Schematic drawing of the optical elements involved in the 2-MGE. Light beam goes from left to right.

at the entrance of the focusing optics module. Three different pinhole masks are available with diameters 1 mm, 0.100 mm and 0.050 mm, that respectively translate in approximate spot sizes of 1.5 mm, 0.200 mm and 0.100 mm.

Light exiting the focusing module passes through the PSG, which consists of a polarizer-PEM pair. The polarizer is attached to the PEM by using a precision manual rotator and is oriented at $\theta_{b0} = 45°$ with respect to the longitudinal axis of the PEM. This PEM has a resonant frequency of 49.986 kHz. The complete PSG is attached to a precision automatic step-by-step rotator.

The sample is placed at the focusing point that falls between the PSG and the PSA. The PSA consists of another PEM-polarizer pair. The nominal frequency of operation of this PEM is 59.963 kHz. As in the PSG, here the polarizer is also mounted on a precision manual rotator and oriented at $\theta_{b1} = 45°$ with respect to the longitudinal axis of this PEM. The PSA is also attached to a precision automatic step-by-step rotator. At the end of the PSA there is a lens that focuses the light onto the core of an optical fiber with a core diameter of 400 μm.

The light from the optical fiber passes through an optical filter (to eliminate second-order effects) before entering the F/number matcher accessory of the monochromator. This accessory uses a pair of mirrors to image the light coming from the fiber to the entrance slit of the monochromator. The light intensity is

detected at the output slit by using a photomultiplier tube (PMT).

5.3.2. Electronic hardware

A considerable number of electronic hardware components have been assembled to run automatically a 2-MGE. They permit the appropriate transformation of the detected light into a digital signal and the automatization of the measurement process. Table 5.2 enumerates the fundamental electronic elements of the 2-MGE and displays some of their main features. In Fig. 5.2 there is a schematic representation of the connections among the different elements. With the exception of the positioning and alignment of the sample the rest of functions are automatic and controlled with a personal computer.

Table 5.2.: List of electronic hardware

Element	Brand, model	Details
Rotator Units	Newport UE31PP (UR80)	Custom controller
Linear translation units	UTS50CC	SMC100CC controller, 0.1 μm precision
PEM 0 control	PEM-90 controller	Remote voltage control
PEM 1 control	PEM-100 controller	RS232 control
Filter wheel	Thorlabs FW102B	USB control
Preamplifier	Hammamatsu C7319	gain of 10^5
PMT control circuit	CRIC[a]	Custom design, uses SDS HV source
Trigger circuit	CRIC[a]	Custom design, selectable gate, 0.5° used
Waveform digitizer	Spectrum MI3130	2 channel 12 bit A/D with 25 MS/s
Personal Computer	Custom PC	Core2Duo, 1 Gb RAM, Windows XP
Oscilloscope	Tektronix	4 channel

[a]Made by "Centre de Recerca i Innovació de Catalunya" (CRIC).

In our 2-MGE the motion control elements consist of two precision stepper rotation units that azimuthally rotate the whole PSG and PSA and two precision linear translation units that allow to position conveniently the sample in the x-y plain. These four motion elements are computer controlled by the software

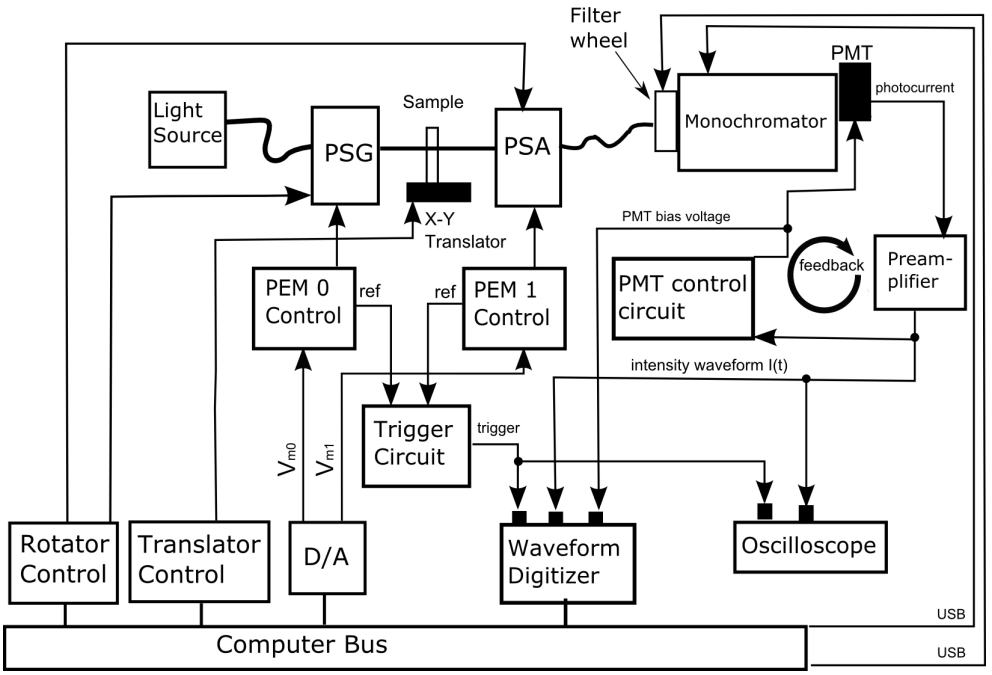

Figure 5.2.: Schematic drawing of the 2-MGE and associated control circuitry.

package developed for the 2-MGE.

The signal from the PMT is in the form of a photocurrent and it is converted to a voltage by using a current-mode preamplifier. The signal coming from the preamplifier is fed to a feedback control circuit for the PMT. This feedback circuit has been specifically developed for our 2-MGE and its objective is to dynamically regulate the high voltage delivered to the dynode chain of the PMT. The circuit is designed so that the dc part of the signal coming from the preamplifier is kept at a constant value, that can be chosen by the user (normally we keep dc at 0.5V). Thus, the high voltage given by the PMT feedback circuit will automatically increase (or decrease) depending on whether the number or photons arriving to the PMT decreases (or increases). The adaptative gain provided by this circuit is essential to have a high dynamic range during a spectroscopic measurement which, otherwise, the measurement of small signals would be limited by the 12-bit resolution of our digitizer. A circuit of this type is described in [133]. The voltage applied to the PMT is permanently visible by means of a LCD display installed in the same circuit enclosure; this feature is useful for the user of the 2-MGE for alignment (usually the best alignment is achieved when this value is

minimized) or even to recognize situations when no light reaches the detector.

The voltage waveform from the preamplifier is digitized by a high-speed 12 bits digitizer installed as a supplementary board in the control computer. Several parameters of the digitization can be controlled, being the most significant the acquisition time, that is usually kept at 0.5 μs (corresponds to a sample rate of 2 MS in a second), and the length of the captured waveform that is kept at 16384. The waveform capture is initialized by a trigger pulse that comes from a coincidence circuit that generates a trigger event each time the monitored reference outputs of the PEM's are in phase. A second channel of the digitizer is used to measure the voltage applied to the PMT (it has been previously attenuated by a factor 1000 so that no longer is a HV), this measure is not a requirement for a 2-MGE, but for some single-wavelengths measurement is useful to distinguish sample area's with different transmissivity or reflectivity.

Each PEM is a resonant device, in which only the amplitude of modulation can be controlled by electronics. The frequency and phase are own characteristics of the PEM and cannot be externally adjusted. The coincidence circuit allows to find the phase coincidences between the reference signals coming from the two PEM's. As the periods of the two modulators are $T_0 \simeq 20\ \mu s$ and $T_1 \simeq 16.67\ \mu s$, after five complete cycles of PEM 0, and after six complete cycles of PEM 1 (repeat time of $T \simeq 100\ \mu s$) we found that the phases come close. The triggering circuit has an adjustable gate time that determines the accuracy of the phase coincidence: the smaller the gate time, the fewer trigger events, but more accurate the phase. For standard measurements the gate time of our coincidence circuit is adjusted so that the monitored reference outputs are within $0^\circ \pm 0.5^\circ$.

The entire instrument is controlled through a personal computer, which interacts with each one of electronic hardware components through the computer bus. An external 4-channel oscilloscope is also used to monitor the voltage waveform and the reference signals that come from the PEMs. This device is not connected to the computer bus and has no contribution in the measurement.

5.4. Determination of the intensity with the Stokes-Mueller representation

The most convenient way to describe the polarization effects of optical elements of the 2-MGE is the Stokes-Mueller calculus introduced in section 1.4. We will use the Stokes-Mueller representation to describe the state of polarization of the light beam as it traverses all the polarization-changing optical elements of the 2-MGE.

In a 2-MGE the PSG is composed of a polarizer-PEM pair. The Mueller matrix

of a modulator $\mathbf{M}_m$ is

$$\mathbf{M}_m = \begin{pmatrix} 1 & 0 & 0 & 0 \\ 0 & 1 & 0 & 0 \\ 0 & 0 & \cos(\delta) & \sin(\delta) \\ 0 & 0 & -\sin(\delta) & \cos(\delta) \end{pmatrix} = \begin{pmatrix} 1 & 0 & 0 & 0 \\ 0 & 1 & 0 & 0 \\ 0 & 0 & Y_\delta & X_\delta \\ 0 & 0 & -X_\delta & Y_\delta \end{pmatrix}, \tag{5.3}$$

where δ is given by Eq. (5.2) and

$$Y_\delta \equiv \cos(\delta), \tag{5.4a}$$

$$X_\delta \equiv \sin(\delta). \tag{5.4b}$$

The Mueller matrix for an horizontal polarizer, $\mathbf{M}_p$, is

$$\mathbf{M}_p = \begin{pmatrix} 1 & 1 & 0 & 0 \\ 1 & 1 & 0 & 0 \\ 0 & 0 & 0 & 0 \\ 0 & 0 & 0 & 0 \end{pmatrix}. \tag{5.5}$$

Considering that the input light is unpolarized, and that the azimuthal angles of the polarizer and PEM are θ_p and θ_m, the Stokes vector for the light beam emerging from the PSG is

$$\mathbf{S}_{PSG} = \mathbf{R}(-\theta_{m0})\mathbf{M}_{m0}\mathbf{R}(\theta_{m0})\mathbf{R}(-\theta_{p0})\mathbf{M}_{p0}\mathbf{R}(\theta_{p0}) \begin{pmatrix} 1 \\ 0 \\ 0 \\ 0 \end{pmatrix}, \tag{5.6}$$

where $\mathbf{R}(\theta_x)$ is the rotation matrix defined in Eq. (1.27):

$$\mathbf{R}(\theta_x) = \begin{pmatrix} 1 & 0 & 0 & 0 \\ 0 & \cos(2\theta_x) & \sin(2\theta_x) & 0 \\ 0 & -\sin(2\theta_x) & \cos(2\theta_x) & 0 \\ 0 & 0 & 0 & 1 \end{pmatrix} = \begin{pmatrix} 1 & 0 & 0 & 0 \\ 0 & C_x & S_x & 0 \\ 0 & -S_x & C_x & 0 \\ 0 & 0 & 0 & 1 \end{pmatrix}, \tag{5.7}$$

where the shorthand notation $\cos(2\theta_x) \equiv C_x$ and $\sin(2\theta_x) \equiv S_x$ has been adopted. We recall that θ is positive when the rotation is counterclockwise looking against the direction of propagation the light beam .

Multiplying out Eq. (5.6) the following Stokes vector for the PSG is obtained:

$$\mathbf{S}_{PSG} = \begin{pmatrix} 1 \\ C_{m0}C_{b0} + S_{m0}S_{b0}Y_{0\delta} \\ S_{m0}C_{b0} - C_{m0}S_{b0}Y_{0\delta} \\ S_{b0}X_{0\delta} \end{pmatrix}, \tag{5.8}$$

where θ_{b0} is the azimuthal angle of the polarizer with respect to the modulator ($\theta_{b0} \equiv \theta_{m0} - \theta_{p0}$). In a 2-MGE the polarizer-PEM pair is configured such that θ_{b0} is $\pm 45^\circ$ (in our instrument we have chosen 45°). However, in practice, even using precise polarizer holders there is always some small angular misplacement that we can represent by ε_{b0}. Therefore, in our 2-MGE, we have $\theta_{b0} = 45^\circ + \varepsilon_{b0}$, which leads to $S_{b0} = 1$ and $C_{b0} = -2\varepsilon_{b0}$. With this angle Eq. (5.8) transforms into

$$\mathbf{S}_{PSG} = \begin{pmatrix} 1 \\ -2C_{m0}\varepsilon_{b0} + S_{m0}Y_{0\delta} \\ -(2S_{m0}\varepsilon_{b0} + C_{m0}Y_{0\delta}) \\ X_{0\delta} \end{pmatrix}. \tag{5.9}$$

In the case of the PSA we can perform an analogous calculation. In the PSA light first passes through the PEM and then through the polarizer:

$$\mathbf{S}_{PSA}^T = \begin{pmatrix} 1 & 0 & 0 & 0 \end{pmatrix} \mathbf{R}(-\theta_{p1})\mathbf{M}_{p1}\mathbf{R}(\theta_{p1})\mathbf{R}(-\theta_{m1})\mathbf{M}_{m1}\mathbf{R}(\theta_{m1}). \tag{5.10}$$

Again, taking the definition $\theta_{b1} \equiv \theta_{m1} - \theta_{p1}$ and considering that we orientate the polarizer such that $\theta_{b1} = 45^\circ + \varepsilon_{b1}$, the matrix multiplication yields the following transposed Stokes vector:

$$\mathbf{S}_{PSA}^T = \begin{pmatrix} 1 & -2\varepsilon_{b1}\mathrm{C}_{m1} + Y_{1\delta}S_{m1} & -2\varepsilon_{b1}S_{m1} - Y_{1\delta}C_{m1} & -X_{1\delta} \end{pmatrix}. \tag{5.11}$$

The intensity of the time-dependent light beam for the 2-MGE is thus given by:

$$I(t) = \mathbf{S}_{PSA}^T \mathbf{M} \mathbf{S}_{PSG}, \tag{5.12}$$

where $\mathbf{M}$ is the transmission or reflection Mueller matrix of the sample given in Eq. (1.26). The result of this multiplication can be parameterized as follows [119]:

$$\begin{aligned} I(t) =& I_{dc} + I_{X0}X_{0\delta} + I_{Y0}Y_{0\delta} + I_{X1}X_{1\delta} + I_{Y1}Y_{1\delta} + I_{X0X1}X_{0\delta}X_{1\delta} \\ &+ I_{X0Y1}X_{0\delta}Y_{1\delta} + I_{Y0X1}Y_{0\delta}X_{1\delta} + I_{Y0Y1}Y_{0\delta}Y_{1\delta}, \end{aligned} \tag{5.13}$$

where the time dependence of the intensity is embedded in the $X_{i\delta}$ and $Y_{i\delta}$ functions, which have been given in Eqs. (5.4).

To simplify expressions we temporally assume that $\varepsilon_{b0} = \varepsilon_{b1} = 0$ (these angles will be later reconsidered in the calibration section), we obtain that the eight coefficients of Eq. (5.13) are functions of the elements of the sample's Mueller

matrix and are given by,

$$\begin{aligned}
&I_{X0} = m_{03},\\
&I_{Y0} = -C_{m0}m_{02} + S_{m0}m_{01},\\
&I_{X1} = -m_{30},\\
&I_{Y1} = -C_{m1}m_{20} + S_{m1}m_{10},\\
&I_{X0X1} = -m_{33},\\
&I_{X0Y1} = S_{m1}m_{13} - C_{m1}m_{23},\\
&I_{Y0X1} = -S_{m0}m_{31} + C_{m0}m_{32},\\
&I_{Y0Y1} = C_{m0}C_{m1}m_{22} - S_{m0}C_{m1}m_{21} - C_{m0}S_{m1}m_{12} + S_{m0}S_{m1}m_{11}.
\end{aligned} \tag{5.14}$$

These 8 terms are usually normalized by the I_{dc} term to eliminate fluctuations of the incident light intensity, and the dependence of the sample transmissivity or reflectivity.

Using Eqs. (5.14) it is possible to define four cases or configurations, determined by the azimuthal angles of the PEMs with respect to plane of incidence (i.e. θ_{m0} and θ_{m1}), where different elements of the sample Mueller matrix are measured. Schematically, this cases can be represented as [134]:

case 1: $\theta_{m0} = \pm 45°$; $\theta_{m1} = \pm 45°$

$$\mathbf{M} = \begin{pmatrix} 1 & \sigma_{0s}I_{Y0} & \bullet & I_{X0} \\ \sigma_{1s}I_{Y1} & \sigma_{0s}\sigma_{1s}I_{Y0Y1} & \bullet & \sigma_{1s}I_{X0Y1} \\ \bullet & \bullet & \bullet & \bullet \\ -I_{X1} & -\sigma_{0s}I_{Y0X1} & \bullet & -I_{X0X1} \end{pmatrix}, \tag{5.15a}$$

case 2: $\theta_{m0} = \pm 45°$; $\theta_{m1} = 0°, 90°$

$$\mathbf{M} = \begin{pmatrix} 1 & \sigma_{0s}I_{Y0} & \bullet & I_{X0} \\ \bullet & \bullet & \bullet & \bullet \\ -\sigma_{1c}I_{Y1} & -\sigma_{0s}\sigma_{1c}I_{Y0Y1} & \bullet & -\sigma_{1c}I_{X0Y1} \\ -I_{X1} & -\sigma_{0s}I_{Y0X1} & \bullet & -I_{X0X1} \end{pmatrix}, \tag{5.15b}$$

case 3: $\theta_{m0} = 0°, 90°$; $\theta_{m1} = \pm 45°$

$$\mathbf{M} = \begin{pmatrix} 1 & \bullet & -\sigma_{0c}I_{Y0} & I_{X0} \\ \sigma_{1s}I_{Y1} & \bullet & -\sigma_{0c}\sigma_{1s}I_{Y0Y1} & \sigma_{1s}I_{X0Y1} \\ \bullet & \bullet & \bullet & \bullet \\ -I_{X1} & \bullet & \sigma_{0c}I_{Y0X1} & -I_{X0X1} \end{pmatrix}, \tag{5.15c}$$

case 4: $\theta_{m0} = 0°, 90°$; $\theta_{m1} = 0°, 90°$

$$\mathbf{M} = \begin{pmatrix} 1 & \bullet & -\sigma_{0c}I_{Y0} & I_{X0} \\ \bullet & \bullet & \bullet & \bullet \\ -\sigma_{1c}I_{Y1} & \bullet & \sigma_{0c}\sigma_{1c}I_{Y0Y1} & -\sigma_{1c}I_{X0Y1} \\ -I_{X1} & \bullet & \sigma_{0c}I_{Y0X1} & -I_{X0X1} \end{pmatrix}, \tag{5.15d}$$

where the sign terms are defined by

$$\begin{aligned} \sigma_{0s} &= \text{sign}[\sin(2\theta_{m0})], \qquad \sigma_{1s} = \text{sign}[\sin(2\theta_{m1})], \\ \sigma_{0c} &= \text{sign}[\cos(2\theta_{m0})], \qquad \sigma_{1c} = \text{sign}[\cos(2\theta_{m1})]. \end{aligned} \tag{5.16}$$

In every case the sample Mueller matrix elements that cannot be measured are signified by bullets (•). With these 4 configurations all the elements of the normalized sample Mueller matrix can be measured, and some elements are measured more than once (for example elements m_{03}, m_{30} and m_{33} are measured in every case).

5.5. Data measurement

In the previous section it was demonstrated that the light intensity detected by the PMT is a function of time and can be represented by Eq. (5.13). The purpose of this section is to show how the coefficients of that equation, namely I_{X0}, I_{Y0}, I_{X1}, I_{Y1}, I_{X0X1}, I_{X0Y1}, I_{Y0X1} and I_{Y0Y1}, can be calculated from the experimentally recorded $I(t)$.

If the static retardation δ_0 and δ_1 of the PEMs, introduced in Eq. (5.2), are small (δ_0, $\delta_1 \ll 1$), as it usually happens, they can be treated to first order[1] and Eqs. (5.4) can be rewritten as follows:

$$X_{0\delta} = \sin\left[A_0 \sin\left(\omega_0 t + \phi_0\right) + \delta_0\right] \simeq X_0 + \delta_0 Y_0, \tag{5.17a}$$

$$Y_{0\delta} = \cos\left[A_0 \sin\left(\omega_0 t + \phi_0\right) + \delta_0\right] \simeq Y_0 - \delta_0 X_0, \tag{5.17b}$$

$$X_{1\delta} = \sin\left[A_1 \sin\left(\omega_1 t + \phi_1\right) + \delta_1\right] \simeq X_1 + \delta_1 Y_1, \tag{5.17c}$$

$$Y_{1\delta} = \cos\left[A_1 \sin\left(\omega_1 t + \phi_1\right) + \delta_1\right] \simeq Y_1 - \delta_1 X_1, \tag{5.17d}$$

where to short notation we have made the equivalences $X_0 \equiv \sin\left[A_0 \sin\left(\omega_0 t + \phi_0\right)\right]$, $Y_0 \equiv \cos\left[A_0 \sin\left(\omega_0 t + \phi_0\right)\right]$, $X_1 \equiv \sin\left[A_1 \sin\left(\omega_1 t + \phi_1\right)\right]$ and $Y_1 \equiv \cos\left[A_1 \sin\left(\omega_1 t + \phi_1\right)\right]$.

If the static retardations are temporally assumed to vanish ($\delta_0 = \delta_1 = 0$), Eq. (5.13) can be rewritten as

$$\begin{aligned} I(t) =& I_{dc} + I_{X0}X_0 + I_{Y0}Y_0 + I_{X1}X_1 + I_{Y1}Y_1 + I_{X0X1}X_0X_1 \\ &+ I_{X0Y1}X_0Y_1 + I_{Y0X1}Y_0X_1 + I_{Y0Y1}Y_0Y_1, \end{aligned} \tag{5.18}$$

which can be also displayed in vector form:

$$I(t) = \mathbf{B}(t)^T \mathbf{I}, \tag{5.19}$$

[1] $\sin\theta_i = \theta_i$ and $\cos\theta_i = 1$.

where the basis vector $\mathbf{B}(t)$ and the intensity coefficient vector $\mathbf{I}$ are given by

$$\mathbf{B}(t)^T = \begin{pmatrix} 1 & X_0 & Y_0 & X_1 & Y_1 & X_0X_1 & X_0Y_1 & Y_0X_1 & Y_0Y_1 \end{pmatrix}, \tag{5.20}$$

$$\mathbf{I}^T = \begin{pmatrix} I_{dc} & I_{X0} & I_{Y0} & I_{X1} & I_{Y1} & I_{X0X1} & I_{X0Y1} & I_{Y0X1} & I_{Y0Y1} \end{pmatrix}. \tag{5.21}$$

The basis functions X_0, Y_0, X_1 and Y_1 are related to the common Fourier basis functions using an infinite series including integer Bessel functions:

$$X_0 = 2\sum_{k=1}^{\infty} J_{2k-1}(A_0)\sin\left[(2k-1)\omega_0 t\right], \tag{5.22a}$$

$$Y_0 = J_0(A_0) + 2\sum_{k=1}^{\infty} J_{2k}(A_0)\cos\left[2k\omega_0 t\right], \tag{5.22b}$$

$$X_1 = 2\sum_{k=1}^{\infty} J_{2k-1}(A_1)\sin\left[(2k-1)\omega_1 t\right], \tag{5.22c}$$

$$Y_1 = J_0(A_1) + 2\sum_{k=1}^{\infty} J_{2k}(A_1)\cos\left[2k\omega_1 t\right]. \tag{5.22d}$$

For many ellipsometric applications, A_i is chosen to be 2.4048 radians, which gives $J_0(A) = 0$, $J_1(A) = 0.5192$, $J_2(A) = 0.4318$, $J_3(A) = 0.1990$, $J_4(A) = 0.0647$, $J_5(A) = 0.0164$, etc. For this value of A, the Fourier expansion of the X and Y basis functions have no dc terms and the series converges rapidly. Also, for this value, the $J_1(A)$ and $J_2(A)$ are within 15% their maximum values

If Eqs. (5.22) are introduced in the time-dependent intensity of Eq. (5.18) we get the following expanded equation for the intensity of the light beam:

$$\begin{aligned}
I(t) = {} & I_{dc} + \\
& + I_{X0}\left[2J_1(A_0)\sin(\omega_0 t + \phi_0) + 2J_3(A_0)\sin(3\omega_0 t + 3\phi_0) + ...\right] + \\
& + I_{Y0}\left[J_0(A_0) + 2J_2(A_0)\cos(2\omega_0 t + 2\phi_0) + 2J_4(A_0)\cos(4\omega_0 t + 4\phi_0) + ...\right] + \\
& + I_{X1}\left[2J_1(A_1)\sin(\omega_1 t + \phi_1) + 2J_3(A_1)\sin(3\omega_1 t + 3\phi_1) + ...\right] + \\
& + I_{Y1}\left[J_0(A_1) + 2J_2(A_1)\cos(2\omega_1 t + 2\phi_1) + 2J_4(A_1)\cos(4\omega_1 t + 4\phi_1) + ...\right] + \\
& + I_{X0X1}\left[2J_1(A_0)\sin(\omega_0 t + \phi_0) + 2J_3(A_0)\sin(3\omega_0 t + 3\phi_0) + ...\right] \times \\
& \qquad \times \left[2J_1(A_1)\sin(\omega_1 t + \phi_1) + 2J_3(A_1)\sin(3\omega_1 t + 3\phi_1) + ...\right] + \\
& + I_{X0Y1}\left[2J_1(A_0)\sin(\omega_0 t + \phi_0) + 2J_3(A_0)\sin(3\omega_0 t + 3\phi_0) + ...\right] \times \\
& \qquad \times \left[J_0(A_1) + 2J_2(A_1)\cos(2\omega_1 t + 2\phi_1) + 2J_4(A_1)\cos(4\omega_1 t + 4\phi_1) + ...\right] + \\
& + I_{Y0X1}\left[J_0(A_0) + 2J_2(A_0)\cos(2\omega_0 t + 2\phi_0) + 2J_4(A_0)\cos(4\omega_0 t + 4\phi_0) + ...\right] \times \\
& \qquad \times \left[2J_1(A_1)\sin(\omega_1 t + \phi_1) + 2J_3(A_1)\sin(3\omega_1 t + 3\phi_1) + ...\right] + \\
& + I_{Y0Y1}\left[J_0(A_0) + 2J_2(A_0)\cos(2\omega_0 t + 2\phi_0) + 2J_4(A_0)\cos(4\omega_0 t + 4\phi_0) + ...\right] \times \\
& \qquad \times \left[J_0(A_1) + 2J_2(A_1)\cos(2\omega_1 t + 2\phi_1) + 2J_4(A_1)\cos(4\omega_1 t + 4\phi_1) + ...\right].
\end{aligned} \tag{5.23}$$

The first four basis functions of the time-dependent intensity of Eq. (5.23) are easily determined from the frequency components of the Fourier expressions given in Eqs. (5.22), but the last four are product functions of that equations. Thanks to the algebra properties of the sin and cos functions[2] the product terms accompanying the factors I_{X0X1}, I_{X0Y1}, I_{Y0X1} and I_{Y0Y1} can be rewritten as frequency components at the sum and difference frequencies of the two modulators. Also, we can now assume that the amplitude of the Bessel function have been already adjusted so that $J_0(A_0) = J_0(A_1) = 0$ (i.e. $A_0 = A_1 = 2.4048$ rad).

The time-dependent intensity can be rewritten as:

$$
\begin{aligned}
I(t) = {} & I_{dc} + \\
& + I_{X0}2\left[J_1(A_0)\sin(\omega_0 t + \phi_0) + J_3(A_0)\sin(3\omega_0 t + 3\phi_0) + ...\right] + \\
& + I_{Y0}2\left[J_2(A_0)\cos(2\omega_0 t + 2\phi_0) + J_4(A_0)\cos(4\omega_0 t + 4\phi_0) + ...\right] + \\
& + I_{X1}2\left[J_1(A_1)\sin(\omega_1 t + \phi_1) + J_3(A_1)\sin(3\omega_1 t + 3\phi_1) + ...\right] + \\
& + I_{Y1}2\left[J_2(A_1)\cos(2\omega_1 t + 2\phi_1) + J_4(A_1)\cos(4\omega_1 t + 4\phi_1) + ...\right] + \\
& + I_{X0X1}2\Big[J_1(A_0)J_1(A_1)\left[\cos[(\omega_0 - \omega_1)t + \phi_0 - \phi_1] - \cos[(\omega_0 + \omega_1)t + \phi_0 + \phi_1]\right] + \\
& \qquad J_1(A_0)J_3(A_1)\left[\cos[(\omega_0 - 3\omega_1)t + \phi_0 - 3\phi_1] - \cos[(\omega_0 + 3\omega_1)t + \phi_0 + 3\phi_1]\right] + \\
& \qquad J_3(A_0)J_1(A_1)\left[\cos[(3\omega_0 - \omega_1)t + 3\phi_0 - \phi_1] - \cos[(3\omega_0 + \omega_1)t + 3\phi_0 + \phi_1]\right] + \\
& \qquad J_3(A_0)J_3(A_1)\left[\cos[(3\omega_0 - 3\omega_1)t + 3\phi_0 - 3\phi_1] - \cos[(3\omega_0 + 3\omega_1)t + 3\phi_0 + 3\phi_1]\right] + ...\Big] + \\
& + I_{X0Y1}2\Big[J_1(A_0)J_2(A_1)\left[\sin[(\omega_0 - 2\omega_1)t + \phi_0 - 2\phi_1] + \sin[(\omega_0 + 2\omega_1)t + \phi_0 + 2\phi_1]\right] + \\
& \qquad J_1(A_0)J_4(A_1)\left[\sin[(\omega_0 - 4\omega_1)t + \phi_0 - 4\phi_1] + \sin[(\omega_0 + 4\omega_1)t + \phi_0 + 4\phi_1]\right] + \\
& \qquad J_3(A_0)J_2(A_1)\left[\sin[(3\omega_0 - 2\omega_1)t + 3\phi_0 - 2\phi_1] + \sin[(3\omega_0 + 2\omega_1)t + 3\phi_0 + 2\phi_1]\right] + \\
& \qquad J_3(A_0)J_4(A_1)\left[\sin[(3\omega_0 - 4\omega_1)t + 3\phi_0 - 4\phi_1] + \sin[(3\omega_0 + 4\omega_1)t + 3\phi_0 + 4\phi_1]\right] + ...\Big] + \\
& + I_{Y0X1}2\Big[J_1(A_0)J_2(A_1)\left[\sin[(\omega_1 - 2\omega_0)t + \phi_1 - 2\phi_0] + \sin[(\omega_1 + 2\omega_0)t + \phi_1 + 2\phi_0]\right] + \\
& \qquad J_2(A_0)J_3(A_1)\left[\sin[(3\omega_1 - 2\omega_0)t + 3\phi_1 - 2\phi_0] + \sin[(3\omega_1 + 2\omega_0)t + 3\phi_1 + 2\phi_0]\right] + \\
& \qquad J_4(A_0)J_1(A_1)\left[\sin[(\omega_1 - 4\omega_0)t + \phi_1 - 4\phi_0] + \sin[(\omega_1 + 4\omega_0)t + \phi_1 + 4\phi_0]\right] + \\
& \qquad J_4(A_0)J_3(A_1)\left[\sin[(3\omega_1 - 4\omega_0)t + 3\phi_1 - 4\phi_0] + \sin[(3\omega_1 + 4\omega_0)t + 3\phi_1 + 4\phi_0]\right] + ...\Big] + \\
& + I_{Y0Y1}2\Big[J_2(A_0)J_2(A_1)\left[\cos[(2\omega_0 - 2\omega_1)t + 2\phi_0 - 2\phi_1] + \cos[(2\omega_0 + 2\omega_1)t + 2\phi_0 + 2\phi_1]\right] + \\
& \qquad J_2(A_0)J_4(A_1)\left[\cos[(2\omega_0 - 4\omega_1)t + 2\phi_0 - 4\phi_1] + \cos[(2\omega_0 + 4\omega_1)t + 2\phi_0 + 4\phi_1]\right] + \\
& \qquad J_4(A_0)J_2(A_1)\left[\cos[(4\omega_0 - 2\omega_1)t + 4\phi_0 - 2\phi_1] + \cos[(4\omega_0 + 2\omega_1)t + 4\phi_0 + 2\phi_1]\right] + \\
& \qquad J_4(A_0)J_4(A_1)\left[\cos[(4\omega_0 - 4\omega_1)t + 4\phi_0 - 4\phi_1] + \cos[(4\omega_0 + 4\omega_1)t + 4\phi_0 + 4\phi_1]\right] + ...\Big].
\end{aligned}
\tag{5.24}
$$

[2] $\cos\theta\cos\varphi = [\cos(\theta - \varphi) + \cos(\theta + \varphi)]/2$,
$\sin\theta\sin\varphi = [\cos(\theta - \varphi) - \cos(\theta + \varphi)]/2$,
$\sin\theta\cos\varphi = [\sin(\theta + \varphi) + \sin(\theta - \varphi)]/2$.

Eq. (5.24) can be generalized to

$$I(t) = I_{dc} + 2\sum_{k=1}^{\infty} R_k \left[\alpha_k \cos(\Omega_k t) + \beta_k \sin(\Omega_k t)\right], \tag{5.25}$$

where Ω_k stands for the frequency (ω_0, ω_1, $2\omega_0$, $2\omega_1$, $\omega_0 - \omega_1$,...) and R_k for the intensities and the Bessel functions. α_k and β_k are, respectively, the coefficients of the cosinus and sinus expansion of each frequency term. For example, assuming $\phi_0 = 0$, the term associated to ω_0 will be described by the parameters $\Omega = \omega_0$; $R = I_{X0}J_1(A_0)$; $\alpha = 1$ and $\beta = 0$. The firsts 31 values for R_k and Ω_k for $\omega_0 = 50$ kHz and $\omega_1 = 60$ kHz are given in table 5.3. There are an infinite number of terms to sum in Eq. (5.25), but the higher-frequency terms (that are proportional to higher-index integer Bessel functions) are small if A_0 and A_1 are set to 2.4048. However, note from table 5.3, that there are many components with frequencies lower than 240 kHz that have significant amplitudes. This makes the detected time-dependent waveform very complicated.

It is possible to write Eq. (5.25) in vector notation:

$$I(t) = \mathbf{C}(t)^T \mathbf{A}, \tag{5.26}$$

with

$$\mathbf{C}(t)^T = \begin{pmatrix} 1 & \cos(\Omega_1 t) & \sin(\Omega_1 t) & \cos(\Omega_2 t) & \sin(\Omega_2 t) & \cos(\Omega_3 t) & \sin(\Omega_3 t) & \ldots \end{pmatrix}, \tag{5.27}$$

$$\mathbf{A}^T = \begin{pmatrix} I_{dc} & 2R_1\alpha_1 & 2R_1\beta_1 & 2R_2\alpha_2 & 2R_2\beta_2 & 2R_3\alpha_3 & 2R_3\beta_3 & \ldots \end{pmatrix}. \tag{5.28}$$

It is worth to remember that the objective here is to calculate the elements of the $\mathbf{A}$ vector (which are related to I_{X0}, I_{Y0}, etc) from the measured time-dependent intensity $I(t)$. The elements of the $\mathbf{C}(t)$ vector form a natural orthogonal basis set for the intensity. The following integration can be used to determine the elements of the $\mathbf{A}$ vector:

$$\int_0^T \mathbf{C}(t) I(t) dt = \left[\int_0^T \mathbf{C}(t)\mathbf{C}^T(t) dt\right] \mathbf{A} = \mathbf{K}\mathbf{A}, \tag{5.29}$$

where $\mathbf{K} = \int_0^T \mathbf{C}(t)\mathbf{C}^T(t)dt$. $\mathbf{K}$ is a diagonal matrix if the chosen period T is a complete number of cycles for both modulators 0 and 1. The vector $\mathbf{A}$ becomes:

$$A = \mathbf{K}^{-1} \int_0^T \mathbf{C}(t) I(t) dt. \tag{5.30}$$

In practice, since our digitized $I(t)$ consists of a long vector of points, we need to use a discrete version of Eq. (5.30) in order to determine I_{X0},I_{Y0},I_{X1}, I_{Y1},

k	Ω_k	Frequency[a] (kHz)	R_k	$J_x(A_0)J_y(A_1)$[b]
1	$\omega_0 - \omega_1$	10	$I_{X0X1}J_1(A_0)J_1(A_1)$	0.269
2	$2(\omega_0 - \omega_1)$	20	$I_{Y0Y1}J_2(A_0)J_2(A_1)$	0.187
3	$4\omega_0 - 3\omega_1$		$I_{Y0X1}J_4(A_0)J_3(A_1)$	0.013
4	$3\omega_0 - 2\omega_1$	30	$I_{X0Y1}J_3(A_0)J_2(A_1)$	0.084
5	$3(\omega_0 - \omega_1)$		$I_{X0X1}J_3(A_0)J_3(A_1)$	0.040
6	$2\omega_0 - \omega_1$	40	$I_{Y0X1}J_2(A_0)J_1(A_1)$	0.224
7	$4(\omega_0 - \omega_1)$		$I_{Y0Y1}J_4(A_0)J_4(A_1)$	0.004
8	ω_0	50	$I_{X0}J_1(A_0)$	0.519
9	ω_1	60	$I_{X1}J_1(A_1)$	0.519
10	$\omega_0 - 2\omega_1$	70	$I_{X0Y1}J_1(A_0)J_2(A_1)$	0.224
11	$2\omega_0 - 3\omega_1$	80	$I_{Y0X1}J_2(A_0)J_3(A_1)$	0.084
12	$4\omega_0 - 2\omega_1$		$I_{Y0Y1}J_4(A_0)J_2(A_1)$	0.027
13	$3\omega_0 - \omega_1$	90	$I_{X0X1}J_3(A_0)J_1(A_1)$	0.103
14	$3\omega_0 - 4\omega_1$		$I_{X0Y1}J_3(A_0)J_4(A_1)$	0.013
15	$2\omega_0$	100	$I_{Y0}J_2(A_0)$	0.423
16	$\omega_0 + \omega_1$	110	$I_{X0X1}J_1(A_0)J_1(A_1)$	0.269
17	$2\omega_1$	120	$I_{Y1}J_2(A_1)$	0.423
18	$\omega_0 - 3\omega_1$	130	$I_{X0X1}J_1(A_0)J_3(A_1)$	0.103
19	$4\omega_0 - \omega_1$	140	$I_{Y0X1}J_4(A_0)J_1(A_1)$	0.033
20	$2\omega_0 - 4\omega_1$		$I_{Y0Y1}J_2(A_0)J_4(A_1)$	0.027
21	$3\omega_0$	150	$I_{X0}J_3(A_0)$	0.199
22	$2\omega_0 + \omega_1$	160	$I_{Y0X1}J_2(A_0)J_1(A_1)$	0.224
23	$\omega_0 + 2\omega_1$	170	$I_{X0Y1}J_1(A_0)J_2(A_1)$	0.224
24	$3\omega_1$	180	$I_{X1}J_3(A_1)$	0.199
26	$\omega_0 - 4\omega_1$	190	$I_{X0Y1}J_1(A_0)J_2(A_1)$	0.033
27	$4\omega_0$	200	$I_{Y0}J_4(A_0)$	0.065
28	$3\omega_0 + \omega_1$	210	$I_{X0X1}J_3(A_0)J_1(A_1)$	0.103
29	$2(\omega_0 + \omega_1)$	220	$I_{Y0Y1}J_2(A_0)J_2(A_1)$	0.187
30	$\omega_0 + 3\omega_1$	230	$I_{X0X1}J_1(A_0)J_3(A_1)$	0.103
31	$4\omega_1$	240	$I_{Y1}J_4(A_1)$	0.065

[a]Assuming $\omega_0 = 50$ kHz and $\omega_1 = 60$ kHz.
[b]Assuming $A_0 = A_1 = 2.4048$. The x and y indices refer to the integer Bessel function indices in the R_k column.

Figure 5.3.: Firsts frequency components of the Fourier analysis of the Time-Dependent Intensity vector. Table reproduced from [119].

I_{X0X1}, I_{X0Y1}, I_{Y0X1} and I_{Y0Y1}. Given a digitized waveform **I** consisting in a vector of T elements, we can generate a basis matrix **C** that contains, at least, eight different frequencies Ω_k (one for each one of the coefficients to determine). This matrix **C** has dimension (0:2N, 0:T-1) where N is the number of frequencies incorporated into the analysis. The elements of this basis matrix are constructed as

$$\begin{aligned} &C_{0,i} = 1.0, \\ &C_{2k,i} = \cos(\Omega_k i \Delta t), \\ &C_{2k-1,i} = \sin(\Omega_k i \Delta t), \quad k = 1, ..., N; \quad i = 0, ..., T-1, \end{aligned} \tag{5.31}$$

where Δt is the inverse of the sampling rate used for digitizing the waveform and $T\Delta t$ is the total time captured by the waveform digitizer.

The matrix **K**, of dimension (0:2N, 0:2N), is calculated from **C**

$$\mathbf{K} = \mathbf{C}\mathbf{C}^T, \tag{5.32}$$

and in analogy with Eq. (5.30) the vector **A**, of dimension (0:2N), is calculated

$$\mathbf{A} = \mathbf{K}^{-1}\mathbf{C}\mathbf{I}, \tag{5.33}$$

whose elements are $A_0 = I_{dc}$; $A_{2k} = \bar{\alpha}_k$; $A_{2k-1} = \bar{\beta}_k$ $k = 1, ...N$. We have made the identifications $\bar{\alpha}_k \equiv R_k \alpha_k$ and $\bar{\beta}_k \equiv R_k \beta_k$ to keep a notation similar to Ref. [119].

The magnitude of each frequency component is given by $(\bar{\alpha}_k^2 + \bar{\beta}_k^2)^{1/2}$ and the sign of the component must be determined from the measured phase ϕ_m and the relative modulator phases ϕ_0 and ϕ_1 [119]. The measured phase can be calculated as $\phi_m = \arg(\bar{\alpha}_k + i\bar{\beta}_k)$ where the arg function is the principal value of the argument $\bar{\alpha}_k + i\bar{\beta}_k$ defined between π and $-\pi$.[3]

We usually use 12 frequencies for this Fourier integration ($N = 12$): ω_0 to determine I_{X0}, $2\omega_0$ to determine I_{Y0}, ω_1 to determine I_{X1}, $2\omega_1$ to determine I_{Y1}, $\omega_0 + \omega_1$ and $|\omega_0 - \omega_1|$ to independently determine I_{X0X1}, $\omega_0 + 2\omega_1$ and $|\omega_0 - 2\omega_1|$ to independently determine I_{X0Y1}, $2\omega_0 + \omega_1$ and $|2\omega_0 - \omega_1|$ to independently determine I_{Y0X1}, and $2\omega_0 + 2\omega_1$ and $|2\omega_0 - 2\omega_1|$ to independently determine I_{Y0Y1}. The value of each of the eight coefficients is determined with the following equations:

$$I_{X0} = \text{sign}\left[\sin(\phi_m + \phi_0)\right] \frac{(\bar{\alpha}^2 + \bar{\beta}^2)^{1/2}}{2J_1(A_0)}_{\Omega=\omega_0}, \tag{5.34a}$$

$$I_{Y0} = \text{sign}\left[\cos(\phi_m + \phi_0)\right] \frac{(\bar{\alpha}^2 + \bar{\beta}^2)^{1/2}}{2J_2(A_0)}_{\Omega=2\omega_0}, \tag{5.34b}$$

[3] In a computer program the measured phase can be calculated with the two-argument function atan2. In this case we use $\phi_m = \text{atan2}(\bar{\beta}_k, \bar{\alpha}_k)$.

$$I_{X1} = \text{sign}\left[\cos(\phi_m + \phi_1)\right] \frac{(\bar{\alpha}^2 + \bar{\beta}^2)^{1/2}}{2J_1(A_1)}_{\Omega=\omega_1}, \tag{5.34c}$$

$$I_{Y1} = \text{sign}\left[\cos(\phi_m + \phi_1)\right] \frac{(\bar{\alpha}^2 + \bar{\beta}^2)^{1/2}}{2J_2(A_1)}_{\Omega=2\omega_1}, \tag{5.34d}$$

$$\begin{aligned} I_{X0X1} = \text{sign}\left[\sin(\phi_m + \phi_0 + \phi_1)\right] \frac{(\bar{\alpha}^2 + \bar{\beta}^2)^{1/2}}{4J_1(A_0)J_1(A_1)}_{\Omega=\omega_0+\omega_1} + \\ + \text{sign}\left[\sin(\phi_m + \phi_0 - \phi_1)\right] \frac{(\bar{\alpha}^2 + \bar{\beta}^2)^{1/2}}{4J_1(A_0)J_1(A_1)}_{\Omega=\omega_0-\omega_1}, \end{aligned} \tag{5.34e}$$

$$\begin{aligned} I_{X0Y1} = \text{sign}\left[\sin(\phi_m + \phi_0 + 2\phi_1)\right] \frac{(\bar{\alpha}^2 + \bar{\beta}^2)^{1/2}}{4J_1(A_0)J_2(A_1)}_{\Omega=\omega_0+2\omega_1} + \\ + \text{sign}\left[\sin(\phi_m + \phi_0 - 2\phi_1)\right] \frac{(\bar{\alpha}^2 + \bar{\beta}^2)^{1/2}}{4J_1(A_0)J_2(A_1)}_{\Omega=\omega_0-2\omega_1}, \end{aligned} \tag{5.34f}$$

$$\begin{aligned} I_{Y0X1} = \text{sign}\left[\sin(\phi_m + 2\phi_0 + \phi_1)\right] \frac{(\bar{\alpha}^2 + \bar{\beta}^2)^{1/2}}{4J_2(A_0)J_1(A_1)}_{\Omega=2\omega_0+\omega_1} + \\ + \text{sign}\left[\sin(\phi_m + 2\phi_0 - \phi_1)\right] \frac{(\bar{\alpha}^2 + \bar{\beta}^2)^{1/2}}{4J_2(A_0)J_1(A_1)}_{\Omega=2\omega_0-\omega_1}, \end{aligned} \tag{5.34g}$$

$$\begin{aligned} I_{Y0Y1} = \text{sign}\left[\cos(\phi_m + 2\phi_0 + 2\phi_1)\right] \frac{(\bar{\alpha}^2 + \bar{\beta}^2)^{1/2}}{4J_2(A_0)J_2(A_1)}_{\Omega=2\omega_0+2\omega_1} + \\ + \text{sign}\left[\sin(\phi_m + 2\phi_0 - 2\phi_1)\right] \frac{(\bar{\alpha}^2 + \bar{\beta}^2)^{1/2}}{4J_2(A_0)J_2(A_1)}_{\Omega=2\omega_0-2\omega_1}, \end{aligned} \tag{5.34h}$$

Note that for the determination I_{X0X1}, I_{X0Y1}, I_{Y0X1} and I_{Y0Y1} we average the measurements of two different frequency components. Moreover we check that the values obtained of each one of this two frequencies matches (within the error limits) the value of its companion. This ensures that the acquisition program can precisely resolve every frequency component.

According to the description of the triggering circuit given in section 5.3.2, we start the digitization whenever the reference signals of the modulators are in phase. As a result, it would be reasonable for the reader to think that thanks to the triggering circuit the modulator phases ϕ_0 and ϕ_1 will close to zero. However this not the case, because them PEMs controllers put out a constant phase that adds to the own optical phase of the modulator acting like an offset. This translates in non vanishing, but constant, values of ϕ_0 and ϕ_1. ϕ_m, ϕ_0 and ϕ_1 are only used to measure the sign of the component of the **I** vector, and they do not need to be determined very accurately. The values of ϕ_0 and ϕ_1 are different for each PEM, and need to be determined. To do so one can use a sample with known

optical behavior, i.e. samples for which we know the sign of the components of **I** vector (e.g. a quarter waveplate and a polarizer) by recursively adjust the values ϕ_0 and ϕ_1 till a correct sign for all of the monitored frequency components is obtained.

5.6. Calibration

In other to measure with accuracy the eight parameters of the intensity (I_{X0}, I_{Y0}, etc) the 2-MGE needs to be calibrated. The calibration allows to determine all the characteristics of the PSG and the PSA, namely the angular orientation of each polarizer with respect to the longitudinal axis of its corresponding PEM (θ_{b0} and θ_{b1}), the control voltage needed to generate the PEM amplitudes such $A_0 = A_1 = 2.4048$ (for this amplitude $J_0(A_0) = J_0(A_1) = 0$), and the static strain-induced retardations δ_0 and δ_1 of each one of the PEMs.

The calibration is done in the straight-through configuration without any sample. In this configuration the detected light intensity is given by multiplying of the Stokes vector of the PSG [Eq. (5.8)] by Stokes vector of the PSA [Eq. (5.11)]:

$$I(t) = \mathbf{S}_{PSA}^T \mathbf{S}_{PSG}. \tag{5.35}$$

The result of this multiplication can be written using the basis vector notation as:

$$I(t) = \mathbf{B}_\delta^T \mathbf{I}, \tag{5.36}$$

where

$$\mathbf{B}_\delta(t)^T = \begin{pmatrix} 1 & X_{0\delta} & Y_{0\delta} & X_{1\delta} & Y_{1\delta} & X_{0\delta}X_{1\delta} & X_{0\delta}Y_{1\delta} & Y_{0\delta}X_{1\delta} & Y_{0\delta}Y_{1\delta} \end{pmatrix}, \tag{5.37}$$

$$\mathbf{I}^T = \begin{pmatrix} 1 & 0 & -2C_{m1}S_{m0}\varepsilon_{b1} & 0 & -2C_{m1}C_{m0}\varepsilon_{b0} & -1 & 0 & 0 & S_{m1}S_{m0} \end{pmatrix}. \tag{5.38}$$

Note that the subscript δ in Eq. (5.36) denotes that the static retardation of the modulators is being considered (compare for example to Eq. (5.20)).

According to Eqs. (5.17) the static strain treated at first order can be included

as follows:

$$\begin{pmatrix} 1 \\ X_{0\delta} \\ Y_{0\delta} \\ X_{1\delta} \\ Y_{1\delta} \\ X_{0\delta}X_{1\delta} \\ X_{0\delta}Y_{1\delta} \\ Y_{0\delta}X_{1\delta} \\ Y_{0\delta}Y_{1\delta} \end{pmatrix} \simeq \begin{pmatrix} 1 & 0 & 0 & 0 & 0 & 0 & 0 & 0 & 0 \\ 0 & 1 & \delta_0 & 0 & 0 & 0 & 0 & 0 & 0 \\ 0 & -\delta_0 & 1 & 0 & 0 & 0 & 0 & 0 & 0 \\ 0 & 0 & 0 & 1 & \delta_1 & 0 & 0 & 0 & 0 \\ 0 & 0 & 0 & -\delta_1 & 1 & 0 & 0 & 0 & 0 \\ 0 & 0 & 0 & 0 & 0 & 1 & \delta_1 & \delta_0 & 0 \\ 0 & 0 & 0 & 0 & 0 & -\delta_1 & 1 & 0 & \delta_0 \\ 0 & 0 & 0 & 0 & 0 & -\delta_0 & 0 & 1 & \delta_1 \\ 0 & 0 & 0 & 0 & 0 & 0 & -\delta_0 & -\delta_1 & 1 \end{pmatrix} \begin{pmatrix} 1 \\ X_0 \\ Y_0 \\ X_1 \\ Y_1 \\ X_0X_1 \\ X_0Y_1 \\ Y_0X_1 \\ Y_0Y_1 \end{pmatrix}. \tag{5.39}$$

In shorthand notation is

$$\mathbf{B}_\delta \simeq \boldsymbol{\delta}\mathbf{B}, \tag{5.40}$$

where $\boldsymbol{\delta}$ is called the strain matrix.

To include the effects of a non-zero $J_0(A_0)$ or $J_0(A_1)$ the basis elements Y_0 and Y_1 should be respectively replaced by $J_0(A_0) + Y_0$ and $J_0(A_1) + Y1$ (see Eqs. (5.22b) and (5.22d)), so that a better approximation to (5.40) can be written as

$$\mathbf{B}_\delta \cong \boldsymbol{\delta} \begin{pmatrix} 1 \\ X_0 \\ J_0(A_0) + Y_0 \\ X_1 \\ J_0(A_1) + Y_1 \\ X_0X_1 \\ X_0J_0(A_1) + X_0Y_1 \\ X_1J_0(A_0) + X_1Y_0 \\ J_0(A_0)Y1 + J_0(A_1)Y_0 + Y_0Y_1 \end{pmatrix}, \tag{5.41}$$

that written as a multiplication of matrices can be put in the form

$$\mathbf{B}_\delta \cong \boldsymbol{\delta}\mathbf{J}_0\mathbf{B}, \tag{5.42}$$

where the $\mathbf{J}_0$ matrix is:

$$\mathbf{J}_0 = \begin{pmatrix} 1 & 0 & 0 & 0 & 0 & 0 & 0 & 0 & 0 \\ 0 & 1 & 0 & 0 & 0 & 0 & 0 & 0 & 0 \\ J_0(A_0) & 0 & 1 & 0 & 0 & 0 & 0 & 0 & 0 \\ 0 & 0 & 0 & 1 & 0 & 0 & 0 & 0 & 0 \\ J_0(A_1) & 0 & 0 & 0 & 1 & 0 & 0 & 0 & 0 \\ 0 & 0 & 0 & 0 & 0 & 1 & 0 & 0 & 0 \\ 0 & J_0(A_1) & 0 & 0 & 0 & 0 & 1 & 0 & 0 \\ 0 & 0 & 0 & J_0(A_0) & 0 & 0 & 0 & 1 & 0 \\ 0 & 0 & J_0(A_1) & 0 & J_0(A_0) & 0 & 0 & 0 & 1 \end{pmatrix}. \quad (5.43)$$

By substituting Eq. (5.42) in Eq. (5.36) we get:

$$I(t) = [\boldsymbol{\delta}\mathbf{J}_0\mathbf{B}]^T\mathbf{I} = \mathbf{B}^T\mathbf{J}_0^T\boldsymbol{\delta}^T\mathbf{I}, \quad (5.44)$$

and from this it is deduced

$$\mathbf{I}_{calibration} = \mathbf{J}_0^T\boldsymbol{\delta}^T\mathbf{I}. \quad (5.45)$$

Once the static strain and the possible non zero values for $J_0(A_0)$ and $J_0(A_1)$ are considered, the intensity coefficients given in Eq.(5.38) become [120]:

$$I_{X0} = 0, \quad (5.46a)$$
$$I_{Y0} = J_0(A_1)\cos(2\theta_m) - 2\sin(2\theta_m)\varepsilon_{b1}, \quad (5.46b)$$
$$I_{X1} = 0, \quad (5.46c)$$
$$I_{Y1} = J_0(A_0)\cos(2\theta_m) + 2\sin(2\theta_m)\varepsilon_{b0}, \quad (5.46d)$$
$$I_{X0X1} = -1, \quad (5.46e)$$
$$I_{X0Y1} = -\delta_1 - \delta_0\cos(2\theta_m), \quad (5.46f)$$
$$I_{Y0X1} = -\delta_0 - \delta_1\cos(2\theta_m), \quad (5.46g)$$
$$I_{Y0Y1} = \cos 2\theta_m, \quad (5.46h)$$

where θ_m is the angle of the PSG with respect to the PSA ($\theta_m = \theta_{m0} - \theta_{m1}$. With the exception of I_{X0X1} and I_{Y0Y1} if the system is well calibrated, the other coefficients of Eq.(5.46) are close to zero.

Equations (5.46) are used to identify the three basic calibration parameters of each PEM: the error in the polarizer angle with respect to the 45° ε_{bi}, the Bessel angle A_i and the static strain $\delta_i(\lambda)$. If we first align parallel the PEMs [$\cos(2\theta_m) = 1$ and $\sin(2\theta_m) = 0$] we get that I_{Y0} measures $J_0(A_1)$, while I_{Y1} measures $J_0(A_0)$. The objective of this first step of the calibration is to determine the control voltage as a function of the wavelength $V_{mi}(\lambda)$ required for setting

$A_i = 2.4048$ and thus to make $I_{Y0} = I_{Y1} = 0$. Assuming that we know with anticipation the approximate voltage that makes $A \sim 2.4$, the automatic procedure to precisely find the desired control voltage is based on measuring at different wavelengths the values of I_{Y0} and I_{Y1} while applying different control voltages slightly deviated from our initial guess. For each wavelength the dispersion of I_{Y0} and I_{Y1} values with respect to the applied voltage is linearly fit, and, from here, we get for every wavelength the voltages[4] V_{m1} and V_{m0} that respectively make $J_0(A_0)$ and $J_0(A_1)$ zero.

The second step of the calibration takes place with the PEMs aligned at $\pm 45°$ with respect to one another [$\cos(2\theta_m) = 0$]. In this configuration the coefficients I_{Y0} and I_{Y1} respectively measure ε_{b1} and ε_{b0} and I_{X0Y1} and I_{Y0X1} respectively measure δ_1 and δ_0. Also the coefficient I_{Y0Y1} can be used to get a precise adjustment in the azimuthal alignment of the two PEMs (this coefficient should vanish if they are oriented at $\pm 45°$). The overall, frequency-independent, gain can be measured with the coefficient I_{X0X1} because this term should be -1 for any value of θ_m. Note that while δ_i and V_{mi} are expected to change with λ, the overall gain and ε_{bi} will approximately remain constant and we can average values taken at different wavelengths.

The relation between the Bessel angle A and the modulator control voltage V_m exhibits dispersion with photon energy or wavelength λ and is of the form [131]:

$$V_{mi}(\lambda) = \frac{K_i A_i \lambda}{\sum_{k=0}^{\infty} \alpha_{ki}/\lambda^{2k}}, \tag{5.47}$$

where K_i is a constant and α_{ki} are coefficients to be determined by the calibration. The static strain is a similar function of wavelength due to the dispersion of fused quartz and is given by [131]

$$\delta_i(\lambda) = \lambda \sum_{k=0}^{\infty} \beta_{ki}/\lambda^{2k}, \tag{5.48}$$

β_{ki} are coefficients to be determined. The spectroscopic values of V_{mi} and δ_i obtained in the calibration are respectively fitted using Eqs. (5.47) and (5.48).

Fig. 5.4 shows the control voltage calibrations V_{m0} and V_{m1} and the measured static strains δ_0 and δ_1 as a function of wavelength. The fitting has been done using Eqs. (5.47) and (5.48) using four parameters for V_{mi} and three parameters for δ_i. For comparison purposes we have also included in the graphs the dispersion curves we obtained for the calibration of one "old" PEM that had been previously

[4]The voltages V_{m1} and V_{m0} that make $J_0(A_0)$ and $J_0(A_1)$ vanish will be sometimes referred in this work as *Bessel voltages*.

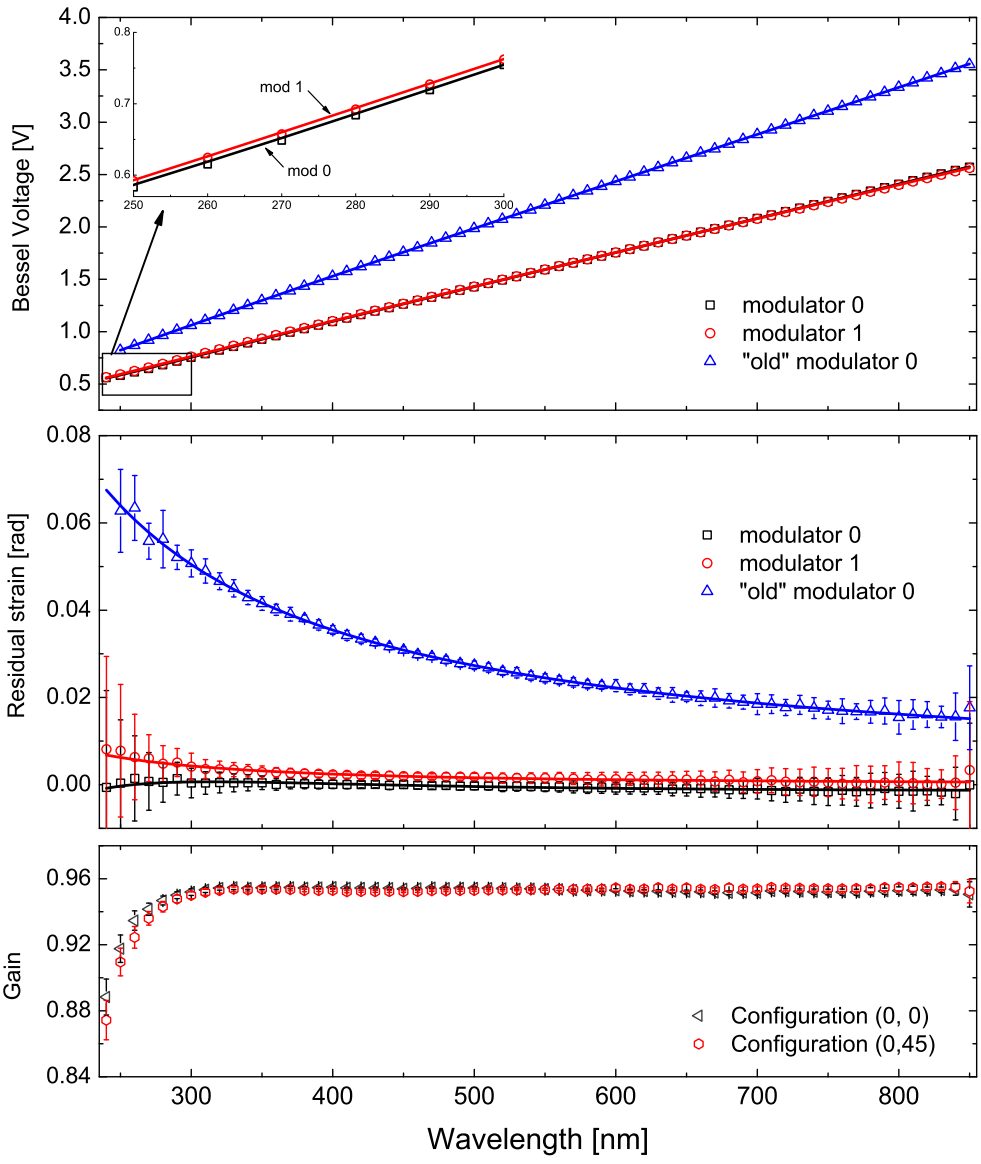

Figure 5.4.: Calibration data for the PEMS used in the 2-MGE. Top panel, the modulator control voltage V_{m0} and V_{m1} required to give $A_0 = A_1 = 2.4048$ where the solid lines represent the fits to the data using Eq. (5.47). The Bessel voltage calibration of an old PEM previously used in our 2-MGE has been added for comparison purposes. Middle panel, static strain of each modulator as a function of wavelength, where the solid curves indicate the fits to the data by using Eq. (5.48). Bottom panel, the overall gain factor for measured at two different orientations of the PSG and the PSA.

used in the instrument as "modulator 0" (it has a resonant frequency $\sim$ 50 kHz). This PEM, also from Hinds Instruments, is more than 15 years old and, remarkably, needs a considerably greater Bessel voltage than the "new" ones (the current PEMs where both purchased during the development of this thesis). The higher inconvenient of this old PEM is the significant amount of static strain it exhibits when compared to new devices (see middle panel of Fig. 5.4). We do not have a clear evidence whether these differences emerge due to a time degradation of the characteristics of the PEM (probably coming from a degradation of the cementing of the optical element with the piezoelectric transducer) or, simply, respond to an improvement in the standards of fabrication of PEMs.

In addition to the overall frequency-independent gain factor that is determined with the calibration, there are additional particular gain factors for every frequency component that plays a role in the determination of the intensity vector. They are all caused by the limited bandwidth of the preamplifier for high frequencies (e.g. the frequency component at 220 kHz has a greater attenuation than the one at 20 kHz) and can be easily calculated if the performance characteristics (bandwidth and roll-off) of the preamplifier are known. These characteristics can be deduced by comparing different frequency components related to the same coefficient of the $\mathbf{I}$ vector (for example, both, the $\sim$ 20 kHz and $\sim$ 220 kHz components should give the same values for the coefficient I_{Y0Y1}). For the preamplifier used in our 2-MGE the particular attenuation factors of each frequency component are calculated with the following roll-off curve:

$$A(\nu) = \frac{1}{(\nu/\nu_0)^2 + 1}, \tag{5.49}$$

where $\nu_0 = 356$ kHz. The attenuation is small for the lower frequency components, but it grows significatively for the higher frequencies of interest. For example, $A(20\text{ kHz}) = 0.997$ and $A(220\text{ kHz}) = 0.724$.

The calibration procedure completely characterizes the PSG and PSA and it needs to be performed periodically to make measurements with high accuracy. The calibration process is automatized, so that a complete spectroscopic calibration routine that uses two different orientations of the PSG with respect to the PSA (a parallel or perpendicular orientation to find V_{mi} and a $\pm 45°$ orientation to find δ_i and ε_{bi}) is done in about 10 min. Fig. 5.4 shows some of the data obtained after a calibration routine and which are also presented in real time during the calibration (see the screenshots shown in appendix B). In addition to the parameters displayed in this figure, the calibration routine also allows us to obtain the values of ε_{bi}, as well as, the residual errors in the alignment of the PEMs [120, 135].

Calibration in a 2-MGE is actually easier and probably more reliable than

in a ellipsometers using a single photoelastic modulator because, as shown in Eqs. (5.46) the measured intensity coefficients, for a particular orientation of the PSG and the PSA, depend only on one calibration parameter. For example, for aligned PEMs I_{Y0} and I_{Y1} directly are $J_0(A_1)$ and $J_0(A_0)$, and thus we have a very sensitive method for measuring the deviation of A_i from 2.4048 that is not available in single PEM instruments.

5.6.1. Using the calibration results into the measurement

To simplify the algebra in several calculations of section 5.5 it was considered that $\delta_0 = \delta_1 = \varepsilon_{b0} = \varepsilon_{b1} = J_0(A_0) = J_0(A_1) = 0$. The calibration made in this section has allowed us to minimize ε_{b0}, ε_{b1}, $J_0(A_0)$ and $J_0(A_1)$ and it is reasonably safe to assume that they are zero. However, although we have spectroscopically determined the static retardations of the modulators, δ_0 and δ_1, we cannot physically remove these strains and they need to be considered in the calculations.

The strain matrix $\boldsymbol{\delta}$ introduced in Eqs. (5.39) and (5.40) can be used to include the effect of a nonzero δ_0 and δ_1 in the coefficients of the $\mathbf{I}$ vector [that were given in Eq. (5.14)]:

$$I_\delta(t) = \boldsymbol{\delta}^T \mathbf{I}, \tag{5.50}$$

so that, including the effect of the static strains, Eqs. (5.14) transform to:

$$\begin{aligned}
I_{dc} =& 1,\\
I_{X0} =& m_{03} + (m_{02}C_{m0} - m_{01}S_{m0})\delta_0,\\
I_{Y0} =& -C_{m0}m_{02} + S_{m0}m_{01},\\
I_{X1} =& -m_{30} + (m_{20}C_{m1} - m_{10}S_{m1})\delta_1,\\
I_{Y1} =& -C_{m1}m_{20} + S_{m1}m_{10},\\
I_{X0X1} =& -m_{33} + (m_{31}S_{m0} - m_{32}C_{m0})\delta_0 + (-m_{13}S_{m1} + m_{23}C_{m1})\delta_1,\\
I_{X0Y1} =& S_{m1}m_{13} - C_{m1}m_{23}\\
&+ (m_{12}S_{m1}C_{m0} - m_{22}C_{m1}C_{m0} + m_{21}C_{m1}S_{m0} - m_{11}S_{m1}S_{m0})\delta_0 - \delta_1 m_{33},\\
I_{Y0X1} =& -S_{m0}m_{31} + C_{m0}m_{32}\\
&+ (m_{12}S_{m1}C_{m0} - m_{22}C_{m1}C_{m0} + m_{21}C_{m1}S_{m0} - m_{11}S_{m1}S_{m0})\delta_0 - \delta_0 m_{33},\\
I_{Y0Y1} =& C_{m0}C_{m1}m_{22} - S_{m0}C_{m1}m_{21} - C_{m0}S_{m1}m_{12} + S_{m0}S_{m1}m_{11}\\
&+ (m_{32}C_{m0} - m_{31}S_{m0})\delta_1 + (m_{13}S_{m1} - m_{23}C_{m1})\delta_0).
\end{aligned} \tag{5.51}$$

Chapter 6.

Quartz-assisted two-modulator generalized ellipsometer

The idea of complementing the 2-MGE setup by adding a quartz plate in each arm of the instrument started with the purpose of increasing the number of elements of the sample Mueller matrix measured without changing the azimuthal orientations of the PSG and the PSA. This was a requirement to do spatially resolved measurements based on the determination of the Mueller matrix.

6.1. Introduction

Due to the imperfect alignment of the optical components that form the PSG and the PSA, the light beam is not fully perpendicular to their surfaces. There will be a small, but usually non negligible, angle of incidence for light upcoming these optical elements (e.g. the polarizers and the PEMs). For example, if we consider, as a rough estimation, that the PSG is a single optical element of SiO_2 with a thickness of 50mm (the thickness of the PEM's optical bar plus the polarizer is usually above this thickness), for a misalignment of 1° the Snell's law indicates that the exiting beam of the PSG will be laterally displaced by about 0.6 mm from the entering beam. This situation is referred as *beam translation*, and has been already described as a problem for imaging ellipsometers involving moving parts [136]. If the azimuthal rotation of the entire PSG is considered one might also take into account that the axis of rotation might not be perfectly parallel to the light beam nor with the surfaces normal. All this leads to deviations in the light beam that translate in small, but noticeable, differences in the spotted area of the sample. For the PSA the problem may be less dramatic if the elements that collect the light after the PSA cover are not too small, but, still, can cause that only fractions of the light probe would be analyzed.

In general these drawbacks do not represent a major problem if a complete measurement of the Mueller matrix is not required (i.e. when only one measurement configuration is used) or if the sample surface is homogeneous enough in reasonably big domains as often happens with thin films. However, it is not com-

patible with samples that require measurements of the complete Mueller matrix with a certain lateral resolution. Over the years, several different instruments have been proposed or build to measure complete Mueller matrices [75, 137–144]; however, Mueller polarimeters are not instruments of mainstream use and their presence in laboratories is still uncommon. In these instruments polarization modulation and analysis is commonly achieved used rotating compensators or liquid crystals with variable retardation. To perform spatially resolved measurements, instruments based on liquid crystals are adequate because they do not have moving parts and are compatible with CCD detectors [145]. However, the optical quality of liquid crystal based modulators is lower than the one offered by PEMs [146], and, in general, these instruments do not reach the level of accuracy and sensitivity of PEM-based polarimeters.

In this chapter we describe an alternative technique to measure transmission or reflection Mueller matrices with a 2-MGE based on the use of thin crystal slabs with rotatory power (e.g. plates of quartz) as a substitute of the mechanical rotator used to orientate the PSG and the PSA. This technique will be referred in this work as *quartz-assisted two-modulator generalized ellipsometry* or *quartz-assisted 2-MGE*, and will be described in detail in this chapter. Nevertheless, its principle of operation includes most of the contents introduced in the previous chapter and, so, this chapter should not be studied independently.

The use of crystals with rotatory power for laser applications is quite common and, in fact, one can find available crystals in the marked[1] cut such to provide a specific amount of rotation for characteristic laser wavelengths. However this optical rotation of the polarization has not been exploited in polarimeters or ellipsometers. The closest reference that we have found related to this subject is a paper by Azzam [147] which describes, but only from a theoretical point of view, the simulation of mechanical rotation by optical rotation and the possible application to a Fourier photopolarimeter (an instrument to measure the Stokes vector of a radiation). To our knowledge, we present here the first experimental realization of a polarimeter that makes use of optical rotation as a substitutive of mechanical rotation.

Previously we had made an attempt to address this problem with a different approach. This previous method consisted on adding one waveplate, tuned to the wavelength of measurement, in both arms of the instrument [148]. In that case the objective of the introduction of waveplates was not to measure more elements of the Mueller matrix (8 elements were still measured), but to strategically select the particular 8 Mueller matrix elements that we wanted to measure instead of being restricted to one of the schemes presented in Eqs. (5.15). Some

[1] They are usually made of quartz and sold under the name "quartz rotators".

results were obtained by this method and they will be reviewed in section 9.2, however we will not give here more details about this method as we consider that the one we present in this section deals with the same experimental problem and is fairly superior. Quartz plates have the advantage that their induced polarization rotation is usually less sensitive to the alignment that retardation of the waveplates.

6.2. Description of the quartz-assisted 2-MGE

The quartz-assisted 2-MGE is similar to the 2-MGE described in the previous chapter, the basic difference consist on the addition of two quartz plates in the setup: one between the PSG and the sample (quartz 0) and the other between the sample and the PSA (quartz 1). Thus, light passes through a plate just before and just after the sample. We use polished z-cut (optical axis perpendicular to the surface) quartz (α-SiO_2) plates. For this type of cut and for light at normal incidence a uniaxial birefringent material such as quartz appears to be isotropic and the only optical effect which introduces is the optical rotation [149]. In our system the quartz plates are mounted in two filter wheels (Thorlabs FW102B) conveniently placed after the PSG and before the PSA, as it is shown in Fig. 6.1. In practice, the filter wheels are used to easily reach any of the following 4 possible configurations which are essential for the method of measurement:

- Configuration I. PSG / Sample / PSA,
- Configuration II. PSG / Quartz 0 / Sample / PSA,
- Configuration III. PSG / Sample / Quartz 1 / PSA,
- Configuration IV. PSG / Quartz 0 / Sample / Quartz 1 / PSA.

Filter wheels allow a fast switch between the different configurations. In contrast to the 2-MGE described in the previous chapter, here, the mechanical rotators devoted to change the azimuthal positions of the PSG and the PSA are not needed for the measurement of the Mueller matrix. However, if they are present, they are still useful for the PEM alignment and to calibrate the static strain of the PEMs as it will be shown later in this chapter.

An important attribute of the quartz plates is their thickness. They must be thin enough to not introduce any appreciable beam translation, even if they are not perfectly aligned perpendicular to the beam. According to the Snell's law the beam translation caused by the introduction of a 1 mm thick quartz plate with an angle of incidence of 1° is around 12 μm. It is worth to note that individual

small quartz plates are easier to align with respect to the light beam that the entire PSG or PSA so angles of incidence $< 1^\circ$ are not difficult to obtain.

The main difficulty arising from the addition of the quartz plates starts from the fact that the measured Mueller matrix contains contributions from all the optical elements between the PSG and the PSA. In this case, this includes the sample (the element to be characterized) and the two quartz plates. Therefore, for a successful measurement of the sample's Mueller matrix, the contribution of the two quartz plates must be carefully determined with the calibration process that will be detailed later in this chapter.

One of the main applications of the quartz-assisted 2-MGE is to obtain spatially resolved Mueller matrix measurements of the sample. In our instrument the optical resolution of the spatially resolved measurements is mainly given by the diameter of the probe beam that illuminate the sample. This diameter can vary greatly from one ellipsometer to another since ellipsometers use either collimated or focused beams. In the case of collimated beams diameters around ~ 5 mm are usual, while for the case of focused beams the diameters can be below 100 μm.

The focusing elements of a polarimeter can be placed inside the space delimited by the PSG and PSA or can be external, i.e. with the elements placed in front of the PSG and behind the PSA. In the case of internal focusing elements it is possible to use lenses with short focal lengths that facilitate a high local resolution but increases the polarization aberration. In this configuration the birefringence of the lenses affects the measurements although, in some cases, it can be corrected [150]. When the focusing elements are external the anisotropies of these elements do not influence the ellipsometric result. These setups usually require comparatively long focal lengths of the optical elements, so that a beam with small divergence hits the sample but, in this case, the lateral resolution is often reduced with respect to the case of internal focusing elements. Our instrument uses external focusing elements (a mirror-based Jobin-Yvon system, see table 5.1) that allows three beam spot sizes being ~ 1 mm the bigger one and ~ 90 μm the smaller one. For this system reducing the spot results in less light intensity reaching the detector, so the resultant signal-to-noise ratio is worse when compared to measurements with a bigger spot.

The sample is placed in a automated precision x−y stage (see Fig. 6.1) that allows to map the sample by taking successive measurements of the Mueller matrix while the sample is moved to different positions. For spatially resolved measurements the instrument operates at a single wavelength, that is resolved by the monochromator. To increase the signal-to-noise ratio in these kind of measurements the monochromator could be substituted by an interference filter and the strong emission lines of a mercury arc lamp could be used as a light source.

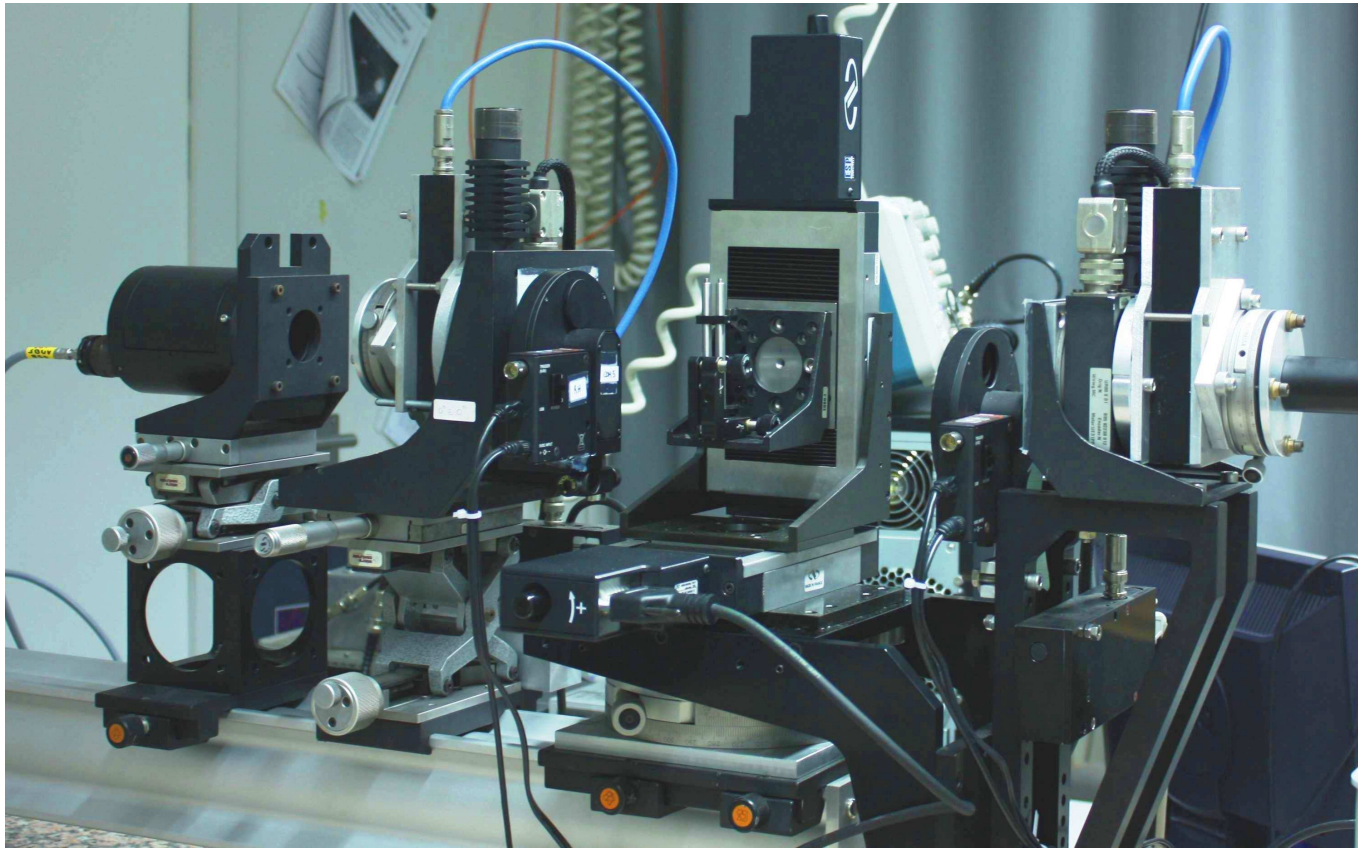

Figure 6.1.: Photography of the 2-MGE built during this thesis. From left to right the picture shows an optical fiber attached to the focusing optics module, and it is followed by the first polarizer-PEM pair mounted in a mechanical rotation stage (PEMs are easily identifiable by the blue cables). The sample appears in the center of the photo, mounted on a x−y automatic translation stage. The elements just before and after the sample are filter wheels containing z-cut quartz rotators. After the second filter wheels comes the second PEM-polarizer pair, also attached to a mechanical rotation stage. Finally light is collected by another optical fiber (not shown in the picture) that guides it to the monochromator.

6.3. Effect of quartz plates in the measurement

A quartz plate can be described in terms of the Mueller matrix of a retarder [Eq. (3.24)]:

$$\mathbf{M}_Q = \begin{pmatrix} 1 & 0 & 0 & 0 \\ 0 & \cos \mathrm{T}_R + \mathrm{LB}^2\alpha & \mathrm{LBLB}'\alpha + \mathrm{CB}\beta & -\mathrm{LBCB}\alpha + \mathrm{LB}'\beta \\ 0 & \mathrm{LBLB}'\alpha - \mathrm{CB}\beta & \cos \mathrm{T}_R + \mathrm{LB}'^2\alpha & -\mathrm{LB}'\mathrm{CB}\alpha - \mathrm{LB}\beta \\ 0 & -\mathrm{LBCB}\alpha - \mathrm{LB}'\beta & -\mathrm{LB}'\mathrm{CB}\alpha + \mathrm{LB}\beta & \cos \mathrm{T}_R + \mathrm{CB}^2\alpha \end{pmatrix}, \tag{6.1}$$

with $\alpha = (1 - \cos \mathrm{T}_R)/\mathrm{T}_R^2$, $\beta = \sin \mathrm{T}_R/\mathrm{T}_R$ and $\mathrm{T}_R = \sqrt{\mathrm{LB}^2 + \mathrm{LB}'^2 + \mathrm{CB}^2}$. For a z-cut plate, if the incident beam is parallel to the optical axis it behaves as an isotropic sample and no longer exhibits linear birefringence ($\mathrm{LB} = \mathrm{LB}' = 0$). But, in general, it may be not possible to have a perfect alignment between the optic axis and the light beam so we assume that they are small ($\mathrm{LB}, \mathrm{LB}' \ll \mathrm{CB}$). The effect of these small birefringences is assimilable to the case of ellipsometry with strained windows (see for example Ref. [150]). For a good orientation of the plates is easy to keep LB and LB′ below the ~ 0.02 rad range, and so we can consider them only to first order; then $\mathrm{T}_R = \mathrm{CB}$ and Eq. (6.1) becomes:

$$\mathbf{M}_Q = \begin{pmatrix} 1 & 0 & 0 & 0 \\ 0 & \cos \mathrm{CB} & \sin \mathrm{CB} & A_3 \\ 0 & -\sin \mathrm{CB} & \cos \mathrm{CB} & A_4 \\ 0 & A_1 & A_2 & 1 \end{pmatrix}, \tag{6.2}$$

where

$$A_1 = -\mathrm{LB}\frac{(1 - \cos \mathrm{CB})}{\mathrm{CB}} - \mathrm{LB}'\frac{\sin \mathrm{CB}}{\mathrm{CB}}, \tag{6.3a}$$

$$A_2 = -\mathrm{LB}'\frac{(1 - \cos \mathrm{CB})}{\mathrm{CB}} + \mathrm{LB}\frac{\sin \mathrm{CB}}{\mathrm{CB}}, \tag{6.3b}$$

$$A_3 = -\mathrm{LB}\frac{(1 - \cos \mathrm{CB})}{\mathrm{CB}} + \mathrm{LB}'\frac{\sin \mathrm{CB}}{\mathrm{CB}}, \tag{6.3c}$$

$$A_4 = -\mathrm{LB}'\frac{(1 - \cos \mathrm{CB})}{\mathrm{CB}} - \mathrm{LB}\frac{\sin \mathrm{CB}}{\mathrm{CB}}. \tag{6.3d}$$

A_1, A_2, A_3, A_4 are not independent, for example:

$$A_1 = A_4 \frac{1}{\sin \mathrm{CB}} + A_2 \frac{\cos \mathrm{CB}}{\sin \mathrm{CB}}, \tag{6.4a}$$

$$A_3 = -A_4 \frac{\cos \mathrm{CB}}{\sin \mathrm{CB}} - A_2 \frac{1}{\sin \mathrm{CB}}. \tag{6.4b}$$

The CB (which is twice the optical rotation, ρ) of each plate can be adjusted to the following dispersion relation [21, 151]:

$$\mathrm{CB} = \frac{m\lambda^2}{(\lambda^2 - \lambda_0^2)^2}, \tag{6.5}$$

where m and λ_0 are parameters that are determined through the calibration.

For each of the four configurations described in the previous section, the Mueller matrix $\mathbf{M}_T$ that describes the optical elements between the PSG and the PSA is:

- Configuration I
$$\mathbf{M}_T = \mathbf{M}, \tag{6.6a}$$
- Configuration II
$$\mathbf{M}_T = \mathbf{M}\mathbf{M}_{Q,0}, \tag{6.6b}$$
- Configuration III
$$\mathbf{M}_T = \mathbf{M}_{Q,1}\mathbf{M}, \tag{6.6c}$$
- Configuration IV.
$$\mathbf{M}_T = \mathbf{M}_{Q,1}\mathbf{M}\mathbf{M}_{Q,0}, \tag{6.6d}$$

where $\mathbf{M}$ is given in Eq. (1.26) and $\mathbf{M}_{Q,i}$, with $i = 0, 1$ to respectively refer to the first and second quartz plates, is given in Eq. (6.2). The results of these matrix multiplications are too large to be explicitly written here but they are the basic calculations to study the effect introduced by the quartz plates on the measurement.

Our measurement procedure uses fixed position for the PSG and PSA ($\theta_{m0} = 0^\circ$ $\theta_{m1} = 0^\circ$) that corresponds to the situation in which the modulation axis of the two modulators are parallel to the primary reference frame. All the calculations of this section are referred to this orientation. The choice of this particular orientation among all the cases given in section 5.4 is partially arbitrary: any of the cases in which the modulation axis of the PEMs are aligned parallel or perpendicular would be equally suitable; however, the cases where the PEMs are aligned at $\pm 45^\circ$ with respect one to another would be less suitable because these positions are incompatible with a complete calibration.

According to Eq. (5.15d) in configuration I the sample's Mueller matrix elements m_{02}, m_{03}, m_{20}, m_{22}, m_{23}, m_{30}, m_{32} and m_{33} can be measured. Configuration II permits to measure m_{01}, m_{21} and m_{31}. With configuration III m_{10}, m_{12} and m_{13} are determined. The remaining element, m_{11}, is accessible in configuration IV. In summary:

$$\mathbf{M} = \begin{pmatrix} 1 & m_{01,II} & m_{02,I} & m_{03,I} \\ m_{10,III} & m_{11,IV} & m_{12,III} & m_{13,III} \\ m_{20,I} & m_{21,II} & m_{22,I} & m_{23,I} \\ m_{30,I} & m_{31,II} & m_{32,I} & m_{33,I} \end{pmatrix}. \tag{6.7}$$

The matrix elements corresponding to configuration I are directly found from the coefficients of the intensity vector as shown in Eq. (5.15d). The expansion of the matrix multiplications shown in Eqs. (6.6) allows us to find that the remaining elements can be found with following relations:

$$m_{01,II} = -\left[I_{Y0,II} + A_{2,0} m_{03,I} + m_{02,I}\cos(\mathrm{CB}_0)\right]\sin^{-1}(\mathrm{CB}_0), \tag{6.8a}$$

$$m_{21,II} = \left[I_{Y0Y1,II} - A_{2,0} m_{23,I} - m_{22,I}\cos(\mathrm{CB}_0)\right]\sin^{-1}(\mathrm{CB}_0), \tag{6.8b}$$

$$m_{31,II} = \left[I_{Y0X1,II} - A_{2,0} m_{33,I} - m_{32,I}\cos(\mathrm{CB}_0)\right]\sin^{-1}(\mathrm{CB}_0), \tag{6.8c}$$

$$m_{10,III} = \left[I_{Y1,III} + A_{4,1} m_{30,I} + m_{20,I}\cos(\mathrm{CB}_1)\right]\sin^{-1}(\mathrm{CB}_1), \tag{6.8d}$$

$$m_{12,III} = \left[-I_{Y0Y1,III} + A_{4,1} m_{32,I} + m_{22,I}\cos(\mathrm{CB}_1)\right]\sin^{-1}(\mathrm{CB}_1), \tag{6.8e}$$

$$m_{13,III} = \left[I_{X0Y1,III} + A_{4,1} m_{33,I} + m_{23,I}\cos(\mathrm{CB}_1)\right]\sin^{-1}(\mathrm{CB}_1), \tag{6.8f}$$

$$\begin{aligned} m_{11,IV} = -\Big[& I_{Y0Y1,IV} - A_{2,0}\left[m_{23,I}\cos(\mathrm{CB}_1) - m_{13,III}\sin\mathrm{CB}_1\right] \\ & - \cos(\mathrm{CB}_0)\left[m_{22,I}\cos(\mathrm{CB}_1) - m_{12,III}\sin(\mathrm{CB}_1) + A_{4,1} m_{32,I}\right] \\ & - \sin(\mathrm{CB}_0)\left[m_{21,II}\cos(\mathrm{CB}_1) + A_{4,1} m_{31,II}\right]\Big]\sin^{-1}(\mathrm{CB}_0)\sin^{-1}(\mathrm{CB}_1). \end{aligned} \tag{6.8g}$$

CB_0, CB_1, $A_{2,0}$ and $A_{4,1}$ are the wavelength-dependent parameters associated to the quartz plates that play a role in measurement of the complete Mueller matrix for a (0°, 0°) orientation of the PSG and PSA . Their values need to be determined during the calibration. Using configurations II, III and IV many elements of the Mueller matrix could be over determined, similarly to what happens with the azimuthal rotation of the PEMs; however, in this work, we have assumed that the configuration that do not uses the quartz rotator (configuration I) is the most reliable one. The remaining ones are only used to determine Mueller matrix elements that cannot be measured in configuration I.

6.4. Calibration

The calibration in the quartz-assisted 2-MGE involves the determination of all the characteristics associated to a standard 2-MGE (most notably the Bessel voltages to make $J_0(A_0) = J_0(A_1) = 0$ and the modulator's static strain δ_0 and δ_1, see section 5.6) as well as the characteristic parameters of the quartz plates CB_0, CB_1, $A_{2,0}$ and $A_{4,1}$.

Table 6.1 shows the light intensity coefficients when the ellipsometer is aligned in the straight-through configuration without sample and with the modulation axis of the two modulators aligned parallel ($\theta_{m0} = \theta_{m1} = 0°$) for the 4 configurations described in section 6.2. Configuration I permits to measure values of $J_0(A_1)$ and $J_0(A_0)$ and it used to determine the control voltage required for setting $A_i = 2.4048$ (for more details see section 5.6 and in particular Eqs. (5.46)). Once this voltage has been found the configurations II and III are set to respectively determine $\cos(\mathrm{CB}_0)$ and $\cos(\mathrm{CB}_1)$ through the coefficient I_{Y0Y1}. From this measurement the values of $\sin(\mathrm{CB}_0)$ and $\sin(\mathrm{CB}_1)$ can also be inferred.

The linear retardation parameters of the quartz plates that interfere the measurement (i.e. $A_{2,0}$ and $A_{4,1}$), appear mixed together with the static retardation of the PEMs in the coefficients I_{X0Y1} and I_{Y0X1} (see the last three columns of table 6.1). The easier way to separate and quantify the linear retardation contributions of the modulators and the quartz plates is to align the PEMs at $\pm 45°$ with respect to one another. This is the case described in section 5.6, where I_{X0Y1} and I_{Y0X1} become, respectively, a direct measurement of PEM strains. Once δ_0 and δ_1 are known, the coefficients I_{X0Y1} and I_{Y0X1} of configuration II allow to measure $A_{2,0}$ and $A_{4,0}$, and the same parameters in configuration III permit to measure $A_{2,1}$ and $A_{4,1}$. In table 6.1 it is shown that $\cos(\mathrm{CB}_0)$ and $\cos(\mathrm{CB}_1)$ can be respectively obtained from configuration II and configuration III. Note that with this approach configuration IV is not required for the calibration.

An alternative calibration procedure would be desirable in case of an instrument without azimuthal rotators attached to the PSG and PSA, i.e. an eventual commercial instrument with fixed PSG and PSA at (0°, 0°). In this case it is possible to construct the following system of equations:

$$
\begin{aligned}
&-\delta_1 - \delta_0 = I_{X0Y1,I},\\
&-A_{4,0} - \delta_1 - \delta_0 \cos(\mathrm{CB}_0) = I_{X0Y1,II},\\
&A_{2,1} - \delta_0 - \delta_1 \cos(\mathrm{CB}_0) = I_{Y0X1,II},\\
&-A_{4,1} - \delta_1 - \delta_0 \cos(\mathrm{CB}_1) = I_{X0Y1,III},\\
&A_{2,1} - \delta_0 - \delta_1 \cos(\mathrm{CB}_1) = I_{Y0X1,III},\\
&-\nu - \delta_1 - \delta_0 \Xi_3 = I_{X0Y1,IV},\\
&\mu - \delta_0 - \delta_1 \Xi_3 = I_{Y0X1,IV},
\end{aligned}
\tag{6.9}
$$

Table 6.1.: Intensity coefficients for different calibration configurations[a]

Coeff.	Config. I	Config. II	Config. III	Config. IV
I_{X0}	0	0	0	0
I_{Y0}	$J_0(A_1)$	$2\varepsilon_{b1}\sin(\mathrm{CB}_0)$	$2\varepsilon_{b1}\sin(\mathrm{CB}_1)$	$2\varepsilon_{b1}\Xi_1$
I_{X1}	0	0	0	0
I_{Y1}	$J_0(A_0)$	$-2\varepsilon_{b0}\sin(\mathrm{CB}_0)$	$-2\varepsilon_{b0}\sin(\mathrm{CB}_1)$	$2\varepsilon_{b1}\Xi_2$
I_{X0X1}	-1	-1	-1	-1
I_{X0Y1}	$-\delta_1-\delta_0$	$-A_{4,0}-\delta_1-\delta_0\cos(\mathrm{CB}_0)$	$-A_{4,1}-\delta_1-\delta_0\cos(\mathrm{CB}_1)$	$-\nu-\delta_1-\delta_0\Xi_3$
I_{Y0X1}	$-\delta_0-\delta_1$	$A_{2,0}-\delta_0-\delta_1\cos(\mathrm{CB}_0)$	$A_{2,1}-\delta_0-\delta_1\cos(\mathrm{CB}_1)$	$\mu-\delta_0-\delta_1\Xi_3$
I_{Y0Y1}	1	$\cos(\mathrm{CB}_0)$	$\cos(\mathrm{CB}_1)$	Ξ_3

[a]In the calibration configurations presented in this table it has been assumed that configuration I is first used to find the Bessel voltages that satisfy $J_0(A_1) = J_0(A_0) = 0$. These voltages are then used for the remaining configurations (this is the reason why the $J_0(A_1)$ and $J_0(A_0)$ terms do not appear in the columns of configurations II, III and IV). Furthermore the following identifications have been made:

$$\begin{aligned}
\Xi_1 &= \cos(\mathrm{CB}_0)\sin(\mathrm{CB}_1) + \cos(\mathrm{CB}_1)\sin(\mathrm{CB}_0),\\
\Xi_2 &= -\cos(\mathrm{CB}_1)\sin(\mathrm{CB}_0) - \cos(\mathrm{CB}_0)\sin(\mathrm{CB}_1),\\
\Xi_3 &= \cos(\mathrm{CB}_0)\cos(\mathrm{CB}_1) - \sin(\mathrm{CB}_0)\sin(\mathrm{CB}_1),\\
\mu &= A_{2,0} + A_{1,1}\sin(\mathrm{CB}_0) + A_{2,1}\cos(\mathrm{CB}_0),\\
\nu &= A_{4,1} - A_{3,0}\sin(\mathrm{CB}_1) + A_{4,0}\cos(\mathrm{CB}_1).
\end{aligned}$$

where, using Eqs. (6.4), we have made the following identifications:

$$\begin{aligned}
\nu &= A_{4,1} + \left[A_{2,0}\tfrac{\cos\mathrm{CB}_0}{\sin\mathrm{CB}_0} + A_{4,0}\tfrac{1}{\sin\mathrm{CB}_0}\right]\sin(\mathrm{CB}_1) + A_{4,0}\cos(\mathrm{CB}_1),\\
\mu &= A_{2,0} + \left[A_{2,1}\tfrac{1}{\sin\mathrm{CB}_1} + A_{4,1}\tfrac{\cos\mathrm{CB}_1}{\sin\mathrm{CB}_1}\right]\sin(\mathrm{CB}_0) + A_{2,1}\cos(\mathrm{CB}_0).
\end{aligned} \tag{6.10}$$

This is a linear system of equations with 6 unknown parameters: δ_0, δ_1, $A_{2,0}$, $A_{2,1}$, $A_{4,0}$ and $A_{4,1}$. Therefore the values of these parameters can be approximated by using a multiple linear regression analysis.

Figure 6.2 shows the measured cosines of the CB of the plates as a function of the wavelength as well as the fit obtained with the dispersion formula of CB given in Eq. (6.5). The small differences in the measured values of $\cos\mathrm{CB}$ for quartz 0 and quartz 1 are due a different thickness of the two plates (1.06 ± 0.01 mm vs 1.02 ± 0.01 mm). The bottom panel shows the parameters $A_{2,0}$, $A_{2,1}$, $A_{4,0}$

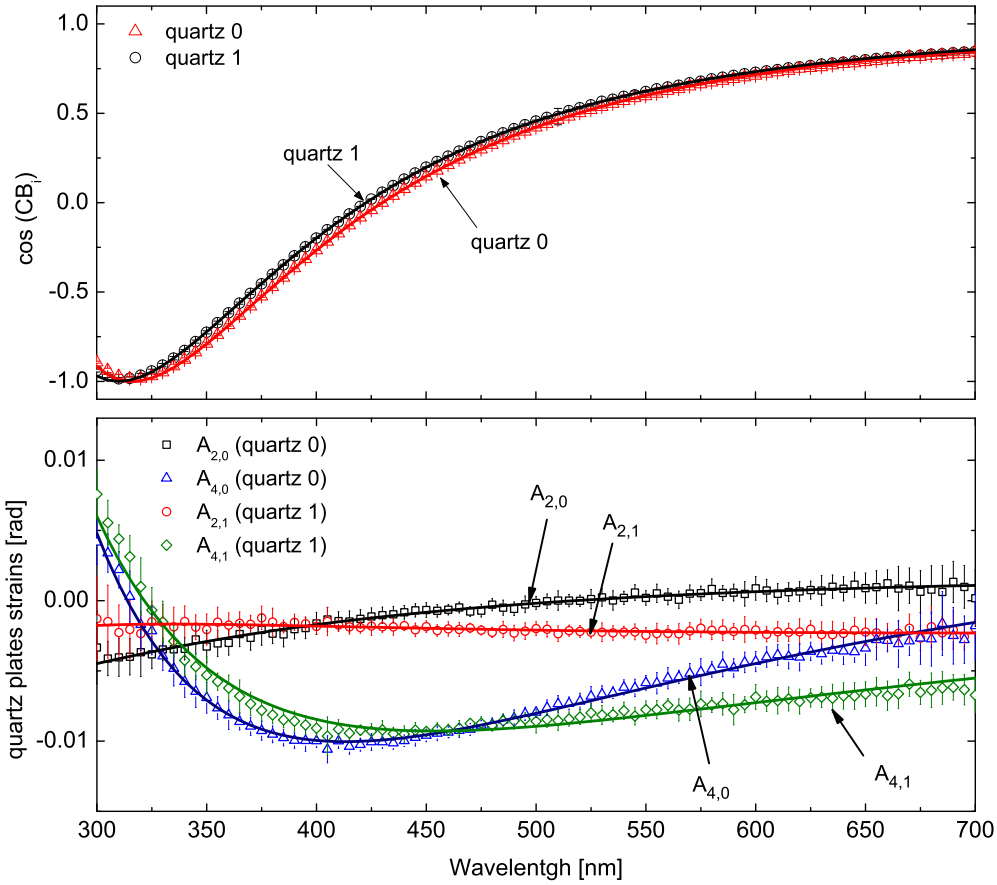

Figure 6.2.: Spectroscopic calibration of the 1 mm quartz plates. Top panel shows the $\cos(\mathrm{CB}_i)$, where the solid curves indicate the fits to the data using Eq. (6.5). Bottom panel shows the parameters $A_{2,0}$, $A_{2,1}$, $A_{4,0}$ and $A_{4,1}$ that are related to the small linear birefringence of the plates. The solid curves are the fits to the experimental data using the approximate model in Eq. (5.48).

and $A_{4,1}$ of the quartz plates as a function of the wavelength as well as the fit to the raw data by using Eq. (5.48). Note that, as a coarse approximation, the dispersion relation used for this fit is the same that was used to fit the static strain of the modulators but, in fact, $A_{2,0}$, $A_{2,1}$, $A_{4,0}$ do not merely represent a linear birefringence, rather they can include non-vanishing trigonometric functions as it is shown in Eqs. (6.3).

To complete the calibration, the coefficients I_{Y0} and I_{Y1} of configurations II or

III can be used to measure the angles of the polarizers with respect to the PEMs (ε_{b0} and ε_{b1}, defined in section 5.4) and the overall gain is measured by I_{X0X1}.

6.5. Measurement schemes

The quartz-assisted 2-MGE offers two different modes of measurement: spectroscopic and spatially resolved. The instrument can work in either of these two modes without significant instrumental changes between both. The characteristics of all the elements involved in the instrument were given in section 5.3.

6.5.1. Spectroscopic mode

The wavelength span of our 2-MGE is around $\sim 210 - 880$ nm. The limitation in the UV is determined by the low output of Xe arc lamp in the UV and the absorption properties of the optical materials involved (polarizers, optical fibers, etc.), whereas the limitation in the near infrared is due to the cutoff of the PMT. The use of the quartz-assisted technique does not narrow the wavelength span of the instrument since quartz is a highly transparent material at these wavelengths; however, and due to the dispersive nature of the optical effects in quartz, a spectroscopic calibration of the quartz plates such the one presented in the previous section is needed.

According to Eqs. (6.8) the values of $\sin \mathrm{CB}_0$, $\sin \mathrm{CB}_1$, that appear in the denominator, are needed to calculate all the elements of the Mueller matrix of the sample. Thus, it is evident that there will be an algebraically unfavorable situation whenever $\sin \mathrm{CB}_i \sim 0$. The value of CB increases when going to shorter wavelengths and is proportional to the thickness of the plate. For quartz, at the wavelengths of measurement the case $\mathrm{CB}_i \simeq 0$ would only be a problem for extremely thin slabs, but the case $\mathrm{CB}_i \simeq 180^\circ$ occurs at ~ 316 nm using 1 mm plates. In this situation a precise measurement of some elements of the Mueller matrix becomes impossible. On the contrary the situation $\mathrm{CB} \sim 90^\circ$ is the more favorable for measurements (note that this corresponds to an optical rotation of $\sim 45^\circ$, that is a typical angle of rotation for instruments with mechanical rotators).

Fig. 6.3 shows the approximate dispersive behavior of the optical rotation, ρ, for two quartz plates as calculated with the dispersion relations given in [152]. The ideal optical rotation for a 2-MGE is 45° (it would correspond to the situation in which the axes of the PEM are at 45° one to the other) which approximately occurs at 240 nm for the 0.25 mm plate and at 430 nm for the 1 mm plate. An adequate calibration of the quartz rotators permits the measurement out of these particular wavelengths: for each plate there is a zone suitable for spectroscopic

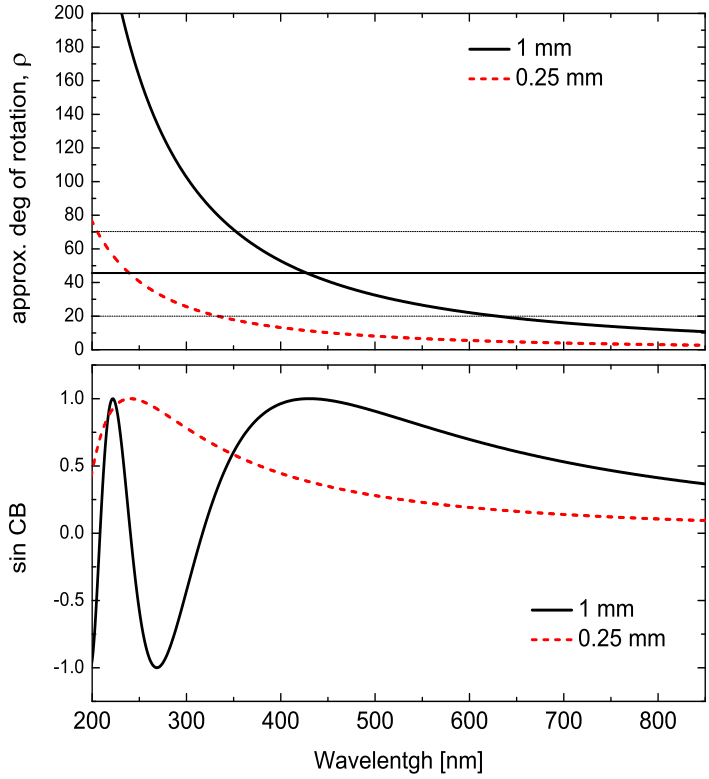

Figure 6.3.: Top panel: angle of rotation, ρ, as a function of the wavelength for two quartz rotator elements with thicknesses of 1 mm and 0.25 mm. The horizontal solid lines identifies a 45° optical rotation, while the horizontal dashed lines indicate optical rotations between 20° and 70°, in which measurements of the Mueller matrix with the quartz-assisted method can be performed with good accuracy. Bottom panel: spectroscopic values of sin CB for the two quartz plates.

measurements in which sin CB is not strictly 1 but varies smoothly and does not take small values. If we assume that optical rotations between 20° and 70° give values of sin CB that are big enough (see bottom panel of Fig. 6.3) to perform the calculations in Eqs. (6.8), the 1 mm rotator permits to cover a wide range of wavelengths from 350 nm to 630 nm while the 0.25 mm rotator is suitable to work in the UV, for wavelengths between 205 nm and 330 nm.

Fig. 6.4 shows the spectroscopic Mueller matrix measurement of a zero-order plate designed to give a $\lambda/4$ retardation at 532 nm which we use to test the measurement modes. The fast axis of the wavelength was placed so that it did

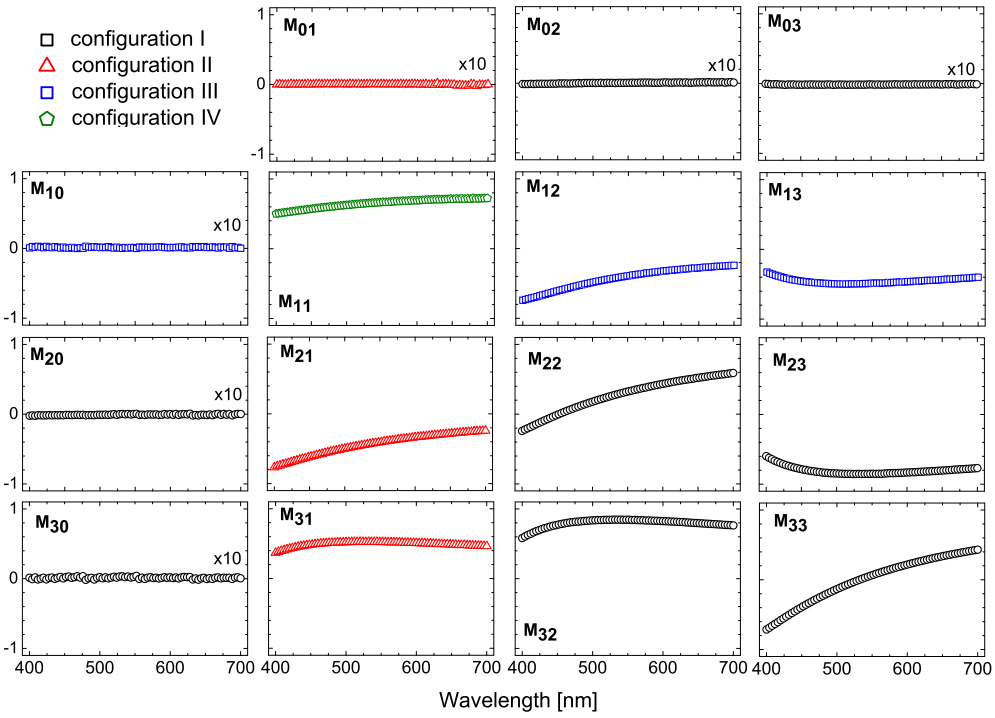

Figure 6.4.: Spectroscopic Mueller matrix of a zero-order quarter wave plate designed for 532 nm. Different colours denote measurements taken at different configurations. For a quarter wave plate the Mueller matrix element m_{33} corresponds to the cosine of the retardance.

not coincide with the x-y or the 45°-135° laboratory axis. The measurement was taken using the quartz-assisted method with quartz plates of thicknesses ~ 1 mm. Note that the wavelength span of this measurement ($400 - 700$ nm) approximately falls within a favorable measurement zone for quartz plates of this thickness (see Fig. 6.3).

6.5.2. Spatially resolved mode

Spatially resolved measurements of the Mueller matrix are done at a single wavelength. Clearly, as commented before for the spectroscopic mode, here it is also convenient to select a wavelength (or select a quartz thickness) for which the quartz plates give an optical rotation such that $|\sin \mathrm{CB}_0|$ and $|\sin \mathrm{CB}_1| \gtrsim 0.6$.

Single detectors such as PMTs are the most suitable to work with PEMs. In contrast, the fast modulation of the PEMs is incompatible with the relative low

speed of the commercially available multi-detectors (e.g. CCD) [153] that would be desirable to use for spatially resolved applications. To sort this difficulty some complex strategies to integrate modulation cycles of the PEMs for use with CCDs have been published in recent years [146, 154–157]. However, these are methods of very difficult application, and most of them suited for instruments using one single PEM. The easiest way to have a polarimeter based on PEMs with imaging capabilities is to keep using fast single point detectors and map the sample (that is mounted on an automatic x-y translator) point by point over a certain area. Each measurement point becomes one "pixel" of the resulting image. In order to have a high lateral resolution with this method only light that has passed through a tiny portion of the sample must reach the detector. This can be done either by reducing the size of the light spot impinging the sample or by placing a pinhole in front of the PMT [85].

To map relatively big areas of the sample several thousands of measurements can are required (values between 20000 and 40000 are common). Although the phase modulation technique allows very fast measurements, the obtention of a Mueller matrix mapping measurement can be a time-consuming process because of the large amount of data that needs to be acquired sequentially. Moreover, it is worth to remember that for every point of measurement the four configurations (I, II, III and IV) are required to measure the complete Mueller matrix. Therefore, it is necessary map the sample four times, one for each configuration and, once the 4 complete sets of data have been acquired, the final Mueller matrix mapping of the sample surface is computed with Eqs. (6.8). This method is much more time-efficient than accessing to each configuration individually for every point of the mapping, due to the limited speed of the filter wheels where the quartz plates are mounted.

The spatial resolution (~ 2 μm) of the automatic x-y translator in which the sample is mounted is higher that the optical resolution of our instrument (~ 80 μm at best). The optical resolution could be significatively increased by including some imaging optics between the sample and the PSA, but such configuration has not been tested in our instrument yet.

As the instrument does not suffer from the beam translation problem it must be able to must map exactly (at least within the optical resolution) the same area in any of the four configurations. To check this correspondence, four transmission intensity mappings, one for each configuration, are recorded during the measurement of the Mueller matrix [2]. Each intensity mapping is obtained from the high dc voltage that the PMT circuit gives to the PMT at each measurement point to maintain a constant dc value of the signal: the lower the voltage, the

[2] The Fig. B.7 of the appendix B exemplifies this.

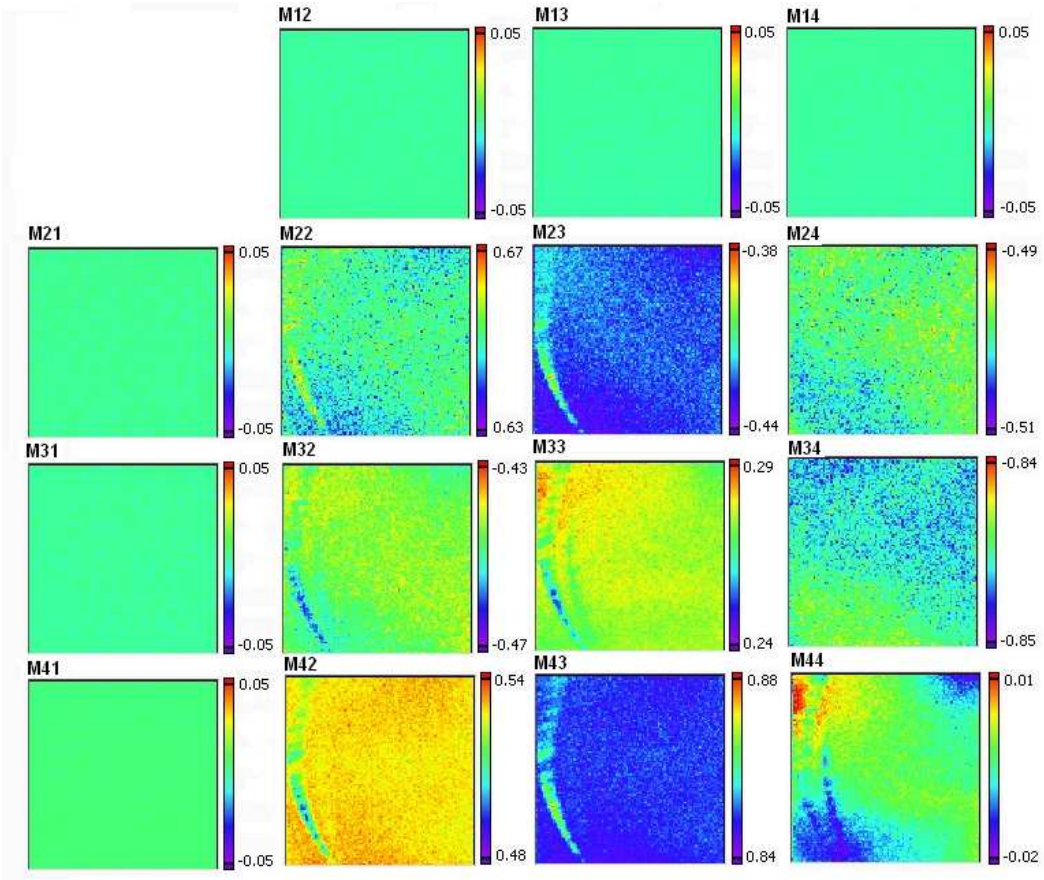

Figure 6.5.: Imaging Mueller matrix elements of the zero order 532 nm quarter wave plate that was spectroscopically measured at Fig. 6.4. The dimension of each frame is 4 mm × 4 mm, where the step size to generate each pixel is 40 μm × 40 μm.

greater the transmittance. If these four intensity mappings are point by point correspondent, then we can assert that, both, the x-y translator and the quartz plates do not limit the lateral precision of the measurement.

In summary, the result of a spatially resolved measurement consist of 15 x-y images that correspond to the 15 elements of the normalized Mueller matrix of the sample, and 4 extra images that represent an intensity map of the transmitted light at each configuration of measurement.

Fig. 6.5 shows the Mueller matrix for the test quarter wave plate. As expected, there are no dramatic changes in the values of the Mueller matrix elements all

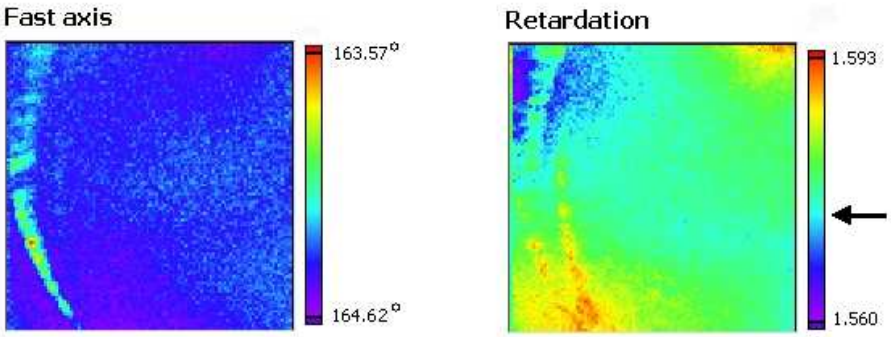

Figure 6.6.: Mapped fast axis and retardation of analyzed quarter wave plate calculated from the Mueller matrix of Fig. 6.5. The arrow indicates the approximate colour that would corresponds to an ideal quarter wave retardation (1.571 rad).

over the plate surface, but changes of the order 0.01 rad are clearly visible in the color scale. They can be probably attributed to defects in the optical material of the plates. The step size used to create this image (40 μm $\times$ 40 μm) is beyond the optical resolution of the instrument, which means that although we can generate images with high pixel resolution, we may not be able to resolve objects with sizes < 80 μm. The values found here fully coincide with those obtained in the spectroscopic measurement of Fig. 6.4.

Fig. 6.6 shows the calculated values of the orientation of the fast axis and the retardation of the plate as obtained from the Mueller matrix of Fig. 6.5. Both parameters fall within the expected values. As expected, the central part of the plate is the area that better approaches to an ideal quarter wave retardation. Some small inhomogeneities that cause retardation defects appear at the periphery.

Part IV.

Experimental measurements

Chapter 7.

Optical activity of α-quartz

α-quartz (SiO_2) is, without any doubt, the crystal that historically has been more investigated from the point of view of its optical activity. Quartz is an uniaxial crystal that belongs to the trigonal system and to the non-centrosymmetric crystallographic point group[1] 32. Quartz is enantiomorphous, that is, it may occur as either right- or left-handed (in order to be enantiomorphous a crystal must have no element of symmetry that changes the handedness). The atomic arrangement of quartz provides a screw axis that produces a right or left helical distribution of atoms, and the optical activity of these two types of handedness has opposite signs. Currently, around 200 years ahead from the first observations of Arago [15] and Biot [16] in the early 1800's, quartz is still used in nearly every text book to introduce the subject of optical activity. As a result of this long-term investigation some of the parameters involved in the optical activity of quartz are known with great accuracy [158, 159], and even their variations with temperature and pressure have been investigated [160, 161]. Nowadays, quartz crystal is available commercially in a great diversity of forms and cuts. The optical rotation of quartz has, for example, applications in laser technology, or as a standard of calibration for commercial polarimeters. Also, in this work, we have taken advantage of the optical rotation properties of quartz plates to devise the novel quartz-assisted 2-MGE technique introduced in chapter 6. However, for all these applications and for the majority of experimental measurements of the optical activity of quartz reported in the literature light propagates along the unique direction of the crystal in which it does not shows linear birefringence and CB is the only effect: the optic axis or c-axis. Therefore most of the available commercial quartz crystals for applications in optics are cut perpendicular to their c-axis.

Although linear birefringence and optical activity have been separately studied using a variety of techniques, very few attempts have been made to quantify the optical activity in presence of linear birefringence. For transparent materials, an accurate measurement of CB cannot be made without a full account of the

[1] There are different notations for crystallographic point group. Using the Schönflies notation quartz belongs to D_3 point group.

related linear birefringence; for absorbent materials, the linear dichroism and CD must also be taken into account. In nature, circular and linear birefringent effects often appear together, so a method to measure CB in presence of linear birefringence is highly desirable. One such measurement technique is the High-Accuracy Universal Polarimeter (HAUP) [55,57,58,162,163], already mentioned in chapter 2. This technique is a variation of the old technique of crossed-polarizers, and it involves making measurements at slightly deviated angles from the position of maximum extinction of the polarizers. Typically, a monochromatic light source is used and the values of the optical activity are determined from the evolution of the detected waveform as a function of the angle of rotation of the polarizers.

In this chapter, we present a method to measure the optical activity of crystals based on the measurement of the Mueller matrix with the 2-MGE technique introduced in chapter 5. Using this technique, it is possible to perform measurements in directions other than along the optic axis of the crystal, where the magnitude of the linear birefringence is significantly larger than the magnitude of the optical activity. As an application of this method we have measured the components of the gyration tensor of a right-handed (RH) and left-handed (LH) quartz crystal. To our knowledge, our investigation [152] is the first measurement of the optical activity of a crystal based on the spectroscopic measurement of the Mueller matrix for directions where linear birefringence and CB appear together.

7.1. Experimental details of the measurement

The basis of our experimental approach is the measurement of transmission Mueller matrix of different quartz plates with precise control of the direction of light propagation through the crystal. The samples studied in this work consist of two z-cut quartz plates with opposite handedness. This kind of quartz plates are widely available commercially and at a low price since this is the most common type of cut. We will present results separately for LH plate and for the right-handed RH plate. The measured thickness the LH plate is 1.02 ± 0.01 mm while the thickness of the RH plate is 1.06 ± 0.01 mm.

A general scheme of the sample positioning in the 2-MGE is shown in Fig. 7.1 and a more precise diagram of the geometry of the problem is presented in Fig. 7.2. A light beam is incident upon the crystal at an angle of incidence ϕ with respect to its c-axis. l, d and θ are respectively the light path through the crystal, the sample thickness and the angle with respect to the c-axis of the wave normal for the wave propagating through the crystal. If d and ϕ are known the light path l can be found by taking the approximation that the wave normal (given by Snell's

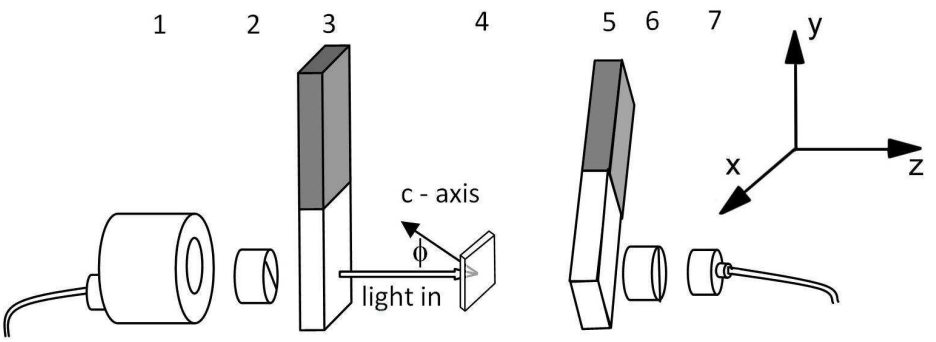

Figure 7.1.: Diagram of the quartz plates positioning inside the 2-MGE. The sample could be precisely tilted by an angle ϕ using a goniometer.

law) in the crystal coincide with the direction of propagation

$$l = \frac{d}{\cos\theta}, \quad \theta = \arcsin\left(\frac{\sin\phi}{\bar{n}}\right), \tag{7.1}$$

where $\bar{n}$ is the mean refractive index, that depends on θ and will be defined in the next section. The sample was tilted[2] in order to perform measurements at different values for ϕ (which also means different values for θ) . The rotation was around the y-axis defined by the modulation axis of the PEMs when PSG and PSA are orientated at 0°.

In the case of quartz crystal, the CB is known to be nonzero in a wide frequency region which includes the whole studied spectrum (220 to 800 nm) [151]. In this region quartz is not absorbent [164] and therefore all parameters related to the absorptive nature of the crystal (including the CD) are zero.

7.2. Method of measurement

To study the light propagation through the quartz plate at oblique incidence, i.e. for directions where linear birefringence is also present, we can use the propagation description first given by Szivessy [165], which uses the constitutive equations given by Born [166]. This model is widely used in the literature [65, 149, 167, 168], particularly in experimental work, and gives the possible values of the refractive index n, for a given direction of the wave normal. Although this approach is only approximate, it has been shown to be accurate as

[2]When these experiments were performed a micrometric manual goniometer was used to tilt the sample. Currently the instrument disposes of a motorized Newport rotation stage (0.002° resolution) that can be used as a tilter for the sample.

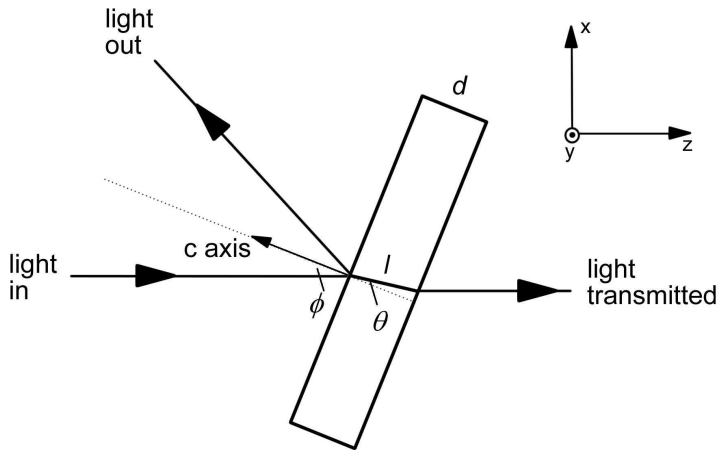

Figure 7.2.: Detail of the off-normal incidence measurement of circular and linear birefringence.

long as the birefringence of the investigated crystal is not huge [169], as this model describes the phenomenon of optical activity within an accuracy of the product of the linear birefringence in the direction of observation by the gyrotropy parameters [168]. In this context the two possible refractive indices are given by the positive roots of the equation [149, 168]:

$$(n^2 - n_{01}^2)(n^2 - n_{02}^2) = G^2, \tag{7.2}$$

where n_{01} and n_{02} are the refractive indices of the eigenwaves in absence of optical activity. G is the scalar gyration parameter and is a measure of the optical activity for the direction in question. G as a function of direction is given by

$$G = g_{ij} l_i l_j, \tag{7.3}$$

in which the convention of summing over repeated indices is used. l_i and l_j are the direction cosines of the normal wave and g_{ij} are the components of the gyration tensor that describe the optical activity of the crystal. For the enantiomorphic uniaxial crystals the gyration tensor [149] is

$$\mathbf{g} = \begin{bmatrix} g_{11} & 0 & 0 \\ 0 & g_{11} & 0 \\ 0 & 0 & g_{33} \end{bmatrix}, \tag{7.4}$$

and G takes the form [167]

$$G = g_{11} \sin^2\theta + g_{33} \cos^2\theta, \tag{7.5}$$

where θ is defined in (7.1).

The solutions of Eq. (7.2) are [167]:

$$n_{1,2}^2 = [n_{01}^2 + n_{02}^2 \mp [(n_{02}^2 - n_{01}^2)^2 + 4G^2]^{1/2}]/2, \tag{7.6}$$

and for an uniaxial crystal ($\varepsilon_{11} = \varepsilon_{22} \neq \varepsilon_{33}$):

$$n_{01}^2 = \varepsilon_{11}, \quad n_{02}^2 = \frac{\varepsilon_{11}\varepsilon_{33}}{(\varepsilon_{11}\sin^2\theta + \varepsilon_{33}\cos^2\theta)}, \tag{7.7}$$

where $\varepsilon_{11} = \varepsilon_o = n_o^2$ and $\varepsilon_{33} = \varepsilon_e = n_e^2$. The refractive indices n_o and n_e of quartz are well-known and are given by the 5 parameters dispersion relation calculated in [170].

The total birefringence (T_R) of the system is a combination of linear (LB and LB') and circular (CB) birefringences:

$$\mathrm{T}_R^2 = \mathrm{LB}^2 + \mathrm{LB}'^2 + \mathrm{CB}^2, \tag{7.8}$$

with

$$\mathrm{T}_R = \frac{2\pi}{\lambda}(n_2 - n_1)l. \tag{7.9}$$

According to Eq.(7.6) and assuming that $G^2 << n_{01}^2 n_{02}^2$, T_R^2 can be approximated to:

$$\mathrm{T}_R^2 \simeq \frac{4\pi^2}{\lambda^2}\left[(n_{02} - n_{01})^2 + \frac{G^2}{n_{01}n_{02}}\right] l^2. \tag{7.10}$$

Due to the geometry of our oblique incidence experiment (see Fig. 7.2) the sample tilting does not cause birefringence in direction 45° to the x axis ($\mathrm{LB}' \simeq 0$) and LB itself can be considered as a measure of the total linear birefringence. Therefore Eq. (7.8) can be simplified to:

$$\mathrm{T}_R^2 \simeq \mathrm{LB}^2 + \mathrm{CB}^2. \tag{7.11}$$

Comparing Eq. (7.11) to Eqs. (7.10) and (7.8), we can make the following identifications,

$$\mathrm{LB} = \frac{2\pi}{\lambda}(n_{02} - n_{01})l, \tag{7.12}$$

$$\mathrm{CB} = \frac{2\pi G l}{\lambda \bar{n}}, \tag{7.13}$$

where $\bar{n}$ stands for a mean refractive index $\bar{n} = \sqrt{n_{01}n_{02}}$.

In the particular case of propagation along the optic axis ($\theta = 0°$) CB is proportional to the g_{33} component of the gyration tensor:

$$g_{33} = \frac{\mathrm{CB}_{\theta=0°}\lambda n_o}{2\pi l}. \tag{7.14}$$

For light propagation along the optic axis in an optically active uniaxial crystal, or for light propagation in any direction in an optically active isotropic medium, the eigenmodes of optical propagation through the material are left and right circularly polarized modes, having both of them their own refractive indices. In contrast, the eigenmodes in an uniaxial material without optical activity are linearly polarized modes that are mutually orthogonal. As a result, in a random direction in an optically active uniaxial crystal the eigenmodes are left and right elliptical polarization modes with a major axis that coincide with the directions of the linearly polarized eigenmodes that would be present in the absence of optical activity.

The ellipticity k that we introduced in chapter 1 is the ratio of the minor to the major axis of the ellipse of polarization and it can be used to define the waves that travel through the crystal unchanged in form. Along the optic axis, $k = 1$ which indicates that the eigenmodes are circularly polarized light. The quantity k can be calculated as follows [149]:

$$k = \tan\left(\frac{\gamma}{2}\right), \tag{7.15}$$

where γ is an angle defined by the ratio between the circular and linear birefringences

$$\tan\gamma = \frac{\mathrm{CB}}{\mathrm{LB}}. \tag{7.16}$$

With the relations of Eqs. (7.12) and (7.13) this ratio can be written as:

$$\frac{\mathrm{CB}}{\mathrm{LB}} = \frac{G}{\bar{n}(n_{02} - n_{01})}, \tag{7.17}$$

and substituting Eq. (7.5) here we can derive an expression to calculate g_{11} from experimental measurements of the ratio CB/LB:

$$g_{11} = \frac{1}{\sin^2\theta}\left[\bar{n}(n_{02} - n_{01})\frac{\mathrm{CB}}{\mathrm{LB}} - g_{33}\cos^2\theta\right]. \tag{7.18}$$

7.2.1. A model for the dispersion of the gyration tensor components

As we commented in chapter 2, the first phenomenological models to describe the optical activity appeared early in the 20th century [158,171], where the first tenuous connections were made between optical rotation and the interaction between atoms. One of the more successful approaches was carried out by Chandrasekhar using classical theory to study the optical rotation of quartz [21, 151]. In this model there are two coupled oscillators that represent the smallest unit of the optically active crystal. The oscillators are assumed to be identical and undamped

(that is, the crystal is non-absorbing). This coupled oscillator-model can also be treated quantum mechanically and describes the optical rotation ρ of quartz in a wide frequency region by:

$$\rho = \frac{k\lambda^2}{(\lambda^2 - \lambda_0^2)^2}. \tag{7.19}$$

The optical rotation ρ is related to CB by $\rho = 1/2\text{CB}$, and k and λ_0 are the two unique parameters of the model. In fact, this model has been already used in this work when we employed it to describe the CB dispersion of our quartz-assisted method [Eq. (6.5)].

To measure the components of the gyration tensor G we propose to use this dispersion model to parameterize g_{11} and g_{33}:

$$g_{ii} = \frac{A_i\lambda^3}{(\lambda^2 - B_i^2)^2}, \tag{7.20}$$

where A_i and B_i are the parameters to be determined. Note that this model can be straightforwardly derived from (7.19) if we consider that $G = \lambda\bar{n}\rho/\pi l$ (see Eq. (7.13)) and we use the approximation that $\bar{n}$ is constant. We have found that Eq. (7.20) is a good fit for our experimental g_{11} and g_{33} data. It is interesting to note that, while for quartz CB ($\propto (n_- - n_+)$) varies by more than one order of magnitude in the interval range from 200 nm to 800 nm, the variation of the mean refractive index $\bar{n}$ ($\propto (n_- + n_+)$) in this same interval is only around 7%. Thus it is not strange that if Eq. (7.19) constitutes a good fit for CB, Eq. (7.20) can be used to fit the gyration tensor with success.

7.3. Data analysis of the Mueller matrix of quartz

The spectroscopic Mueller matrices measured at different small incident angles for RH and LH plates are respectively presented in Fig. 7.3 and Fig. 7.4. In both cases, and for all the orientations of the plates, Mueller matrix elements m_{01}, m_{02}, m_{03}, m_{10}, m_{20} and m_{30} are approximately zero in all the studied spectral range (note in the figures that these elements have been multiplied by a factor 10). This indicates that at this wavelength range and for these small angles of incidence there is not significant diattenuation and the Mueller matrices of the quartz plates basically take the form of a general retarder given in Eq. (3.24).

However, a crystal with retardation properties that vary rapidly with wavelength may induce depolarization if the system collects a band of wavelengths rather than a single wavelength. Since the retardation is proportional to the inverse of the wavelength, a band of wavelengths will result in a different retardation for each wavelength, resulting in partially polarized light [172]. To minimize this depolarization, the monochromator slit width can be reduced and/or a

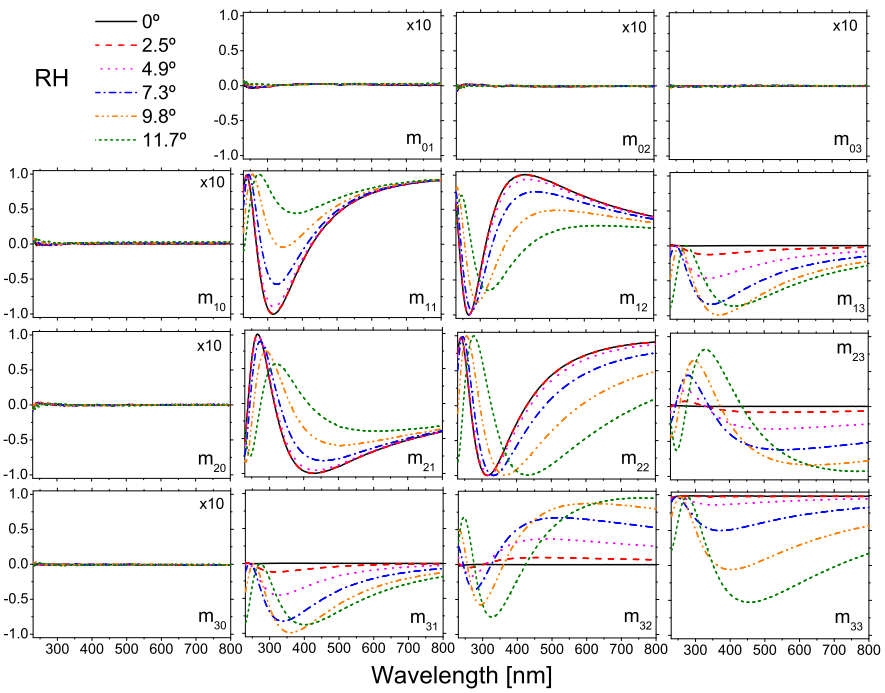

Figure 7.3.: Spectroscopic Mueller matrix for a RH plate of quartz at small incidence angles (ϕ).

smaller core optical fiber used at the input of the monochromator [86]. Fig. 7.5 depicts a comparison between the fraction of polarized light β (see Eq. (1.33)at normal incidence and at 60° incidence. As it can be seen in the figure the depolarization becomes particularly significant for big angles of incidence, where the observed retardation has an important variation with wavelength, and it needs to be considered.

In order to consider the depolarization of the measured Mueller matrices we have factorized them according to the Lu-Chipman decomposition given in Eq. (4.23). This factorization allows the separation of the depolarization properties from the retardation and dichroic properties. For an uniaxial crystal the Mueller matrices $\mathbf{M}_R$ and $\mathbf{M}_D$ commute [173], so the Lu-Chipman decomposition can be used to factor the experimental Mueller matrix. Once the retardation matrix $\mathbf{M}_R$ has been calculated we use Eqs. (4.31d), (4.31e) and (4.31f) to extract the values of linear and circular birefringence.

When dealing with samples that introduce significant retardations, such as crystals, the determination of the sample Mueller matrix may not be sufficient to determine all its birefringent characteristics. In Eq. (3.24) it can be seen that

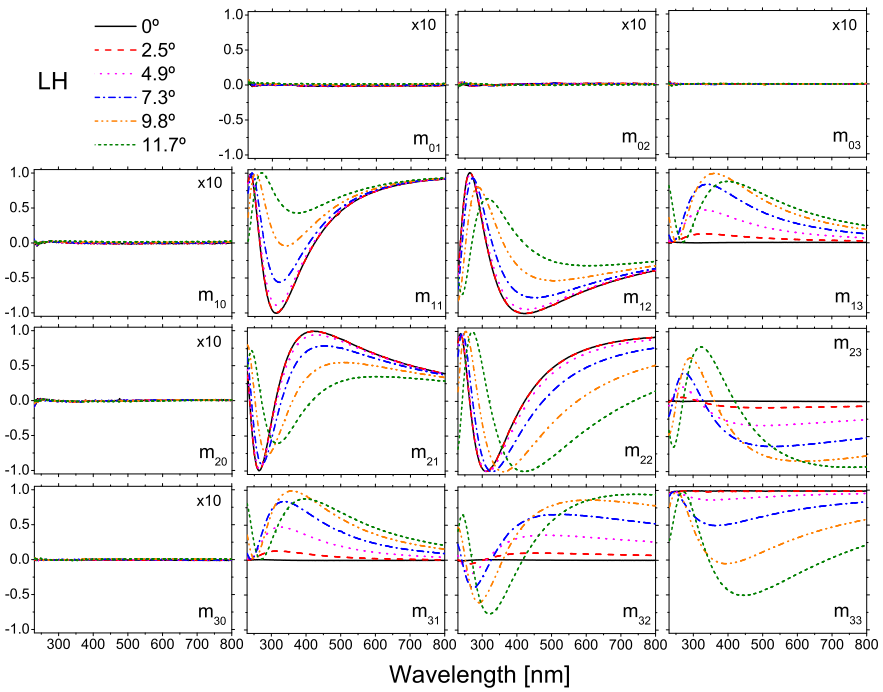

Figure 7.4.: Spectroscopic Mueller matrix for a LH plate of quartz at small incidence angles (ϕ).

many of the Mueller matrix elements contain trigonometric functions. Furthermore, the *arccos* function, which is multi-valued, is required to determine the total birefringence (see Eq. (4.32)). For systems with small retardations this does not constitute a problem since the total retardation must fall in the $[0,\pi]$ interval. However, for systems with big retardances (e.g. some crystals) this problem prevents us from determining the birefringences unless we know their order. For example at 252 nm the Mueller matrix of the left handed plate of quartz with an angle of incidence of 9° is the following:

$$\mathbf{M} = \begin{bmatrix} 1 & 0.002 & 0.003 & 0.006 \\ 0.005 & 1.002 & 0.009 & 0.010 \\ 0.001 & 0.011 & 1.000 & 0.002 \\ 0.000 & 0.010 & -0.006 & 0.988 \end{bmatrix} \tag{7.21}$$

This matrix is nearly the same as the identity Mueller matrix, which, one would obtain in transmission for an isotropic medium. Of course, the sample is not isotropic, although its Mueller matrix appears to be that of an isotropic medium at this wavelength. The importance of the order must always be considered when

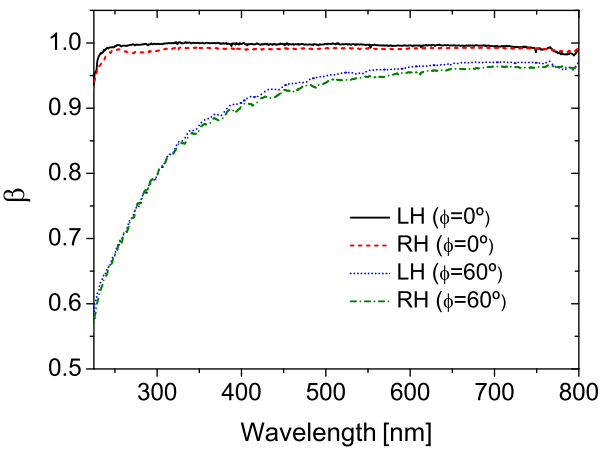

Figure 7.5.: Fraction β of polarized light for normal and oblique incidences. For the same conditions the RH plate is a bit more depolarizing because it is a slightly thicker than the LH plate.

analyzing these results, since a single Mueller matrix is not always sufficient to provide the characterization of a polarization element.

For large angles of incidence a significant linear diattenuation appears in the measured Mueller matrices as they no longer have all the vanishing elements shown in Eq. (3.24). In this case the linear diattenuation is not due to an anisotropic absorbance in quartz, but rather is caused by the different reflectivities of s- and p- polarized light [174]. The polar decomposition allows us to obtain the linear diattenuation of the sample from the matrix factor $\mathbf{M}_D$ [84]. The top panel of Fig. 7.6 displays the linear diattenuation for a quartz plate at an angle of incidence of 60°.

The bottom panel of Fig. 7.6 shows the total retardance T_R as determined using Eq. (4.32) for the RH quartz plate with a incidence angle of 60°. At this large incident angle the linear birefringence of quartz is big compared to π and, the total retardance goes through several oscillations between 0 and π as a function of wavelength. To determine the real T_R we should also know their order to unfold the "folded" spectrum of Fig. 7.6. Fortunately we do not need to know the order of the birefringence to determine the ellipticity and the gyration tensor of quartz. Eqs. (7.16) and (7.18) show that it is only necessary to determine the ratio of CB to LB rather than determining LB and CB separately. That is, we do not have to determine T_R. In terms of Mueller matrix elements, the ratio

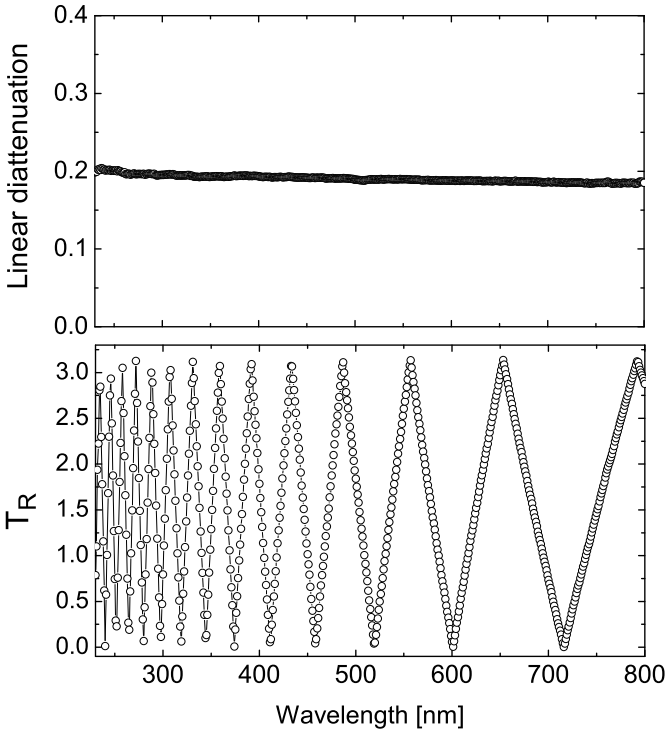

Figure 7.6.: Linear diattenuation and "folded" total retardation T_R induced by a 1 mm thick, z-cut, RH quartz plate at an incidence angle of 60°.

CB/LB is given by:

$$\frac{\mathrm{CB}}{\mathrm{LB}} = \frac{m_{R_{12}} - m_{R_{21}}}{m_{R_{32}} - m_{R_{23}}}. \tag{7.22}$$

Therefore, the ratio CB/LB can be straightforward determined once the matrix $\mathbf{M}_R$ is known. Although Eq. (7.22) is a significant simplification, each of the Mueller matrix elements must be measured accurately. Obviously, a large error occurs when the denominator $(m_{R_{32}} - m_{R_{23}})$ approaches to zero, which occurs at several wavelengths for these samples. Fortunately, as it will be discussed in the next section, these points can be easily identified and can be removed from the calculation. Another experimental issue is that the retardation oscillation frequency increases at small wavelengths (See bottom panel of Fig. 7.6), and the consecutive maxima and minima may be separated only by few nanometers. Thus, a good spectral resolution as determined by the monochromator must be sufficient to resolve these oscillations. Thinner samples would also reduce the total retardation and therefore avoid this problem.

7.4. Results

We have examined the retarding properties of the quartz plates at angles slightly deviated from the position of normal incidence by measuring their Mueller matrices. These measurements show the decrease on the ellipticity k as we deviate from the optic axis. Figs. 7.3 and 7.4, respectively show the normalized Mueller matrix for a RH and a LH plate of quartz at small angles of incidence. Small deviations from the condition of normal incidence translate in obvious differences in the matrices, which indicate that even for situations close to the propagation along the optical axis the LB becomes comparable to CB. Qualitatively these matrices resemble the matrix for a general retarder given in Eq. (3.24), where the different handedness is denoted by the opposite signs that Mueller matrix elements m_{12}, m_{21}, m_{13}, m_{31} present in Figs. 7.3 and 7.4. Elements m_{23} and m_{32} do not change in sign but this is due to the geometry of our oblique incidence measurements. The only elements that are not sensitive to the handedness of quartz, no matter the orientation of the plates, are the diagonal elements.

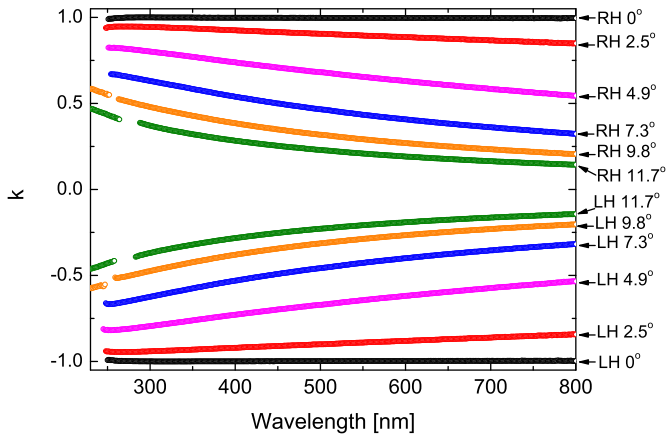

Figure 7.7.: Spectroscopic evolution of the ellipticity k for small angles of incidence.

Fig. 7.7 shows the ellipticity k for the RH and LH plates of quartz calculated from the values of LB and CB according to Eq. (7.15). The ellipticity describes the polarization state of the waves that propagate unchanged through the crystal. As expected, at normal incidence, the ellipticity is 1 for the RH and -1 for the LH, and it quickly diminishes as the angle of incidence becomes more oblique. The points missing in Fig. 7.7 are points placed at wavelengths at which the total

retardance, T_R, is close to 2π where an accurate measurement of the ellipticity is not possible.

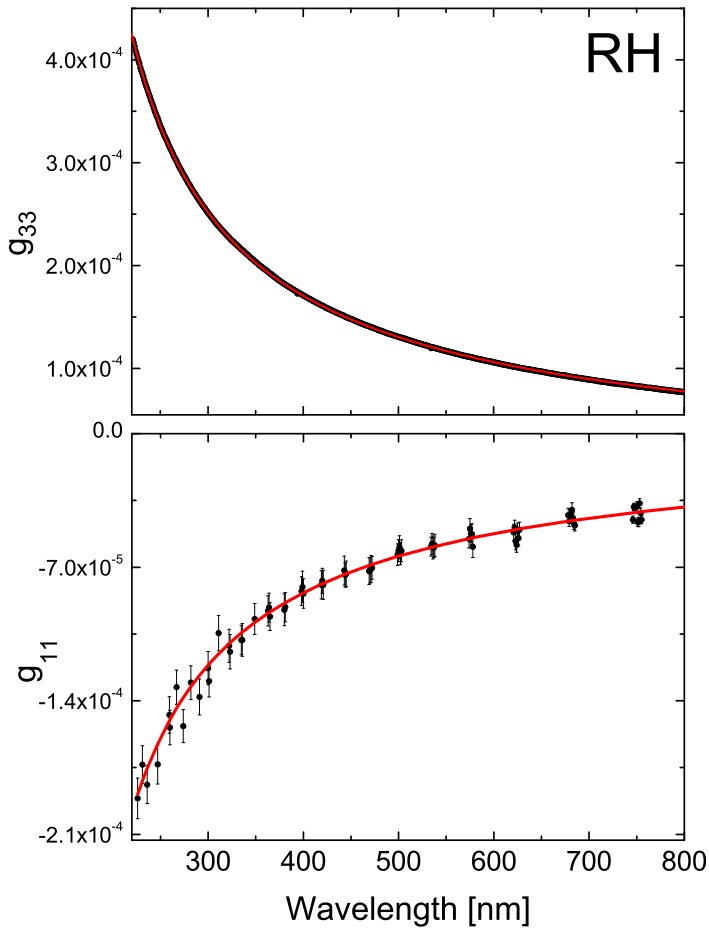

Figure 7.8.: Measured components of the gyration tensor (•) and fitted dispersion relation (solid line) for the RH plate.

The measurement of the 2 independent components of the gyration tensor of quartz requires the orientation of the samples in two different configurations. The first measurement is made at normal incidence ($\theta = \phi = 0°$) where g_{33} is calculated using Eq. (7.14). This is the usual measurement configuration where the sample does not show LB, so the determination is straight-forward. The determination of g_{11} is obtained using Eq. (7.18) and requires that the measurements be taken at a large incidence angle to avoid small values for the $\sin\theta$ that would translate in large errors in g_{11}. We have chosen $\phi = 60°$ ($\theta \sim 33°$) which

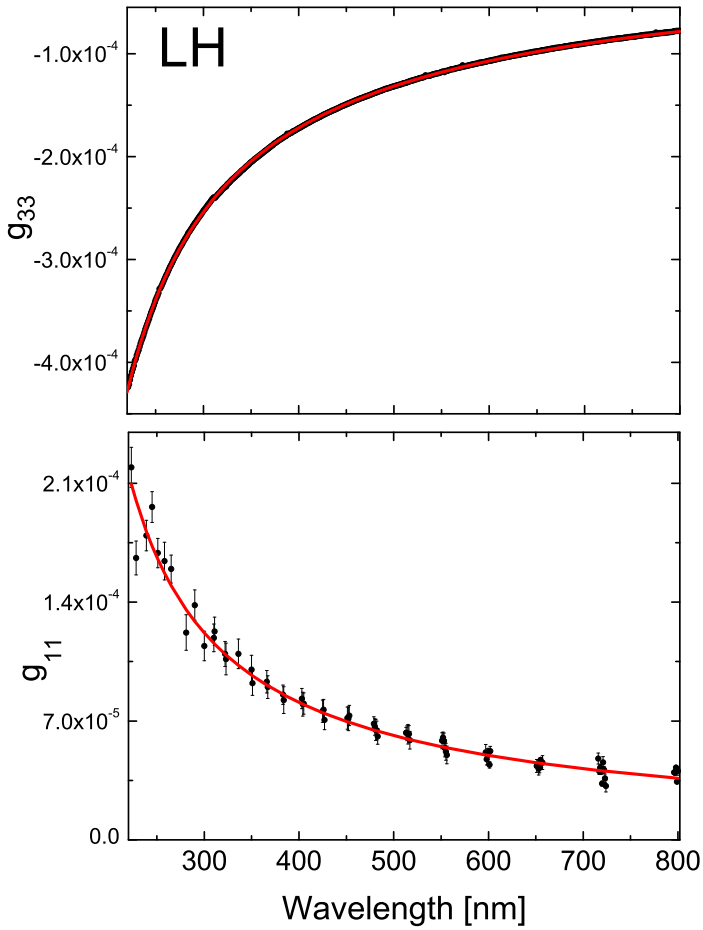

Figure 7.9.: Measured components of the gyration tensor (•) and fitted dispersion relation (solid line) for the LH plate.

is close to the maximum incidence angle for which we can guarantee that both the extraordinary and ordinary rays are collected by the detector.

The experimental values and the fitted curves for the g_{11} and g_{33} components of the RH and the LH quartz plates are shown in Figs. 7.8 and 7.9. The fitting to the model of Eq. (7.20) has been performed with a weighted Levenberg-Marquadt nonlinear minimization procedure using the reduced χ^2 as a figure of merit. Not all the experimental points have been used for the fitting (see bottom panels of Figs. 7.8 and 7.9), since we have only used those points that correspond to wavelengths for which the ratio CB/LB can be measured with good accuracy. In particular we have only considered points for which $|\mathrm{m}_{R_{32}} - \mathrm{m}_{R_{23}}|/2 \geq 0.98$, i.

Table 7.1.: Fitted parameters for the model in (7.20) with λ expressed in nm.

Component	LH	RH
g_{11}	$A_1 = 0.0277 \pm 0.0017$ $B_1 = 105.6 \pm 5.7$ $\chi^2 = 0.82$	$A_1 = -0.0298 \pm 0.0015$ $B_1 = 91.1 \pm 4.2$ $\chi^2 = 0.59$
g_{33}	$A_3 = -0.0609 \pm 0.0002$ $B_3 = 97.54 \pm 0.05$ $\chi^2 = 1.33$	$A_3 = 0.0604 \pm 0.0005$ $B_3 = 97.33 \pm 0.05$ $\chi^2 = 0.94$

e. points for which the absolute value of the denominator of (7.22) is near its maximum value.

Table 7.1 summarizes the fitting parameters for the four fits presented in Figs. 7.8 and 7.9. In all cases the dispersion relation given in Eq. (7.20) constitutes a good fit for experimental g_{33} and g_{11} data. Although the accuracy of g_{11} is considerably lower than g_{33}, it is clear that the shape of the dispersion curves for both components are fairly similar.

A comparison between our data and some of the previously published data is presented in table 7.2 at two wavelengths. There are few experimental measurements of g_{11} of quartz available in the literature and most of them are restricted to a single wavelength. With the exception of Ref. [56], our results agree with literature values for g_{33} within the stated error limits, and the agreement for g_{11} is within 2 standard deviations with all the literature values.

We also calculated the experimental ratio of the two gyration tensor components g_{11}/g_{33}. In the nonabsorptive wavelength regime this ratio should be -0.5 due to a symmetry argument that applies to the tetrahedron building units of crystalline quartz [176]. Fig. 7.10 shows our spectroscopic experimental results for the g_{11}/g_{33} ratio. They are consistent with the symmetry argument as most points are within 5% of the theoretical ideal value, and the calculated mean value is -0.486 ± 0.028. Using this value in Eq. (7.5) we can deduce that there is no optical rotation (G=0), that is, there exists an isotropic point for the optical activity that is cylindrically symmetric around the optic axis, for propagation directed $\sim 55^\circ$ from the optic axis.

In summary, we have presented in this chapter a technique for measuring the optical activity in uniaxial crystals in situations where both linear birefringence and circular birefringent effects are present. Hence this technique allows one to measure the CB of optically-active crystals in directions different from the opti-

Table 7.2.: Comparison of data for the components of the gyration tensor of quartz at room temperature determined from this study and from selected values in the literature.

Wavelength (nm)	Ref.	$\lvert g_{33}\rvert \times 10^{-5}$	$\lvert g_{11}\rvert \times 10^{-5}$
632.8	[58]	10.1 ± 0.2	5.9 ± 0.4
	[163]	10.11	6.11
	[56]	13.6 ± 0.5	5.7 ± 0.5
	[175]	10.528	5.39
	[162]	–	~ 5.2
	This work*	10.06 ± 0.07	4.8 ± 0.5
510	[165]	12.96 ± 0.2	5.82 ± 0.4
	[162]	–	~ 6.5
	This work*	12.81 ± 0.08	6.1 ± 0.6

* Values obtained from the average of RH and LH results

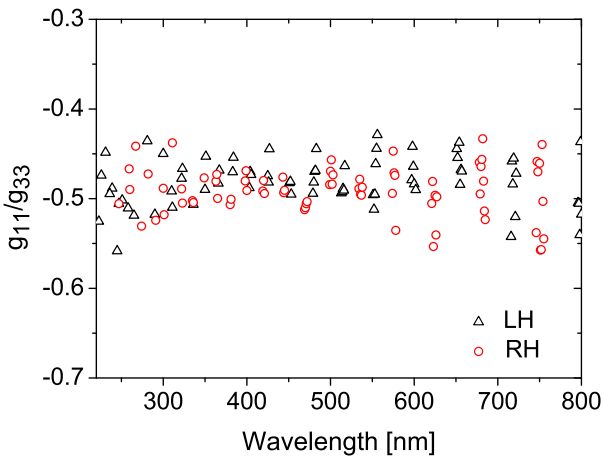

Figure 7.10.: Ratio of the two independent gyration tensor components g_{11}/g_{33}.

cal axis. The objective of applied methodology has been the measurement of the ellipticity for the waves that transmit unchanged in their state of polarization through the crystal. For directions out of the optical axis the ellipticity of these waves is very small and precise measurements require a highly sensitive experimental approach, such as provided by a transmission 2-MGE experiment. To

our knowledge this is the first description of a systematic methodology to obtain spectroscopic measurements of the optical activity in crystals for direction out of the optic axis.

The presented results show the ability of the 2-MGE to deal with the phenomenon of optical activity in presence of linear birefringence. Although the 2-MGE is a suitable instrument for this kind of measurements, we have presented a general approach accessible to any instrument capable of measuring a sample Mueller matrix, so this method could be applied in several laboratories using different types of Mueller matrix polarimeter.

Another advantage of this technique is that different components of the gyration tensor of the crystal can be determined without having to use samples cut according to several different crystallographic planes. This is because we do not exclusively analyze light transmitted in directions perpendicular to these planes, besides we also use a more general oblique incidence configuration where more than one component of the gyration tensor contributes to the observed optical activity. As a clear example in this chapter we have measured the g_{11} and g_{33} components of quartz using only a z-cut crystal with light incident at 60° from the optic axis. In this configuration both components g_{11} and g_{33} contribute to the optical activity, but as g_{33} can be well determined from normal incidence measurements the only remaining incognita is g_{11}.

We envision that a similar approach to the one presented here can be used for several other crystals with point groups 3, 4, 6, 32, 422 and 622 (International notation), which are optically active and have linear birefringence. Moreover, this technique may also be useful for crystals with point groups $\bar{4}$ and $\bar{4}2m$ which do not show optical activity for light propagating along the optic axis, but do show optical rotation in directions where there is also birefringence.

Chapter 8.

Chiral induction by hydrodynamic effects

In recent years the induction of chirality by hydrodynamic forces has been a focus of interest and debate in chemistry. This interest has attracted new experimental efforts in an attempt to understand a phenomenon that still is quite unknown and that, until very recently, remained mostly unexplored.

The action of mechanical forces originated by flows on chemical phenomena has been generally considered to be insignificant. Consequently the experimental observations claiming that flows can play a certain role in the emergence of supramolecular chirality were surprising and, at some point, remained controversial. Two pioneering reports, published in 1976 [177] and 1993 [178], initiated the investigation on two different species of molecular aggregates. However, they were widely refuted because their results were not easily reproducible and the mainstream opinion was to associate them to measurement errors. The first report which demonstrated the inductive effect of flows on supramolecular chirality, was published by the group of Ribó in 2001 [179]. It showed that the direction of stirring in a swirling vortex can be irreversibly transferred to the chiral sign of the CD-spectra for a certain type of porphyrin J-aggregates.

Many investigations dealing with this subject have been carried out in some supramolecular species of J-aggregates. These type of aggregates tend to be thin and long-shaped particles that, even in solution show relatively strong linear polarization-dependent optical effects (if there exists some level of orientation). Solutions of these aggregates constitute a good example of optically anisotropic liquids, in which the measurement of the optical activity by using the Mueller matrix method described in this thesis is a fairly more accurate approach than conventional chiroptical methods.

During the development of this thesis a large number of experiments on this subject were performed but in this chapter only some most remarkable ones will be presented. *A priori* it was important to study this phenomenon extensively because of the great number of factors that could be involved in the experiments (species of aggregates, level of aggregation, size of aggregates, geometry of the cuvette, stirring speed, etc), but also, and none less important, to assure the reproducibility of each one of the described measurements.

8.1. Spectroscopic measurements

8.1.1. Porphyrin aggregates

Porphyrin aggregates considered herein have an UV/Vis absorption band that is clearly separated from those of their monomers, so that the dichroic contributions can be easily studied in spite of the presence of monomer species in the solution. We have measured J-aggregates of the porphyrins $TPPS_1$, $TPPS_{2o}$, H_2TPPS_3 and H_2TPPS_4. All of them are achiral amphiphilic porphyrins and their J-aggregates have thin long acicular shapes (nanoribbons).

In Ref. [179] it was shown for the first time that the chiral sign (understood as the sign of CD spectra) of the H_2TPPS_3 porphyrin could be selected by the direction of vortical stirring during the formation of the J-aggregates. This was an irreversible induction of CD and it did not manifest in the other cited porphyrins, but constituted the first clear evidence that supramolecular chirality in porphyrin J-aggregates could be induced by hydrodynamic forces.

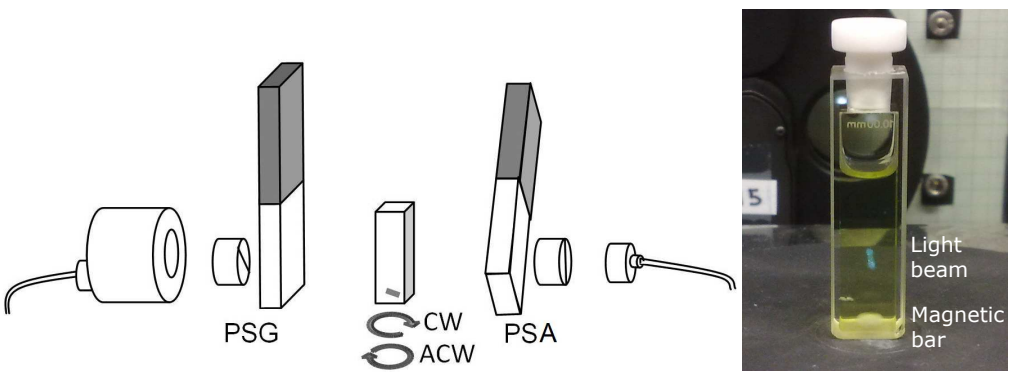

Figure 8.1.: Scheme of the experimental disposition used in the measurements involving a stirred cuvette. The cuvette was equipped with a small magnetic bar that, that in conjunction with a magnetic stirrer, permitted stirring in CW and CCW directions at a selectable speed. The light beam was directed to the central part of the generated vortex.

In the framework of this thesis we observed a surprising new type of induction when a cuvette containing a water solution of J-aggregates was *in situ* stirred while taking polarimetric measurements. In these J-aggregates the stirring effect caused and instantaneous and reversible emergence of CD, i.e. the observation of a certain sign or just the opposite one depended on the direction of stirring during the measurement. This effect has been reported in a number of recent publications that contained interpretations not really supported by experiments [180–182]. Our approach to the problem has been directed towards the

obtention of as much information as possible from polarimetric experiments on stirred solutions.

Fig. 8.1 shows the basic experimental setup used for the measurements presented in this section: the solution was contained in a 10 mm pathlength square section quartz UV/Vis cuvette. During the spectroscopic measurement of the Mueller matrix the cuvette was *in situ* stirred at a constant speed in clockwise (CW) or counter-clockwise (CCW) directions using a small magnetic bar.

We first observed this reversible mechanical induction of supramolecular optical activity in J-aggregates of H_2TPPS_4 and it is the porphyrin that we have studied more in detail. The size and shape of the H_2TPPS_4 J-aggregates depend on the procedure of their preparation[1]. The H_2TPPS_4 J-aggregates, as inferred from the AFM analysis, are straight nanoribbons about 200 nm long, 50 nm wide, and with a thickness of 3.2 nm (bilayer structure), but those in aged solutions can show lengths in the μm range and thicknesses of 4.8 nm (see Fig. 8.2).

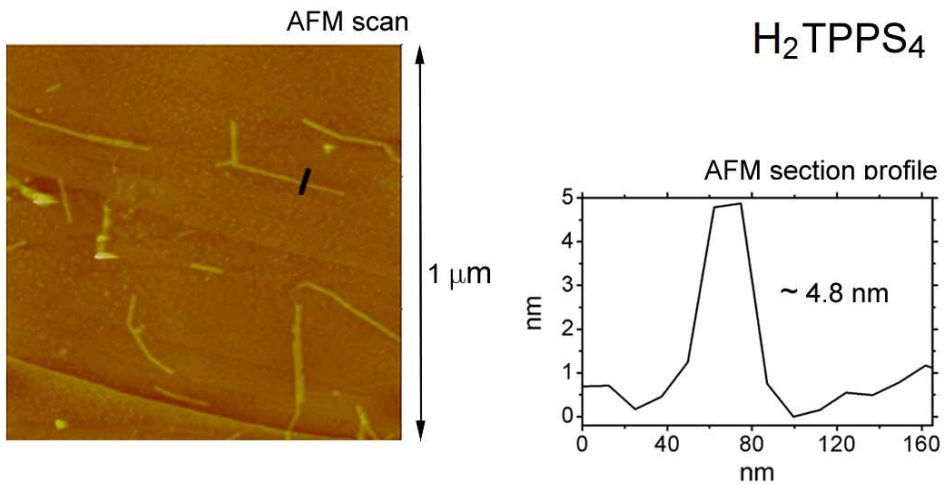

Figure 8.2.: AFM topography with section analysis of aged H_2TPPS_4 J-aggregates.

Spectroscopic Mueller matrix measurements of a solution, prepared from 25 μ**l** of an aged solution (one year old) of H_2TPPS_4 $1.4{\cdot}10^{-3}$ M were taken in the central part of the generated vortex at each nm in the interval from 350 nm to 800 nm with 1 nm resolution, so that, 451 nm normalized Mueller matrices were measured for each sample configuration (stagnant, CW and CCW). Fig. 8.3 depicts spectroscopic generalized ellipsometry data in the interval range between 400 and 600 nm for the aggregated porphyrin. Considerable differences between

[1]The details about the preparation of the aggregate solutions can be checked in Refs. [183,184].

the stagnant (no stirred) solution and the CW and CCW stirred solutions are observed except for the elements of the diagonal. In particular, for the elements of the anti-diagonal (m_{03}, m_{12}, m_{21}, m_{30}) dramatic differences between the CW and CCW directions are seen.

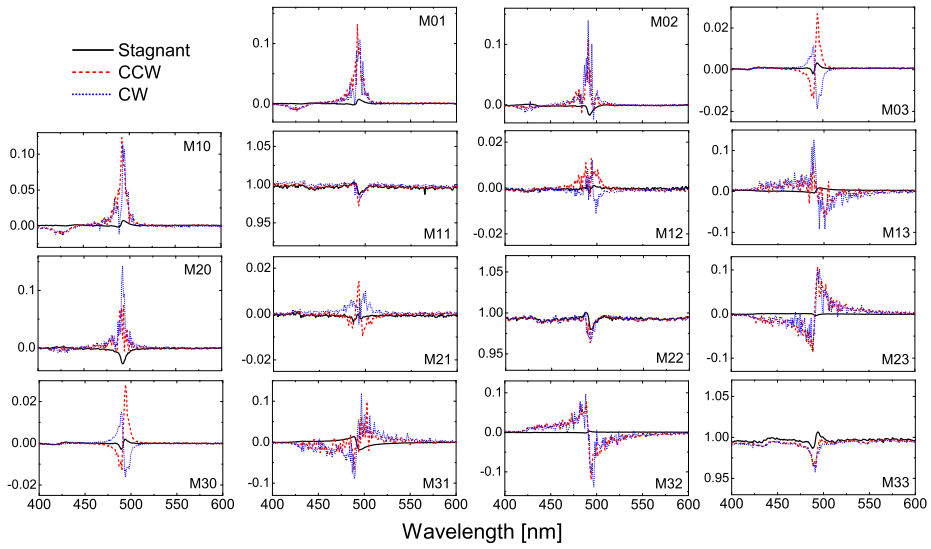

Figure 8.3.: Detail of the experimental normalized spectroscopic Mueller matrices for CW stirring, CCW stirring and stagnant (no stirring).

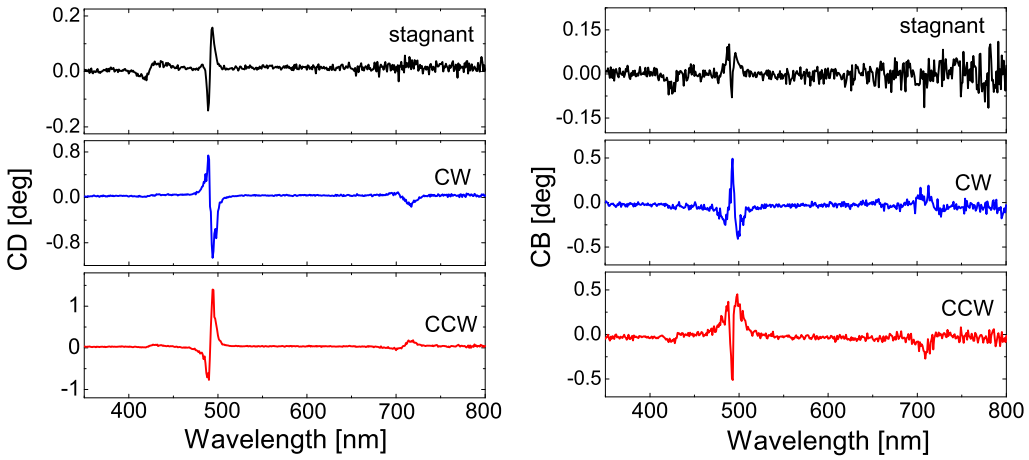

Figure 8.4.: Spectroscopic determination of CD and CB as a function of the stirring direction.

Fig. 8.4 shows the CD and CB wavelength dependencies obtained from the data analysis following the analytic inversion method (introduced in section 4.1) of the experimental matrices shown in Fig. 8.3. The J-aggregates of H_2TPPS_4 in stagnant solutions show a permanent low intense CD signal (< 0.2 deg.) because this molecule is chiral, but by vortex stirring a much intense CD signal emerges (~ 1 deg.) Thus, the natural chirality of the porphyrin is overruled by the mechanical stirring effect and the chiral sign is determined by the stirring direction. Also, the wavelength dependence of the measured CD spectra is bisignate and is Kramers-Kronig consistent with the measured CB spectra. This consistency can be easily verified if we compare the CB profiles of Fig. 8.4 with the theoric CB spectrum corresponding to a CD bisignated shown in Fig. 4.3: the expected type of correspondence between CD and CB is found experimentally.

The reversible flow-induced CD was also detected for the micelle-like aggregates of the porphyrin $TPPS_1$, the J-aggregates of the $TPPS_{2o}$ porphyrin, but the CD spectra of the H_2TPPS_3 J-aggregates was not sensitive to the stirring [183]. In the case of the H_2TPPS_3 there exists an irreversible mechano-chiral effect during the aggregation process [179] but, once induced, the CD spectra remains unchanged independently of the stirring direction. Although the J-aggregates of the porphyrins showing the irreversible and the reversible effect belong to different compounds, (H_2TPPS_3 and H_2TPPS_4 respectively), there is no chemical reason to expect different signs of the CD for the chiral exciton arising by folding or bending of the mesophases of these two different compounds.

In the following sections we will present new experimental data that will offer us additional information about this phenomenon and we leave to the last part of the chapter the explanation underlying in these experimental measurements. However at this point and, in order to motivate the contents of the following sections, it is worth to anticipate that our hypothesis is that the emergence of chirality through the effect of the hydrodynamic forces originated by a swirling vortex must be related to the feasibility of the flow to orient, fold and twist the particles in the fluid. Consequently, the shape and the elasticity of the aggregates as well as the characteristics of the flows in the cuvette may have influence on the occurrence of this phenomenon.

Cuvette geometry. Cylindrical flasks

The evidence that the flow regime inside the cuvette was responsible for the observed induction of supramolecular chirality made us suspect that the stirring experiment might yield different results placing the solution in containers of different geometry. To study this possibility, the stirring experiments on solutions of the H_2TPPS_4 porphyrin were repeated in the same conditions as in the

previous section but, in this case, using cylindrical flasks as containers. These experiments revealed that the CD values obtained from Mueller measurements in stirred cylindrical flask where substantially different to our previous results, as Fig. 8.5 shows.

In the case of an square section cuvette the sign and intensity of the CD showed a low dependence on the rotation speed, for example, they were quite similar for 1500 rpm and 5000 rpm (see left column of Fig. 8.5). In contrast, we found that the CD values in the cylindrical flask were strongly dependent on the rotation speed. At low rotation speeds the CD signals did not have a well defined sign and showed a noisy pattern (top right panel of Fig. 8.5). However, at a high rotation speed a clear bisignated CD signal emerged (bottom right panel of Fig. 8.5), but it was of opposite sign to those obtained in the square section cuvette.

The differences in the determined CD spectra can be explained on the basis of the flow regime dependence with the cuvette geometry. Fig. 8.6 shows a schematic representation of the flow patterns for a square section cuvette and a a cylindrical flask. The main difference between the two cuvettes is that the ascending flow is irregular for the square section cuvette whereas for the cylindrical flask is chiral. These patterns have been observed by video recording at the millisecond-range of the frames [185]. Thus, in the case of the cylindrical flask, due to the presence of the ascending chiral flow around the walls, stirring would be expected to lead to two mechano-chiral effects of opposite sign: a descending vortex in the middle region and an ascending vortex around the walls. Therefore, the CD signal observed in our transmission experiments (light propagation orthogonal to the long flask axis) must correspond to the addition of two CDs of opposite sign. Obviously, as the rotation speed of the magnetic bar increases more liquid is expelled towards the walls, the gradients of shear rate at the flask wall increases and its effect overcomes that of the central vortex.

The observed different flow regimes as a function of the geometry of container explains the previous results on the irreversible stirring effect observed during the formation of the J-aggregates of H_2TPPS_3. In those experiments [179, 184] solutions were stirred at high rotation speeds in small cylindrical tubes (0.8 cm diameter), where the correlation between the CD sign and the stirring direction must be attributed to the ascending flow.

According to our interpretation, in the square section cuvette the CD signal would only emerge in the middle of the cuvette and not at its walls because the irregular flow in the walls would yield a racemic mixture or a small chiral bias of folded/bent mesophases. Therefore, the chiral bias observed would be caused by the gradients of shear rate in the descending vortex in the center of the cuvette which acts as an attractor of the particles in solution. Spatially resolved measurements, presented later in this chapter, reveal that in square-

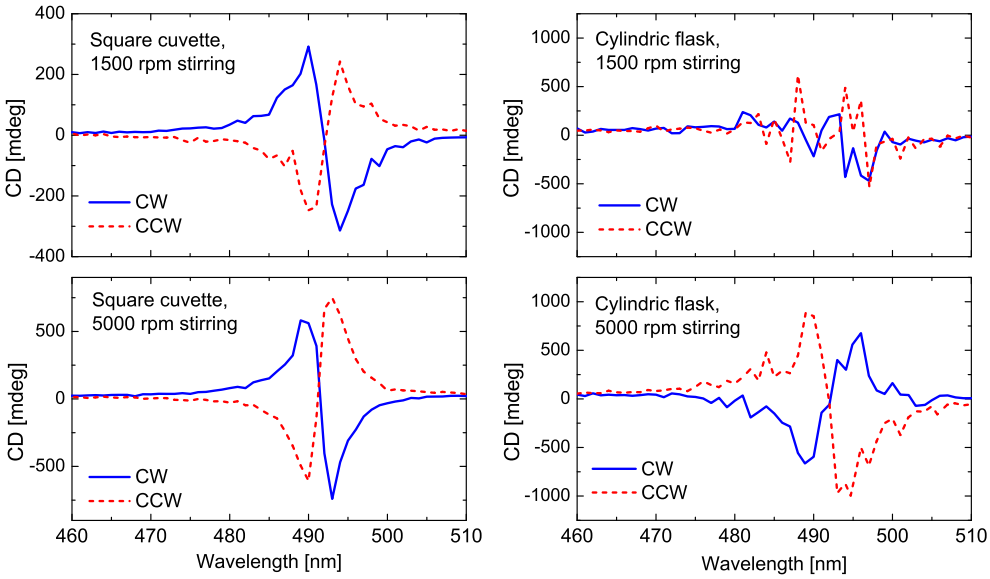

Figure 8.5.: Comparison of the CD spectra obtained at different stirring speeds for square section and cylindrical section cuvettes.

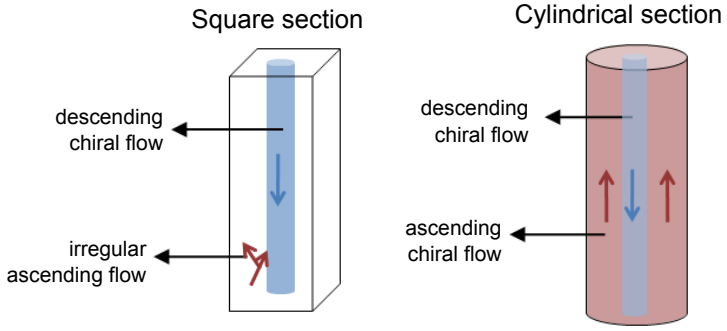

Figure 8.6.: Schematic representation of the flow pattern for two different cuvette geometries.

section cuvettes the CD emergence only takes place in the central part of the cuvette.

Polarization-independent transmittance/absorbance measurements confirm the above results. In the square-section cuvette, stirring led to significant changes in the absorbance values compared to stagnant conditions (see panel a of Fig. 8.7); in the central part of the cuvette there was an increase of absorbance in the J-aggregate bands (490 nm and 705 nm), but no absorbance differences were detected for the monomer absorption (434 nm). In contrast, measurements took

on cylindrical flask did not show such absorbance changes.

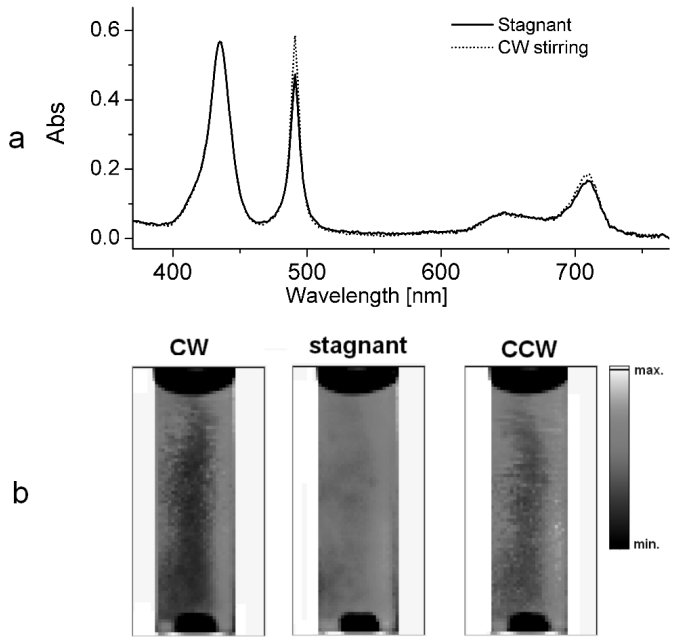

Figure 8.7.: Panel a: Absorbance of stirred and stagnant solutions of long-shaped H_2TPPS_4 J-aggregates in the central part of a square section UV/Vis cuvette (1 cm). There are changes for the J-aggregate absorption (490 nm and 705 nm bands) but not for the diprotonated monomer (434 nm and 650 nm bands). Panel b: Cuvette mapping of the polarization-independent transmittance at 490 nm (J-aggregate band) for stirred and stagnant solutions. It shows the attractor role of the central descending vortex upon the J-aggregate particles. These intensity mappings were obtained as a complement of the measurements that will be shown in section 8.2.

8.1.2. Rosette nanotubes

The induction of optical activity upon stirring was observed in a different system from the porphyrin J-aggregates presented above. We carried out experiments with stirred solutions of a new class of adaptive nanotubular architectures know as rosette nanotubes (RNT) resulting from the self-assembly and self-organization of biologically inspired materials [186–188]. The results presented here correspond to solutions of organic compounds featuring 2 synthetic heterobicyclic base (G∧C) that contain the hydrogen bonding arrays of the DNA bases, guanine and cytosine, on opposite faces of the molecule. This twin system self-assembles

spontaneously to form a six-membered supermacrocycle (rosette) maintained by 18 H-bonds, which in turn self-organizes into stable and architecturally complex 1-D helical stacks defining an unoccluded central channel, the rosette nanotube (Fig. 8.8). The diameters of the nanotubes are about 5 nm, while they can have lengths of several hundreds of nm. The nanotube RNT samples were provided by H. Fenniri[2].

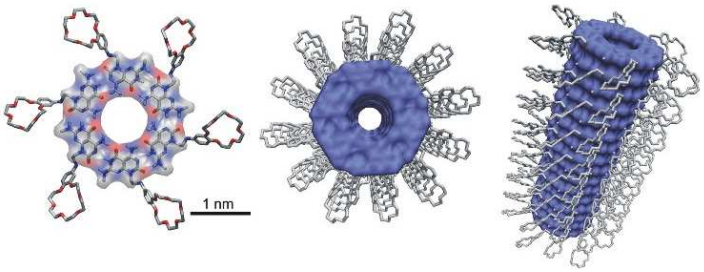

Figure 8.8.: Rosette structure obtained from the self-assembly of 6 G∧C motifs (left). Middle and right figures show, respectively, a top and side views of the rosette nanotubes.

Fig. 8.9 shows the measured spectroscopic Mueller matrix normalized to the m_{00} element for CW and CCW stirring of a methanol RNT solution contained in a square section cuvette. Samples were scanned from 235 - 340 nm in intervals of 1nm using the spectroscopic mode of the quartz-assisted method using 0.25 mm thick quartz plates. The CD profiles shown in Fig. 8.10a were calculated from the analytic inversion of the Mueller matrix in Fig. 8.9 and evidence the induction of chiral sign as function of the direction of stirring. Note from this figure that the measurement with 2-MGE in stagnant configuration on RNTs solutions did not yield any discernible value of CD. However the sensitivity of our 2-MGE at wavelengths around 240 nm is not sufficient to discern CD from noise in samples with circular dichroic signals below 10 mdeg. The total in-plane linear dichroism LD_m is taken as $\mathrm{LD}_m = (\mathrm{LD}^2 + \mathrm{LD}'^2)^{1/2}$ and is displayed in Fig. 8.10b. Analogously, the in-plane linear birefringence LB_m is $\mathrm{LB}_m = (\mathrm{LB}^2 + \mathrm{LB}'^2)^{1/2}$ and it is shown in Fig. 8.10c. The great values of LD_m and LB_m obtained for CW and CCW stirring show that, as result of the vortical flows, the long shaped RNTs increase their degree of orientation with respect to the stagnant configuration.

An interesting fact is that RNTs that are not made of twin compounds (i.e. they feature only a single G∧C) do not show any change in CD upon stirring, something similar to what happened to the H_2TPPS_3 described in the previous section.

[2]National Institute of Nanotechnology, Department of Chemistry, University of Alberta, Canada.

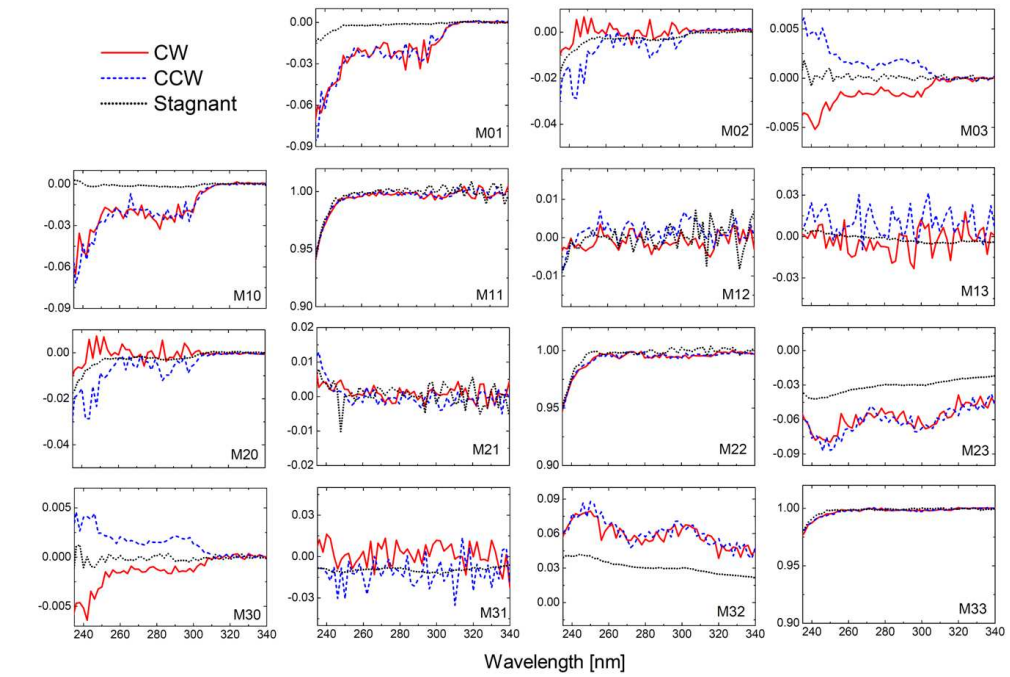

Figure 8.9.: Normalized spectroscopic Mueller matrix of a solution of RNTs obtained for CW and CCW stirring and no stirring (stagnant).

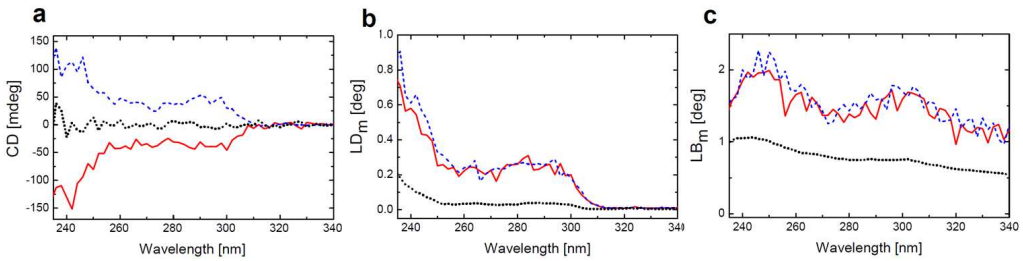

Figure 8.10.: Comparison of the retrieved optical effects for CW stirring (solid line), CCW stirring (dashed line) and stagnant (dotted line).

At the moment we have not extracted any final conclusion of these different behaviours, but we think that they can be significant in the near future for a further understanding of the phenomenon.

8.2. Spatially resolved measurements in square section stirred cuvettes

Spectroscopic measurements taken at different zones of the square section cuvette (for example comparing the central part to a lateral) had shown differences in the measured effects [183]. This motivated the necessity to obtain a map of the optical polarization properties of the entire cuvette in order to be able to detect differences on the measured effects at the different parts of the container. Consequently, spatially resolved measurements were performed in square section stirred cuvettes following to the methodology described in chapter 6. For cylindrical flasks spatially resolved measurements are not possible because of the reflections produced by the non-planar flask surface in the laterals.

The experiments shown in this section where performed with a solution of H_2TPPS_4 J-aggregates in stagnant and stirred conditions. Figs. 8.11, 8.12 and 8.13 show, respectively, the normalized scanning Mueller matrices for no stirring, CW stirring and CCW stirring. All three measurements were recorded with the same sample and using a beam spot with a diameter of 1.5 mm. Each complete Mueller matrix mapping was done in about 20 minutes.

The optical effects CD, CB, LD, LB, LD′ and LB′, calculated with the analytic inversion of the measured Mueller matrices, are displayed in Fig. 8.14. These results confirm that the induction of optical activity takes place in the central part of the cuvette (see Fig. 8.14), in coincidence with the central chiral descending vortex. At 485 nm the switch of optical activity is clearly visible in the CD maps, because this wavelength corresponds to the high-energy peak of a bisignate CD absorption band. For the CB the change of sign can also be noted, but is less appreciable because this wavelength does not correspond to any peak of CB.

The values of LD and LD′ (or alternatively LB and LB′) presented in Fig. 8.14 can be used to construct a vectorial representation of the measured projections of linear dichroism (see Fig. 8.15). The length of the vectors, l, and their orientation with respect to the horizontal laboratory axis, θm have been calculated according to

$$l \propto \sqrt{\mathrm{LD}^2 + \mathrm{LD}'^2}, \tag{8.1}$$

$$\theta = \frac{1}{2} \arctan \frac{\mathrm{LD}'}{\mathrm{LD}}. \tag{8.2}$$

The vectors drawn can be correlated with the average orientation of the nanophases in the solution.

Figure 8.16 shows a superposition of the CD false color map and calculated axes of linear dichroism. For both, CW and CCW stirring, there appears to be a small bend of the vortex axis at the top of cuvette. This fact allows areas

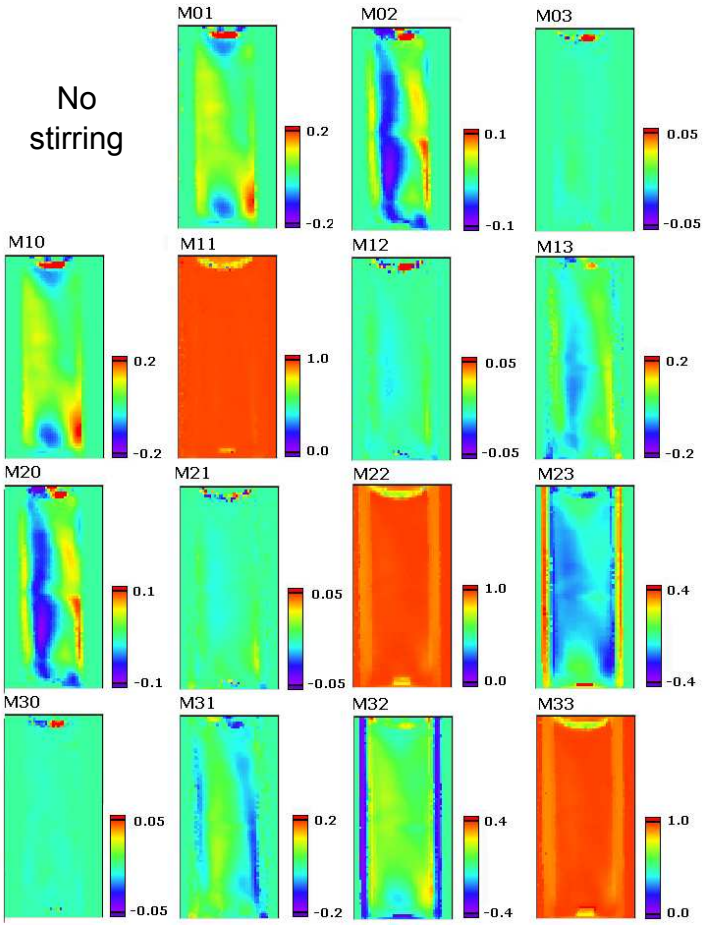

Figure 8.11.: Normalized spatially resolved Mueller matrix of a stagnant solution of H_2TPPS_4 J-aggregates measured at 485 nm. The dimension of each frame is 29 mm × 14.4 mm and each pixel measures 0.35 mm × 0.35 mm.

with weak flows (top-left corner for CW stirring and top-right corner for CCW stirring), where the particles can maintain more stable orientation, yielding big values of LD and LD′ that translate in longer vectors.

8.3. Discussion

The phenomenon reviewed in this chapter represents the selection of the chirality of a supramolecular structure, i.e. a process of chiral symmetry breaking. The first published interpretation [181, 182] about vortex-induced optical activity attributed this phenomenon to a cholesteric-like alignment of the particles in the

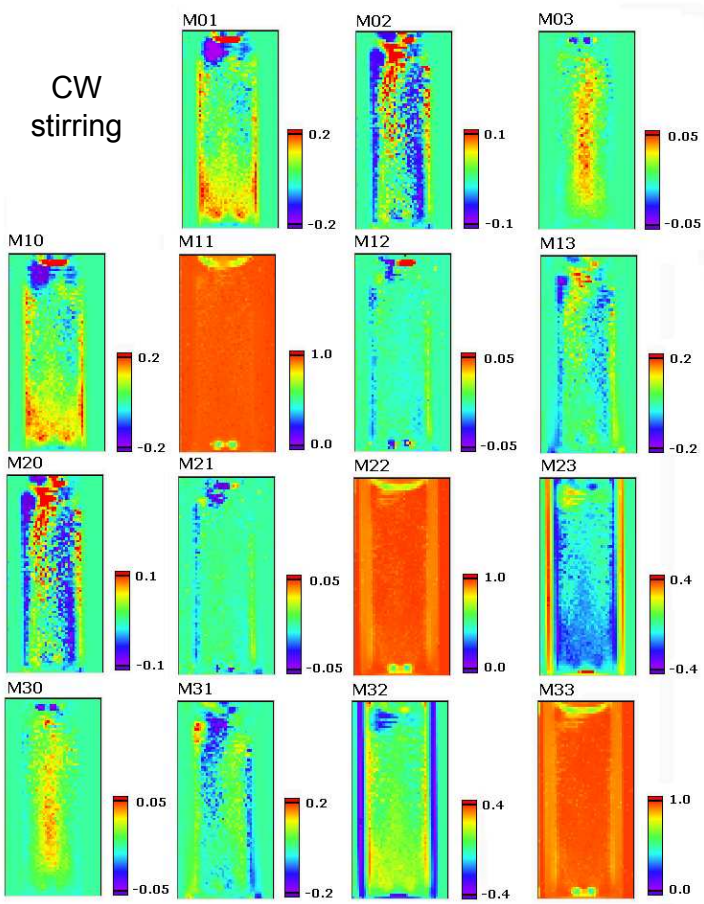

Figure 8.12.: Normalized spatially resolved Mueller matrix of a CW stirred solution of H_2TPPS_4 J-aggregates measured at 485 nm. The dimension of each frame is 29 mm × 14.4 mm and each pixel measures 0.35 mm × 0.35 mm.

stirring vortex analog to the twisted-crystal structure described in section 3.2.4. According to this interpretation the observed CD would be due to the macroscopic arrangement of the aggregates, but not due to structural changes in the interacting chromophores of the aggregates. This is an elegant explanation but it was proposed without any further demonstration. Even leaving aside the fact that it is questionable that a vortical stirring would result, in a square-section cuvette, to a perfect helical arrangement of the nanofibers in the light path as the one they described, we do not think that such arrangement is responsible for the measured signals. There exist several reasons that support this opinion:

i) A supposed vortex-induced macroscopic helical arrangement would have an

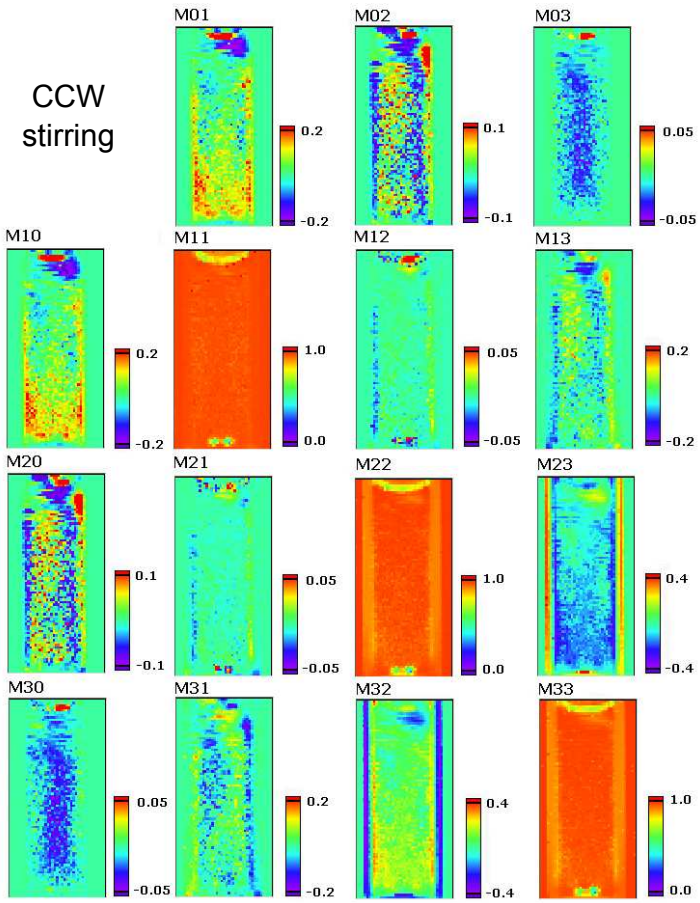

Figure 8.13.: Normalized spatially resolved Mueller matrix of a CCW stirred solution of H_2TPPS_4 J-aggregates measured at 485 nm. The dimension of each frame is 29 mm × 14.4 mm and each pixel measures 0.35 mm × 0.35 mm.

approximate pitch of twice the dimensions of the cuvette (20 mm for the 10 mm pathlength cuvette used), which is several orders of magnitude greater than the wavelength of light. Therefore, from the point of view of the light beam, the helical arrangement would act as an inhomogeneous medium. However, the measured spectroscopic Mueller matrices do not have the exotic profiles found in inhomogeneous systems described by a sequence of optical elements. Quite the contrary, the simple interpretation of the spectroscopic profiles according to the homogeneous model introduced in chapter 3 yields the expected simple and Kramers-Kronig consistent values of linear dichroism and linear birefringence of a molecular absorption band.

ii) Table 8.1 shows that the stochastic errors associated to the LD, LB, LD′,

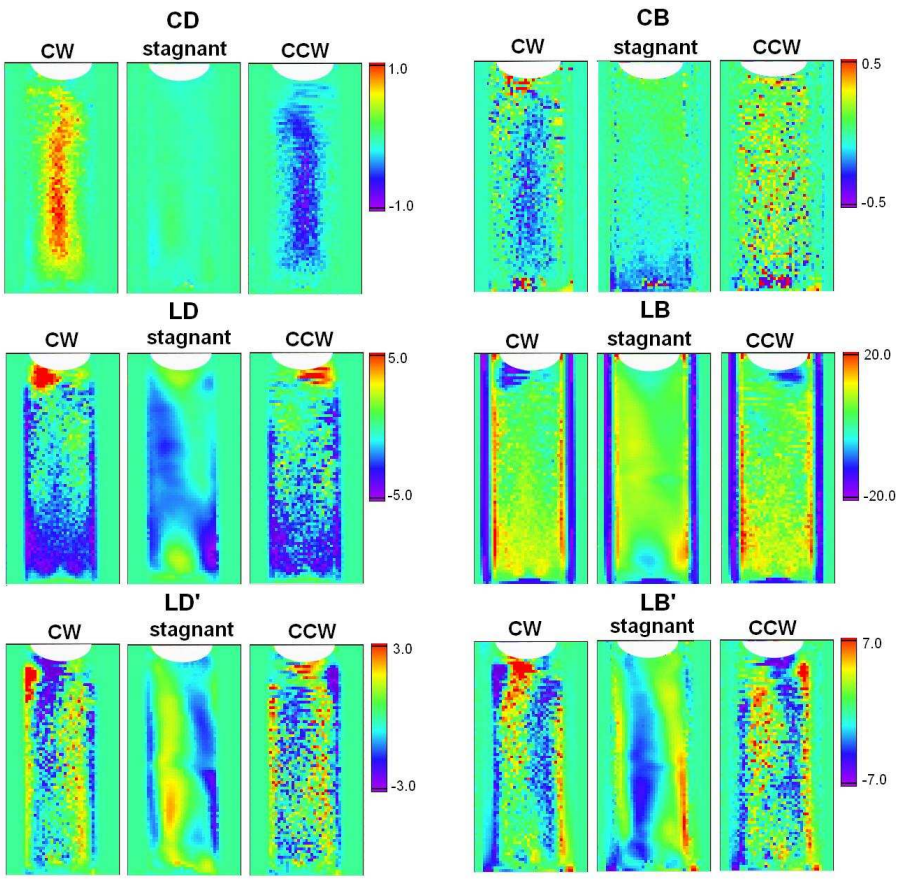

Figure 8.14.: Optical effects calculated from the scanned Mueller matrices. The scales are given in degrees.

LB′ effects suffer an important increase when switching from a stagnant measurement condition to a stirred situation. This is easily understandable considering that, when the stirring starts, immediate violent flows appear in the cuvette. The stirring mechanism supposes a new source of "noise" for the measurement of Mueller matrix, that acts by quickly changing the position and orientation of particles in solution. However, the errors of CD and CB, although they may show some logical increase, appear to be much less affected by the mechanical stirring than of linear effects. Fig. 8.17 shows that this behaviour is already appreciable when comparing the spectroscopic errors associated to the measurement of the Mueller matrix element m_{03}, that for this system is mainly contributed by CD, with the errors of m_{01}, here dominated by LD. The errors of these two Mueller matrix elements evolve to very different values when the stirring starts: while for

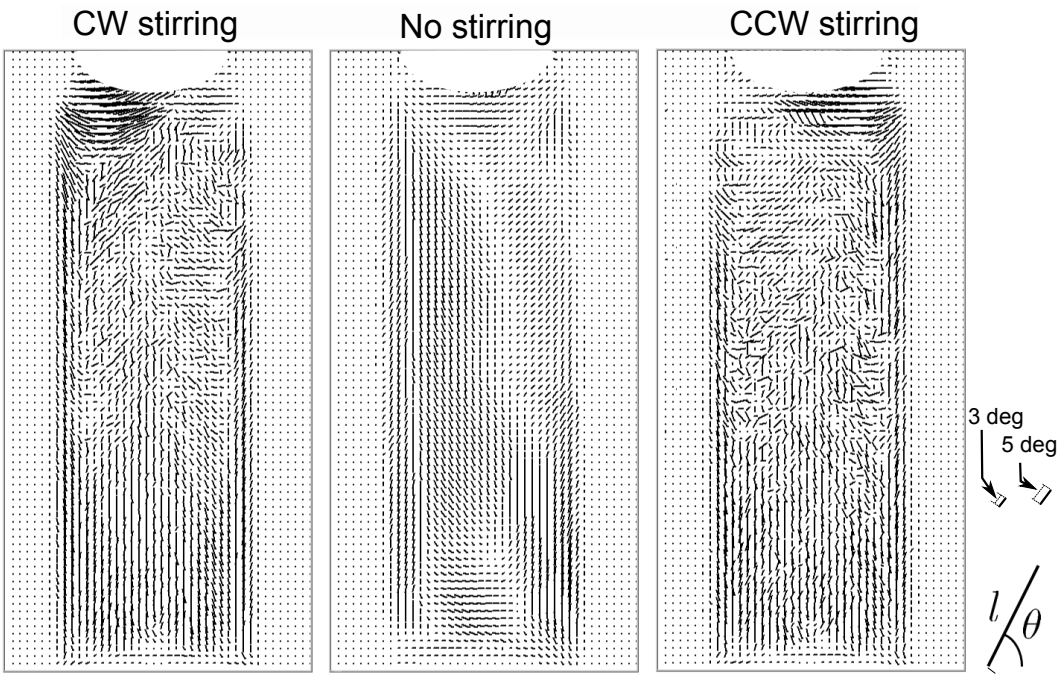

Figure 8.15.: Representation of the calculated axes of linear dichroism for the spatially resolved measurements of the cuvette in stagnant and stirred solutions. The length of vectors is proportional to the magnitude of linear dichroism $\sqrt{\mathrm{LD}^2 + \mathrm{LD}'^2}$. The approximate scale length of the vectors is given in the right margin of the figure.

m_{01} the measured standard deviation increases in nearly two orders of magnitude, the changes in the standard deviation of m_{03} are much more subtle. Therefore, the low noise observed for CD when stirring discards the formation of the proposed helical arrangement of the fibres, because it would involve greater noise levels than the observed ones.

iii) It is reasonable to think that an helical arrangement is possible in a cylindrical section cuvette. We envisage that in a cylindric flask such macroscopic helical arrangement could be more perfect than in the standard squared-section cuvettes. Therefore, if such macroscopic arrangement was responsible for the CD signal we should observe the same type of chiral induction in cylindrical flasks.

Another group [180] has recently pointed out that the deposition of chiral aggregates on the cuvette walls during prolonged stirring could have significant contributions to the measured signals. While we agree that a deposition of a certain amount of chiral aggregates in the cuvette walls can occur, none of our

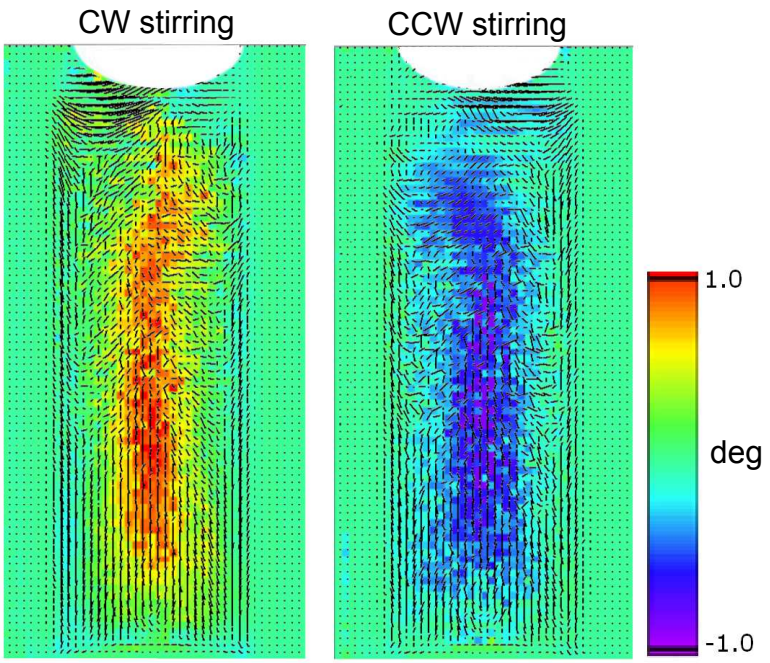

Figure 8.16.: Superposition of the CD color map (already presented in Fig. 8.14) with a vectorial representation of in-plane projection of the linear dichroism (Fig. 8.15).

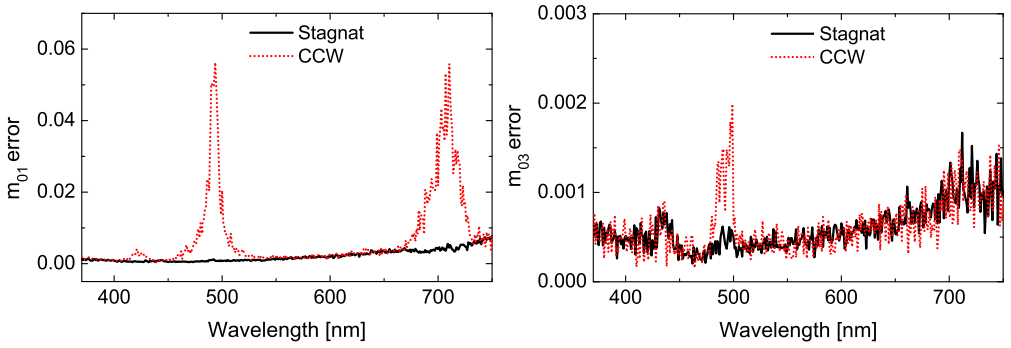

Figure 8.17.: Comparison of the errors associated to the measurement of the Mueller matrix elements m_{01} and m_{03} in stagnant and CCW stirring conditions. Element m_{01} is mainly contributed here by LD whereas element m_{03} is mainly contributed by CD.

experiments[3] have indicated a significant contribution from the wall-deposited

[3]These experiments consisted on measuring emptied cuvettes after leaving them several hours

Table 8.1.: Summary of the average errors[a] of the spectroscopic measurements made on stirred cuvettes

	Porphyrin J-aggregates (470-520 nm)[b]				RNTs (240-300 nm)[b]		
Parameter	CW	CCW	CCW_{cyl}[c]	stagnant	CW	CCW	stagnant
CD	0.0013	0.0011	0.0069	0.0005	0.0012	0.0011	0.0011
CB	0.0031	0.0032	0.0261	0.0016	0.0079	0.0078	0.0080
LD	0.0149	0.0152	0.0417	0.0007	0.0154	0.0151	0.0019
LD′	0.0130	0.0136	0.0456	0.0006	0.0124	0.0118	0.0016
LB	0.0159	0.0164	0.0435	0.0009	0.0164	0.0162	0.0018
LB′	0.0191	0.0204	0.0508	0.0011	0.0238	0.0274	0.0024

[a] The errors shown in this table are of stochastic nature and can be regarded as "noise" level of the measurements. All the errors are given in radians.
[b] The quoted average errors are the average of the errors in the interval 470-520 nm for the case of the porphyrin J-aggregates and in the interval 240-300 nm for the case of RNTs. These intervals correspond to the range of wavelengths where the induction of chirality is observed.
[c] CCW_{cyl} corresponds to a stirred experiment made in a cylindric cuvette. All the other columns of this table refer to measurements made in square section cuvettes.

aggregates to the observed effect .

Rather than rigid structures, the J-aggregates of the studied porphyrins are soft-matter nanophases that have been demonstrated to be foldable by effect of hydrodynamic forces [184]. The elastic characteristics of the H_2TPPS_4 and H_2TPPS_3 J-aggregates were studied by scanning probe microscopy techniques yielding typical results for soft polymers and without significant differences for both porphyrins [183]. The effect of mechanical forces on the conformational shape of macromolecules is well known: gradients of shear rate and viscous drag forces acting on the moving particles exert a net torque on the particles that may lead to folding and twisting. This effect will be greater when the elastic modulus of the particles is low, i.e. the reversible stationary effect described in this thesis would be due to a pure mechanical effect upon elastic mesophases and the irreversible effect would be due to a "freezing".

The surprising fact pointed out by the experiments reported in this chapter is that the deformation of a classical object (although nanosized) to a chiral shape is being detected at the level of the electronic transition[4]. The apparent size scale

containing stirred solutions of J-aggregates.

[4] In section 2.2.2 we showed how the excitonic transitions between chromophores are responsible for the CD signals.

paradox between macroscopically induced hydrodynamic forces and the changes detected in the electronic transitions disappears when it is taken into account that the phenomenon of light absorption involves the interaction of the photon with an exciton of the solid (the nano- or microparticles in suspension). The exciton structure may depend on the distortion originated by the hydrodynamic forces, i.e. the modified excitonic absorption may be intrinsically chiral. According to our perspective, the understanding of the nanosized aggregates of the solution would be not so different to those of metallic macroscopic helices (a free electron in a helix) where optical activity had already been detected by the year 1920, [189,190]. In our opinion the mechanical effect that manifests in the induction of optical activity by stirring would be assimilable to the effect of stress in certain symmetry classes of achiral crystals that makes them exhibit optical activity, a phenomenon that is referred as piezo-rotation or piezo-gyration [65, 191]. As piezo-gyration can only occur for certain groups of symmetry, our assumption that mechanical stress leads to changes of the gyration tensor could explain our experimental results that show that the stirring effect is observed in solutions of certain porphyrin J-aggregates or RNTs but not in others of the same family, if inducible and non-inducible systems belonged to different symmetry point groups. Future work should be oriented to identify the symmetry changes that occur in the nanophases when they are bent and/or folded under gradients of shear rates of flows.

Chapter 9.

Measurements on heterogeneous solid-state samples

This chapter groups experiments carried out in solid heterogeneous samples, for which the optical properties have been scanned in a selected area of their surface.

9.1. Chiral domain in crystallizations

One of the most promising applications of Mueller matrix polarimetry is to investigate chiral domains in transparent solid crystalline samples. When the structure or composition of the sample varies from point to point, imaging or mapping techniques are the only way to discern the different optical effects that may be present in the sample.

Many experiments involving the study of the chiral symmetry breaking occurring at solidification processes have been performed in sodium chlorate ($NaClO_3$). One of the main reasons for this selection is that sodium chlorate belongs to the cubic tetrahedral class and, therefore, as it is isotropic, the posterior identification of crystallites of different handedness is very easy. One of the famous experiments with $NaClO_3$ was done by Kondepudi [192], who noticed that the stirring of Na^+ and ClO_3^- ions solution caused all the subsequent crystals to adopt the same chirality. More recently Viedma [193] presented, in a related experiment, that an initially equal mixture of crystals in a supersaturated solution can achieve complete homochirality thanks to the action of grinding and stirring the crystals. With the experimental approach used in this thesis, we can go beyond cubic crystals and investigate other anisotropic solids that are of interest for the study of chiral symmetry breaking processes.

The experiments presented in this section deal with achiral substances in the liquid phase, that, after solidification, yield chiral enantiomorphs. The main difference with the experiments cited before is that, in our case, we were interested in systems made of one single chemical compound[1] so that from a thermodynamic

[1] Note that in the experiments by Kondepudi and Viedma there are two compounds: $NaClO_3$ and H_2O.

point of view the problem can be merely presented as liquid-solid phase transition. As from an effective point of view, left-handed and right-handed enantiomers are energetically identical and none of them should be preferred over the other, the identification and study of possible chiral domains after crystallization may be in close correlation with symmetry breaking scenarios.

9.1.1. Benzil polycrystalline films

Benzil is a molecular crystal; its molecules do not exhibit any optical activity when they are in solution [194], but they crystallize in the chiral enantiomorphic groups of symmetry D_3^4 or D_3^6 (the same group of symmetry than α-quartz). The crystal of benzil is built upon a hexagonal lattice and the unit cell accommodates three molecules disposed spirally around the trigonal axis [195]. Therefore the benzil crystal is uniaxial and shows optical activity, which at visible regions of the spectra manifest not only in CB, but also in CD because benzil molecules have absorption bands.

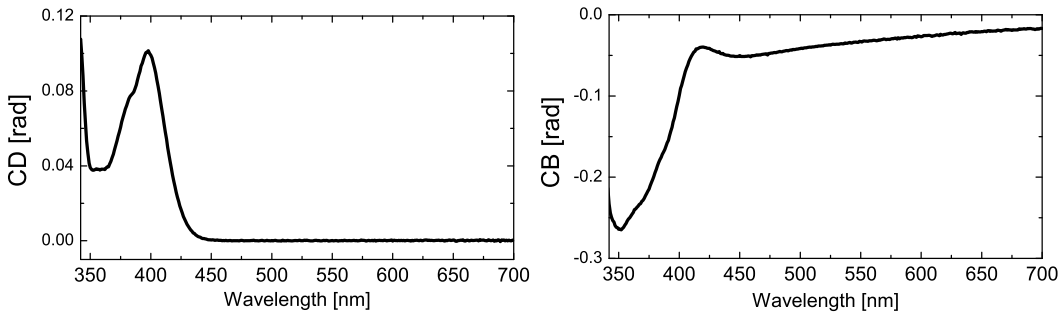

Figure 9.1.: CD and CB of a benzil crystal for light propagating parallel to the optical axis. These data were obtained from spectroscopic measurements of the Mueller matrix with the quartz-assisted 2-MGE in a small benzil crystal grown by evaporation.

Fig. 9.1 shows the CD and CB spectra of a benzil crystal for light propagating parallel to the optic axis. A CD absorption band centered around 400 nm can be clearly seen, while at higher wavelengths the crystal shows no CD, but its optical activity can still be traced with CB. As it is common for anisotropic crystals (see the case of quartz in chapter 7), optical activity in benzil can be easily measured for light propagating along the optical axis, but in other directions it is more difficult because linear birefringence and linear dichroism effects become important.

Benzil (1,2-diphenyl-1,2-ethanedione, Aldrich) was recrystallized twice from toluene, as means of purification, yielding six-sided prisms of about 5 mm in

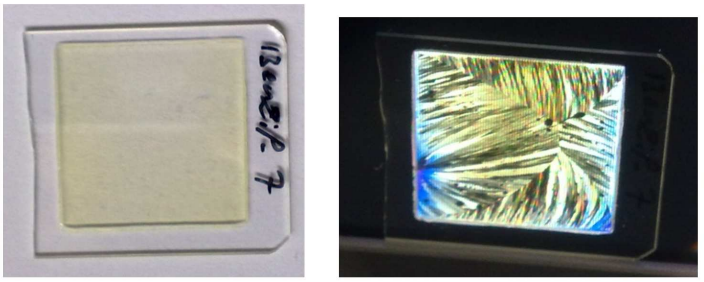

Figure 9.2.: The picture on the left shows one of the studied thin polycrystalline films of benzil under standard illumination. The picture on the right was captured after putting the same sample between crossed polarizers.

length. Later they were manually ground in an agate mortar to get a fine powder. 2-3 mg of the powder were sandwiched between a blank microscope slide and a glass cover slips. The slide was raised to a temperature above the melting point of benzil (378 K) in a hot stage, held for 15 minutes, and left to cool at room temperature. A polycrystalline film is eventually developed from the metastable melt. Fig. 9.2 shows the type of samples we obtained after this preparation process.

Most of the surface of the sample was scanned by the 2-MGE using the assistance of quartz plates to maintain a high lateral resolution during the measurement. Imaging representations of the transmission Mueller matrix of the sample in regions around 10 x 10 mm were obtained for several different samples (see one of them in Fig. 9.3). The pixel size used for generating these mapping plots is 60 μm, which is slightly below the optical resolution of the measurement (85-90 μm). In our case, this resolution is determined by the size of the light spot and the width and height of the monochromator slits placed before the detector.

Fig. 9.4 shows the CD, CB and fraction β of polarized light (1 for completely polarized and 0 for completely depolarized) calculated from the Mueller matrix of Fig. 9.3. Well delimited zones with CD values of opposite signs are observed. A similar separation is obtained for CB, but, in this case, it is not as well defined because the average error of this CB measurement (~ 0.003) is greater than the average error associated to CD (~ 0.001). Table 9.1 shows the typical values for several of the studied values, along with their average errors.

The small area delimited by a black square in Fig. 9.4 is presented in more detail in Fig. 9.5. This figure displays the vectorial representation of the projections of linear birefringence, calculated with Eqs. (8.1) and (8.2) but, in this case, using LB and LB' instead of LD and LD', superposed to the color map of CD. This superposition reveals that the boundaries between areas of positive and

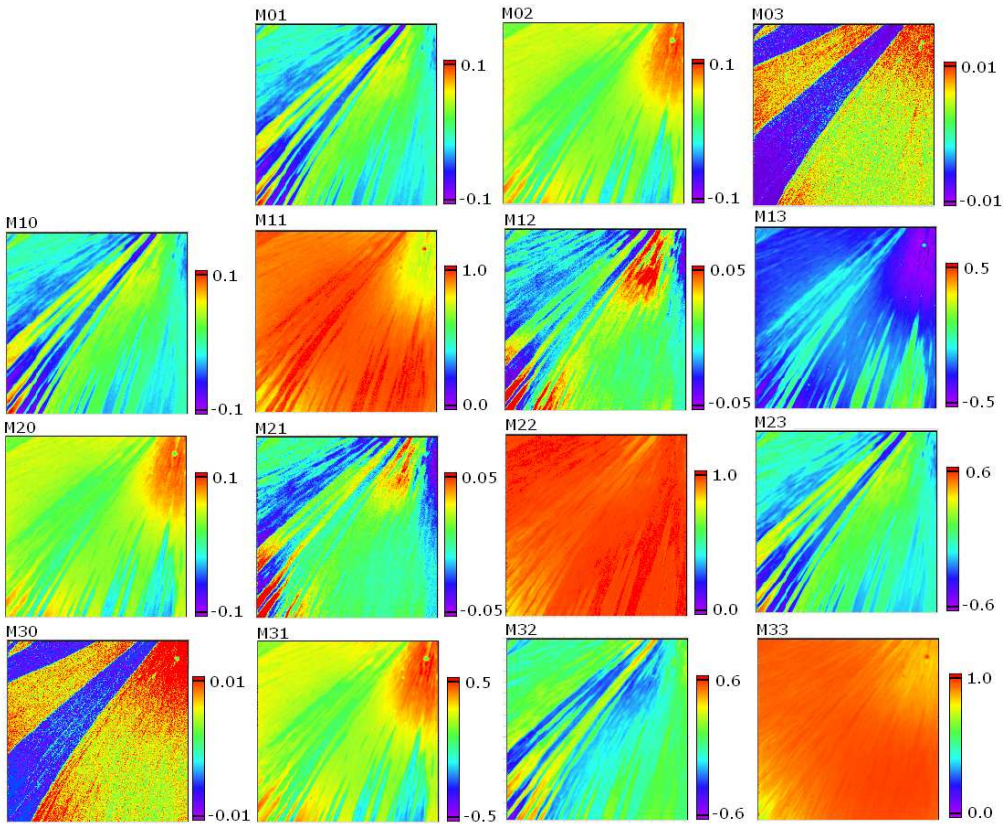

Figure 9.3.: Mapping of the normalized Mueller matrix of a thin polycrystalline film of benzil measured at 400 nm. It covers an area of 10×10 mm with a pixel size of 60×60 μm.

negative CD (mostly delimited by straight lines) do not correspond with changes on the orientation of the projected directions of the optic axis. Thus, zones in distinct false colour correspond to enantiomorphs otherwise in comparable optical orientations.

In Fig. 9.6 we show the positive and negative CD domains found experimental for several different benzil samples. In general, the formation of well-defined and spatially segregated chiral domains can be appreciated. The boundaries between areas of opposite sign of CD in benzil are in almost all cases straight lines. These results were interesting for us, because some theoretical works about dynamics of the Frank chiral amplification model, that leads to homochirality, already predict the formation of separate "colonies" of the two kinds of enantiomers bounded by racemic surfaces [196,197]. Such colonies could only survive if the two areas were delimited by a straight line. These works describe that any initial curvature in

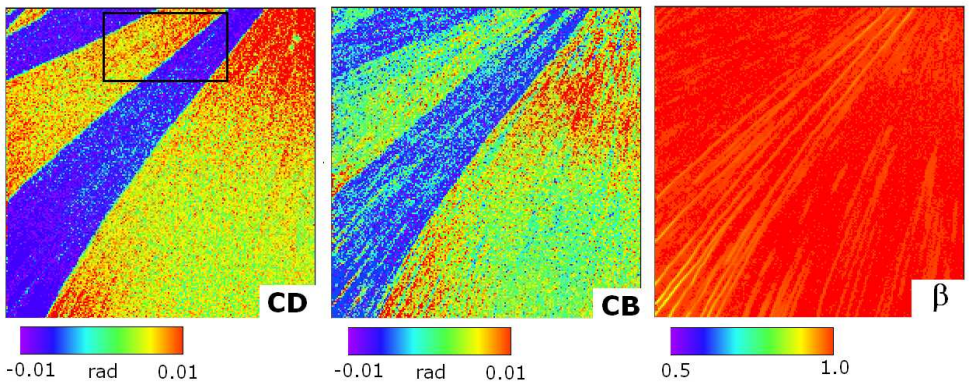

Figure 9.4.: Values of CD, CB and β obtained from the Mueller matrix of Fig. 9.3 using the inversion process of section 4.2. The black square of the right picture indicates the area that is presented with more detail in Fig. 9.5.

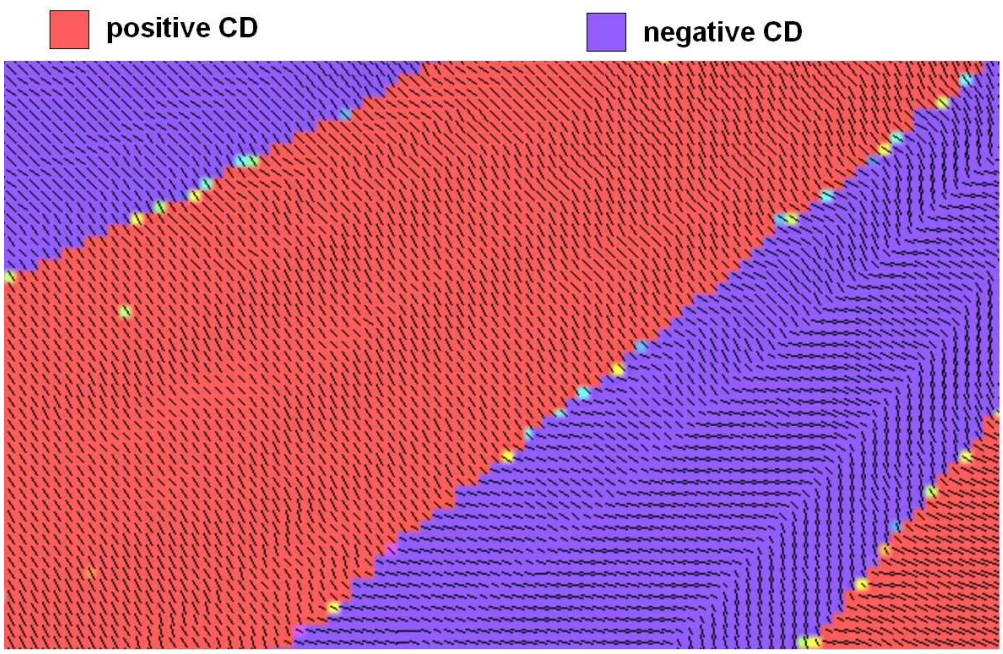

Figure 9.5.: Superposition of the CD color map (squared area in Fig. 9.4) with a vectorial representation of in-plane projection of the linear birefringence, also calculated from the Mueller matrix. The vectors of this figure correspond to linear birefringence projections with magnitudes around 0.5 rad.

these boundaries would make the boundary move towards the side from which it is concave and, as a consequence, one species will eventually shrink, and the

Table 9.1.: Summary of the measurements made on benzil films cuvettes

Parameter	Typical values	Average error[a]
CD	~ 0.007	0.0008
CB	~ 0.004	0.0026
LD_m^b	~ 0.07	0.0012
LB_m^b	~ 0.5	0.0020

[a] The average error is the average of the errors in all the 40000 points that compose the scan.
[b] $\mathrm{LB}_m = (\mathrm{LB}^2 + \mathrm{LB}'^2)^{1/2}$, $\mathrm{LD}_m = (\mathrm{LD}^2 + \mathrm{LD}'^2)^{1/2}$.

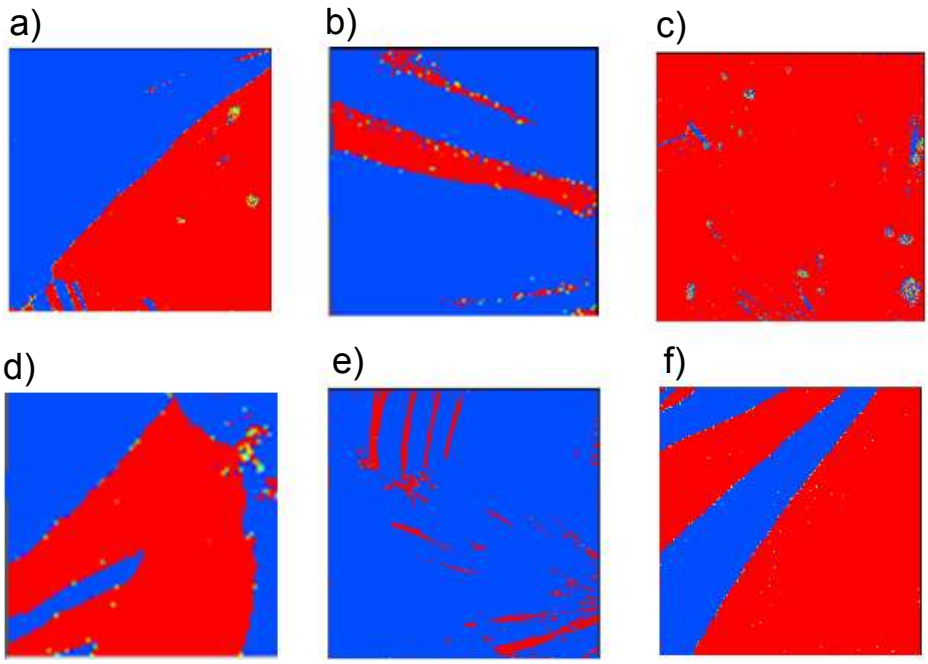

Figure 9.6.: Chiral domains obtained experimentally for several different benzil thin film samples. Colour red indicates positive CD, while negative values are represented in blue. Areas without a well-defined red or blue colour correspond to air blisters that were present in the samples. Case f) corresponds to the sample that has been presented in more detail in this section.

other will survive, giving situations where only one of the enantiomers would be present (for example the case c of Fig. 9.6 seems to be near to this situation).

Therefore, our results seem to be consistent with these predictions.

9.1.2. Other polycrystalline films

Analogous experiments to those of benzil have been performed with other organic compounds, in particular with benzophenone and binaphthyl. These samples were prepared in a similar way to benzil thin films, but taking into account that the heating/cooling process must be adjusted to the melting temperature of each substance. Nevertheless, the optical measurements of this compounds have carried many more problems than in the case of benzil. There are probably a variety of reasons for this different behavior; one of them is that this samples tend to show a more grained structure, where the crystallites appear to be very small and, eventually, superposed one to another. All these structural facts probably lead to scattering phenomena or interface effects that complicate the optical measurement. For example Fig. 9.7 shows that the depolarization introduced by these samples is quite stronger than in the case of benzil, as it is revealed when we compare the β values (calculated with Eq. 1.33) of Fig. 9.7 with those of Fig. 9.4. Another important issue is that these compounds do not have an accessible absorption band of CD in the visible as benzil (see Fig. 9.1). The identification of chiral domains in these compounds in the visible part of the spectra (which are the only wavelengths were the samples are transparent enough) should be done with CB, which is usually more difficult to recognize than CD because CB is more masked by linear birefringence than CD.

Despite these difficulties, our intention is to pursue more experimental work on this topic in order to identify other solids or other preparation methods that permit the extension of the study carried out in benzil to other organic compounds.

9.2. Meteorites

Although this section is situated at the end of this thesis, the measurements presented herein were chronologically obtained before most of the data shown in previous chapters. Also they are the only measurements presented in this thesis that were not obtained with the instrument described in Part III, that refers to the 2-MGE available in the facilities of the Faculty of Physics of the University of Barcelona. Instead, measurements of this section were also performed with a transmission 2-MGE but, this time, with one instrument built and kept by Gerald. E. Jellison at the Oak Ridge National Laboratory (Tennessee, USA).

In contrast to previous chapters, the conclusions we will reach in this section are somewhat speculative, mostly because the difficulty associated to meteorite samples is beyond our current technical capabilities for the analysis of complex

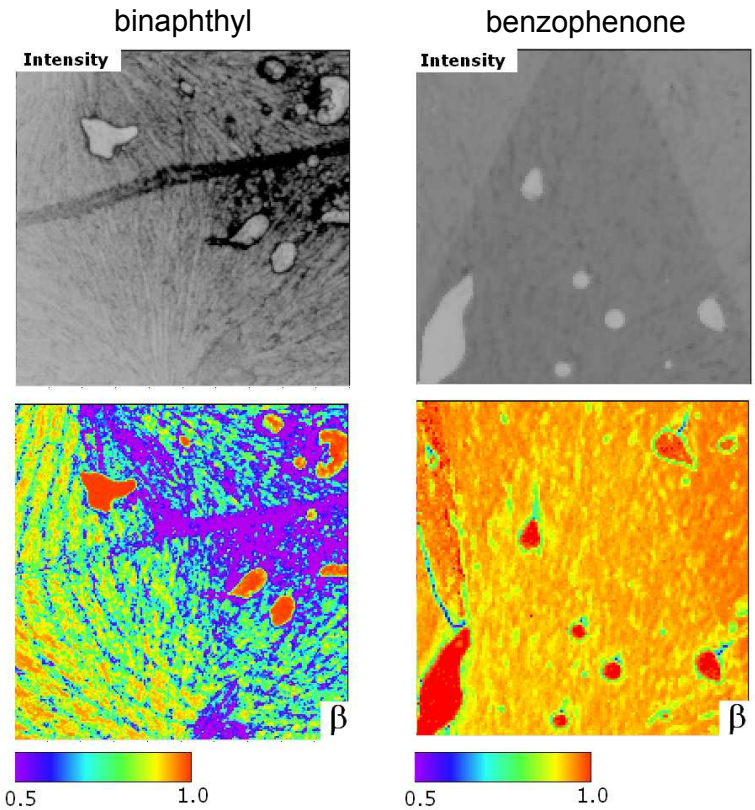

Figure 9.7.: Detected intensity and fraction of polarized light (β) for crystallizations of binaphthyl and benzophenone. Binaphthyl sample was scanned at 390 nm aver an area of 12×12 mm, while benzophenone sample was scanned at 370 nm over an area of 6×6 mm. The pixel size in both pictures is 80×80 μm. Round areas with fractions of polarized light close to 1 correspond to air blisters.

samples with polarimetry. Therefore, this section, rather than offering conclusive results, opens new perspectives for original and unprecedented work in polarimetry. The contents of this section are a summary of the results published in [198].

9.2.1. Motivation

The interest on meteorites in the scope of this thesis may sound a little awkward, but it supposes a continuation of our work about the study of processes of chiral induction that can act upon a specific chemical process showing spontaneous mirror symmetry breaking. Furthermore, the investigation reported here could be included in the more general topic of the understanding of the chemical evolution

towards biological homochirality (see section 2.3). In fact, strictly speaking, our more evident objective here was almost the same that in the previous section: the identification of chiral bias and chiral domains in solid samples. The major difference is that instead of using artificially-prepared samples in the laboratory, we have to deal with natural solid meteorite samples with much more complex characteristics.

We started the work on meteorites, or more precisely in carbonaceous chondrites[2], with the hypothesis that the action of shear force gradients during the accretion of materials and solidification processes in the formation of planetesimal bodies and comets, could lead to a chiral bias (enantiomeric excess) of chiral fractures, screw distortions or step-kink chiral centers on the surfaces of inorganic matrices, which could later transfer a chiral bias to organic reactions.

Carbonaceous chondrites are the remnants of first chemical stages where chiral sign selection and chirality amplification could have occurred. This is suggested in CM[3] meteorites by the presence of significant chiral organic compounds [199, 200] and, principally, because a real chiral bias has been detected in aminoacids [38, 201, 202] and in insoluble meteorite powders [203]. Furthermore, in CM chondrites inorganic matrices, as those proposed in some abiotic reaction scenarios, are ubiquitously present in CM chondrites. Many studies of CM reported the presence of products of aqueous alteration, e.g. phyllosilicates, namely Fe-rich serpentines and poorly characterized phases (PCPs) in chondrules, aggregates, and within fine-grained rims.

9.2.2. Experiment

Meteorite samples or, more in general petrological samples, represent one of most difficult types of samples one can investigate in polarimetry. They usually are heterogeneous even at the microscopic scale, which means that the optical characteristics of two near points, even if they are separated only by a few microns, may be different. Also there are difficulties associated to the manipulation and cut of the rocks, to obtain specimens thin enough to have the level of transparency necessary to allow some light reaching the detector.

Measurements were carried out with a transmission 2-MGE that shares the fundamentals indicated in chapter 5. The method involving quartz rotators described in chapter 6 was not applied to these measurements because it was de-

[2] Carbonaceous chondrites are a class of chondritic meteorites. They include some of the most primitive known meteorites, but represent only a small proportion $\sim 4.6\%$ of meteorite falls.

[3] CM carbonaceous chondrites are composed of about 70% fine-grained material (matrix), and most have experienced extensive aqueous alteration. Some of these chondrites are well known to contain a rich mix of complex organic compounds.

veloped later. In this work we were mainly interested in the measurement of CB which, assuming that the measured Mueller matrix corresponds to the Mueller matrix of a retarder [Eq. (3.24)], can be obtained from the difference between m_{12} and m_{21} Mueller matrix elements, as shown in Eq. (3.46a). Therefore our main objective here was the determination of m_{12} and m_{21}. As the 2-MGE is not able to measure simultaneously m_{12} and m_{21} for any relative orientation of the PSG and PSA [see Eqs. (5.15)] we addressed this issue by placing two zero-order quarter wave plates (QWP) tuned to the measuring wavelength (546 nm) just before and after the sample that permit the simultaneous measurement of m_{12} and m_{21}. The details about this method are available in Ref. [148]. We do not devote more attention to them in this thesis, because in case we would repeat the measurement right now we would use the quartz rotators technique described in chapter 6.

The measurements included in this chapter were performed on three mineralogic pristine cuts ($\sim$ 30 μm thickness) of the CM2 meteorites Murchison (ASU828-A-1), Murray (ASU635-A-3) and Cold-Bokkeveld (ASU578-A-2) on loan from the Center for Meteorite Studies of the Arizona State University.

9.2.3. Results

Figs. 9.8, 9.9 and 9.10 display the most relevant results of the three meteorite section surfaces. The characteristic representations of CB, calculated according to CB $\sim (m_{12} - m_{21})/2$, are shown in the series b of these figures. Most of the transparent area do not show CB, however, at specific sites of the sample positive and negative CB values are detected. The statistical errors associated to the experimental measurement in the points with zero CB values should, in principle, give a Gaussian distribution centered at zero. Points with CB should give a bimodal distribution at positive and negative values and a chiral bias should be indicated by a distribution different to 50% for both signs. The series c of these figures show the distribution of CB values for the Murchison, Murray and Cold-Bokkeveld thin sections. We have excluded from this statistic representation points which exhibited a percent of transmittance below 0.65%, which corresponds to opaque points in which the measurement has a poor signal to noise ratio (darker points of series a of the Figs. 9.8, 9.9 and 9.10). Also very transparent points (percent transmittance above 20%) which are, most of them, attributable to areas out the meteorite sections were not considered in the recount.

The Murchison sample (panel c of Fig. 9.8 and Fig. 9.11) shows, in addition to the Gaussian distribution value around zero, a bimodal distribution with a clear bias towards negative CB values. The results of the Murray sample (Fig. 9.9) indicate the absence of a clear sign bias in the CB. However, when observed

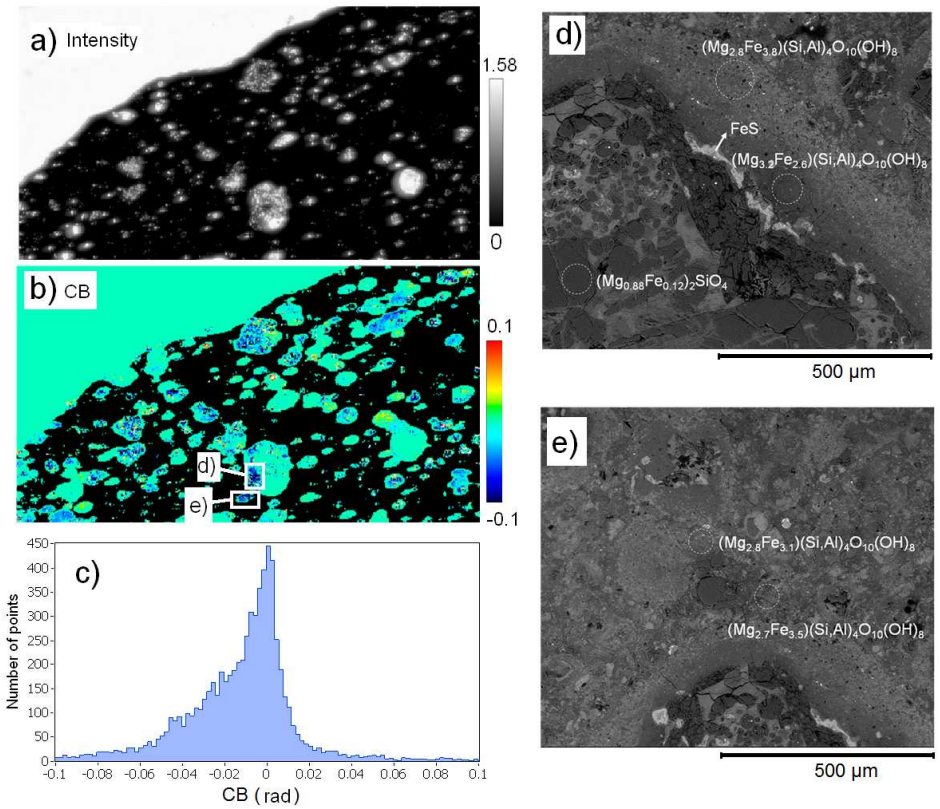

Figure 9.8.: Measurements of a section of a Murchison thin cut ($\sim$ 30 μm thickness); a) optical density measured at 546 nm; b) CB mapping of a) (the dimension of each frame is 12 mm $\times$ 6 mm, where each pixel measures 30 μm $\times$ 30 μm); c) Distribution of the CB values of the image pixels in b), once eliminated the non-transparent and the more transparent pixels; d) and e) SEM images of specific areas (marked in panel b) and EDX composition analysis .

in detail, the CB distribution of Murray section also shows a subtle bimodal distribution with a similar bias than that of the Murchison sample, but it is of low significance and could be also attributed to experimental errors. The presence of a biased CB distribution is clearly observed in the Cold-Bokkeveld sample (Fig. 9.10), however, in this last case the number of measured points with good transparency values is low for a chiral bias estimation, but it shows clearly the bimodal distribution of CB values.

In order to identify the materials corresponding to the areas of the Murchison meteorite that showed optical activity, the thin sections were carefully analyzed by SEM-EDX. The series d and e of Fig 9.8 constitute a representative example of the composition of the areas exhibiting strong optical activity. The results

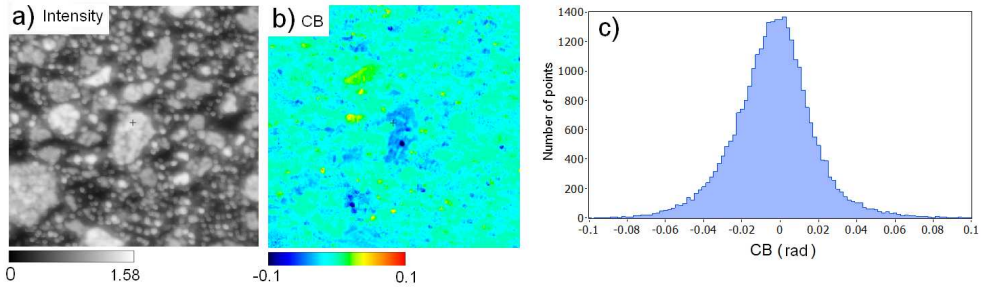

Figure 9.9.: Measurements of a section of a Murray thin cut ($\sim 30\ \mu m$ thickness); a) optical density measured at 546 nm; b) CB mapping of a) (the dimension of each frame is 4 $mm \times 4\ mm$, where each pixel measures 20 $\mu m \times 20\ \mu m$); c) Distribution of the CB values of the image pixels in b), once eliminated the non-transparent and the more transparent pixels.

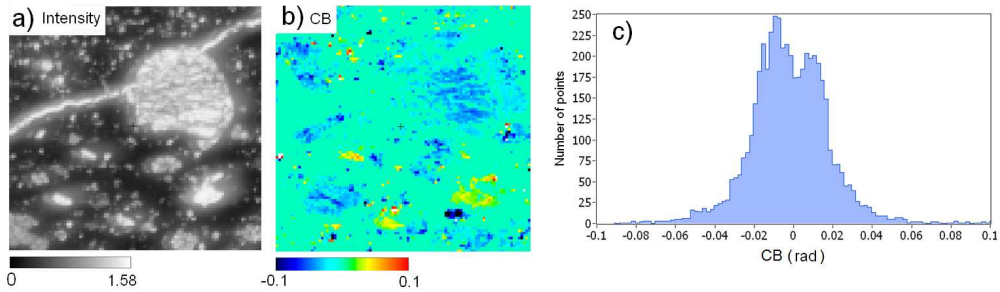

Figure 9.10.: Measurements of a section of a Cold-Bokkeveld thin cut ($\sim 30\ \mu m$ thickness); a) optical density measured at 546 nm: b) CB mapping of a) (the dimension of each frame is 2 $mm \times 2\ mm$, where each pixel measures 20 $\mu m \times 20\ \mu m$); c) distribution of the CB values of the image pixels in b, once eliminated the non-transparent and the more transparent pixels

indicate that CB signals are not originated by intrinsically chiral crystals such as heptahydrated sodium sulfate or quartz crystals because this type of crystal have not been identified . Specifically, CB signals are originated in phyllosilicates sites and poorly characterized phases[4]. Although CB active sites coincide with the location of serpentines (phyllosilicate structures of the meteorite where aminoacids have been detected), it is not reasonable to assume that the relatively high measured CB contributions could arise from the low enantiomeric excesses of organic chiral compounds, because these compound would show very low CB values at

[4]Poorly characterized phases are usually fine-grain ($< 1\ \mu m$ in size) areas which are difficult to characterize with optical or X-ray techniques

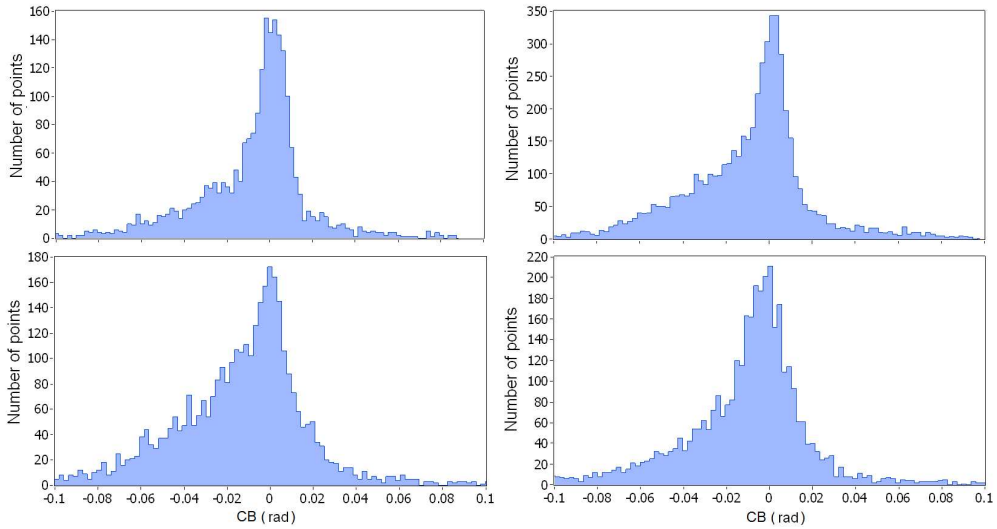

Figure 9.11.: Distribution of the CB values of other sections of the Murchison thin cut than that of Figs. 9.8, once eliminated the non-transparent and the more transparent pixels, showing in all cases the bias towards negative CB values.

the visible wavelength region. The presence of statistical chiral bias is a chemical reasonable scenario, which agrees with the strong heterogeneous structure of carboneaceous chondrites and with the different distribution of enantiomeric excesses of chiral aminoacids in different samples of CM [38, 203].

We think that strong shear gradients could originate a surface chiral bias by the formation of screw chiral distortions and step-kinks by the effect of flow shear gradients. For example, it is known that hydrothermal chrysotile, which shows similarities with the serpentines identified in some meteorites [204], forms chiral nanotubes by the curling to spirals of the crystalline flakes of the phylosilicate bilayered structure. Moreover, the effect of mechanical forces on the structure of these phyllosilicates is probably significant; for instance, it has been previously reported that grinding on phylosilicates and specifically on serpentines originate transitions from crystalline to amorphous phases by the creation of structural defects [205]. The obtained results, albeit preliminary, are not in contradiction with our initial hypothesis and should be considered as a stimulus for further work on the topic.

In this section we have presented a first experimental approach to the study of the chiral properties of solid state meteorite samples. As commented above these measurements involve an important technical complexity together with a higher difficulty than encountered by any previous work done in this field. The

experimental procedure presented constitutes a good starting point and describes the problems that need to be considered and improved in further research. It should be noticed that, in addition to the feasibility to obtain results concerning to the detection of chirality, the used methodology may be a new tool for the petrographical characterization of meteorites.

Part V.

Conclusions and appendices

Chapter 10.

Conclusions

The conclusions of this thesis have been grouped in three categories that correspond to the three parts in which the main contents of this work have been divided: theory (Part II), experimental sets (Part III) and measurements (Part IV).

10.1. Theory

The constitutive relations of an optically active (gyrotropic) and anisotropic medium are considerably more complex than those of a non-gyrotropic medium and, consequently, the resolution of the Maxwell equations with gyrotropic constitutive relations involves a great added difficulty with respect to the non-gyrotropic case. In practice, the solutions of Maxwell equations for a gyrotropic medium can only be handled numerically and, therefore, it is difficult to construct a model based on the dielectric and gyration tensors of the medium that describes, in terms of the Jones or Mueller matrices, the interaction of light with anisotropic chiral media.

1. The infinitesimal matrix representation of an optical system introduced by Jones permits obtaining an analytic Jones or Mueller-Jones matrix. This matrix describes light transmission through any homogenous anisotropic chiral medium as a function of the thickness-dependent optical effects of the medium. This method has the limitation that it does not take into account the effect of the interfaces between different media. However, we have shown that for light at normal incidence onto a bulk anisotropic sample, the change in the polarization occurring at the interfaces is small enough to be safely omitted.

2. In contrast to what some authors have suggested, from the work of R.C. Jones it is not possible to infer the existence of any new type of birefringence or dichroism (which were eventually known as Jones birefringence and Jones dichroism in the literature) independent from the common birefringence or

dichroism. Jones used for his optical calculus two different in-plane projections of linear birefringence (LB, LB′) and linear dichroism (LD, LD′), but they do not identify different physical phenomena.

3. We have introduced the analytic equations that permit the inversion of the most general Jones or Mueller-Jones matrix obtained with the Jones infinitesimal formalism. These equations can be applied to the interpretation of experimental Mueller matrices if they do not include depolarization effects.

4. Mueller matrix product decompositions can be used to factorize experimental matrices into more simple terms. This can serve for the interpretation of the experimental Mueller matrices, and they are specially interesting for depolarizing media. However, product-decompositions are order-dependent, i.e., they depend on the order in which the matrix factors are multiplied, which, in practice, means that not always the optical properties of original Mueller matrix can be derived from the optical properties of the individual factors. In the case of the polar decomposition we have derived a set of conditions that, if fulfilled, assure the commutativity of the diattenuating and retarding factors of the decomposition. They can be used as a criteria for the applicability of the polar/Lu-Chipman decompositions.

5. A new product decomposition, which we have named "pseudopolar decomposition", has been proposed. It is a product factorization that yields a diattenuating factor, a retarding factor and infinite succession of correction terms that account for the non-commutative optical properties of the medium. In case of media with commutative optical effects the pseudopolar decomposition simplifies to the polar decomposition.

10.2. Experimental sets

The time-dependent intensity generated by the 2-MGE is complicated and can be written as a Fourier expansion with an infinite number of terms of different frequency. However, it can be described by a dc term and eight independent functions allowing to determine eight different elements of the Mueller matrix of the sample in a given configuration. The choice of the measured Mueller matrix elements is entirely determined by the azimuthal angles of the PSG and the PSA. A complete Mueller matrix determination requires four measurement configurations.

6. A spectroscopic 2-MGE, a type of polarimeter based on the use of two free

running PEMs operating at their own distinct frequencies, has been entirely built. It has been designed to be used either in transmission or in reflection, and in both cases the angle of incidence can be adjusted. Acquisition and calibration routines for the different measurement modes, together with a complete graphical user interface, have been programmed to operate the instrument.

7. We have demonstrated the usefulness of the 2-MGE to investigate optical activity in a wide spectral range from UV, to near-IR. The use of PEMs as elements with variable retardance allows a high purity and efficiency in the modulation that, together with the synchronous signal acquisition, are the basis for the high sensitivity and high resolution that the measurements of optical activity require.

8. We have developed a novel technique that can expand and improve the capabilities of 2-MGE or other types of ellipsometers/polarimeters. This new experimental proposal is based on the use of an element with optical rotation as a substitute of the precision mechanical rotation stages that are typically used to change the azimuthal orientation of the PSG and the PSA. This technique was conceived to solve the beam translation problem occurring when the azimuthal angles of the PSG and PSA are changed.

9. The optical rotation method has been put in practice in the 2-MGE by using two thin z-cut α-quartz plates as elements with rotatory power. With the assistance of the quartz plates, the 2-MGE is able to measure all the elements of the normalized Mueller matrix while keeping the PSG and PSA static. The four different measurement configurations needed to measure a Mueller matrix with a 2-MGE are reached by selectively introducing/removing the quartz elements present at both arms of the instrument. Besides spectroscopic measurements, the quartz elements have permitted us to obtain spatially resolved measurements of the Mueller matrix that were impossible with the mechanical rotators because of the beam translation problem. Calibration routines for the use of quartz-plates have also been designed.

10.3. Experiments

The determination of optical activity in anisotropic samples supposes, in many situations, an experimental challenge. Optical activity signals arising at molecular and supramolecular levels, of interest in chemistry, tend to be so small that they can be below the resolution of many polarimeters or ellipsometers. In

anisotropic crystals, despite they can exhibit much intense optical activity than molecular non-crystalline substances, optical activity may be even more difficult to detect, because their linear birefringence is often huge and hides the effect of optical activity.

10. We have conducted the first experimental determination of the gyration tensor of a crystal (α-quartz) based on spectroscopic Mueller matrix measurements. We faced the long-standing problem associated to the determination of optical activity of quartz in birefringent directions of the crystal, in order to be able to measure the g_{11} component of the gyration tensor. The experimental approach we have used is based on obtaining the transmission Mueller matrix measurements of z-cut quartz plates at oblique angles of incidence. The same methodology could be used to measure components of the gyration tensor of other crystals.

11. Spectroscopic Mueller matrix measurements have been applied to the study the induction and switching of chirality in solutions of certain soft-matter nanoribbons under the effect of a stirring vortex. We have shown that the handedness of the induced optical activity depends on the direction of stirring in a completely reversible process, which supposes a modification of the supramolecular chirality of the nanophases.

12. Spatially resolved measurements of the Mueller matrix in square section cuvettes containing solutions of certain soft-matter nanoribbons have revealed that the induction of optical activity takes place only in the central part of the cuvette, and have permitted to establish a spatial correlation between chiral flows and the emergence of supramolecular chirality. Our experiments suggest that the measured supramolecular chirality arises due to a bending/folding of the nanoribbons under chiral hydrodynamic force. Such mechanical effect would be produced by the flow shear gradients and the observed phenomenon could be described as piezorotation. We have also found out the importance of the design of stirred containers to optimize such chiral inductions.

13. Obtaining measurements of optical activity with spatial resolution and in anisotropic samples represents an important step forward towards the characterization of chiral materials. To our knowledge this analysis has not been carried out with any other technique. We have used it to examine chiral domains in thin polycrystalline solidifications of benzil from a melt. Domains corresponding to different crystals enantiomorphs have been unambiguously identified through measurement of CD and CB. It has been verified that the boundaries between different domains are straight lines.

14. We have presented a first experimental approach to the study of the chiral properties of solid state meteorite samples. These measurements involve an important technical complexity because the samples are highly heterogeneous and tend to be opaque. Differences in the optical response of samples corresponding to different meteorites have been observed, and a chiral bias has been glimpsed in a Murchison meteorite sample. The experimental procedure presented constitutes a good starting point and describes the problems that need to be considered and improved in further research.

10.4. Future perspectives

In this final section we discuss, without a particular order, several directions in which the work presented in this thesis could be extended. Some of them are topics that are already under investigation at the moment of writing this section.

One of the main areas that we think that still requires an intense study is the measurement of optical activity in anisotropic samples in reflection. It would require a quite different vision from transmission studies, because while transmission measurements are based on long path-lengths measurements and they can be described by a set of "thickness-dependent" parameters, in reflection, optical activity is purely an interface effect. This is a quite virgin area of research, where only a small number of measurements in isotropic optical active samples have been reported [206, 207]. However if appropriate models are constructed (probably using the Berreman formalism), the analysis of anisotropic chiral samples in reflection should be feasible. It would be really worthy to start a two-sided work, theoretical and experimental, to examine in which kind of samples (if any) analyzing the reflected beam (instead of the transmitted beam, as is has been done in this thesis) would be better for the characterization of the optical activity.

In our opinion, many of the more interesting future applications of Mueller matrix polarimetry would require instruments with imaging capabilities. Having a Mueller polarimeter acting as a high resolution optical microscope would nearly be a dream made true. In fact we are not so far from this objective because there are many recent works [68,208] (and even the instrumental part of this thesis) that propose experimental setups going in this direction. The main issue here is that, while getting non-precise, nearly qualitative measurements of the Mueller matrix of a sample is relatively easy from an experimental point of view, applications that require a high precision and resolution, such the measurement of optical activity, need a much higher experimental effort that is not always compatible with the requirements imposed by microscopy. For example, the photoelastic modulators we employ are an excellent source of phase modulation, but at the

moment, due to speed mismatches, they are not compatible with CCD detectors usually employed in microscopy.

A really appealing apparatus to develop, and the "natural" continuation of the instrumental work presented in this thesis, would be a polarimeter/ellipsometer running with 4 PEMs at different resonant frequencies (2 of them in the PSG and the other 2 in the PSA). This instrument would be able to measure all the elements of the Mueller matrix in a single configuration and with a completely static setup. Another interesting objective to pursue would be extending the optical activity measurements based on the determination of the Mueller matrix to other wavelength regions. In particular, it would be very attractive to go to the mid-IR because it would permit the measurement of optical activity associated with molecular vibrations in anisotropic samples. Some experimental work aimed at determining the Mueller matrix in this IR domain is planned in our research group.

The construction and tuning of the 2-MGE took to the author of this thesis more time than any other topics discussed in this work. Considerable efforts were also put in the development of theoretical tools for the analysis of experimental data. At the moment these instrumental and theoretical tools have been exploited for a restricted number of samples. We are aware that there is an almost endless list of chiral samples susceptible to be studied by Mueller polarimetry. A very clear example are chiral crystals, where there are many gyration tensors waiting to be measured. Besides the measurements on quartz and benzil presented in this thesis, we have also worked (and still there is some work in process) in the measurement of the gyration tensor of $AgGaS_2$. Anyway, it must be remarked that having a set of theoretical and experimental tools does not mean that the analysis of a new chiral sample can be done on a routine basis; rather each sample supposes a new challenge.

Going to more particular applications, there are several fields that we think that could benefit from optical activity measurements pioneered in this thesis. Liquid crystals is one of the main research areas where we believe that our tools could have a more straightforward application. The study of the chiroptical properties of liquid crystals represents a vast area of investigation and it also attracts the interest from the industry. Many more applications could located in the biosciences, where there are lots of biopolymers, for example DNA, with chiral anisotropic structures. Another novel and very active area of research that demands of advanced optical activity measurements is nanotechnology. For example, for a further understanding of the interesting optical properties of 2D and 3D chiral periodic structures in the sub-wavelength scale known as metamaterials.

Apèndix A.

Resum en català

A.1. Introducció

L'objectiu d'aquesta tesi ha estat estudiar la quiralitat de medis anisòtrops mitjançant polarimetria de matriu de Mueller. Per aconseguir aquest objectiu hem tractat aspectes diversos i, en bona mesura, multidisciplinaris, però tots ells importants per a l'assoliment dels objectius de la tesi. Per exemple, hem considerat diferents formalismes per la descripció de la propagació de la llum polaritzada per aquest tipus de medis. També hem abordat qüestions plenament instrumentals, com ara la construcció d'un polarímetre o el · lipsòmetre de matriu de Mueller. Així mateix, hem tractat aspectes relatius a la química supramolecular per interpretar alguns dels nostres resultats.

L'activitat òptica és la manifestació de com interaccionen els medis quirals amb la llum polaritzada. Va ser observada per primer cop pel astrònom François Arago (en català Francesc Aragó, ja que va nèixer a la Catalunya Nord) que va descriure una rotació en la direcció de polarització quan llum polaritzada linealment travessava un cristall de quars al llarg del seu eix òptic. En l'actualitat, gairebé 200 anys després d'aquest descobriment, els científics coneixen moltes substàncies i materials que posseeixen activitat òptica i la seva mesura ha esdevingut d'una importància essencial en moltes àrees de recerca: química, biologia, ciència de materials, farmàcia, etc.

Els primers treballs experimentals sobre activitat òptica estaven basats en la mesura de la rotació de la direcció de polarització quan llum polaritzada linealment travessava alguns medis quirals. Aviat es va descobrir que aquesta rotació òptica, anomenada a vegades *poder rotatori*, es podia explicar per una diferencia en els índex de refracció del medi per llum polaritzada circularment cap a la esquerra o cap a la dreta, una diferència que es coneix habitualment com *birefringència circular* (CB[1]). No va ser fins dècades més tard, després dels treballs d'Aimé Cotton, que va començar la mesura de les diferències d'absorció per llum polaritzada circularment cap a l'esquerra i per llum polaritzada circularment cap

[1]En aquest resum en català hem optat per mantenir els mateixos acrònims d'origen anglès emprats al llarg de tots els capítols anteriors de la tesi.

a la dreta, que es coneix amb el nom de *dicroisme circular* (CD).

Malgrat que en l'actualitat el fenomen de l'activitat òptica és àmpliament conegut, la seva mesura encara presenta dificultats pels científics, especialment en el que fa referència a medis anisòtrops. Una raó és que els efectes de CB i CD són en general petits, i, a més a més, en medis anisòtrops hi ha birefringència lineal i/o dicroisme lineal que són ordres de magnitud més grans i emmascaren l'efecte de CB i CD. Un exemple de gran importància és la mesura de CB en un cristall per direccions diferents de l'eix òptic, ja que la petita pertorbació que causa la CB sobre la polarització de la llum, en comparació amb la gran pertorbació causada per la birefringència lineal, és difícilment detectada des d'un punt de vista experimental. Els aparells comercials disponibles en l'actualitat no es poden usar per mesurar CD i/o CB en mostres anisòtropes, perquè estan dissenyats sota la premissa que el medi estudiat és òpticament isòtrop, és a dir, que té les mateixes propietats òptiques en totes les direccions.

Mitjançat una tècnica com la polarimetria es pot mesurar experimentalment CD i CB. Per medis isòtrops els instrument destinats a la mesura de CB són simples i estan constituïts únicament per una font de llum i dos polaritzadors, entre els quals es situa la mostra. Pel cas del CD l'aparell haurà de disposar també d'algun element retardador o compensador en el camí òptic. Quan es tracta de medis anisòtrops veurem que la mesura de CD i CB esdevé més complexa i, idealment, s'haurà de basar en la determinació de la matriu de Mueller de la mostra.

A.2. Propagació de la llum en medis òpticament actius i anisòtrops

La descripció de la propagació de la llum per medis òpticament actius i anisòtrops no està exempta de dificultats. La teoria electromagnètica es va fonamentar degudament a partir de la formulació de les equacions de Maxwell però, tot i això, Maxwell no va considerar els medis quirals. No s'ha trobat una solució analítica per a la resolució de les equacions de Maxwell emprant les equacions constitutives més generals d'un medi anisòtrop i quiral i és per això que el problema s'ha de tractar numèricament.

Per facilitar la resolució de les equacions en medis anisòtrops s'han desenvolupat alguns mètodes matricials que permeten sistematitzar els càlculs i, a l'hora, asseguren el compliment de les condicions de contorn lligades a les interfícies de canvi de medi. El mètode més conegut és el desenvolupat per Berreman [70], que ha estat àmpliament difós dins de l'àmbit de l'el · lipsometria, ja que és fàcilment adaptable a sistemes multicapa. Malgrat aquests avantatges tampoc amb aquest

mètode es poden trobar equacions analítiques i generals que descriguin com evoluciona la polarització de la llum quan travessa un medi quiral i anisòtrop.

En aquesta tesi hem fet servir un mètode alternatiu de tipus semi-fenomenològic que no requereix considerar les equacions constitutives del medi. Aquest mètode va ser introduït per R. C. Jones en l'àmbit del seu formalisme per descriure llum polaritzada [78]. Es basa en una representació infinitesimal del medi a partir de les vuit variables necessàries per descriure el comportament de qualsevol sistema òptic complex que no introdueixi despolarització[2] [79]. Aquestes vuit variables es defineixen com:

- retard isòtrop de fase,
$$\eta = \frac{2\pi}{\lambda}(n_x + n_y)l, \tag{A.1a}$$
- retard isòtrop d'amplitud,
$$\kappa = \frac{2\pi}{\lambda}(k_x + k_y)l, \tag{A.1b}$$
- projecció horitzontal del dicroisme lineal,
$$\mathrm{LD} = \frac{2\pi}{\lambda}(k_x - k_y)l, \tag{A.1c}$$
- projecció horitzontal de la birefringència lineal,
$$\mathrm{LB} = \frac{2\pi}{\lambda}(n_x - n_y)l, \tag{A.1d}$$
- projecció a 45° del dicroisme lineal,
$$\mathrm{LD}' = \frac{2\pi}{\lambda}(k_{45} - k_{135})l, \tag{A.1e}$$
- projecció a 45° de la birefringència lineal,
$$\mathrm{LB}' = \frac{2\pi}{\lambda}(n_{45} - n_{135})l, \tag{A.1f}$$
- dicroisme circular,
$$\mathrm{CD} = \frac{2\pi}{\lambda}(k_- - k_+)l, \tag{A.1g}$$

[2]Un medi que no introdueix despolarització és aquell pel qual la llum que incideix totalment polaritzada continua estan totalment polaritzada després d'interactuar amb el medi. L'efecte d'un medi que despolaritzi no es pot descriure amb una matriu de Jones.

- birefringència circular,

$$\mathrm{CB} = \frac{2\pi}{\lambda}(n_- - n_+)l, \tag{A.1h}$$

on n indica l'índex de refracció, k és el coeficient d'extinció, l és el camí òptic dins del medi i λ és la longitud d'ona en el buit. Els subíndex especifiquen la polarització de la llum segons x, y, a 45° de l'eix x, a 135° de l'eix x, circularment cap a la dreta $+$, o cap a l'esquerra $-$. És interessant remarcar que LB i LB$'$ (de la mateixa manera que LD i LD$'$) no descriuen efectes físics diferents, sinó diferents projeccions de la birefringència (o del dicroisme) [99].

Aquest mètode, almenys en la forma en que es presenta en aquesta tesi, només està descrit per llum polaritzada en incidència normal sobre la mostra, i no té en compte les reflexions que puguin ocórrer a les interfícies de la mostra. Tot i aquestes limitacions, es tracta d'un sistema molt útil per estudiar la transmissió de llum a través d'un medi homogeni, anisòtrop i amb activitat òptica, ja que empra àlgebra senzilla i ofereix resultats analítics que són fàcilment relacionables amb l'experiment.

La matriu de Jones $\mathbf{J}$ que descriu la transmissió de llum a través de qualsevol tipus de medi homogeni que no introdueixi despolarització es pot obtenir a partir de l'exponencial [81]:

$$\mathbf{J}(\omega, z) = \exp[z\mathbf{N}(\omega)], \tag{A.2}$$

on ω és la freqüència, z és la distància dins del medi ($z = 0$ indicaria el punt de la interfície). La matriu $\mathbf{N}$ és el generador infinitesimal de $\mathbf{J}$, i satisfà:

$$\mathbf{N}(\omega) = lim_{z\to 0}\frac{\mathbf{J}(\omega, z) - \mathbf{I}}{z}. \tag{A.3}$$

$\mathbf{N}$ és una matriu infinitesimal que es pot construir a partir d'una versió infinitesimal de les variables definides a les Eqs. (A.1). La matriu de Jones de l'Eq. (A.2) es pot calcular com [78, 173]:

$$\mathbf{J} = e^{-i\chi/2}\begin{pmatrix} \cos\frac{\mathrm{T}}{2} - \frac{i\mathrm{L}}{\mathrm{T}}\sin\frac{\mathrm{T}}{2} & \frac{(\mathrm{C}-i\mathrm{L}')}{\mathrm{T}}\sin\frac{\mathrm{T}}{2} \\ -\frac{(\mathrm{C}+i\mathrm{L}')}{\mathrm{T}}\sin\frac{\mathrm{T}}{2} & \cos\frac{\mathrm{T}}{2} + \frac{i\mathrm{L}}{\mathrm{T}}\sin\frac{\mathrm{T}}{2} \end{pmatrix}, \tag{A.4}$$

on hem definit un retard complex per cada parella de birefringència i dicroisme:

$$\chi = \eta - i\kappa, \tag{A.5}$$

$$\mathrm{L} = \mathrm{LB} - i\mathrm{LD}' \tag{A.6}$$

$$\mathrm{L}' = \mathrm{LB}' - i\mathrm{LD}', \tag{A.7}$$

$$\mathrm{C} = \mathrm{CB} - i\mathrm{CD}, \tag{A.8}$$

i $\mathrm{T} = \sqrt{\mathrm{L}^2 + \mathrm{L}'^2 + \mathrm{C}^2}$.

La matriu de Mueller $\mathbf{M}$ corresponent a la matriu de Jones[3] de l'Eq. (A.4) es pot calcular a partir de la relació [3]:

$$\mathbf{M} = A(\mathbf{J} \otimes \mathbf{J}^*)A^{-1}, \tag{A.9}$$

on $\otimes$ indica un producte de Kronecker i A és

$$A = \frac{1}{\sqrt{2}} \begin{pmatrix} 1 & 0 & 0 & 1 \\ 1 & 0 & 0 & -1 \\ 0 & 1 & 1 & 0 \\ 0 & i & -i & 0 \end{pmatrix}. \tag{A.10}$$

La matriu de Mueller resultant es pot calcular doncs analíticament [42, 173] i l'hem presentada a l'Eq. (3.21) d'aquesta memòria.

A.3. Inversió i descomposició de les matrius de Mueller

Donada una matriu de Mueller experimental, en aquesta secció ens interessarem en l'obtenció dels paràmetres òptics rellevants definits a l'apartat anterior. Distingirem dos mecanismes, un consistent en la inversió analítica de la matriu de Jones o de Mueller-Jones descrita a l'apartat anterior, i l'altre basat en descomposicions algebraiques de la matriu de Mueller.

A.3.1. Inversió analítica d'un matriu de Mueller-Jones corresponent a un medi homogeni

Per conveniència expressarem els elements d'una matriu de Jones en forma polar:

$$\mathbf{J} = e^{i\theta_{00}} \begin{pmatrix} r_{00} & r_{01}e^{i(\theta_{01}-\theta_{00})} \\ r_{10}e^{i(\theta_{10}-\theta_{00})} & r_{11}e^{i(\theta_{11}-\theta_{00})} \end{pmatrix}. \tag{A.11}$$

Per tal de determinar LB, LB', CB, LD, LD' i CD a partir d'una matriu de Jones expressada segons l'Eq. (A.11) es poden emprar les següents equacions [102]:

$$\mathrm{LB} = \mathrm{Re}\left[i\Omega\left(r_{00} - r_{11}e^{i(\theta_{11}-\theta_{00})}\right)\right], \tag{A.12a}$$

$$\mathrm{LB}' = \mathrm{Re}\left[i\Omega\left(r_{01}e^{i(\theta_{01}-\theta_{00})} + r_{10}e^{i(\theta_{10}-\theta_{00})}\right)\right], \tag{A.12b}$$

[3] La matriu de Mueller corresponent a una matriu de Jones sovint s'anomena matriu de Mueller-Jones i és una matriu de Mueller que no introdueix despolarització. Tota matriu de Jones sempre té una matriu de Mueller equivalent, però l'invers no és cert.

$$\mathrm{CB} = \mathrm{Re}\left[\Omega\left(r_{01}e^{i(\theta_{01}-\theta_{00})} - r_{10}e^{i(\theta_{10}-\theta_{00})}\right)\right], \tag{A.12c}$$

$$\mathrm{LD} = -\,\mathrm{Im}\left[i\Omega\left(r_{00} - r_{11}e^{i(\theta_{11}-\theta_{00})}\right)\right], \tag{A.12d}$$

$$\mathrm{LD}' = -\,\mathrm{Im}\left[i\Omega\left(r_{01}e^{i(\theta_{01}-\theta_{00})} + r_{10}e^{i(\theta_{10}-\theta_{00})}\right)\right], \tag{A.12e}$$

$$\mathrm{CD} = -\,\mathrm{Im}\left[\Omega\left(r_{01}e^{i(\theta_{01}-\theta_{00})} - r_{10}e^{i(\theta_{10}-\theta_{00})}\right)\right], \tag{A.12f}$$

amb

$$K = \left[r_{00}r_{11}e^{i(\theta_{11}-\theta_{00})} - r_{01}r_{10}e^{i(\theta_{01}-\theta_{00})}e^{i(\theta_{10}-\theta_{00})}\right]^{-1/2}, \tag{A.13}$$

i on $\Omega = \mathrm{T}K/[2\sin(\mathrm{T}/2)]$ i $\mathrm{T} = 2\cos^{-1}\left[K(r_{00} + r_{11}e^{i(\theta_{11}-\theta_{00})})/2\right]$. Els símbols Re i Im indiquen, respectivament, la part real i la part imaginària.

Les Eqs. (A.12) permeten invertir d'una manera directa i ràpida una matriu de Jones. Les mateixes equacions es poden fer servir per invertir una matriu de Mueller-Jones si es té en compte que els factors r_{00}, r_{01}, r_{10}, r_{11}, $e^{i(\theta_{01}-\theta_{00})}$, $e^{i(\theta_{11}-\theta_{00})}$ and $e^{i(\theta_{11}-\theta_{00})}$ són fàcilment calculables a partir d'una matriu de Mueller-Jones, tal com es mostra a [7]. Tot i això, aquestes equacions, per elles soles, no són útils des d'un punt de vista experimental, ja que, en general, el resultat d'un experiment de polarimetria és una matriu de Mueller, però no estrictament una matriu de Mueller-Jones.

Per invertir una matriu de Mueller experimental primer haurem de calcular la matriu de Mueller-Jones més propera a la matriu de Mueller experimental. Això es pot fer emprant l'anomenada matriu de coherència que fou introduïda per Cloude [103]. Els valors propis de la matriu de coherència permeten calcular la matriu de Mueller-Jones estimada corresponent a una matriu de Mueller experimental, tot seguint el procediment descrit a [102]. La validesa d'aquest procés estimatiu dependrà de si la matriu de Mueller experimental original era, ja d'entrada, propera a una matriu de Mueller-Jones. En general els resultats només seran fiables en el cas que el medi estudiat no introdueixi despolarització.

A.3.2. Descomposició de les matrius de Mueller

En aquest apartat descriurem un metodologia d'anàlisi de les matrius de Mueller completament diferent. El nostre objectiu aquí és descompondre la matriu de Mueller experimental en components més simples i que tinguin una interpretació física més senzilla. Aquests procediments de descomposició no es basen en un model teòric que descrigui la interacció d'una ona electromagnètica amb una mostra, sinó que estan basats en les diferents propietats algebraiques que presenten les matrius de Mueller corresponents a diferents tipus de medi.

Qualsevol matriu de Mueller $\mathbf{M}$ es pot descompondre en el producte d'un diatenuador $\mathbf{M}_D$, un retardador $\mathbf{M}_R$ i un despolaritzador $\mathbf{M}_\Delta$

$$\mathbf{M} = \mathbf{M}_\Delta \mathbf{M}_R \mathbf{M}_D. \tag{A.14}$$

Aquesta factorització es coneix amb el nom de descomposició de Lu-Chipman [84] i es pot aplicar a totes les matrius de Mueller experimentals. Si s'assumeix que no hi ha despolarització ($\mathbf{M}_\Delta = \mathbf{I}$) la descomposició passa a tenir només dos termes i es coneix generalment com a descomposició polar [104, 105].

Els tres factors de la descomposició de Lu-Chipman de l'Eq. (A.14) en general no commuten entre ells, és a dir, el seu producte depèn de l'ordre en què els termes es multipliquen. Això fa que la descomposició no sigui única, i que es puguin definir diferents variacions de la descomposició en funció de l'ordre en què els factors són multiplicats [107]. Aquest fet fa que els factors resultants de la descomposició puguin perdre el seu significat físic, en el sentit que les dicroisme de la matriu $\mathbf{M}_D$ i la birefringència de la matriu $\mathbf{M}_R$ poden no coincidir, respectivament, amb el dicroisme i la birefringència de la matriu de Mueller $\mathbf{M}$ original.

Descomposició pseudopolar

La descomposició pseudopolar està molt relacionada amb la descomposició de Lu-Chipman, però ofereix un tractament per a la no commutabilitat dels efectes òptics involucrats en el càlcul. Aquesta descomposició es pot deduir a partir la forma exponencial d'una matriu de Jones o de Mueller-Jones [vegeu Eq. (A.2)] si es fa servir la fórmula de Zassenhaus [115]. Aquesta fórmula indica que l'exponencial de la suma de dos operadors que no commuten es pot obtenir com un producte infinit dels exponencials dels operadors i dels seus commutadors. Per fer més simple l'ús de la descomposició, ens quedarem només ens els dos primers termes de la successió. En termes de la matriu de Mueller la descomposició pseudopolar truncada la podem escriure com

$$\mathbf{M} \cong \mathbf{M}_\Delta \mathbf{M}_R \mathbf{M}_D \mathbf{M}_{1C} \mathbf{M}_{2C}, \tag{A.15}$$

on $\mathbf{M}_R$ és un retardador que té la mateixa birefringència que $\mathbf{M}$ i $\mathbf{M}_D$ és una diatenuador amb el mateix dicroisme que $\mathbf{M}$. $\mathbf{M}_{1C}$ i $\mathbf{M}_{2C}$ son els dos primers termes d'una successió infinita de matrius, on cada terme d'ordre superior s'apropa més a la matriu unitat. Anomenem a les matrius $\mathbf{M}_{1C}$ i $\mathbf{M}_{2C}$ com matrius de correcció.

El càlcul de tots els factors de la descomposició pseudopolar a partir de d'una matriu de Mueller experimental es realitza a través d'un procés iteratiu que es

detalla a [173]. És important remarcar un altre cop que malgrat que $\mathbf{M}_R$ i $\mathbf{M}_D$ que apareixen tant a l'Eq. (A.15) com també a l'Eq. (A.14) i que, en ambdós casos, $\mathbf{M}_D$ es refereix a un diatenuador i $\mathbf{M}_R$ a un retardador, només en el cas de la descomposició pseudopolar les propietats d'aquests elements corresponen a les de la matriu $\mathbf{M}$ original.

En un sistema que només presenti efectes òptics que commuten la descomposició pseudopolar es transforma automàticament en la descomposició polar (si no considerem despolarització) o de Lu-Chipman (si la despolarització és considerada), ja que, en aquestes condicions, els infinits termes de la successió convergeixen cap a la matriu identitat $\mathbf{M}_{1C} = \mathbf{M}_{2C} = ... = \mathbf{I}$. Posat que coneixem l'estructura del les matrius de correcció [173] és possible derivar les condicions que asseguren la commutabilitat dels efectes òptics. Són aquestes:

$$\begin{aligned} &\mathrm{CBLD}' - \mathrm{LB}'\mathrm{CD} = 0, \\ &\mathrm{CDLB} - \mathrm{LDCB} = 0, \\ &\mathrm{LBLD}' - \mathrm{LB}'\mathrm{LD} = 0. \end{aligned} \tag{A.16}$$

Aquestes condicions mostren que en un medi anisotrop i quiral (CD, CB $\neq 0$) sempre hi haurà algun grau de no commutativitat. Un medi aquiral (CD = CB = 0) tindrà propietats òptiques commutatives si els eixos de birefringència i dicroisme lineal coincideixen, ja que aleshores també es satisfà $\mathrm{LBLD}' - \mathrm{LB}'\mathrm{LD} = 0$.

A.4. Dispositius experimentals

Els aparells que permeten la mesura d'elements de la matriu de Mueller d'una mostra es coneixen com polarímetres o el · lipsòmetres. Tots ells es basen en una configuració elemental comuna: primer la llum travessa un generador d'estats de polarització (PSG), després interacciona amb la mostra i, seguidament, travessa un analitzador d'estats de polarització (PSA). La diferències més importants entre diferent tipus de el · lipsòmetres o polarímetres venen donades pels elements òptics que componen el PSG i el PSA. Les característiques del PSG i el PSA també determinen quins elements de la matriu de Mueller (eventualment tots) són mesurats en cada tipus d'aparell.

En aquesta tesi hem emprat un el · lipsòmetre generalitzat de doble modulador (2-MGE) [119, 120] per obtenir mesures completes de la matriu de Mueller normalitzada. Aquest instrument, de construcció pròpia, utilitza dos parells polaritzador-modulador fotoelàstic, un en el PSG i l'altre en el PSA. Els moduladors fotoelàstics (PEMs) son dispositius ressonants d'alta freqüència (en el nostre instrument $\sim$ 50 kHz el del PSG i $\sim$ 60 kHz el del PSA) que introdueixen un

desfasament periòdic entre les components del camp elèctric. Com que en aquest treball estem interessats en realitzar mesures d'activitat òptica que requereixen una alta sensibilitat és molt convenient utilitzar PEMs com a moduladors de la polarització de la llum enlloc d'altres tipus de moduladors, ja que els PEMs posseeixen un alt grau de puresa, eficiència i estabilitat en la modulació.

Les taules 5.1 i 5.2 enumeren tots els components òptics i electrònics que componen el 2-MGE, mentre que les Figs. 5.1 i 5.2 són, respectivament, representacions esquemàtiques del muntatge òptic i de les connexions electròniques de l'aparell. La llum que arriba al detector del 2-MGE és una funció temporal complicada que es pot expressar com

$$\begin{aligned} I(t) =& I_{dc} + I_{X0}X_0 + I_{Y0}Y_0 + I_{X1}X_1 + I_{Y1}Y_1 + I_{X0X1}X_0X_1 \\ &+ I_{X0Y1}X_0Y_1 + I_{Y0X1}Y_0X_1 + I_{Y0Y1}Y_0Y_1. \end{aligned} \tag{A.17}$$

Els termes I_{dc}, I_{X0}, I_{Y0},... són constats que multipliquen les funcions base que depenen del temps:

$$X_0 = \sin\left[A_0 \sin\left(\omega_0 t + \phi_0\right)\right] \tag{A.18a}$$

$$Y_0 = \cos\left[A_0 \sin\left(\omega_0 t + \phi_0\right)\right] \tag{A.18b}$$

$$X_1 = \sin\left[A_1 \sin\left(\omega_1 t + \phi_1\right)\right] \tag{A.18c}$$

$$Y_1 = \cos\left[A_1 \sin\left(\omega_1 t + \phi_1\right)\right] \tag{A.18d}$$

on A_0 i A_1 són les amplituds de modulació, i les freqüències dels moduladors són $2\pi\omega_0$ i $2\pi\omega_1$.

La informació sobre la mostra està continguda en els vuit paràmetres I_{X0}, I_{Y0}, I_{X1}, etc. que normalment s'expressen ja normalitzats a la intensitat continua de la llum I_{dc}. En funció de l'orientació azimutal del PSG i del PSA aquests vuit paràmetres es poden relacionar directament amb vuit elements de la matriu de Mueller de la mostra. Per exemple, en el nostre instrument si el PSG i el PSA s'orienten a (0°, 0°) dels eixos primaris de referència de l'aparell, els elements de la matriu de Mueller mesurables són:

$$\mathbf{M} = \begin{pmatrix} 1 & \bullet & -I_{Y0} & I_{X0} \\ \bullet & \bullet & \bullet & \bullet \\ -I_{Y1} & \bullet & I_{Y0Y1} & -I_{X0Y1} \\ -I_{X1} & \bullet & I_{Y0X1} & -I_{X0X1} \end{pmatrix}, \tag{A.19}$$

on els símbols (•)indiquen elements no mesurables en la configuració donada. Tanmateix, si es fan servir 4 configuracions de mesura diferents [per exemple les orientacions (0°, 0°), (0°, 45°), (45°, 0°) i (45°, 45°)] es poden mesurar tots els elements de la matriu de Mueller normalitzada.

A.4.1. Rotació òptica aplicada a la mesura

Un dels usos principals del 2-MGE durant aquesta tesi ha estat la mesura espectroscòpica de la matriu de Mueller però, a mesura que augmentava la complexitat de les mostres que caracteritzaven, ens vam adonar que el 2-MGE tenia problemes a l'hora de mesurar mostres heterogènies al llarg de la seva superfícies, és a dir, quan les propietats òptiques variaven de punt a punt. De fet, el problema sorgeix quan canvia l'angle azimutal del PSG i/o del PSA: com que l'eix de rotació no coincideix exactament amb la direcció del feix de llum, es produeix una desplaçament d'aquest sobre la mostra. A la pràctica, això significa que en diferents configuracions de mesura s'estan analitzant punts lleugerament diferents de la mostra. El desplaçament del feix depèn, evidentment, de la qualitat de l'alineació, però també del gruix del PSG i el PSA. En el nostre cas en tenir el PSG i el PSA gruixos de desenes de mm es fa palès que si s'aplica la rotació del PSG i del PSA l'instrument disposa d'una resolució lateral pobre, cosa que suposa un problema en mostres heterogènies.

Per solucionar aquest problema hem ideat un sistema on no es necessari moure el PSG i el PSA. En comptes d'això introduïm làmines de quars cristal · lí amb l'eix òptic perpendicular a la superfície com elements generadors d'una rotació òptica. La intenció és substituir la rotació mecànica del PSG i del PSA per la rotació òptica generada per un element amb CB. Utilitzem dos conjunts de làmines de quars de diferents gruixos muntats cadascun d'ells en una roda de filtres, una situada entre el PSG i la mostra (quars 0), i l'altra entre la mostra i el PSA (quars 1). Les rodes de filtres permeten posar o treure les làmines de quars en el camí òptic d'una manera automàtica i ràpida.

Tal com mostra l'Eq. A.12c, el gruix de les làmines de quars és proporcional a l'angle de rotació òptica (CB es el doble de la rotació òptica). Però, a més, CB és un efecte dispersiu, és a dir, per a un determinat gruix del cristall de quars la rotació òptica varia amb la longitud d'ona [152]. Des del punt de vista del 2-MGE, la rotació òptica "ideal" per a qualsevol longitud d'ona seria 45°, que per a una làmina d'1 mm de gruix es produeix aproximadament a 430 nm. Tot i això també és possible realitzar mesures amb angles de rotació òptica diferents de 45° si l'efecte de les làmines de quars s'ha calibrat amb antelació. Per a angles de rotació òptica arbitraris, en comptes de mesurar elements de la matriu de Mueller aïllats, mesurarem combinacions d'elements. Amb tot, com que el 2-MGE, ja és capaç de mesurar 8 elements de la matriu de Mueller sense necessitat de fer servir làmines de quars, podrem determinar tots elements de la matriu de Mueller si es fan servir les següents configuracions:

- Configuració I. PSG / Mostra / PSA,

- Configuració II. PSG / Quars 0 / Mostra / PSA,
- Configuració III. PSG / Mostra / Quars 1 / PSA,
- Configuració IV. PSG / Quars 0 / Mostra / Quars 1 / PSA.

Els elements de la matriu de Mueller que mesurem a cada configuració venen donats per:

$$\mathbf{M} = \begin{pmatrix} 1 & m_{01,II} & m_{02,I} & m_{03,I} \\ m_{10,III} & m_{11,IV} & m_{12,III} & m_{13,III} \\ m_{20,I} & m_{21,II} & m_{22,I} & m_{23,I} \\ m_{30,I} & m_{31,II} & m_{32,I} & m_{33,I} \end{pmatrix}. \tag{A.20}$$

Noteu que amb la configuració I mesurem 8 elements de la matriu de Mueller, amb cadascuna de les configuracions II i III mesurem 3 nous elements i que només fem servir la configuració IV per mesurar l'element restant. La característica més important d'aquest mecanisme de mesura és que en tot moment el PSG i el PSA romanen en la mateixa posició i les làmines de quars no produeixen cap desplaçament apreciable del feix. Les rodes de filtres permeten accedir d'una manera ràpida i automàtica a qualsevol de les configuracions esmentades.

A part de l'efecte de rotació òptica, les làmines de quars poden produir també algunes pertorbacions a la mesura si el seu eix òptic no es perfectament paral · lel al feix lluminós. En aquest cas, es farà manifesta alguna traça de birefringència lineal. Per poder calibrar i corregir aquest petit efecte, es poden fer servir les mateixes estratègies que s'utilitzen en el · lipsometria generalitzada per calibrar les finestres d'un el · lipsòmetre [150].

A.5. Mesures experimentals

A.5.1. Quars

El quars és un cristall enantiomorf molt comú a la Terra. Històricament, la seva activitat òptica ha estat molt estudiada, ja que les primeres mesures d'activitat òptica de començaments del segle XIX es van fer en quars [15]. Tot i això, la majoria de mesures que s'han fet sobre l'activitat òptica del quars tenen en comú que s'han realitzat per llum propagant-se a través de l'única direcció del cristall que no mostra birefringència lineal (l'eix òptic) [158]. Tanmateix és ben conegut en cristal · lografia que el quars també mostra activitat òptica (en aquest cas només CB i no CD, ja que és un cristall transparent) en altres direccions del cristall. En aquestes circumstancies, però, la mesura esdevé molt més complexa.

La dependència de CB segons la direcció de propagació de la llum a través d'un cristall de quars es pot expressar rigorosament en termes del tensor de girotropia.

En el cas del quars aquest tensor té dos elements diferents: g_{33} per direccions paral · leles a l'eix òptic (senzill de mesurar) i g_{11} per direccions perpendiculars a l'eix òptic (difícil de mesurar):

$$\mathbf{g} = \begin{bmatrix} g_{11} & 0 & 0 \\ 0 & g_{11} & 0 \\ 0 & 0 & g_{33} \end{bmatrix}. \tag{A.21}$$

En aquest treball ens hem centrat en la mesura de l'element g_{11} del quars. El nostre procediment de mesura està basat en la mesura de la matriu de Mueller en transmissió per incidència obliqua de la llum sobre la superfície del cristall. La Fig. 7.2 mostra la geometria bàsica del nostre experiment. Amb aquesta geometria hem demostrat que l'element g_{11} es pot determinar experimentalment si els següents paràmetres són coneguts amb antelació: l'element g_{33}, l'angle d'incidència i els índex de refracció ordinari i extraordinari del quars. Els detalls sobre com calcular aquest element del tensor es poden consultar a [152] o al capítol 7 d'aquesta tesi.

Les Figs. 7.8 i 7.9 mostren, respectivament, les mesures experimentals espectroscòpiques dels components del tensors de girotropia d'un cristall de quars "dretà" (RH) i d'un cristall "esquerrà" (LH). Tal com s'espera ambdós enantiomorfs tenen signes oposat en els elements del tensor de girotropia.

A.5.2. Induccions quirals per efectes hidrodinàmics

L'estudi de les induccions quirals com a conseqüència d'efectes hidrodinàmics engloba tot un seguit d'experiments realitzats en el transcurs d'aquesta tesis que tenen en comú l'estudi de l'activitat òptica de solucions que s'agiten en sentit horari (CW) o anti-horari (CCW) durant la mesura de la matriu de Mueller. L'interès d'aquests experiments rau en el fet de que per certes solucions que contenen estructures supramoleculars de formes allargades i mides nanomètriques, s'indueix una activitat òptica supramolecular que ve determinada pel sentit de l'agitació. Es tracta d'un fenomen totalment reversible i que dura només el temps en què l'agitació està activa, cosa que la fa diferent a altres induccions descrites prèviament [179, 192]. Aquest efecte ha estat focus de certes controvèrsies i en diverses publicacions recents [180–182] s'ha especulat amb diverses interpretacions de les observacions experimentals. La nostra aproximació al problema ha estat obtenir tanta informació com fos possible sobre el fenomen a partir de mesures experimentals amb el 2-MGE, cosa que finalment ha donat lloc a diferents publicacions [100, 183, 209].

Els experiments es van desenvolupar en cubetes de 10 mm de camí òptic i agitades emprant petites barretes magnètiques. En la major part d'experiments

que hem realitzat les cubetes contenien J-agregats de porfirines. En certes porfirines no es mostrava cap efecte en agitar (per exemple en la porfirina H_2TPPS_3) mentre que en d'altres, com la H_2TPPS_4, apareixia una forta inducció d'activitat òptica. Els J-agregats d'aquestes porfirines son estructures allargades de matèria tova que arriben a fer uns quants centenars de nm de longitud i pocs nm de gruix. S'ha vist com els gradients de fluxos poden esculpir (tòrcer o doblegar) la forma d'aquestes estructures [184], i, possiblement, modificar els patrons d'ordre de les interaccions electròniques que sostenen l'agregat.

Mitjançant mesures espectroscòpiques de la matriu de Mueller en aquestes solucions [100] vam comprovar com la inducció d'activitat òptica es podia resseguir tant en els valors de CD com els de CB calculats a partir de la matriu de Mueller (vegeu Fig. 8.4). Això va permetre confirmar que un procés d'inducció i canvi d'activitat era el responsable de l'efecte observat. També hem realitzat mesures de la matriu de Mueller amb alta resolució espaial de les cubetes agitades, tot fent servir el mètode descrit a l'apartat A.4.1. Les mesures de CD fetes amb resolució espaial, tal com la mostrada a la Fig. 8.14 demostren que la inducció té lloc a la part central de la cubeta, en coincidència amb el vòrtex descendent generat per l'agitador. Addicionalment, l'escanejat de la matriu de Mueller al llarg de tota la cubeta també permet veure l'evolució de les anisotropies lineals a les diferents parts i, en certa manera, això defineix el patró de fluxos dins de la cubeta (vegeu els exemples de les Figs. 8.15 i 8.16, on es fa servir les projeccions de dicroisme lineal per mostrar una representació vectorial dels eixos de dicroisme).

Experiments anàlegs als descrits en aquest apartat s'han repetit en flascons o cubetes cilíndriques en comptes de les de secció quadrada i hem observat canvis en el signe dels senyals induïts. Atribuïm aquestes diferències al fet que per una cubeta cilíndrica, degut a la seva major simetria, també hi ha un flux quiral ascendent que actua en sentit contrari que el flux quiral descendent. Aquest fet es descriu detalladament a la secció 8.1.1 d'aquesta tesi.

A.5.3. Mostres sòlides heterogènies

Una de les aplicacions més útils de les mesures de la matriu de Mueller amb resolució espaial és l'estudi de mostres sòlides heterogènies que tenen propietats òptiques canviants al llarg de la seva superfície.

Dominis quirals en cristal · litzacions primes de compostos orgànics

La possibilitat d'identificar dominis quirals en cristal · litzacions preparades al laboratori a partir de fusions de compostos orgànics dóna peu a estudiar els processos de trencament i evolució de la simetria quiral que tenen lloc durant un canvi de fase com és la solidificació.

A partir de fusions de diversos compostos orgànics, com ara bencil, benzofenona, o binaftil vam preparar pel · lícules primes policristal · lines de compostos que formen cristalls quirals i enantiomorfs. Això significa que poden cristal · litzar en dues formes diferents, una imatge especular de l'altra, i cadascuna de elles amb signes oposats d'activitat òptica. Com que el cost energètic per formar els dos enantiomorfs és idèntic s'hauria d'esperar que els dos enantiòmers es formarien amb la mateixa probabilitat. Tanmateix se sap que poden ocórrer processos, com ara certes reaccions autocatalítiques, que trenquen aquesta simetria quiral.

Els millors resultats d'aquestes mesures es van obtenir per cristal · litzacions de bencil. Aquest cristall té una banda prou intensa de CD al voltant de 400 nm (vegeu Fig. 9.1) que facilita la identificació dels dominis quirals si les mesures es fan a aquesta longitud d'ona. La Fig. 9.3 mostra un exemple de les matrius de Mueller obtingudes i, a la Fig. 9.4, es poden apreciar clarament els dominis quirals identificats en aquesta mostra. Els dominis quirals identificats en la majoria de mostres (Fig. 9.6) estan separats per línies rectes. Segons certs models teòrics sobre processos de trencament de simetria [196, 197] aquest tipus de fronteres és la única manera mitjançant la qual dominis quirals de diferent signe poden sobreviure en sistemes que evolucionen cap a la homoquiralitat.

Meteorits

La possibilitat de realitzar mesures polarimètriques acurades i amb una gran resolució espaial en mostres de condrites carbonàcies (un tipus de meteorit amb abundant presencia de compostos de carboni i on s'han detectat aminoàcids) representarien un pas important en la recerca dels orígens de l' homoquiralitat terrestre. Com a primera incursió en aquest àmbit d'estudi vam realitzar algunes mesures preliminars [198] en talls prims i polits dels meteorits Murchison, Murray i Cold Bekkeveld. La nostra hipòtesi a l'hora de plantejar l'estudi era que els processos d'estrès (gradients de cisalla principalment) en que aquests cossos van estar sotmesos durant la seva solidificació podrien haver donar lloc a un excés enantiomèric de fractures o distorsions en la matriu inorgànica del meteorit que, posteriorment, es podria haver transmès a les reaccions orgàniques.

L'objectiu de les nostres mesures era, doncs, similar a la mencionada a l'apartat anterior: la identificació de dominis quirals en mostres sòlides. En aquest cas, però, la dificultat era molt més gran ja que les mostres estudiades eren altament heterogènies i caldria una resolució submicromètrica per poder-les caracteritzar adequadament. Quan vam analitzar estadísticament els resultats obtinguts per la mostra de Murchison (Fig. 9.8) vam observar una desviació de CB no esperada que no apareixia en les altres mostres. Això sembla refermar la nostra hipòtesi, ja que és precisament en el meteorit Murchison on s'ha descrit amb més claredat

una desviació quiral del aminoàcids continguts en ell [38, 201, 202].

Les mesures en condrites carbonàcies representen tot un desafiament experimental i requeririen estudis molt més amplis i amb més recursos. Per ara les nostres mesures han posat de relleu una forma d'estudiar aquestes mostres que fins ara no s'havia ni plantejat i els resultats obtinguts haurien de servir com a estímul per futurs treballs en aquest àmbit.

A.5.4. Conclusions

La resolució de les equacions de Maxwell que descriuen la interacció d'un medi anisòtrop i giròtrop amb llum no es pot tractar analíticament en la majoria de casos i es difícil modelitzar les matrius de Jones o de Mueller a partir del tensor dielèctric i de girotropia del medi. Tanmateix, es pot fer servir la representació infinitesimal del medi, introduïda per Jones, i basada en efectes òptics bàsics per descriure el comportament de qualsevol component òptic. Aquest mètode genera equacions analítiques molt útils per interpretar resultats experimentals. A més, en contra del suggerit per alguns autors, del treball original de Jones no es pot inferir l'existència de cap nou tipus de birefringència i dicroisme. LB i LB'(a l'igual que LD i LD') són només projeccions del mateix fenomen físic.

Hem determinat equacions analítiques que permeten invertir qualsevol matriu de Jones o de Mueller-Jones. Aquesta inversió és pot aplicar a qualsevol matriu de Mueller experimental, si no inclou una despolarització important, i permet la determinació dels efectes físics d'interès, com ara CD i CB. Una altra alternativa per a la interpretació de les matrius de Mueller experimentals és l'ús d'una descomposició tipus producte com la descomposició polar o de Lu-Chipman, que permet factoritzar una matriu de Mueller en termes més simples. El problema que presenten les descomposicions és que, en general, els factors de la descomposició depenen de l'ordre en què són multiplicats. En aquest treball hem derivat les condicions que ha de satisfer un medi, per assegurar la commutatibilitat dels factors de la descomposició. Quan aquestes condicions es compleixen, la descomposició pot ésser aplicada. El treball en aquesta àrea ens ha portat a descriure una nova descomposició i batejar-la com descomposició pseudopolar.

Dins d'un àmbit ja plenament instrumental hem construït un el · lipsòmetre espectroscòpic conegut com 2-MGE. La característica més distintiva del 2-MGE és l'ús de dos PEMs funcionant independentment, cosa que li permet ésser capaç de mesurar la matriu de Mueller d'una mostra, ja sigui en transmissió o en reflexió. Hem demostrat que aquest tipus d'aparell pot ser utilitzat per mesures d'activitat òptica que requereixen una gran sensibilitat, i que pot ser usat tant en líquids com en sòlids, en un ampli rang de longituds d'ona, des de el UV fins al IR proper.

Hem desenvolupat un nou mètode de mesura que pot expandir i/o millorar les capacitats del 2-MGE o d'altres tipus d'el · lipsòmetres o polarímetres. Aquest nou mètode experimental es basa en la utilització d'elements amb rotació òptica com substituts de les unitats de rotació mecànica que es fan servir per orientar el PSG i el PSA i així evitar problemes relacionats amb la desviació del feix. Aquest mètode ens permet realitzar mesures de la matriu de Mueller amb alta resolució espaial que no serien possibles emprant les unitats de rotació mecànica.

Mitjançant la mesura de la matriu de Mueller hem realitzat nombrosos experiments dirigits a determinar l'activitat òptica de diversos sistemes. Podem destacar que per primer cop s'ha mesurat completament el tensor de girotropia d'un cristall com el quars a partir de mesures espectroscòpiques de la matriu de Mueller. Un altre grup de mesures importants han estat les realitzades en solucions agitades que contenien nanopartícules allargades de matèria tova. En aquest cas es van estudiar tant mitjançant mesures espectroscòpiques com mitjançant mesures de tipus "mapping". Això han permès estudiar amb detall i aclarir aspectes desconeguts d'un fenomen, fins ara controvertit, d'inducció de quiralitat supramolecular per efectes hidrodinàmics.

Un dels àmbits de mesura que creiem que pot tenir més perspectives de futur és la caracterització mitjançant la matriu de Mueller de mostres sòlides amb propietats òptiques que varien al llarg de la seva superfície. Exemples d'aquest tipus de mesures, realitzades dins del marc d'aquesta tesi, són la determinació de dominis quirals en pel · lícules policristal · lines d'alguns compostos orgànics i les mesures preliminars en seccions primes de meteorits.

Appendix B.

Computer software

The construction of a 2-MGE also involved the development a certain amount of computer software. All the theoretical descriptions of the instrument given in Part III of this thesis would not be of utility without an interface able to communicate with the different components of the 2-MGE and to handle several different routines of data acquisition and calibration. The 2-MGE was developed with the idea of offering a friendly and complete GUI (Graphic User Interface) that was easy to handle for any eventual user of the equipment. The inspiration we used for the organization of this GUI was the one programmed by Gerald E. Jellison for the control of the 2-MGEs built by him and available at Oak Ridge National Laboratory facilities.

2-MGE software has been developed in Labview, which is a visual programming language from National Instruments. One benefit of Labview is the extensive support for accessing instrumentation hardware. Another interesting feature of Labview is the easiness to create attractive GUIs without the necessity of being a very skilled programmer. Moreover, despite Labview is sometimes regarded as a limited language, only convenient for controlling instrumentation, we have been surprised by its versatility and it has suited all our demands.

This appendix is intended to give a general vision of the software developed. The details of the operation of every acquisition type will be not presented and only some selected important screenshots of the 2-MGE software will be included.

Fig. B.1 shows the front panel of the 2-MGE software. Buttons on the left column give access to the basic functionalities of the 2-MGE when using mechanical rotators for the PSG and PSA: “calibration” for a complete calibration of the instrument, “oscilloscope” for a real time visualization of the signal, “transmission measurement” for a partial or complete determination of the transmissive Mueller matrix, “reflection measurement” for a partial or complete determination of the reflective Mueller matrix using the NSC notation and “scattering measurement” for a partial or complete determination of the scattering Mueller matrix (this is a prototype routine in which the light source has to be switched to a laser). Buttons on the right column of Fig. B.2 give access to different functions that involve the quartz assisted method introduced in chapter 6. Prior to the

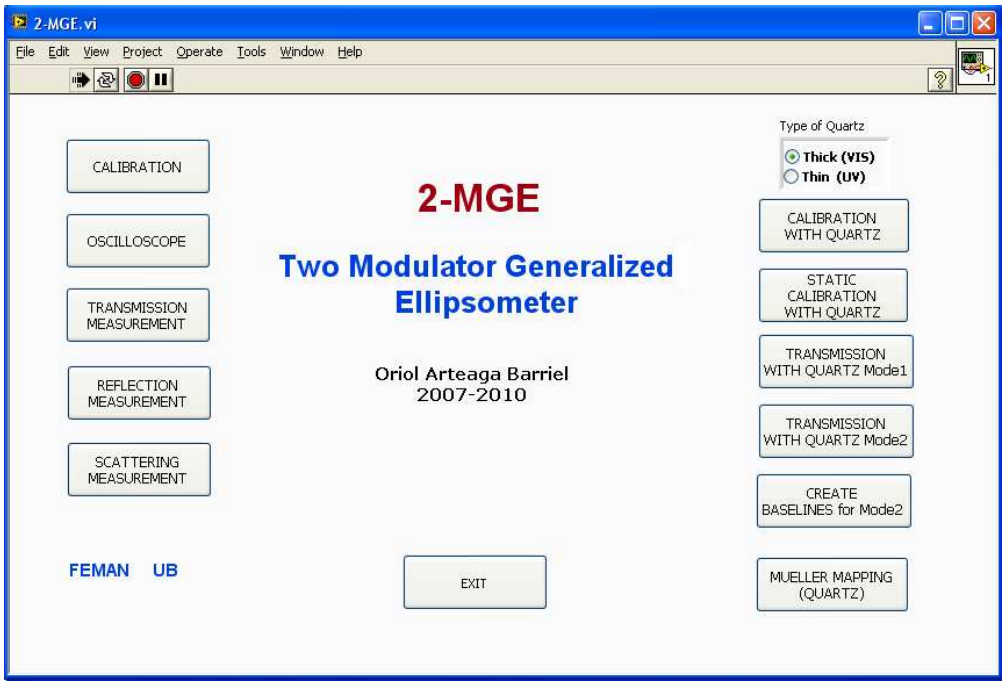

Figure B.1.: Front panel of the 2-MGE software. It gives access to every function of the program.

selection of any of these options the thickness of the set of quartz plates needs to be chosen: "thick" for measurements in the VIS and "thin" for measurements in the UV. After that, users can choose between two types of calibrations and two different modes of spectroscopic Mueller matrix transmission measurements. The button "Mueller mapping" is used to obtain spatially resolved measurements of the Mueller matrix.

The 2-MGE software is structured in a very decentralized manner. Each of the enumerated acquisition types is mostly independent from the others. They only share the configuration parameters of the 2-MGE which are accessible in every acquisition type and saved in a computer file. Fig. B.2 shows the configuration windows available in the 2-MGE software. Three of them are used to configure the mechanical elements of our 2-MGE: rotator stages of the PSG and PSA, the X−Y translation units used to scan the sample and tilting mechanism used to set the angle of incidence. One more window is used to set the parameters of the digitizer and the remaining panel is used to define the wavelengths of measurement and the configuration of the monochromator.

Figs. B.3, B.4, B.5, B.6 and B.7 show various screenshots of the 2-MGE software while performing different functions. At the present status of development

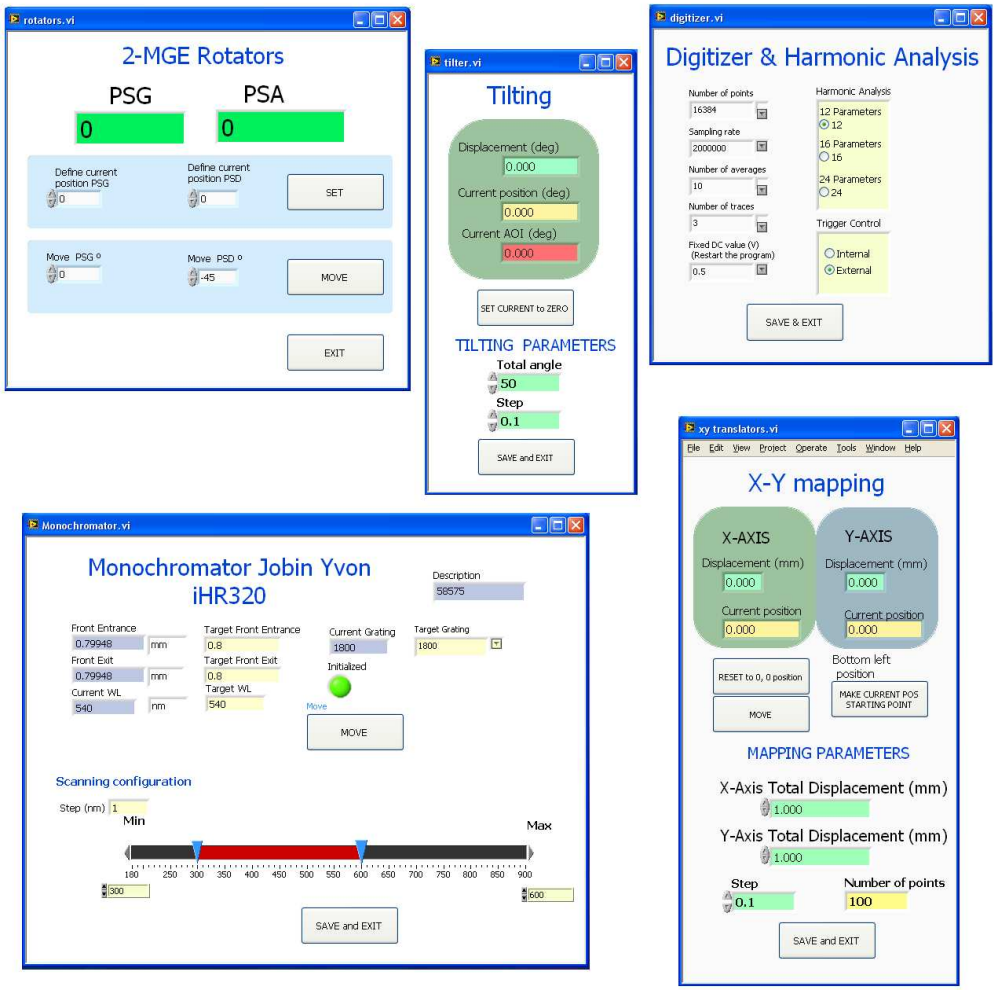

Figure B.2.: Configuration panels of the 2-MGE. The "rotators", "monochromator" and "digitizer" windows are available for all acquisition routines. The "tilting" and "mapping" windows are exclusive of certain acquisition types.

the software is useable in all their most significant functions. However, we are aware that it contains many bugs and several functions could be still improved. Despite the user interface looks quite accessible, the software still needs to be handled by a trained user and with some knowledge about the contents of this thesis.

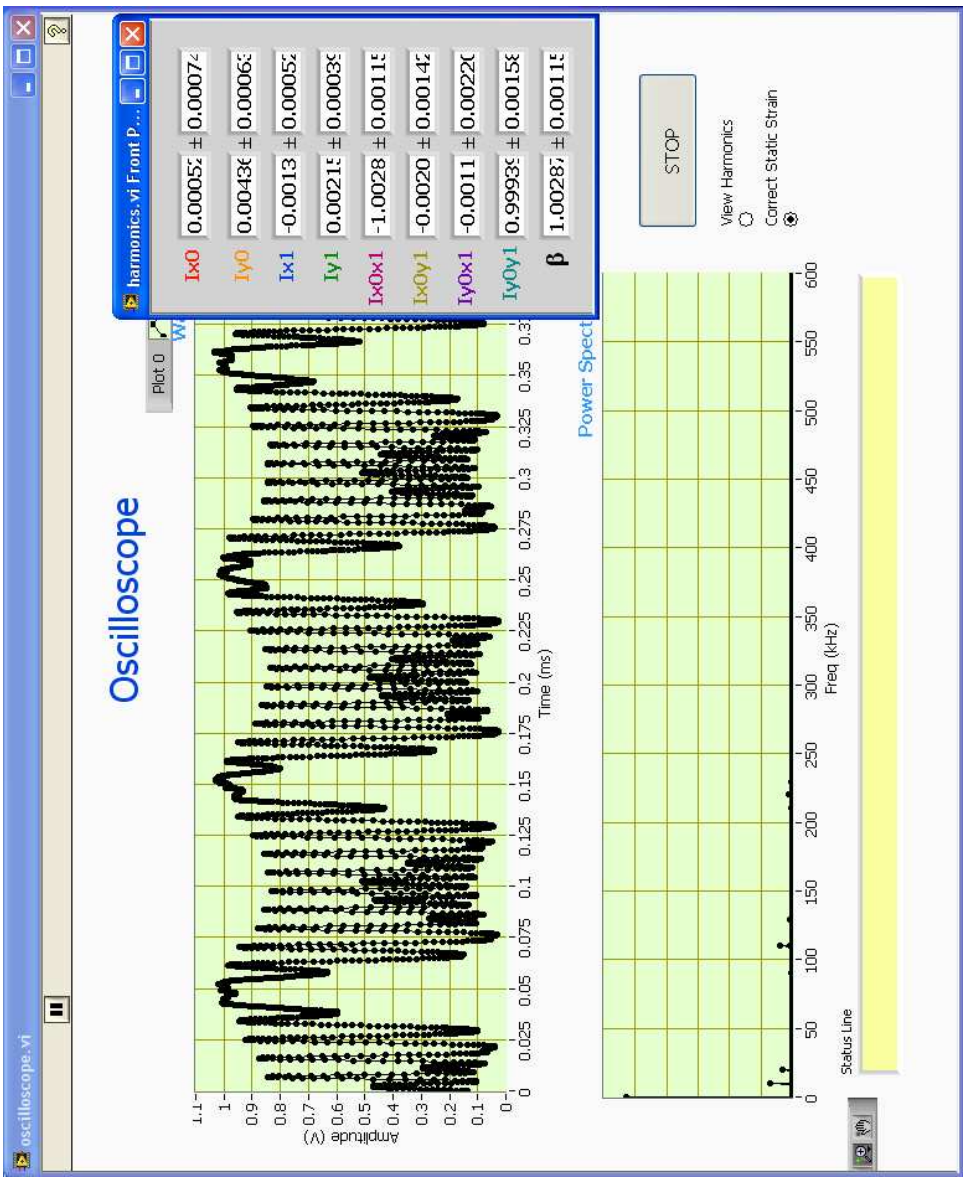

Figure B.3.: Oscilloscope panel included in the 2-MGE software. It permits a real time visualization of the digitized signal and the eight independent parameters I_{X0}, I_{Y0}, I_{X1}, I_{Y1}, I_{X0X1}, I_{X0Y1}, I_{Y0X1} and I_{Y0Y1} that the 2-MGE measures. The waveform shown here is characteristic of the instrument in the straight-through configuration with PSG and PSA oriented at (0°, 0°).

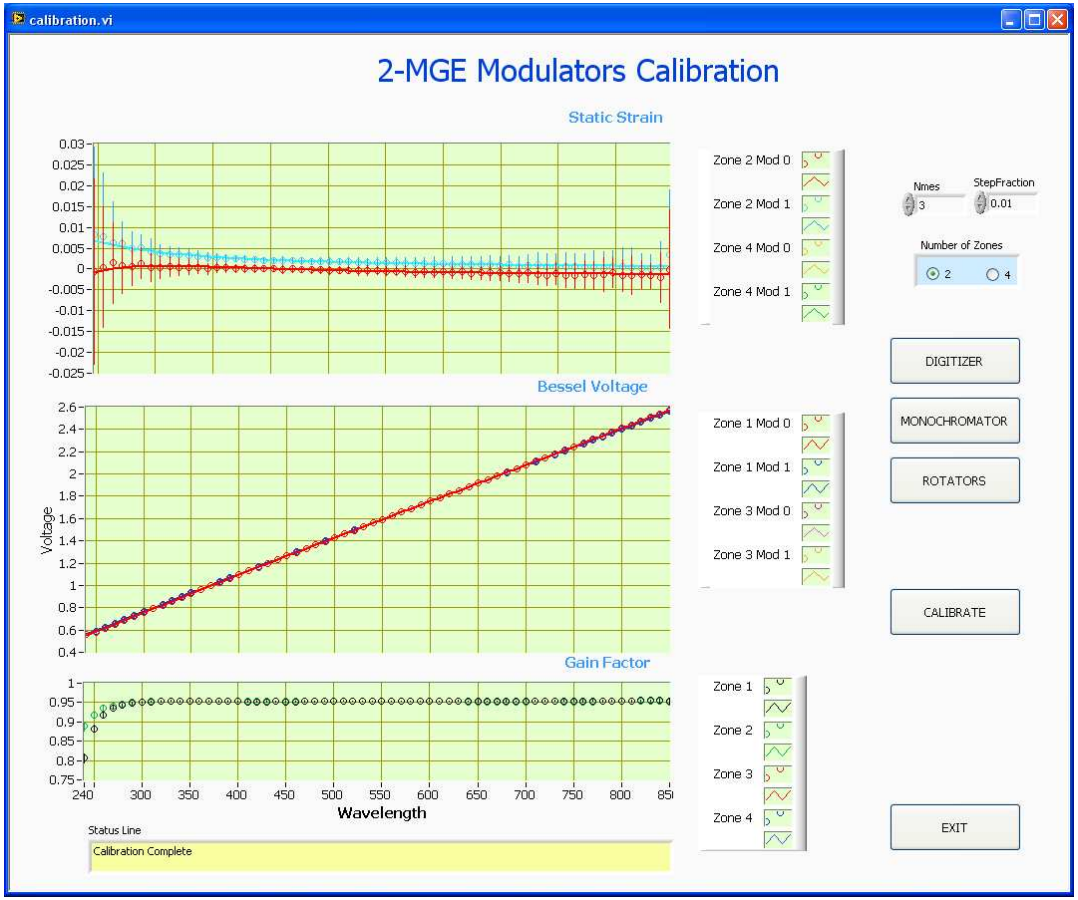

Figure B.4.: Spectroscopic calibration of the 2-MGE. Circles depict experimental data points while solid lines are calibration fittings. This panel shows a 2 zone calibration in which the (PSG, PSA) orientation (0°, 0°) is used for the calibration of the Bessel voltage (middle graph) and the orientation (0°, 45°) is used for the calibration of the PEM's static strain (top graph). The bottom graph shows the electronic frequency-independent gain factor for both orientations.

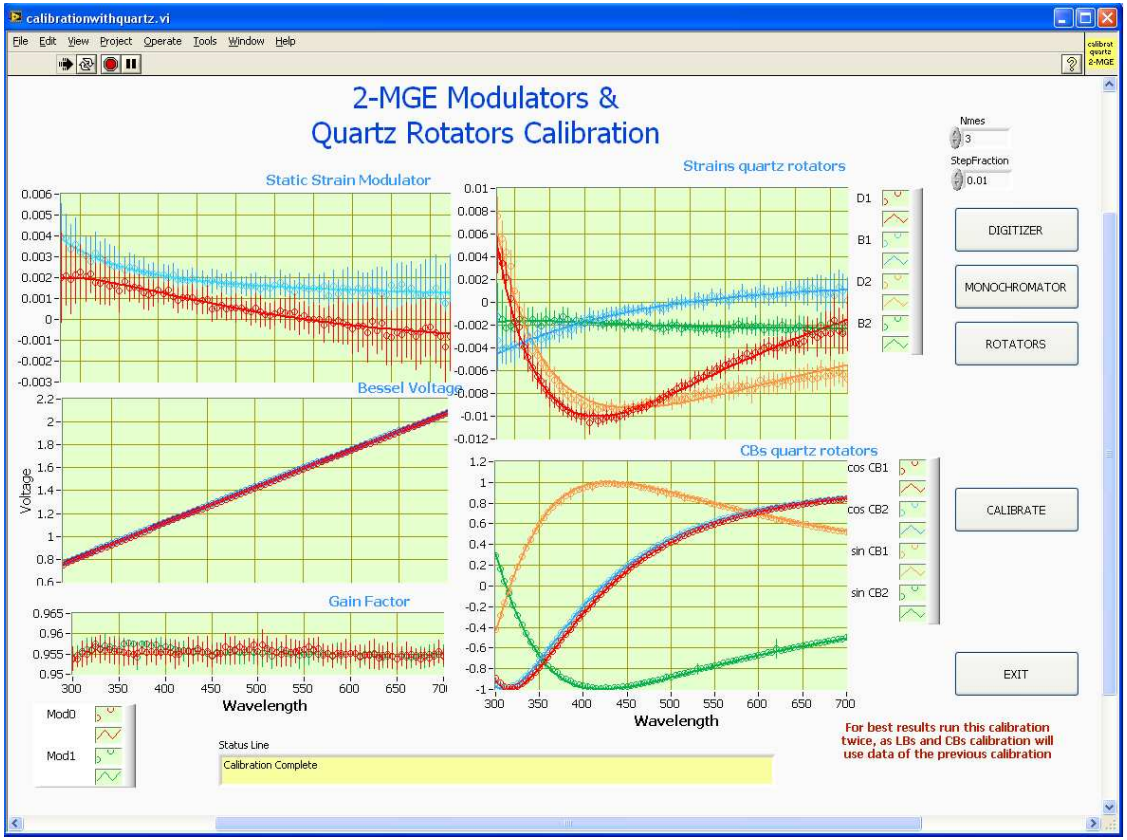

Figure B.5.: Panel shown during the simultaneous spectroscopic calibration of the PEMs and the quartz rotators ("calibration with quartz" button o the front panel. This calibration window contains the same parameters shown that in Fig. B.4 (i.e. the static strain of the modulators, the Bessel voltage needed to set the amplitude of modulation to 2.4048 rad and the electronic frequency-independent gain factor) but, in addition, the static strains of the two quartz plates and their respective CB are also shown. The data shown in the picture corresponds to quartz plates of ∼1 mm thick and opposite handedness.

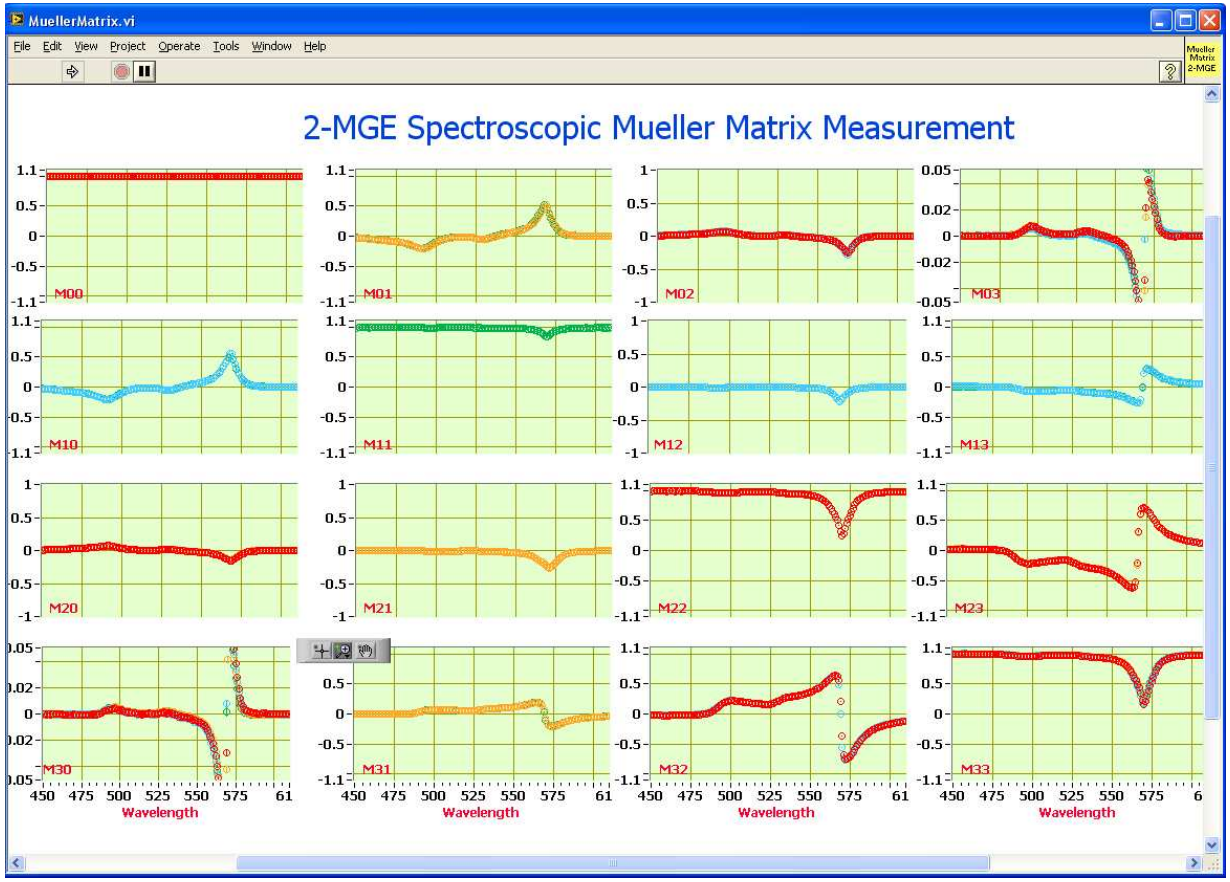

Figure B.6.: Example of the panel window shown during a spectroscopic Mueller matrix measurement. The Mueller matrix is presented on screen in real time during the data acquisition. Mueller matrix elements measured at different orientations of the PSG and the PSA are presented with different colours.

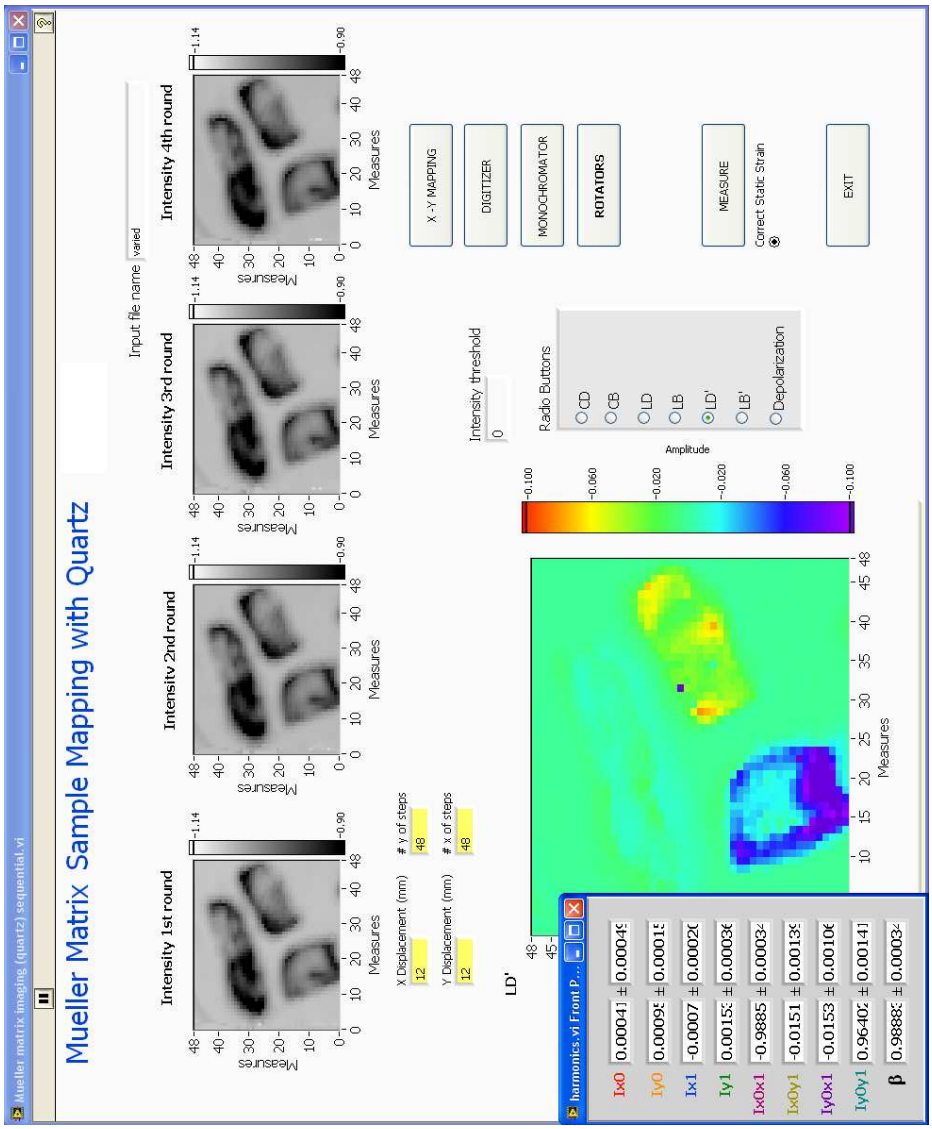

Figure B.7.: Spatially resolved measurements are obtained with this panel. Each Mueller matrix scanning takes four measurement configurations accessed by quartz plates (they are described in chapter 6). The intensity mapping corresponding to each one of the four measurements are presented on the top. Once the measure has finished, the bottom window displays the selected optical effect as calculated from the measured Mueller matrices with the analytic inversion.

List of publications

The scientific results produced during the duration of this thesis have been published by means of a number of refereed publications.

1. O. Arteaga, A. Canillas, J. Crusats, Z. El-Hachemi, J. Llorens, E. Sacristan and J. M. Ribó "Emergence of supramolecular chirality by flows", ChemPhysChem **11**, 3511—3516, (2010).

2. O. Arteaga, Z. El-Hachemi, A. Canillas and J. M. Ribó "Transmission Mueller Matrix Ellipsometry of Chirality Switching Phenomena", accepted in Thin Solid Films, (2010).

3. O. Arteaga, "On the existence of Jones birefringence and Jones dichroism", Opt. Lett. **35**, 1359–1360 (2010).

4. O. Arteaga and A. Canillas, "Analytic inversion of the Mueller-Jones polarization matrices for homogeneous media", Opt. Lett. **35**, 559–561 (2010).

5. O. Arteaga, A. Canillas, J. Crusats, Z. El-Hachemi, G. Jellison, J. Llorca, and J. M. Ribó, "Chiral biases in solids by effect of shear gradients: A speculation on the deterministic origin of biological homochirality", Origins of Life and Evolution of Biospheres **40**, 27–40 (2010).

6. O. Arteaga, A. Canillas, and J. Jellison, "Determination of the components of the gyration tensor of quartz by oblique incidence transmission two-modulator generalized ellipsometry", Appl. Opt. **48**, 5307–5317 (2009).

7. O. Arteaga, A. Canillas, R. Purrello, and J. M. Ribó, "Evidence of induced chirality in stirred solutions of supramolecular nanofibers", Opt. Lett. **34**, 2177–2179 (2009).

8. O. Arteaga, C. Escudero, G. Oncins, Z. El-Hachemi, J. Llorens, J. Crusats, A. Canillas, and J. M. Ribó, "Reversible mechanical induction of optical activity in solutions of soft-matter nanophases", Chemistry - An Asian Journal **4**, 1687–1696 (2009).

9. O. Arteaga and A. Canillas, "Pseudopolar decomposition of the Jones and Mueller-Jones exponential polarization matrices", J. Opt. Soc. Am. A **26**, 783–793 (2009).

10. Z. El-Hachemi, C. Escudero, O. Arteaga, A. Canillas, J. Crusats, G. Mancini, R. Purrello, A. Sorrenti, A. D'Urso, and J. M. Ribo, "Chiral sign selection on the J-aggregates of diprotonated tetrakis-(4-sulfonatophenyl)porphyrin by traces of unidentified chiral contaminants present in the ultra-pure water used as solvent", Chirality **21**, 408–412 (2009).

11. O. Arteaga, Z. El-Hachemi, and A. Canillas, "Application of transmission ellipsometry to the determination of CD spectra of porphyrin J-aggregates", Phys. Status Solidi. (a) **205**, 797–801 (2008).

12. S. Portal, M. Vallve, O. Arteaga, J. Ignes Mullol, A. Canillas, and E. Bertran, "Optical characterization of colloidal crystals based on dissymmetric metal-coated oxide submicrospheres", Thin Solid Films **517**, 1053–1057 (2008).

13. Z. El-Hachemi, O. Arteaga, A. Canillas, J. Crusats, C. Escudero, R. Kuroda, T. Harada, M. Rosa, and J. M. Ribó , "On the mechano-chiral effect of vortical flows on the dichroic spectra of 5-phenyl-10,15,20-tris(4-sulfonatophenyl) porphyrin J-aggregates", Chemistry - A European Journal **14**, 6438–6443 (2008).

Patent

1. O. Arteaga, A. Canillas, and J. M. Ribó, "Method and system for determining a plurality of elements of a Mueller matrix", Patent application submitted, May 2010.

Bibliography

[1] R. C. Jones, "A new calculus for the treatment of optical systems," J. Opt. Soc. Am. **31**, 488–493 (1941).

[2] H. Mueller, "The foundations of optics," Journal of the Optical Society of America **38**, 661–662 (1948).

[3] R. M. A. Azzam and N. M. Bashara, *Ellipsometry and Polarized Light* (North Holland, 1988).

[4] R. Barakat, "Bilinear constraints between elements of the 4×4 Mueller-Jones transfer matrix of polarization theory," Optics Communications **38**, 159–161 (1981).

[5] J. W. Hovenier, "Structure of a general pure Mueller matrix," Appl. Opt. **33**, 8318–8324 (1994).

[6] J. J. Gil, "Polarimetric characterization of light and media," The European Physical Journal Applied Physics **40**, 1–47 (2007).

[7] R. A. Chipman, *Handbook of Optics, Vol. 2: Devices, Measurements, and Properties, Second Edition* (McGraw-Hill Professional, 1994), 2nd ed.

[8] A. A. Kochanovskij, *Light scattering reviews 4: single light scattering and radiative transfer* (Springer, 2008).

[9] C. Brosseau, *Fundamentals of Polarized Light: A Statistical Optics Approach* (Wiley-Interscience, 1998).

[10] D. Goldstein, *Polarized Light, Revised and Expanded (Optical Science and Engineering)* (CRC, 2003), 2nd ed.

[11] J. J. Gil and E. Bernabeu, "A depolarization criterion in Mueller matrices," Journal of Modern Optics pp. 259–261 (1985).

[12] J. J. Gil and E. Bernabeu, "Depolarization and polarization indices of an optical system," Journal of Modern Optics **33**, 185–189 (1986).

[13] S. R. Cloude and E. Pottier, "Concept of polarization entropy in optical scattering," Optical Engineering **34**, 1599–1610 (1995).

[14] R. Ossikovski, "Alternative depolarization criteria for Mueller matrices," J. Opt. Soc. Am. A **27**, 808–814 (2010).

[15] D. F. Arago, "Sur une modification remarquable qu' éprouvent les rayons lumineux dans leur passage à travers certains corps diaphanes, et sur quelques autres nouveaux phénomènes d'optique," Mem. Inst. **1**, 93–134 (1811).

[16] J. B. Biot, "Mémoire sur un nouveau genre d'oscillations que les molécules de la lumière éprouvent, en traversant certains cristaux," Mem. Inst. **1**, 1–372 (1812).

[17] Fresnel, "Ueber das Licht," Annalen der Physik und Chemie **81**, 223–256 (1825).

[18] W. Haidinger, "Beobachtung der licht-polarisations-büschel auf flächen, welche das licht in zwei senkrecht auf einander stehenden richtungen polarisiren," Annalen der Physik und Chemie **144**, 305–319 (1846).

[19] A. Cotton, "Absorption inégale des rayons circulaires droit et gauche dans certains corps actifs," C. R. Acad. Sci. **120**, 989–991 (1895).

[20] T. M. Lowry, *Optical rotatory power* (Longman Scientific and Technical, 1935).

[21] S. Chandrasekhar, "Simple model for optical activity," American Journal of Physics **24**, 503–506 (1956).

[22] P. L. Polavarapu, A. G. Petrovic, and P. Zhang, "Kramers-Kronig transformation of experimental electronic circular dichroism: Application to the analysis of optical rotatory dispersion in dimethyl-L-tartrate," Chirality **18**, 723–732 (2006).

[23] M. Krykunov, M. D. Kundrat, and J. Autschbach, "Calculation of circular dichroism spectra from optical rotatory dispersion, and vice versa, as complementary tools for theoretical studies of optical activity using time-dependent density functional theory," The Journal of Chemical Physics **125**, 194110 (2006).

[24] J. Frenkel, "On the transformation of light into heat in solids. I," Physical Review Online Archive (Prola) **37**, 17–44 (1931).

[25] V. Agranovich, *Excitations in Organic Solids (International Series of Monographs on Physics)* (Oxford University Press, USA, 2009).

[26] C. A. Schalley, ed., *Analytical Methods in Supramolecular Chemistry* (Wiley-VCH, 2007), 1st ed.

[27] S. E. Boiadjiev and D. A. Lightner, "Exciton chirality. (A) Origins of and (B) applications from strongly fluorescent dipyrrinone chromophores," Monatshefte für Chemie / Chemical Monthly **136**, 489–508 (2005).

[28] E. E. Jelley, "Spectral absorption and fluorescence of dyes in the molecular state," Nature **138**, 1009–1010 (1936).

[29] G. Scheibe, "Über die veränderlichkeit der absorptionsspektren in lösungen und die nebenvalenzen als ihre ursache," Angewandte Chemie **50**, 212–219 (1937).

[30] V. Avetisov, "Question 4: Short remarks about the origin of homochirality," Origins of Life and Evolution of Biospheres **37**, 367–370 (2007).

[31] A. Guijarro and M. Yus, *The origin of chirality in the molecules of life: A revision from awareness to the current theories and perspectives of this unsolved problem* (Royal Society of Chemistry, 2008).

[32] I. Weissbuch, L. Leiserowitz, and M. Lahav, ""stochastic mirror symmetry breaking" via self-assembly, reactivity and amplification of chirality: Relevance to abiotic conditions," in "Prebiotic Chemistry," , vol. 259 of *Topics in Current Chemistry*, P. Walde, ed. (Springer-Verlag, Berlin/Heidelberg, 2005), chap. 137067, pp. 123–165.

[33] D. K. Kondepudi and K. Asakura, "Chiral autocatalysis, spontaneous symmetry breaking, and stochastic behavior," Accounts of Chemical Research **34**, 946–954 (2001).

[34] P. L. Luisi, *The emergence of life: from chemical origins to synthetic biology* (Cambridge University Press, 2006).

[35] F. C. Frank, "On spontaneous asymmetric synthesis." Biochimica et biophysica acta **11**, 459–463 (1953).

[36] K. Soai, T. Shibata, H. Morioka, and K. Choji, "Asymmetric autocatalysis and amplification of enantiomeric excess of a chiral molecule," Nature **378**, 767–768 (1995).

[37] S. Pizzarello, "The chemistry of life's origin: A carbonaceous meteorite perspective," Accounts of Chemical Research **39**, 231–237 (2006).

[38] J. R. Cronin and S. Pizzarello, "Enantiomeric excesses in meteoritic amino acids," Science **275**, 951–955 (1997).

[39] R. L. Disch and D. I. Sverdlik, "Apparent circular dichroism of oriented systems," Analytical Chemistry **41**, 82–86 (1969).

[40] Y. Shindo, M. Nakagawa, and Y. Ohmi, "On the problems of CD spectropolarimeters. II: Artifacts in CD spectrometers," Applied Spectroscopy pp. 860–868 (1985).

[41] N. Berova, K. Nakanishi, and R. Woody, *Circular dichroism: principles and applications* (Wiley-VCH, 2000).

[42] J. Schellman and H. P. Jensen, "Optical spectroscopy of oriented molecules," Chemical Reviews **87**, 1359–1399 (1987).

[43] H. P. Jensen, J. A. Schellman, and T. Troxell, "Modulation techniques in polarization spectroscopy," Appl. Spectrosc. **32**, 192–200 (1978).

[44] J. A. Schellman, "Circular dichroism and optical rotation," Chemical Reviews **75**, 323–331 (1975).

[45] Y. Shindo and M. Nakagawa, "On the artifacts in circularly polarized emission spectroscopy," Applied Spectroscopy pp. 32–38 (1985).

[46] Y. Shindo, "On the problems of CD spectropolarimeter (IV) artifacts due to the light scattering by small particles," Applied Spectroscopy **39**, 713–715 (1985).

[47] Y. Shindo and Y. Ohmi, "New polarization-modulation spectrometer for simultaneous circular dichroism and optical rotary dispersion measurements (I): Instrument design, analysis, and evaluation," Review of Scientific Instruments **56**, 2237–2242 (1985).

[48] Y. Shindo and M. Nakagawa, "Circular dichroism measurements. I. Calibration of a circular dichroism spectrometer," Review of Scientific Instruments **56**, 32–39 (1985).

[49] R. Kuroda, T. Harada, and Y. Shindo, "A solid-state dedicated circular dichroism spectrophotometer: Development and application," Review of Scientific Instruments **72**, 3802–3810 (2001).

[50] R. Kuroda and T. Honma, "CD spectra of solid-state samples," Chirality **12**, 269–277 (2000).

[51] R. Kuroda, *Chiral photochemistry*, Molecular and supramolecular photochemistry (Marcel Dekker, 2004).

[52] T. Harada, H. Hayakawa, and R. Kuroda, "Vertical-type chiroptical spectrophotometer (I): Instrumentation and application to diffuse reflectance circular dichroism measurement," Review of Scientific Instruments **79**, 073103+ (2008).

[53] T. Harada, Y. Miyoshi, and R. Kuroda, "High performance diffuse reflectance circular dichroism spectrophotometer," Review of Scientific Instruments **80**, 046101+ (2009).

[54] E. Castiglioni, P. Biscarini, and S. Abbate, "Experimental aspects of solid state circular dichroism," Chirality **21**, E28–E36 (2009).

[55] J. Kobayashi and Y. Uesu, "A new optical method and apparatus "HAUP" for measuring simultaneously optical activity and birefringence of crystals. I. Principles and construction," Journal of Applied Crystallography **16**, 204–211 (1983).

[56] J. Kobayashi, T. Asahi, S. Takahashi, and A. M. Glazer, "Evaluation of the systematic errors of polarimetric measurements: application to measurements of the gyration tensors of α-quartz by the HAUP," Journal of Applied Crystallography **21**, 479–484 (1988).

[57] J. R. L. Moxon and A. R. Renshaw, "The simultaneous measurement of optical activity and circular dichroism in birefringent linearly dichroic crystal sections. I. Introduction and description of the method," Journal of Physics: Condensed Matter **2**, 6807–6836 (1990).

[58] P. Gomez and C. Hernandez, "High-accuracy universal polarimeter measurement of optical activity and birefringence of α-quartz in the presence of multiple reflections," J. Opt. Soc. Am. B **15**, 1147–1154 (1998).

[59] K. Claborn, J. Herreros Cedres, C. Isborn, A. Zozulya, E. Weckert, W. Kaminsky, and B. Kahr, "Optical rotation of achiral pentaerythritol," Journal of the American Chemical Society **128**, 14746–14747 (2006).

[60] W. Kaminsky, M. A. Geday, J. Herreros-Cedres, and B. Kahr, "Optical rotatory and circular dichroic scattering," The Journal of Physical Chemistry A **107**, 2800–2807 (2003).

[61] K. Claborn, E. Puklin-Faucher, M. Kurimoto, W. Kaminsky, and B. Kahr, "Circular dichroism imaging microscopy: Application to enantiomorphous twinning in biaxial crystals of 1,8-dihydroxyanthraquinone," Journal of the American Chemical Society **125**, 14825–14831 (2003).

[62] J. H. Cedrés, C. H. Rodriguez, and W. Kaminsky, "Absolute optical rotation of $CsLiB_6O_10$," Journal of Applied Crystallography **38**, 544–554 (2005).

[63] W. Kaminsky, E. Weckert, H. Kutzke, A. M. Glazer, and H. Klapper, "Non-linear optical properties and absolute structure of metastable 4-methyl benzophenone," Zeitschrift für Kristallographie **221**, 294–299 (2006).

[64] K. Claborn, C. Isborn, W. Kaminsky, and B. Kahr, "Optical rotation of achiral compounds," Angewandte Chemie International Edition **47**, 5706–5717 (2008).

[65] W. Kaminsky, "Experimental and phenomenological aspects of circular birefringence and related properties in transparent crystals," Reports on Progress in Physics **63**, 1575–1640 (2000).

[66] M. F. Maestre and J. E. Katz, "A circular dichroism microspectrophotometer," Biopolymers **21**, 1899–1908 (1982).

[67] W. Kaminsky, K. Claborn, and B. Kahr, "Polarimetric imaging of crystals," Chem. Soc. Rev. **33**, 514–525 (2004).

[68] J. H. Freudenthal, E. Hollis, and B. Kahr, "Imaging chiroptical artifacts," Chirality **21**, S20–S27 (2009).

[69] B. Kahr, J. Freudenthal, and E. Gunn, "Crystals in light," Accounts of Chemical Research **43**, 684–692 (2010).

[70] D. W. Berreman, "Optics in stratified and anisotropic media: 4×4-matrix formulation," J. Opt. Soc. Am. **62**, 502–510 (1972).

[71] M. Schubert, "Polarization-dependent optical parameters of arbitrarily anisotropic homogeneous layered systems," Phys. Rev. B **53**, 4265–4274 (1996).

[72] E. Georgieva, "Reflection and refraction at the surface of an isotropic chiral medium: eigenvalue–eigenvector solution using a 4×4 matrix method," Journal of the Optical Society of America A **12**, 2203–2211 (1995).

[73] E. U. Condon, "Theory of optical rotatory power," Reviews of modern physics **9**, 432–457 (1937).

[74] M. Schubert, *Infrared Ellipsometry on Semiconductor Layer Structures: Phonons, Plasmons, and Polaritons (Springer Tracts in Modern Physics)* (Springer, 2005), 1st ed.

[75] R. M. A. Azzam, "Photopolarimetric measurement of the Mueller matrix by Fourier analysis of a single detected signal," Opt. Lett. **2**, 148–150 (1978).

[76] P. J. Lin-Chung and S. Teitler, "4X4 Matrix formalisms for optics in stratified anisotropic media," J. Opt. Soc. Am. A **1**, 703–705 (1984).

[77] H. Wöhler, G. Haas, M. Fritsch, and D. A. Mlynski, "Faster 4×4 matrix method for uniaxial inhomogeneous media," J. Opt. Soc. Am. A **5**, 1554–1557 (1988).

[78] C. R. Jones, "New calculus for the treatment of optical systems. VII. Properties of the N-matrices," J. Opt. Soc. Am. **38**, 671–685 (1948).

[79] R. M. A. Azzam, "Propagation of partially polarized light through anisotropic media with or without depolarization: A differential 4×4 matrix calculus," J. Opt. Soc. Am. **68**, 1756–1767 (1978).

[80] *Complex Component Characterization Based on Elementary Matrices*, OSA Technical Digest (CD) (Optical Society of America, 2009).

[81] R. Barakat, "Exponential versions of the Jones and Mueller-Jones polarization matrices," J. Opt. Soc. Am. A **13**, 158–163 (1996).

[82] R. C. Jones, "New calculus for the treatment of optical systems. VIII. Electromagnetic theory," J. Opt. Soc. Am. **46**, 126–131 (1956).

[83] O. Arteaga, "Mesura de dicroisme circular i activitat òptica molecular mitjançant el·lipsometria generalitzada." Master's thesis, University of Barcelona (2007).

[84] S.-Y. Lu and R. A. Chipman, "Interpretation of Mueller matrices based on polar decomposition," J. Opt. Soc. Am. A **13**, 1106–1113 (1996).

[85] G. E. Jellison, J. D. Hunn, and C. M. Rouleau, "Normal-incidence generalized ellipsometry using the two-modulator generalized ellipsometry microscope," Appl. Opt. **45**, 5479–5488 (2006).

[86] G. E. Jellison, C. O. Griffiths, D. E. Holcomb, and C. M. Rouleau, "Transmission two-modulator generalized ellipsometry measurements." Applied optics **41**, 6555–6566 (2002).

[87] E. B. Graham and R. E. Raab, "On the Jones birefringence," Proceedings of the Royal Society of London. Series A, Mathematical and Physical Sciences **390**, 73–90 (1983).

[88] C. Graham and R. E. Raab, "Eigenvector approach to the evaluation of the Jones N matrices of nonabsorbing crystalline media," J. Opt. Soc. Am. A **11**, 2137–1944 (1994).

[89] R. E. Raab, "Some unmeasured crystal properties," Crystal Research and Technology **38**, 202–214 (2003).

[90] T. Roth and G. L. J. A. Rikken, "Observation of magnetoelectric Jones birefringence," Physical Review Letters **85**, 4478–4481 (2000).

[91] D. Budker and J. E. Stalnaker, "Magnetoelectric Jones dichroism in atoms," Physical Review Letters **91**, 263901+ (2003).

[92] V. V. Chernushkin, P. V. Mironova, and V. D. Ovsiannikov, "Magnetoelectric Jones spectroscopy of alkali atoms," Journal of Physics B: Atomic, Molecular and Optical Physics **41**, 115401+ (2008).

[93] P. V. Mironova, V. D. Ovsiannikov, and V. V. Chernushkin, "Magnetoelectric Jones birefringence and dichroism in a medium of free atoms," Journal of Physics B: Atomic, Molecular and Optical Physics **39**, 4999–5011 (2006).

[94] A. Rizzo and S. Coriani, "Jones birefringence in gases: Ab initio electron correlated results for atoms and linear molecules," The Journal of Chemical Physics **119**, 11064–11079 (2003).

[95] M. Izdebski, W. Kucharczyk, and R. E. Raab, "Effect of beam divergence from the optic axis in an electro-optic experiment to measure an induced Jones birefringence," J. Opt. Soc. Am. A **18**, 1393–1398 (2001).

[96] V. A. De Lorenci and G. P. Goulart, "Magnetoelectric birefringence revisited," Physical Review D **78**, 045015 (2008).

[97] D. L. Andrews, G. J. Daniels, and G. E. Stedman, "Magnetoelectric Jones dichroism," Journal of Physics B: Atomic, Molecular and Optical Physics **36**, L357–L364 (2003).

[98] L. D. Barron, *Molecular light scattering and optical activity* (Cambridge University Press, 2004).

[99] O. Arteaga, "On the existence of Jones birefringence and Jones dichroism," Opt. Lett. **35**, 1359–1360 (2010).

[100] O. Arteaga, A. Canillas, R. Purrello, and J. M. Ribó, "Evidence of induced chirality in stirred solutions of supramolecular nanofibers," Opt. Lett. **34**, 2177–2179 (2009).

[101] Chandrasekhar, *Liquid Crystals* (Cambridge University Press, 1993), 2nd ed.

[102] O. Arteaga and A. Canillas, "Analytic inversion of the Mueller-Jones polarization matrices for homogeneous media," Opt. Lett. **35**, 559–561 (2010).

[103] S. R. Cloude, "Conditions for physical realizability of matrix operators in polarimetry," in "Society of Photo-Optical Instrumentation Engineers (SPIE) Conference Series," , vol. 1166, R. A. Chipman, ed. (1990), vol. 1166, pp. 177–185.

[104] S. Y. Lu and R. A. Chipman, "Homogeneous and inhomogeneous Jones matrices," J. Opt. Soc. Am. A **11**, 766+ (1994).

[105] C. Whitney, "Pauli-algebraic operators in polarization optics," J. Opt. Soc. Am. **61**, 1207+ (1971).

[106] J. J. Gil and E. Bernabeu, "Obtainment of the polarizing and retardation parameters of nondepolarizing optical system from polar decomposition of its Mueller matrix," Optik **76**, 67–71 (1987).

[107] R. Ossikovski, A. De Martino, and S. Guyot, "Forward and reverse product decompositions of depolarizing Mueller matrices," Opt. Lett. **32**, 689–691 (2007).

[108] S. N. Savenkov, O. I. Sydoruk, and R. S. Muttiah, "Conditions for polarization elements to be dichroic and birefringent," J. Opt. Soc. Am. A **22**, 1447–1452 (2005).

[109] M. K. Swami, S. Manhas, P. Buddhiwant, N. Ghosh, A. Uppal, and P. K. Gupta, "Polar decomposition of 3×3 Mueller matrix: a tool for quantitative tissue polarimetry," Opt. Express **14**, 9324–9337 (2006).

[110] N. Ghosh, M. F. G. Wood, and A. I. Vitkin, "Mueller matrix decomposition for extraction of individual polarization parameters from complex turbid media exhibiting multiple scattering, optical activity, and linear birefringence," Journal of Biomedical Optics **13** (2008).

[111] J. Chung, W. Jung, M. J. Hammer-Wilson, P. Wilder-Smith, and Z. Chen, "Use of polar decomposition for the diagnosis of oral precancer," Appl. Opt. **46**, 3038–3045 (2007).

[112] C. Collet, J. Zallat, and Y. Takakura, "Clustering of Mueller matrix images for skeletonized structure detection," Opt. Express **12**, 1271–1280 (2004).

[113] S. Manhas, M. K. Swami, P. Buddhiwant, N. Ghosh, P. K. Gupta, and J. Singh, "Mueller matrix approach for determination of optical rotation in chiral turbid media in backscattering geometry," Opt. Express **14**, 190–202 (2006).

[114] R. M. Wilcox, "Exponential operators and parameter differentiation in quantum physics," Journal of Mathematical Physics **8**, 962–982 (1967).

[115] D. Scholz and M. Weyrauch, "A note on the Zassenhaus product formula," Journal of Mathematical Physics **47** (2006).

[116] M. Suzuki, "On the convergence of exponential operators: the Zassenhaus formula, BCH formula and systematic approximants," Communications in Mathematical Physics **57**, 193–200 (1977).

[117] R. Ossikovski, "Analysis of depolarizing Mueller matrices through a symmetric decomposition," J. Opt. Soc. Am. A pp. 1109–1118 (2009).

[118] C. Fallet, A. Pierangelo, R. Ossikovski, and A. De Martino, "Experimental validation of the symmetric decomposition of Mueller matrices," Opt. Express **18**, 831–842 (2010).

[119] G. E. Jellison and F. A. Modine, "Two-modulator generalized ellipsometry: theory," Appl. Opt. **36**, 8190–8198 (1997).

[120] G. E. Jellison and F. A. Modine, "Two-modulator generalized ellipsometry: experiment and calibration," Appl. Opt. **36**, 8184–8189 (1997).

[121] G. E. Jellison and F. Modine, "Two modulator generalized ellipsometer for complete Mueller matrix measurement," U.S. patent **5,956,147** (1999).

[122] S. N. Jasperson and S. E. Schnatterly, "An improved method for high reflectivity ellipsometry based on a new polarization modulation technique," Review of Scientific Instruments **40**, 761–767 (1969).

[123] B. Drévillon, J. Perrin, R. Marbot, A. Violet, and J. L. Dalby, "Fast polarization modulated ellipsometer using a microprocessor system for digital Fourier analysis," Review of Scientific Instruments **53**, 969–977 (1982).

[124] O. Acher, E. Bigan, and B. Drévillon, "Improvements of phase-modulated ellipsometry," Review of Scientific Instruments **60**, 65–77 (1989).

[125] A. Canillas, E. Pascual, and B. Drévillon, "An IR phase-modulated ellipsometer using a Fourier transform spectrometer for in situ applications," Thin Solid Films **234**, 318–322 (1993).

[126] A. Canillas, E. Pascual, and E. Bertran, "Calibration improvement of Fourier transform infrared phase-modulated ellipsometry," J. Opt. Soc. Am. A **13**, 2461–2467 (1996).

[127] P. Hauge, "Recent developments in instrumentation in ellipsometry," Surface Science **96**, 108–140 (1980).

[128] J. C. Kemp, "Piezo-optical birefringence modulators: new use for a long-known effect," J. Opt. Soc. Am. **59**, 950–953 (1969).

[129] J. C. Canit and J. Badoz, "New design for a photoelastic modulator," Appl. Opt. **22**, 592–594 (1983).

[130] B. Wang, E. Hinds, and E. Krivoy, "Basic optical properties of the photoelastic modulator part II: residual birefringence in the optical element," (SPIE, 2009), vol. 7461, pp. 746110+.

[131] G. E. Jellison and F. A. Modine, "Accurate calibration of a photoelastic modulator in polarization modulation ellipsometry," in "Society of Photo-Optical Instrumentation Engineers (SPIE) Conference Series," , vol. 1166, R. A. Chipman, ed. (1990), vol. 1166, pp. 231–241.

[132] H. Tompkins and E. A. Irene, *Handbook of Ellipsometry (Materials Science and Process Technology)* (William Andrew, 2004).

[133] F. A. Modine, "Circuit for maintaining constant phototube current in polarization modulation spectroscopy," Review of Scientific Instruments **50**, 386–387 (1979).

[134] G. E. Jellison and F. A. Modine, "Two-modulator generalized ellipsometry: Theory-erratum," Appl. Opt. **42**, 3765 (2003).

[135] G. E. Jellison, F. A. Modine, and C. Chen, "Calibration procedures for a two-modulator generalized ellipsometer," in "Society of Photo-Optical Instrumentation Engineers (SPIE) Conference Series," , vol. 3754 (1999), vol. 3754, pp. 150–160.

[136] H. K. Pak and B. M. Law, "2D imaging ellipsometric microscope," Review of Scientific Instruments **66**, 4972–4976 (1995).

[137] A. De Martino, Y.-K. Kim, E. Garcia-Caurel, B. Laude, and B. Drévillon, "Optimized Mueller polarimeter with liquid crystals," Opt. Lett. **28**, 616–618 (2003).

[138] P. S. Hauge, "Mueller matrix ellipsometry with imperfect compensators," J. Opt. Soc. Am. **68**, 1519–1528 (1978).

[139] J. S. Baba, J.-R. R. Chung, A. H. DeLaughter, B. D. Cameron, and G. L. Coté, "Development and calibration of an automated Mueller matrix polarization imaging system." Journal of biomedical optics **7**, 341–349 (2002).

[140] E. Compain and B. Drévillon, "Complete high-frequency measurement of Mueller matrices based on a new coupled-phase modulator," Review of Scientific Instruments **68**, 2671–2680 (1997).

[141] R. W. Collins and J. Koh, "Dual rotating-compensator multichannel ellipsometer: instrument design for real-time Mueller matrix spectroscopy of surfaces and films," J. Opt. Soc. Am. A **16**, 1997–2006 (1999).

[142] C. Chen, I. An, G. M. Ferreira, N. J. Podraza, J. A. Zapien, and R. W. Collins, "Multichannel Mueller matrix ellipsometer based on the dual rotating compensator principle," Thin Solid Films **455-456**, 14–23 (2004).

[143] F. Delplancke, "Automated high-speed Mueller matrix scatterometer," Appl. Opt. **36**, 5388–5395 (1997).

[144] E. Garcia-Caurel, A. De Martino, and B. Drévillon, "Spectroscopic Mueller polarimeter based on liquid crystal devices," Thin Solid Films **455-456**, 120–123 (2004).

[145] A. De Martino, "General methods for optimized design and calibration of Mueller polarimeters," Thin Solid Films **455-456**, 112–119 (2004).

[146] J. O. Stenflo, "Solar polarimetry with ZIMPOL. Plans for the future," Memorie della Societa Astronomica Italiana **78** (2007).

[147] R. M. A. Azzam, "Simulation of mechanical rotation by optical rotation: Application to the design of a new Fourier photopolarimeter," J. Opt. Soc. Am. **68**, 518–521 (1978).

[148] O. Arteaga, A. Canillas, J. Crusats, Z. El-Hachemi, G. E. Jellison, J. Llorca, and J. M. Ribó, "Chiral biases in solids by effect of shear gradients: A speculation on the deterministic origin of biological homochirality," Origins of Life (2009).

[149] J. F. Nye, *Physical Properties of Crystals: Their Representation by Tensors and Matrices* (Oxford University Press, USA, 1985).

[150] G. E. Jellison, "Windows in ellipsometry measurements." Applied optics **38**, 4784–4789 (1999).

[151] S. Chandrasekhar, "Optical Rotatory Dispersion of Crystals," Proceedings of the Royal Society of London. Series A, Mathematical and Physical Sciences **259**, 531–553 (1961).

[152] O. Arteaga, A. Canillas, and G. E. Jellison, "Determination of the components of the gyration tensor of quartz by oblique incidence transmission two-modulator generalized ellipsometry," Appl. Opt. **48**, 5307–5317 (2009).

[153] T. Yoshizawa, ed., *Handbook of Optical Metrology: Principles and Applications* (CRC, 2009), 1st ed.

[154] C. Y. Han and Y. F. Chao, "Photoelastic modulated imaging ellipsometry by stroboscopic illumination technique," Review of Scientific Instruments **77**, 023107+ (2006).

[155] P. Gleyzes, A. C. Boccara, and H. Saint-Jalmes, "Multichannel Nomarski microscope with polarization modulation: performance and applications," Opt. Lett. **22**, 1529–1531 (1997).

[156] H.-M. Tsai and Y.-F. Chao, "Optimization of a four-temporal phase lock for photoelastic-modulated polarimetry," Opt. Lett. **34**, 2279–2281 (2009).

[157] D. J. Diner, A. Davis, B. Hancock, S. Geier, B. Rheingans, V. Jovanovic, M. Bull, D. M. Rider, R. A. Chipman, A.-B. Mahler, and S. C. McClain, "First results from a dual photoelastic-modulator-based polarimetric camera," Appl. Opt. **49**, 2929–2946 (2010).

[158] T. M. Lowry, "Optical Rotatory Dispersion. Part I: The Natural and Magnetic Rotatory Dispersion in Quartz of Light in the Visible Region of the Spectrum," Royal Society of London Philosophical Transactions Series A **212**, 261–297 (1913).

[159] C. Chou, Y.-C. Huang, and M. Chang, "Precise optical activity measurement of quartz plate by using a true phase-sensitive technique," Appl. Opt. **36**, 3604–3609 (1997).

[160] D. Yogev-Einot and D. Avnir, "The temperature-dependent optical activity of quartz: from Le Châtelier to chirality measures," Tetrahedron: Asymmetry **17**, 2723–2725 (2006).

[161] M. B. Myers and K. Vedam, "Effect of pressure on the optical rotatory power and dispersion of crystalline sodium chlorate," J. Opt. Soc. Am. **57**, 1146–1148 (1967).

[162] J. R. L. Moxon, A. R. Renshaw, and I. J. Tebbutt, "The simultaneous measurement of optical activity and circular dichroism in birefringent linearly dichroic crystal sections. II. Description of apparatus and results for quartz, nickel sulphate hexahydrate and benzil," Journal of Physics D: Applied Physics **24**, 1187–1192 (1991).

[163] C. Hernandez-Rodriguez and P. Gomez-Garrido, "Optical anisotropy of quartz in the presence of temperature-dependent multiple reflections using a high-accuracy universal polarimeter," Journal of Physics D: Applied Physics **33**, 2985–2994 (2000).

[164] G. L. Tan, M. F. Lemon, D. J. Jones, and R. H. French, "Optical properties and London dispersion interaction of amorphous and crystalline SiO_2 determined by vacuum ultraviolet spectroscopy and spectroscopic ellipsometry," Physical Review B **72**, 205117+ (2005).

[165] G. Szivessy and C. Münster, "Über die prüfung der gitteroptik bei aktiven kristallen," Annalen der Physik **412**, 703–736 (1934).

[166] M. Born, *Optik: Ein Lehrbuch der elektromagnetische Lichttheorie* (Springer, 1933).

[167] A. Konstantinova, B. Nabatov, E. Evdishchenko, and K. Konstantinov, "Modern application packages for rigorous solution of problems of light propagation in anisotropic layered media: II. Optically active crystals," Crystallography Reports **47**, 815–823 (2002).

[168] Konstantinova, A., Evdishchenko, E., Imangazieva, and K., "Manifestation of optical activity in crystals of different symmetry classes," Crystallography Reports **51**, 998–1008 (2006).

[169] D. Eimerl, "Quantum electrodynamics of optical activity in birefringent crystals," J. Opt. Soc. Am. B **5**, 1453–1461 (1988).

[170] G. Ghosh, "Dispersion-equation coefficients for the refractive index and birefringence of calcite and quartz crystals," Optics Communications **163**, 95–102 (1999).

[171] T. Bradshaw and G. H. Livens, "The formula for the optical rotatory dispersion of quartz," Proceedings of the Royal Society of London. Series A, Containing Papers of a Mathematical and Physical Character **122**, 245–250 (1929).

[172] S.-L. Lu and A. P. Loeber, "Depolarization of white light by a birefringent crystal," J. Opt. Soc. Am. **65**, 248+ (1975).

[173] O. Arteaga and A. Canillas, "Pseudopolar decomposition of the Jones and Mueller-Jones exponential polarization matrices," J. Opt. Soc. Am. A **26**, 783–793 (2009).

[174] G. E. Jellison and C. M. Rouleau, "Determination of optical birefringence by using off-axis transmission ellipsometry," Appl. Opt. **44**, 3153–3159 (2005).

[175] A. Konstantinova, K. Rudoy, B. Nabatov, E. Evdishchenko, V. Stroganov, and O. Pikul', "The influence of optical activity on the intensity and polarization parameters of transmitted light in crystals," Crystallography Reports **48**, 823–831 (2003).

[176] J. Jerphagnon and D. S. Chemla, "Optical activity of crystals," The Journal of Chemical Physics **65**, 1522–1529 (1976).

[177] C. Honda and H. Hada, "Circular dichroism of poly-molecular associate, J-aggregate, of 1,12-diethyl-2,22-cyanine chloride by regular stirring of the solution," Tetrahedron Letters **17**, 177–180 (1976).

[178] O. Ohno, Y. Kaizu, and H. Kobayashi, "J-aggregate formation of a water-soluble porphyrin in acidic aqueous media," The Journal of Chemical Physics **99**, 4128+ (1993).

[179] J. M. Ribo, J. Crusats, F. Sagues, J. Claret, and R. Rubires, "Chiral sign induction by vortices during the formation of mesophases in stirred solutions," Science **292**, 2063–2066 (2001).

[180] A. D'Urso, R. Randazzo, L. Lo Faro, and R. Purrello, "Vortexes and nanoscale chirality," Angewandte Chemie International Edition **49**, 108–112 (2010).

[181] A. Tsuda, Md, T. Harada, T. Yamaguchi, N. Ishii, and T. Aida, "Spectroscopic visualization of vortex flows using dye-containing nanofibers," Angewandte Chemie International Edition **46**, 8198–8202 (2007).

[182] M. Wolffs, S. J. George, Z. Tomović, S. C. Meskers, A. P. Schenning, and E. W. Meijer, "Macroscopic origin of circular dichroism effects by alignment of self-assembled fibers in solution." Angewandte Chemie (International ed. in English) **46**, 8203–8205 (2007).

[183] O. Arteaga, C. Escudero, G. Oncins, Z. El-Hachemi, J. Llorens, J. Crusats, A. Canillas, and J. M. Ribó, "Reversible mechanical induction of optical activity in solutions of soft-matter nanophases," Chemistry - An Asian Journal **4**, 1687–1696 (2009).

[184] C. Escudero, J. Crusats, I. Díez-Pérez, Z. El-Hachemi, and J. M. Ribó, "Folding and hydrodynamic forces in J-aggregates of 5-phenyl-10,15,20-tris(4-sulfophenyl)porphyrin13," Angewandte Chemie **118**, 8200–8203 (2006).

[185] O. Arteaga, A. Canillas, J. Crusats, E.-H. Z., L. J., S. E., and J. M. Ribó, "Emergence of supramolecular chirality by flows," accepted in ChemPhysChem (2010).

[186] H. Fenniri, B.-L. L. Deng, and A. E. Ribbe, "Helical rosette nanotubes with tunable chiroptical properties." Journal of the American Chemical Society **124**, 11064–11072 (2002).

[187] J. G. Moralez, J. Raez, T. Yamazaki, R. K. Motkuri, A. Kovalenko, and H. Fenniri, "Helical rosette nanotubes with tunable stability and hierarchy," Journal of the American Chemical Society **127**, 8307–8309 (2005).

[188] R. S. Johnson, T. Yamazaki, A. Kovalenko, and H. Fenniri, "Molecular basis for water-promoted supramolecular chirality inversion in helical rosette nanotubes," Journal of the American Chemical Society **129**, 5735–5743 (2007).

[189] A. Y. Elezzabi and S. Sederberg, "Optical activity in an artificial chiral media: a terahertz time-domain investigation of Karl F. Lindman's 1920 pioneering experiment," Opt. Express **17**, 6600–6612 (2009).

[190] K. F. Lindman, "Über eine durch ein isotropes system von spiralförmigen resonatoren erzeugte rotationspolarisation der elektromagnetischen wellen," Annalen der Physik **368**, 621–644 (1920).

[191] G. S. Ranganath and S. Ramaseshan, "Piezo-rotatory coefficients and crystal symmetry," J. Opt. Soc. Am. **59**, 1229–1232 (1969).

[192] D. K. Kondepudi, R. J. Kaufman, and N. Singh, "Chiral symmetry breaking in sodium chlorate crystallizaton," Science **250**, 975–976 (1990).

[193] C. Viedma, "Chiral symmetry breaking during crystallization: Complete chiral purity induced by nonlinear autocatalysis and recycling," Physical Review Letters **94**, 065504+ (2005).

[194] N. K. Chaudhuri and M. A. El-Sayed, "Molecular origin of the optical rotatory dispersion of the benzil crystal," J. Chem. Phys. **47**, 1133–1143 (1967).

[195] J. Ríha, I. Vysín, and H. Lapanská, "Theory, measurement, and origin of optical activity in benzil crystal," Molecular Crystals and Liquid Crystals **442**, 181–201 (2005).

[196] D. Hochberg and M. Zorzano, "Reaction-noise induced homochirality," Chemical Physics Letters **431**, 185–189 (2006).

[197] A. Giaquinta and D. Hochberg, "Chiral symmetry breaking: (I) limited enantioselectivity and (II) mutual inhibition," Physica D: Nonlinear Phenomena **237**, 2563–2576 (2008).

[198] O. Arteaga, A. Canillas, J. Crusats, Z. El-Hachemi, G. Jellison, J. Llorca, and J. Ribó, "Chiral biases in solids by effect of shear gradients: A speculation on the deterministic origin of biological homochirality," Origins of Life and Evolution of Biospheres **40**, 27–40 (2010).

[199] K. Kvenvolden, J. Lawless, K. Pering, E. Peterson, J. Flores, C. Ponnamperuma, I. R. Kaplan, and C. Moore, "Evidence for extraterrestrial amino-acids and hydrocarbons in the Murchison meteorite," Nature **228**, 923–926 (1970).

[200] G. Cooper, N. Kimmich, W. Belisle, J. Sarinana, K. Brabham, and L. Garrel, "Carbonaceous meteorites as a source of sugar-related organic compounds for the early Earth," Nature **414**, 879–883 (2001).

[201] S. Pizzarello, Y. Huang, and M. Fuller, "The carbon isotopic distribution of Murchison amino acids," Geochimica et Cosmochimica Acta **68**, 4963–4969 (2004).

[202] D. P. Glavin and J. P. Dworkin, "Enrichment of the amino acid l-isovaline by aqueous alteration on CI and CM meteorite parent bodies," Proceedings of the National Academy of Sciences **106**, 5487–5492 (2009).

[203] T. Kawasaki, K. Hatase, Y. Fuj, K. Jo, K. Soai, and S. Pizzarello, "The distribution of chiral asymmetry in meteorites: An investigation using asymmetric autocatalytic chiral sensors," Geochimica et Cosmochimica Acta **70**, 5395–5402 (2006).

[204] T. Zega, "Serpentine nanotubes in the Mighei CM chondrite," Earth and Planetary Science Letters **223**, 141–146 (2004).

[205] G. E. Christidis, F. Dellisanti, G. Valdre, and P. Makri, "Structural modifications of smectites mechanically deformed under controlled conditions," Clay Minerals **40**, 511–522 (2005).

[206] M. P. Silverman, J. Badoz, and B. Briat, "Chiral reflection from a naturally optically active medium," Opt. Lett. **17**, 886–888 (1992).

[207] A. Ghosh and P. Fischer, "Chiral molecules split light: Reflection and refraction in a chiral liquid," Physical Review Letters **97**, 173002 (2006).

[208] D. Lara and C. Dainty, "Axially resolved complete Mueller matrix confocal microscopy," Appl. Opt. **45**, 1917–1930 (2006).

[209] Z. El-Hachemi, O. Arteaga, A. Canillas, J. Crusats, C. Escudero, R. Kuroda, T. Harada, M. Rosa, and J. M. Ribó, "On the mechano-chiral effect of vortical flows on the dichroic spectra of 5-phenyl-10,15,20-tris(4-sulfonatophenyl) porphyrin J-aggregates," Chemistry - A European Journal **14**, 6438–6443 (2008).